SLAC-R-868
May 2007

Hyperon AND Hyperon Resonance Properties From Charm Baryon Decays At BaBar

Veronique Ziegler

SLAC-R-868

Prepared for the Department of Energy
under contract number DE-AC02-76SF00515

Printed in the United States of America. Available from the National Technical Information Service, U.S. Department of Commerce, 5285 Port Royal Road, Springfield, VA 22161.

HYPERON AND HYPERON RESONANCE PROPERTIES FROM CHARM BARYON DECAYS AT *BABAR*

by

Veronique Ziegler

An Abstract

Of a thesis submitted in partial fulfillment of the
requirements for the Doctor of Philosophy
degree in Physics
in the Graduate College of
The University of Iowa

May 2007

Thesis Supervisor: Professor Usha Mallik

Work supported in part by U.S. Department of Energy contract DE-AC02-76SF00515

ABSTRACT

This thesis describes studies of hyperons and hyperon resonances produced in charm baryon decays at *BABAR*.

Using two-body decays of the Ξ_c^0 and Ω_c^0, it is shown, for the first time, that the spin of the Ω^- is 3/2.

The Ω^- analysis procedures are extended to three-body final states and properties of the $\Xi(1690)^0$ are extracted from a detailed isobar model analysis of the $\Lambda_c^+ \to \Lambda \bar{K}^0 K^+$ Dalitz plot. The mass and width values of the $\Xi(1690)^0$ are measured with much greater precision than attained previously. The hypothesis that the spin of the $\Xi(1690)$ resonance is 1/2 yields an excellent description of the data, while spin values 3/2 and 5/2 are disfavored. The $\Lambda a_0(980)^+$ decay mode of the Λ_c^+ is observed for the first time.

Similar techniques are then used to study $\Xi(1530)^0$ production in Λ_c^+ decay. The spin of the $\Xi(1530)$ is established for the first time to be 3/2. The existence of an S-wave amplitude in the $\Xi^-\pi^+$ system is shown, and its interference with the $\Xi(1530)^0$ amplitude provides the first clear demonstration of the Breit-Wigner phase motion expected for the $\Xi(1530)$. The $\Xi^-\pi^+$ mass distribution in the vicinity of the $\Xi(1690)^0$ exhibits interesting structure which may be interpreted as indicating that the $\Xi(1690)$ has negative parity.

Abstract Approved: _____

Thesis Supervisor

_____

Title and Department

_____

Date

HYPERON AND HYPERON RESONANCE PROPERTIES FROM CHARM BARYON DECAYS AT *BABAR*

by

Veronique Ziegler

A thesis submitted in partial fulfillment of the
requirements for the Doctor of Philosophy
degree in Physics
in the Graduate College of
The University of Iowa

May 2007

Thesis Supervisor: Professor Usha Mallik

Graduate College
The University of Iowa
Iowa City, Iowa

CERTIFICATE OF APPROVAL

PH.D. THESIS

This is to certify that the Ph.D. thesis of

Veronique Ziegler

has been approved by the Examining Committee for the thesis requirement for the Doctor of Philosophy degree in Physics at the May 2007 graduation.

Thesis Committee: _____
Usha Mallik, Thesis Supervisor

_____
Paul Kleiber

_____
Craig Kletzing

_____
William Klink

_____
Helen Quinn

ACKNOWLEDGEMENTS

I am very much indebted to my parents for their love and support, and mostly for teaching me to never give up.

I wish to thank Karl Lonngren for setting me on the path toward the completion of this degree.

I wish to thank my advisor, Usha Mallik, for giving me the opportunity to obtain this degree. Her support and encouragements have been most appreciated.

I also wish to thank the present and past members of the *BABAR* group at the University of Iowa for their support.

I am grateful to the members of Group B for welcoming me as part of their team. As am very happy about the prospect of working with them.

I am especially grateful to Helen Quinn for sharing her time and ideas, and for being a great source of inspiration for me.

Finally, I would like to express my deepest gratitude to the person who has had the largest impact on this thesis work and completion, Bill Dunwoodie. I thank him for his caring, guidance and mentoring. His sharing of ideas has truly been the foundation around which this research has grown.

ABSTRACT

This thesis describes studies of hyperons and hyperon resonances produced in charm baryon decays at *BABAR*.

Using two-body decays of the Ξ_c^0 and Ω_c^0, it is shown, for the first time, that the spin of the Ω^- is 3/2.

The Ω^- analysis procedures are extended to three-body final states and properties of the $\Xi(1690)^0$ are extracted from a detailed isobar model analysis of the $\Lambda_c^+ \to \Lambda \bar{K}^0 K^+$ Dalitz plot. The mass and width values of the $\Xi(1690)^0$ are measured with much greater precision than attained previously. The hypothesis that the spin of the $\Xi(1690)$ resonance is 1/2 yields an excellent description of the data, while spin values 3/2 and 5/2 are disfavored. The $\Lambda a_0(980)^+$ decay mode of the Λ_c^+ is observed for the first time.

Similar techniques are then used to study $\Xi(1530)^0$ production in Λ_c^+ decay. The spin of the $\Xi(1530)$ is established for the first time to be 3/2. The existence of an S-wave amplitude in the $\Xi^-\pi^+$ system is shown, and its interference with the $\Xi(1530)^0$ amplitude provides the first clear demonstration of the Breit-Wigner phase motion expected for the $\Xi(1530)$. The $\Xi^-\pi^+$ mass distribution in the vicinity of the $\Xi(1690)^0$ exhibits interesting structure which may be interpreted as indicating that the $\Xi(1690)$ has negative parity.

TABLE OF CONTENTS

LIST OF TABLES

Table

LIST OF FIGURES

Figure

CHAPTER 1
INTRODUCTION

The world around us is composed of baryons, bound-states of three quarks, whose dynamics is governed by strong interactions. Therefore, understanding the dynamical degrees of freedom necessary to describe these systems is essential to the development of the theory strong interactions (QCD).

Historically, the properties of light baryons have played a central role leading to the invention of the quark model and the emergence of an understanding of the symmetry structure underlying baryon spectroscopy. The comparison of the experimentally measured properties of these states with model predictions is therefore crucial in establishing the validity of such models.

This thesis contributes to the field of baryon spectroscopy by establishing the spin of the Ω^- hyperon and of the $\Xi(1530)$ to be 3/2 in confirmation of the quark model predictions, and by providing precise mass and width measurements for the $\Xi(1690)$, together with evidence favoring a spin value of 1/2. This state is of significance because it seems to be the lowest-mass Cascade resonance above the $\Xi(1530)$. Models typically use the $\Xi(1320)$ and $\Xi(1530)$ as input to define the mass scale, so that the $\Xi(1690)$ provides a clear test of predictive power as it pertains to mass, spin and parity; indeed this state is absent from certain quark model predictions of Cascade baryon spectra.

The prediction and discovery of the baryons studied in this thesis are discussed in the next sections, in connection with the motivation for analyzing the properties

of these particles.

1.1 The Ω^-, a Triply Strange Particle

By the early fifties, the first modern accelerators had begun producing newly discovered heavy baryons such as the Δ's, Σ's and Ξ's. The behavior of these particles appeared "strange" in the sense that although they were produced with high rates (i.e. via strong interactions), they appeared to decay rather slowly (i.e. via weak interactions), indicating clearly that their production mechanisms differed from their decay processes. Furthermore, experimental evidence indicated that a strange particle was always produced with another. A clever idea proposed by Gell-Mann and others [1, 2, 3, 4, 5, 6] provided an explanation of this phenomenon. They assigned a new quantum number, called "strangeness" (S), to each particle. The fact that strangeness is conserved in the strong interactions and is not in weak decays explained the production and decay behavior of strange particles.

A decade later, hadron physics was flooded with newly discovered strongly decaying meson and baryon states (i.e. resonances) which could be characterized by charge, mass, strangeness, and when known, spin and parity. There was a clear need for an underlying principle which might lead to a procedure to organize the plethora of newly discovered states.

At that time strong isospin (I) symmetry was known, and it explained the near degeneracy in mass between the proton and the neutron. Although the proton has a positive charge, and the neutron is neutral, the strength of the strong interaction

between any pair of nucleons is the same, independent of whether they are interacting as protons or as neutrons. Strong isospin is an $SU(2)$ symmetry in which the neutron and proton form an isospin doublet.

Gell-Mann, and independently Ne'eman [7, 8, 9], extended isospin symmetry by proposing a model in which strong interactions are invariant under unimodular unitary transformations of the the group $SU(3)$. The irreducible representations (called multiplets) of $SU(3)$ correspond to *groups* of strongly interacting particles with identical quantum numbers, J^P for baryons, and J^{PC} for mesons[1]. The vector ($J = 1$) and pseudoscalar ($J = 0$) mesons are assigned to the octet[2] irreducible representation, and the ground-state baryons to octets and a decuplet. The arrangement of particles in a given multiplet is according to I_3, the third component of isospin, and strangeness such that $Q = I_3 + (S + B)/2$, where Q is charge, S is strangeness, and B is baryon number. In nature this symmetry of strong interactions is broken, its brokenness made manifest by the differences in mass among the isospin multiplets incorporated in a given octet or decuplet.

Combining the pseudoscalar meson and baryon octets to yield a multiplet (Fig. 1.1) including the $I = 3/2$ Δ resonance with $J^P = 3/2^+$ restricts the possible representations to a **10** (decuplet) and a **27** [3]. Once the **27** had been ruled out by

[1]Where J is the spin quantum number, P, is parity and C, charge conjugation (for neutral, non-strange mesons only).

[2]This arrangement was referred to by Gell-Mann as the "Eightfold Way".

[3]It was believed that the Δ and $\Sigma(1385)$ must be in a **27** which had this symmetry, and as a consequence experimenters were urged to look for states with positive strangeness. The assignment to the **27** representation was based on a wrong experiment which seemed

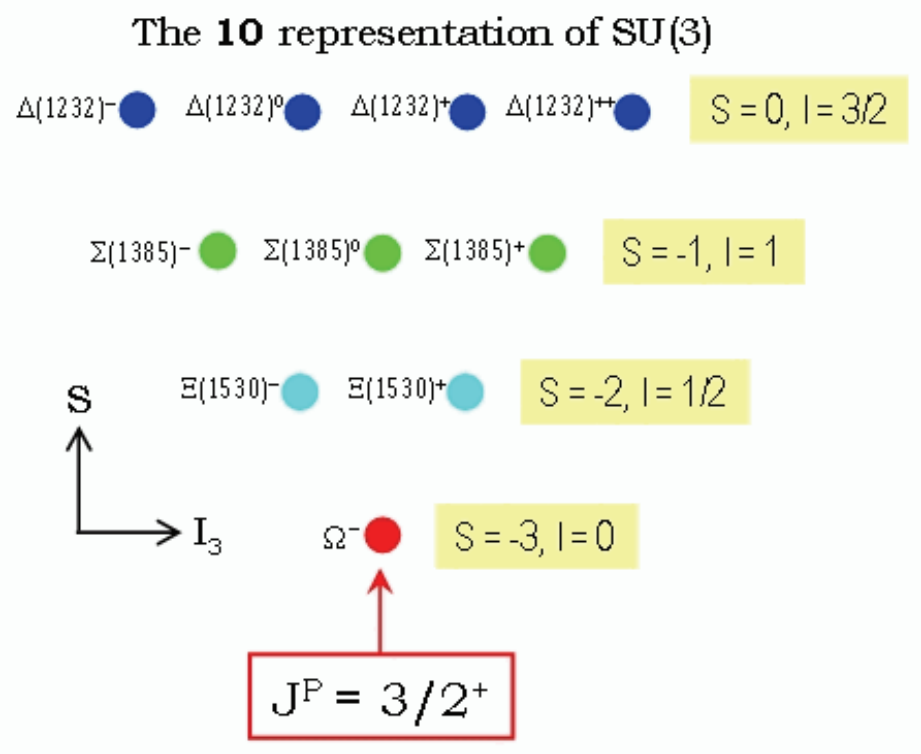

Figure 1.1: The $J^P = 3/2^+$ **10** representation of $SU(3)$ containing the Δ quartet, the $\Sigma(1385)$ $Y = 0$ triplet, the $\Xi(1530)$ doublet with $Y = -1$ and the Ω^-, a singlet with $Y = -2$.

the absence of any $I = 1$, $Y = 2$ ($Y = S + B$ is hypercharge, where B corresponds to baryon number) low-mass resonance in $K\,N$ interactions, only an equal-mass-spacing decuplet containing the Δ quartet, the $\Sigma(1385)$ triplet with $Y = 0$, a doublet with $Y = -1$ and a singlet with $Y = -2$ was left. The $\Sigma(1385)$ was believed to have $J^P = 3/2^+$, and thus satisfied the triplet requirement, leading to mass estimates of $\sim$ 1530 MeV and $\sim$ 1680 MeV for the remaining members, on the basis of the equal-mass splitting prediction resulting from the Eightfold Way (Fig. 1.1).

---

to show that the $\Sigma(1385)$ decayed only into $\Lambda\pi$ and not into $\Sigma\pi$. The **27** gave a selection rule forbidding decay to $\Sigma\pi$. The decuplet predicted the correct ratio of $\Sigma\pi$ to $\Lambda\pi$, however it took several years for this to be confirmed experimentally.

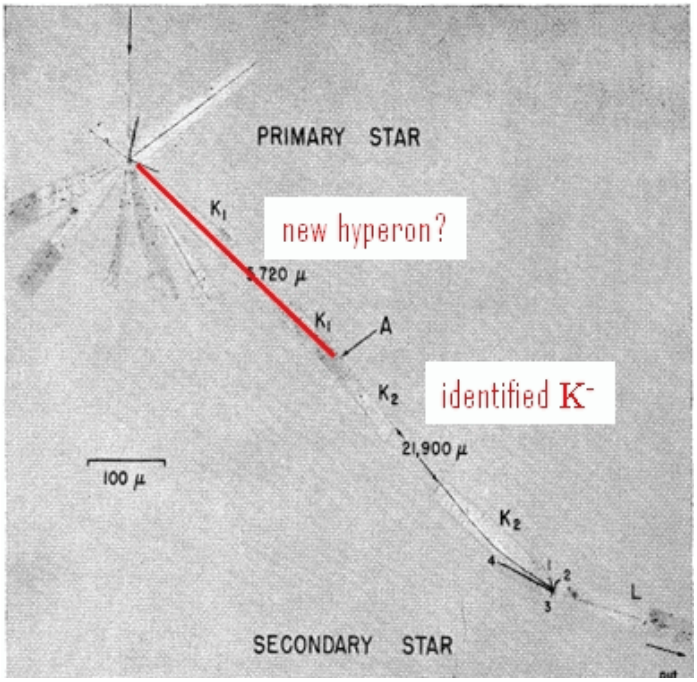

Figure 1.2: The Eisenberg Cosmic-ray event was the first observation of a hyperon thought to decay to a kaon. The event was later analyzed by Alvarez and understood to be the interaction of the Ω^- with a silver nucleus ($\Omega^- + Ag \rightarrow \Xi^0 + K^- + Ag$) [13].

At the 1962 ICHEP conference, evidence was presented for a Ξ^* resonance of mass $\sim$ 1530 MeV, which was later shown to have $J^P = 3/2^+$. Gell-Mann [10] following the relevant rapporteur talk, pointed out that the Ξ^* could belong to this multiplet and suggested that a search be carried out for the last particle of the decuplet, the Ω^-, as he named it[4], with $S = -3$ and $I = 0$ and a mass $\sim$ 1685 MeV. He predicted that the Ω^- should decay weakly to ΛK^-, $\Xi^0\pi^-$ (the mode in which it was first observed) and $\Xi^-\pi^0$. He suggested that it might explain the "old Eisen-

[4]Gell-Mann actually used this symbol for an $S = -3$ baryon in 1956 in the Appendix of refce. [6]. There he speculated that such a particle would decay weakly to $\Xi\pi$, and possibly ΛK^- if it were sufficiently massive.

berg event" (Fig. 1.2)[11], which it did, and that it might be found in the reaction $K^- p \to K^0 K^+ \Omega^-$, which it was (Fig. 1.3)[12].

Shortly after the $SU(3)$ classification scheme predicted the existence of the Ω^- hyperon[5], it was observed with the predicted mass in a bubble chamber experiment [12]. In subsequent attempts to confirm the spin of the Ω^- [14, 15, 16], K^- p interactions in a liquid hydrogen bubble chamber were studied. In each case only a small Ω^- data sample was obtained, and the Ω^- production mechanism was not well understood. As a result, these experiments succeeded only in establishing that the Ω^- spin is greater than 1/2. At *BABAR* exclusive hyperon production from charm baryons (see section 1.3), enables the determination of the spin of the Ω^- unambiguously[6], as described in chapter 4. Later, the quark model put the $SU(3)$ classification on more solid ground and the Ω^- was understood to be a hyperon with three strange quarks.

The quark model as it pertains to the symmetry structure of light (i.e. u, d, s) baryon spectroscopy is reviewed briefly in the next section.

1.2 The Quark Model

Theoretical descriptions of hadrons are based on the concept of constituent quarks. The assignment of quantum numbers to quarks sets the foundation for the Quark Model.

[5] A hyperon is a baryon with non-zero strangeness

[6] Under the assumption that the charm baryon spin is 1/2.

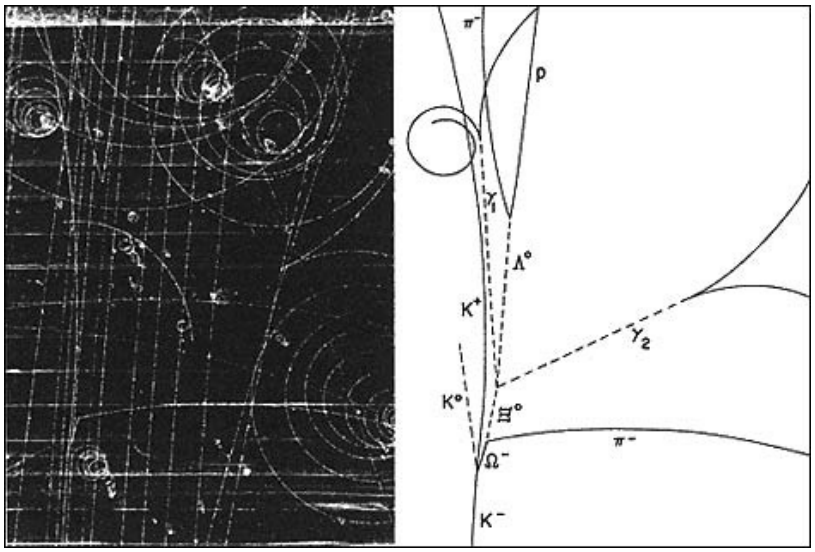

Figure 1.3: The first observation of the Ω^- in a bubble chamber experiment at Brookhaven National Laboratory. An incoming K^- meson interacts with a proton in the liquid hydrogen of the bubble chamber and produces an Ω^-, a K^0 and a K^+.

1.2.1 The Mathematics of Quarks

The name "quark" first appeared in the literature 1964 in a paper by Gell-Mann entitled "A Schematic Model of Baryons and Mesons" [17][7]. The u, d and s quarks belong to the fundamental representation of $SU(3)$, which is a triplet with spin 1/2 and baryon number 1/3. This triplet contains the strong-isospin doublet, (u, d), with electric charge assignments (2/3, -1/3) and strangeness 0, as well as the singlet, s, with electric charge -1/3 and strangeness -1. The quantum numbers assigned to the (u, d, s) quarks are summarized in Table 1.1. In $SU(3)$ there are two non-equivalent fundamental representations, the quark ($\mathbf{3}$) and antiquark ($\bar{\mathbf{3}}$) multiplets (Fig. 1.4). The fundamental $SU(3)_F$ (Flavor) multiplets are in the (Y, I_3) plane, where

[7] A similar model in which mesons and baryons were constructed by a set a 3 fundamental constituents called *aces* was implemented by Zweig [18] around the same time.

Table 1.1: The (u, d, s) quark quantum numbers.

Quark	Spin	S	B	Y	I_3	Q
u	1/2	0	1/3	1/3	1/2	2/3
d	1/2	0	1/3	1/3	-1/2	-1/3
s	1/2	-1	1/3	-2/3	0	-1/3

Note: Hypercharge is $Y(= B + S)$ and the charge is $Q = I_3 + \frac{Y}{2}$.

the additive quantum number hypercharge $(Y = B + S)$ is related to strong-isospin by the charge $Q = I_3 + \frac{Y}{2}$. The triangular arrangement of the fundamental multiplets of $SU(3)_F$ of Fig. 1.4 is such that the centroid coincides with the origin and that the conjugate configuration is obtained by means of a reflection in the origin.

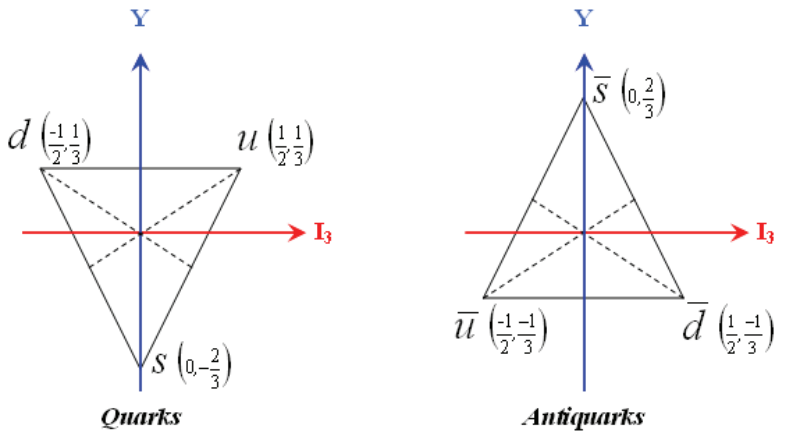

Figure 1.4: The $SU(3)$ quark and antiquark multiplets. The relationship between strangeness and hypercharge is given by $Y = B + S$.

1.2.2 Degeneracies

In a world of *perfect* symmetries, the members of a particular $SU(3)_F$ multiplet would be degenerate, meaning that in addition to having the same spin-parity they

would have the same mass, thereby looking like one state.

This degeneracy is removed by the interactions which break the symmetry. The $SU(3)_F$ multiplets are of rank 2 and can therefore contain $SU(2)$ symmetries. The mass degeneracy of the $SU(2)_F$ multiplet members is broken primarily because of mass difference between the u and d quarks[8] which yield observed mass splittings typically of a few MeV/c^2. However, $SU(2)_F$ remains a good approximate symmetry due to the fact that the u and d quark mass difference is much smaller than Λ_{QCD}[9]. Electromagnetic interactions contribute to a lesser extent to $SU(2)_F$ symmetry breaking. The degeneracy of $SU(3)_F$ is further broken by the mass splitting between the (u, d) doublet and the s quarks, resulting in mass splittings among the $SU(2)_F$ multiplets of typically $\sim 100 - 150$ MeV/c^2. As a consequence, of the three $SU(2)$ symmetries, $SU(2)_I$ (I-spin), $SU(2)_V$ (V-spin), and $SU(2)_U$ (U-spin), contained in $SU(3)_F$, the latter two are badly broken[10].

[8]The d quark mass is approximately twice that of the u quark.

[9]Λ_{QCD} (100 MeV$< \Lambda_{QCD} <$500 MeV) sets the scale of strong interactions.

[10]The symmetries of $SU(2)_I$, $SU(2)_V$, and $SU(2)_U$ are characterized by the raising and lowering operators

$$I_{\pm} = \frac{1}{2}\left[q^{\dagger}\left(\lambda^1 \pm i\lambda^2\right) q - \bar{q}^{\dagger}\left(\lambda^1 \pm i\lambda^2\right)^* \bar{q}\right] = \begin{pmatrix} u^{\dagger}d - \bar{d}^{\dagger}\bar{u} \\ d^{\dagger}u - \bar{u}^{\dagger}\bar{d} \end{pmatrix},$$

for I-spin;

$$V_{\pm} = \frac{1}{2}\left[q^{\dagger}\left(\lambda^4 \pm i\lambda^5\right) q - \bar{q}^{\dagger}\left(\lambda^4 \pm i\lambda^5\right)^* \bar{q}\right] = \begin{pmatrix} s^{\dagger}u - \bar{s}^{\dagger}\bar{u} \\ u^{\dagger}s - \bar{u}^{\dagger}\bar{s} \end{pmatrix},$$

for V-spin;

$$U_{\pm} = \frac{1}{2}\left[q^{\dagger}\left(\lambda^6 \pm i\lambda^7\right) q - \bar{q}^{\dagger}\left(\lambda^6 \pm i\lambda^7\right)^* \bar{q}\right] = \begin{pmatrix} s^{\dagger}d - \bar{s}^{\dagger}\bar{d} \\ d^{\dagger}s - \bar{d}^{\dagger}\bar{s} \end{pmatrix},$$

for U-spin.

1.2.3 Light Baryon Flavor Multiplets

Light baryons (qqq bound-states, with $q = u, d, s$) belong to the multiplets obtained from the decomposition

$$3 \otimes 3 \otimes 3 = \mathbf{1} \oplus \mathbf{8} \oplus \mathbf{8} \oplus \mathbf{10},$$

yielding a singlet, two octets and a decuplet, corresponding to 27 states.

The wave-function describing a hadron is factorizable, and may be written

$$\psi(hadron) = \psi(space) \cdot \psi(spin) \cdot \psi(flavor).$$

Fermi-Dirac statistics require the baryon wave-function to be totally anti-symmetric under the exchange of two quarks, since baryons are fermions. The ground-state baryonic space configuration is symmetric[11] under an interchange of position in any two quarks.

The decuplet is fully symmetric. It contains in its corners the symmetric combinations (uuu), (ddd), and (sss) (Fig. 1.5). This symmetry for the ground state poses a problem: the spin-flavor wave-function describing the spin 3/2 Δ^{++} $(u\uparrow u\uparrow u\uparrow)$, for example, is completely symmetric. Therefore the Δ^{++} overall wave-function $\psi(space)\cdot\psi(spin)\cdot\psi(flavor)$ does not obey the fermi-required antisymmetry under the exchange of identical quarks.

The $\lambda^a/2$ $(a = 1, ..., 8)$ matrices are the traceless Hermitian generators of the Lie algebra of $SU(3)$. The quark fields which transform according to the **3** of $SU(3)$ are $q^\dagger$, q, and the anti-quark fields which transform according to the $\mathbf{3}^*$ of $SU(3)$ are $\bar{q}^\dagger$, $\bar{q}$.

[11] An antisymmetric two-quark wave-function $\psi = (q_1(\vec{r_1})q_2(\vec{r_2}) - q_2(\vec{r_2})q_1(\vec{r_1}))/\sqrt{2}$ vanishes when $\vec{r_1} = \vec{r_2}$, which implies that the spatial baryon wave-function is required to be symmetric.

This problem almost caused the demise of the quark model, until it was realized that one could incorporate into the model a new quantum number which would make the wave-function antisymmetric with respect to interchanges in its assignments. If the quarks possess an additional attribute called color, which takes values R, G, or B, a combination of three quarks can be written such that the color wave-function is completely antisymmetric, as follows:

$$\psi(color) = \frac{1}{\sqrt{6}}\left(RGB - RBG + GBR - GRB + RBG - BRG\right).$$

The anti-symmetry of the baryon wave-function implies that baryons are singlets under color $SU(3)$, and as such are "colorless". Colorlessness is postulated to be a property of all hadrons. In addition, unlike $SU(3)_F$, the color symmetry $SU(3)_c$ is believed to be exact.

The $SU(3)_F$ octets, $\mathbf{8}$, have mixed symmetry, i.e. there states transform differently when quarks 1 and 2 or quarks 2 and 3 are exchanged. One of the octets, the $\mathbf{8}_{MA}$, is anti-symmetric w.r.t. the exchange of quarks 1 and 2. So in the case of the (uud) state, for example, the flavor wave function of this state in the mixed-anti-symmetric (MA) octet is

$$\psi(uud) = \frac{1}{\sqrt{2}}[(ud - du)u].$$

The mixed-symmetric (MS) octet, the $\mathbf{8}_{MS}$, is symmetric w.r.t. the exchange of quarks 1 and 2. So in the case of (uud), the flavor wave function of this state in the mixed-symmetric octet is

$$\psi(uud) = \frac{1}{\sqrt{6}}[(ud + du)u - 2uud].$$

Thus, under $SU(3)_F$ the ground state baryons belong to the multiplets on the right side of

$$\mathbf{3} \otimes \mathbf{3} \otimes \mathbf{3} = \mathbf{10}_S \oplus \mathbf{8}_{MS} \oplus \mathbf{8}_{MA} \oplus \mathbf{1}_A \tag{1.1}$$

Note that since the $SU(3)_F$ singlet is completely anti-symmetric, it is not a suitable multiplet for a ground state baryon.

The spin wave-function of the states in the $L = 0$ baryon octets (Fig. 1.5) must also be mixed-(anti-)symmetric so that their total spin-flavor be symmetric, as required by Fermi statistics.

Under the spin symmetry group $SU(2)$,

$$\mathbf{2} \otimes \mathbf{2} \otimes \mathbf{2} = \mathbf{4} \oplus \mathbf{2} \oplus \mathbf{2}.$$

Here the **4** is fully symmetric, i.e.

$$\psi_S = \frac{1}{\sqrt{3}}[\uparrow\uparrow\downarrow + (\uparrow\downarrow + \downarrow\uparrow)\uparrow].$$

One of the **2** representations is mixed-anti-symmetric

$$\psi_{MA} = \frac{1}{\sqrt{2}}[(\uparrow\downarrow - \downarrow\uparrow)\uparrow],$$

and the other **2** is mixed-symmetric

$$\psi_{MS} = \frac{1}{\sqrt{6}}[(\uparrow\downarrow + \downarrow\uparrow)\uparrow - 2\uparrow\uparrow\downarrow].$$

So that

$$\mathbf{2} \otimes \mathbf{2} \otimes \mathbf{2} = \mathbf{4}_S \oplus \mathbf{2}_{MS} \oplus \mathbf{2}_{MA}. \tag{1.2}$$

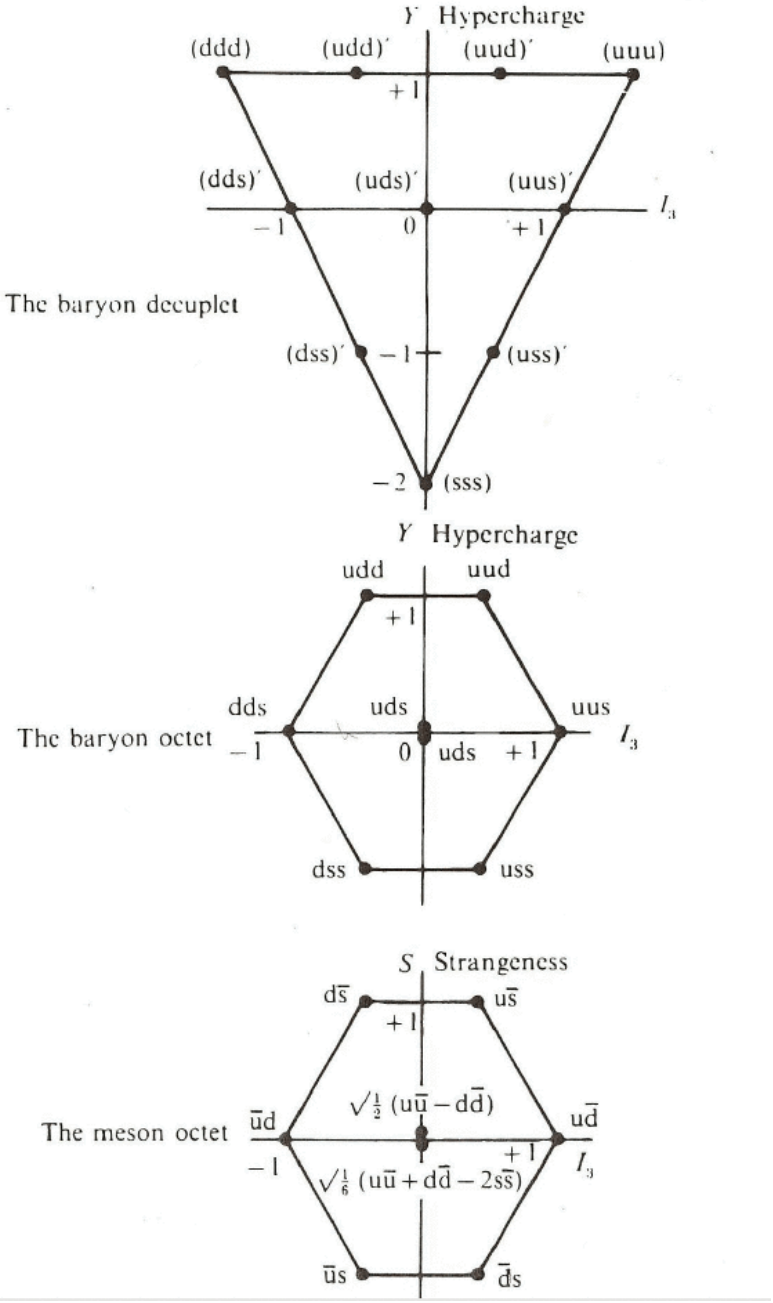

Figure 1.5: The representations of $SU(3)_F$ under which elementary particles are arranged according to their quantum numbers. The constituents of the baryon decuplets are symmetric under cyclic permutation of the quarks.

Therefore, combining Eqs. 1.1 and 1.2,

$$\begin{aligned}(3,2)\otimes(3,2)\otimes(3,2) &= (\mathbf{10}_S,\mathbf{4}_S)\oplus(\mathbf{10}_S,\mathbf{2}_{MS})\oplus(\mathbf{10}_S,\mathbf{2}_{MA}) \\ &\oplus (\mathbf{8}_{MS},\mathbf{4}_S)\oplus(\mathbf{8}_{MS},\mathbf{2}_{MS})\oplus(\mathbf{8}_{MS},\mathbf{2}_{MA}) \\ &\oplus (\mathbf{8}_{MA},\mathbf{4}_S)\oplus(\mathbf{8}_{MA},\mathbf{2}_{MS})\oplus(\mathbf{8}_{MA},\mathbf{2}_{MA}) \\ &\oplus (\mathbf{1}_A,\mathbf{4}_S)\oplus(\mathbf{1}_A,\mathbf{2}_{MS})\oplus(\mathbf{1}_A,\mathbf{2}_{MA})\end{aligned} \tag{1.3}$$

Ground state baryons (which are required to have symmetric combinations of quark spin and flavor wave-functions) live in the symmetric representation $(\mathbf{8},\mathbf{2})_S$, so that their spin-flavor wave-functions satify $\psi(\mathbf{8}_{MS},\mathbf{2}_{MS})+\psi(\mathbf{8}_{MA},\mathbf{2}_{MA}) = \sqrt{2}\psi(\mathbf{8},\mathbf{2})_S$. On the other hand, the orthogonal representation $(\mathbf{8},\mathbf{2})_A$, $\psi(\mathbf{8}_{MS},\mathbf{2}_{MS})-\psi(\mathbf{8}_{MA},\mathbf{2}_{MA}) = \sqrt{2}\psi(\mathbf{8},\mathbf{2})_A$ is antisymmetric. So that the representations can be re-arranged in terms of symmetry criteria as follows,

$$(\mathbf{8}_{MS},\mathbf{2}_{MS})\oplus(\mathbf{8}_{MA},\mathbf{2}_{MA}) = (\mathbf{8},\mathbf{2})_S\oplus(\mathbf{8},\mathbf{2})_A. \tag{1.4}$$

Therefore, the baryon octet $(\mathbf{8},\mathbf{2})_S$ ($J^P = 1/2^+$) and the decuplet $(\mathbf{10},\mathbf{4})_S$ ($J^P = 3/2^+$) are the only totally symmetric representations of $SU(3)_F\otimes SU(2)_S$ and thus, the only representations allowed for ground state baryons.

Re-combining terms in Eq. 1.4 according to symmetry criteria, gives

$$\begin{aligned}(3,2)\otimes(3,2)\otimes(3,2) &= (\mathbf{10},\mathbf{4})_S\oplus(\mathbf{10},\mathbf{2})_{MS}\oplus(\mathbf{10},\mathbf{2})_{MA} \\ &\oplus (\mathbf{8}_{MS},\mathbf{4}_S)\oplus(\mathbf{8},\mathbf{2})_S\oplus(\mathbf{8}_{MS},\mathbf{2}_{MA}) \\ &\oplus (\mathbf{8}_{MA},\mathbf{4}_S)\oplus(\mathbf{8}_{MA},\mathbf{2}_{MS})\oplus(\mathbf{8},\mathbf{2})_A \\ &\oplus (\mathbf{1}_A,\mathbf{4}_S)\oplus(\mathbf{1}_A,\mathbf{2}_{MS})\oplus(\mathbf{1},\mathbf{2})_A\end{aligned} \tag{1.5}$$

In the approximate symmetry called spin-flavour $SU(6)$ there are six quark basis states: three flavors with two spins per flavor. States are then classified in $SU(6) \times O(3)$ supermultiplets (Fig. 1.6), where the group $O(3)$ gives the orbital angular momentum of the particles in a multiplet. The $SU(6)$ baryon multiplets of Fig. 1.6 decompose into $SU(3)_F \times SU(2)_S$ according to the right side of:

$$\begin{aligned} \mathbf{56}_S &= {}^4\mathbf{10} \oplus {}^2\mathbf{8} \\ \mathbf{70}_M &= {}^2\mathbf{10} \oplus {}^4\mathbf{8} \oplus {}^2\mathbf{8} \oplus {}^2\mathbf{1} \\ \mathbf{20}_A &= {}^2\mathbf{8} \oplus {}^4\mathbf{1}, \end{aligned} \tag{1.6}$$

where the upper index corresponds to $2J + 1$, where J corresponds to spin. Orbital angular momentum separates states which would otherwise be degenerate, such as those belonging to the **56** representation of supermultiplets shown in Fig. 1.6, for example.

In Fig. 1.6, the Ω^- and $\Xi(1530)$ are assigned to the $[56, 0^+]_0$ decuplet, although spin 3/2 has never been established for these states. The analyses presented in chapters 4 and 6 of this thesis take advantage of their production in charm baryon decay to demonstrate that the spin 3/2 assignments are in fact correct.

Very little is known about Cascade states which might populate the $[70, 1^-]_1$ and $[56, 2^+]_2$ multiplets indicated in Fig. 1.6 (see section 1.5 below). Only four states are considered to be well-established and of these only the $\Xi(1820)$ has some semblance of a spin-parity assignment ("$J^P = 3/2^-$ favored by the data"). The analysis of chapter 5 of this thesis focuses on the $\Xi(1690)$, concluding that spin 1/2 is the

favored assignment.

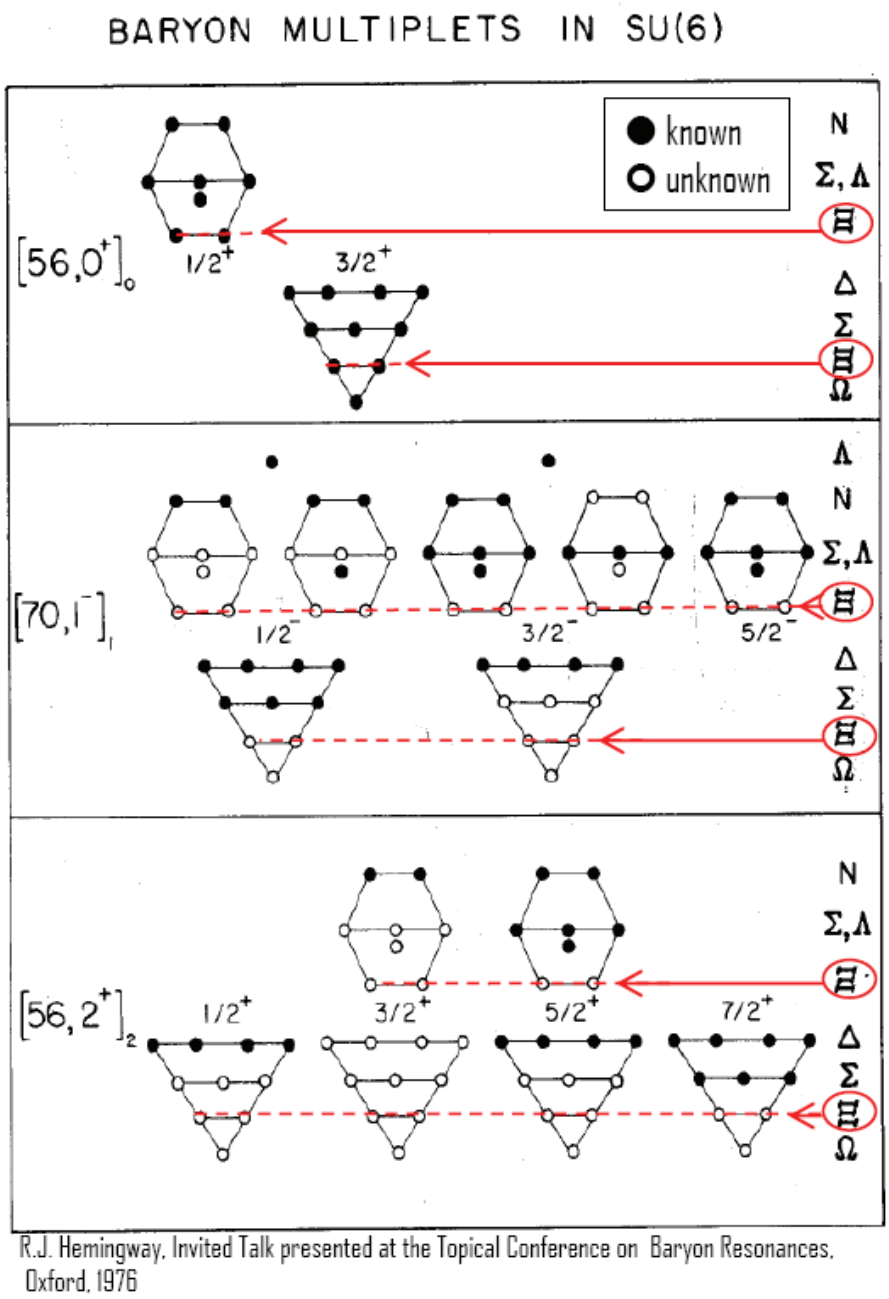

Figure 1.6: The baryon multiplets in $SU(6)$. The Cascade states are indicated in red. Only the octet and decuplet states of the **56** representation have been assigned.

1.3 Addition of the Charm Quark

In 1970, Glashow, Iliopoulos and Maiani (GIM) predicted the existence of a fourth quark, the charm (c) quark, that paired with the strange quark.

In 1973, Burton Richter (SLAC) led the group that designed and built the Stanford Positron Electron Asymmetric Ring (SPEAR). Experiments at SPEAR looked at the rate of occurrence of events in which a colliding electron and positron annihilate to produce other particles. At certain energies, the rate seemed inexplicably large. On November 10, 1974, measurements in the problematic energy range confirmed a dramatic rate increase. Many further checks found that this peak is due to the production of particles containing a new kind of quark – the charm quark [19].

The observation of charm baryons (i.e. hyperons in which a strange quark is replaced by a charm quark) soon followed, with the discovery of the Σ_c^+ (cud) in a liquid hydrogen bubble chamber at the Brookhaven National Laboratory [20] (Fig. 1.7).

Subsequent work at SPEAR by the Goldhaber-Trilling group of Lawrence Berkeley National Lab demonstrated the existence of D mesons, thereby also explicitly confirming the charm discovery [21].

The bare mass of the c quark is of the order of 10 times that of the bare s quark mass and approximately 300 times the (u, d) averaged bare mass. The large mass splitting between the c quark mass and the (u, d, s) quark masses results in the brokenness of $SU(4)$ by multiplet mass difference of the order of 1 GeV/c^2. In contrast, recall that $SU(3)$ flavor symmetry is broken by baryon mass differences of

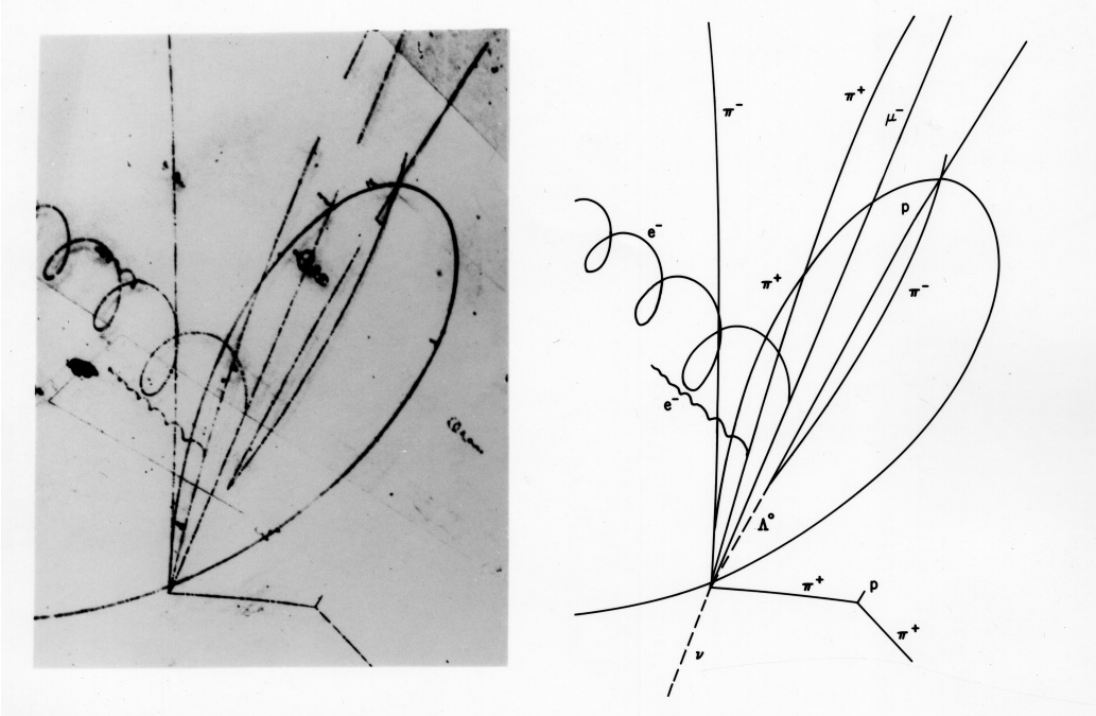

Figure 1.7: The photograph of the event in the Brookhaven 7-foot bubble chamber which led to the discovery of a charm baryon, the Σ_c^+. A neutrino enters the picture from below (dashed line) and collides with a proton in the chamber's liquid. The collision produces five charged particles (a negative muon, three positive pions, and a negative pion), and a Λ (decaying to a proton and a pion in a characteristic 'V' pattern). The kinematics of the decay imply that the Λ and four pions were produced from the decay of a Σ_c with mass ~ 2.4 GeV/c^2 [20].

the order of 100 MeV/c^2. Baryons with (u, d, s) quark-content are referred to as "light baryons", and charm (or "heavy") baryon ground state configurations are obtained by replacing a strange quark in a light hyperon ground state (Λ, Σ, Ξ, or Ω) with a charm quark. The resulting charm baryon states are denoted $\Lambda_c, \Sigma_c, \Xi_c$, or Ω_c, and the ground states are $\sim 1.0 - 1.25$ GeV/c^2 heavier than their hyperon ground state counterparts as a consequence of the mass difference between the charm and strange quarks. The quark content of the charm baryon ground states of relevance to the

analyses described in chapters 4-6 of this thesis is indicated in Fig. 1.8.

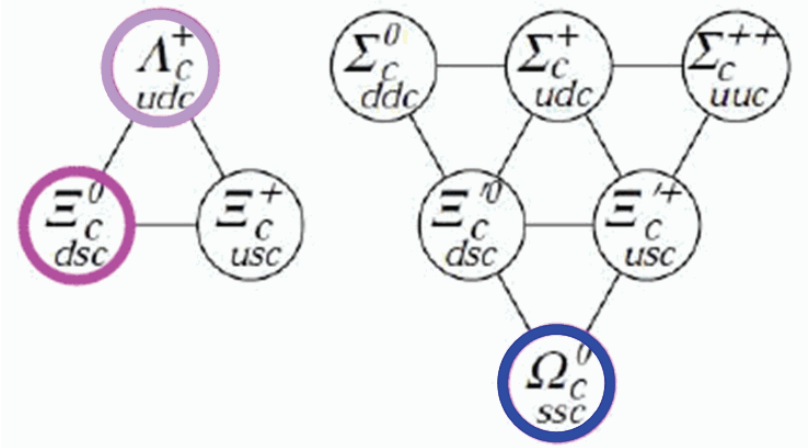

Figure 1.8: The ground state charm baryons. The charm baryons used in the analyses presented in this thesis are indicated by the colored rings.

Baryons containing a charm quark are produced copiously at *BABAR*. As a result, charm baryon decays to light baryons containing at least one strange quark are available in large numbers, and hence provide an excellent laboratory in which to perform the hyperon and hyperon resonance analyses described in this thesis.

The decay of the Ξ_c^0 (cds) to $\Omega^- K^+$, used in the analysis presented in chapter 4, is an example of one such process. It is characterized by the W-exchange diagram of Fig. 1.9 (a), and is listed by the PDG only as "seen" [22]. The *BABAR* measurement [23]

$$\frac{\mathcal{B}(\Xi_c^0 \to \Omega^- K^+)}{\mathcal{B}(\Xi_c^0 \to \Xi^- \pi^+)} = 0.294 \pm 0.018 \text{ (stat.)} \pm 0.016 \text{ (sys.)}$$

indicates that $\mathcal{B}(\Xi_c^0 \to \Omega^- K^+)$ should be small. Nevertheless the analysis sample of chapter 4 is found to contain ∼800 signal events over a very small background.

Furthermore, the even rarer charm baryon decay process $\Omega_c^0 \to \Omega^-\pi^+$, characterized by the external spectator quark diagram of Fig. 1.9 (b), is observed in the *BABAR* experiment at a statistical level sufficient to corroborate the result of the Ξ_c^0 analysis (see chapter 4).

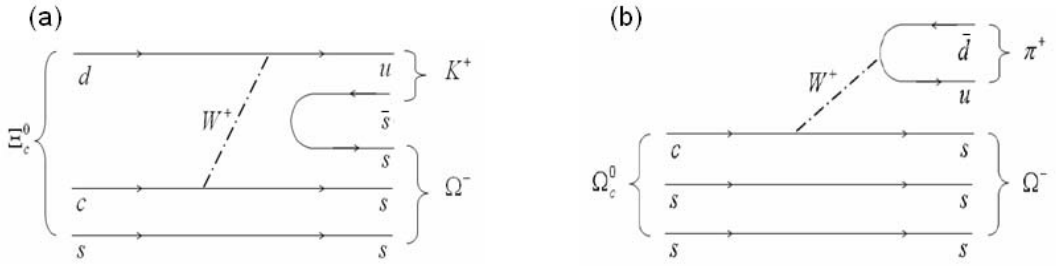

Figure 1.9: Tree-level Feynman diagram illustrating the transition of c to s quark in the decays (a) $\Xi_c^0 \to \Omega^-K^+$ (W-exchange diagram). and (b) $\Omega_c^0 \to \Omega^-\pi^+$ (external spectator quark diagram).

1.4 Cascade Physics

The beginning of Cascade physics was marked by the discovery of the Ξ^- hyperon in a Cloud Chamber photograph. The original paper [24], however, did not claim discovery but stated that the photograph of Fig. 1.10 shows the apparent association of a V^0 track with a V^- track, and gave the possible explanation that $V^- \to V^0_{1\,or\,2}\pi^-$. If the V^- decayed to V_1^0 (i.e. a Λ), the mass of the V^- particle would be about 2600 m_e, corresponding to $\sim$ 1315 MeV/c^2. The current mass value of the Ξ^- is 1321 MeV/c^2[22]. Cascade hyperons have strangeness -2 and the first excited state is the $\Xi(1530)$, corresponding to the $Y = -1$ doublet of the decuplet of Fig. 1.1.

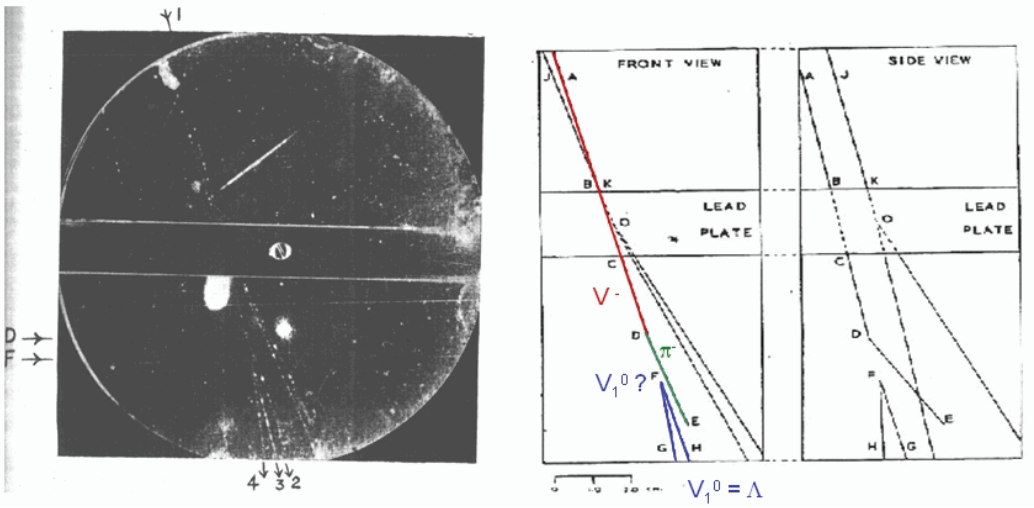

Figure 1.10: A Cloud Chamber picture showing the apparent association of a V^0 track with a V^- track; this in fact was the first observation of the decay of a Ξ^- hyperon.

The small observed widths of Cascade resonances makes them valuable experimentally, since this characteristic reduces potential overlap complications with neighboring states. From a theoretical point of view, their quark content, one light u or d quark with two comparatively massive strange quarks allows for simplifications in the calculations of their properties. In particular, Ξ^* states are much easier to handle in Lattice QCD than N^*, Δ^*, Λ^* or Σ^* states as they have only one u or d quark which reduces the reliance on chiral extrapolation[12]. These advantages are offset, however, by the lack of experimental information on excited Cascade states, as discussed in section 1.5.

[12]Lattice QCD simulations involve the use of light quarks at their physical mass values. The chiral extrapolation is an extrapolation in the light quark masses to the physical up and down quark masses.

1.5 Present Status of Cascade Resonance Spectroscopy

Only a few Ξ resonances are well-established (****) or at least fairly likely to exist (***), as indicated in Table 1.2 [22]. In addition it is pointed out in refce. [22] that "...nothing of significance on Ξ resonances has been added since our 1988 edition," thus indicating that there has been very little development in this area of spectroscopy in the last decades. The only resonance with measured J^P is the $\Xi(1530)$, but its spin-parity assignment still suffers from uncertainty, as will be discussed in chapter 6. The mass and width of this resonance are fairly well-established. The spin-parity of the next resonance in the mass scale, the $\Xi(1690)$, has not yet been measured, and the existing mass and width measurements have large uncertainties due to limited statistics.

It is for this reason that the analysis techniques employed in the Ω^- spin measurement of chapter 4 of this thesis have been extended to the study of quasi-two-body production of the $\Xi(1690)$ described in chapter 5. The precise mass and width parameter values obtained, and the evidence favoring spin 1/2 should be of considerable help in assessing the merits of models predicting the Cascade spectrum.

Predictions of the mass, width, decay modes and spin/parity of Cascade states rely on model-based calculations (e.g. constituent quark models) which make use of a momentum-dependent potential, and rely on kinematic approximations[13]. Exper-

[13]Such covariant quark model calculations are based on confining mass operators, that contain a spatial-separation-dependent confining term and a hyperfine coupling correction.

Table 1.2: The three- and four-star Ξ resonances listed in the 2006 edition of the Particle Data Book.

Particle	$L_{2I\cdot 2J}$	Overall Status	Seen in $\Xi\pi$	Seen in ΛK	Seen in ΣK	Seen in $\Xi(1530)\pi$	Seen in other Channels
$\Xi(1318)$	P_{11}	****					Decays weakly
$\Xi(1530)$	P_{13}	****	****				
$\Xi(1690)$		***		***	**		
$\Xi(1820)$	D_{13}	***	**	***	**	**	
$\Xi(1950)$		***	**	**			
$\Xi(2030)$		***		**	***		

Note: **** existence is certain, and properties are at least fairly well explored; *** existence ranges from very likely to certain, but further confirmation is desirable and/or quantum numbers, branching fractions, etc. are not well determined [22].

imental validations of these predicitions are badly lacking. The relativized[14] quark-model calculations by Capstick and Isgur [25] (Fig. 1.11 (a)) yield 45 Ξ states with mass less than 2.4 GeV/c^2, only three of which have been identified experimentally. The $\Xi(1690)$ is notably absent from Fig. 1.11 (a).

The covariant quark model of Coester, Dannbom and Riska [26] obtains baryon spectra based on a phenomenological model for the hyperfine interaction where the parameters of the flavor-spin operator are determined by the empirical spectrum (Fig. 1.11 (b)). In particular, the properties of the $\Xi(1690)$ are crucial in this regard, as it is the is the first Cascade excited state not used as input in QCD calculations.

Finally, recent developments in fast algorithms have raised expectations for

[14]Non-relativistic quark models do not take into account the kinetic energy of the quarks in the hadrons. This model assumes individual quark momentum distributions making use of Jacobi coordinates.

predictions of Ξ spectra from Lattice QCD, resulting in renewed interest in the existence and properties of excited Cascade states. There is ongoing discussion at Jefferson Lab. concerning a future experimental program dedicated to the investigation of this spectroscopy [27], and this community has already shown considerable interest in the capability of the charm baryon analysis procedures described in this thesis to provide new and precise experimental results in this area.

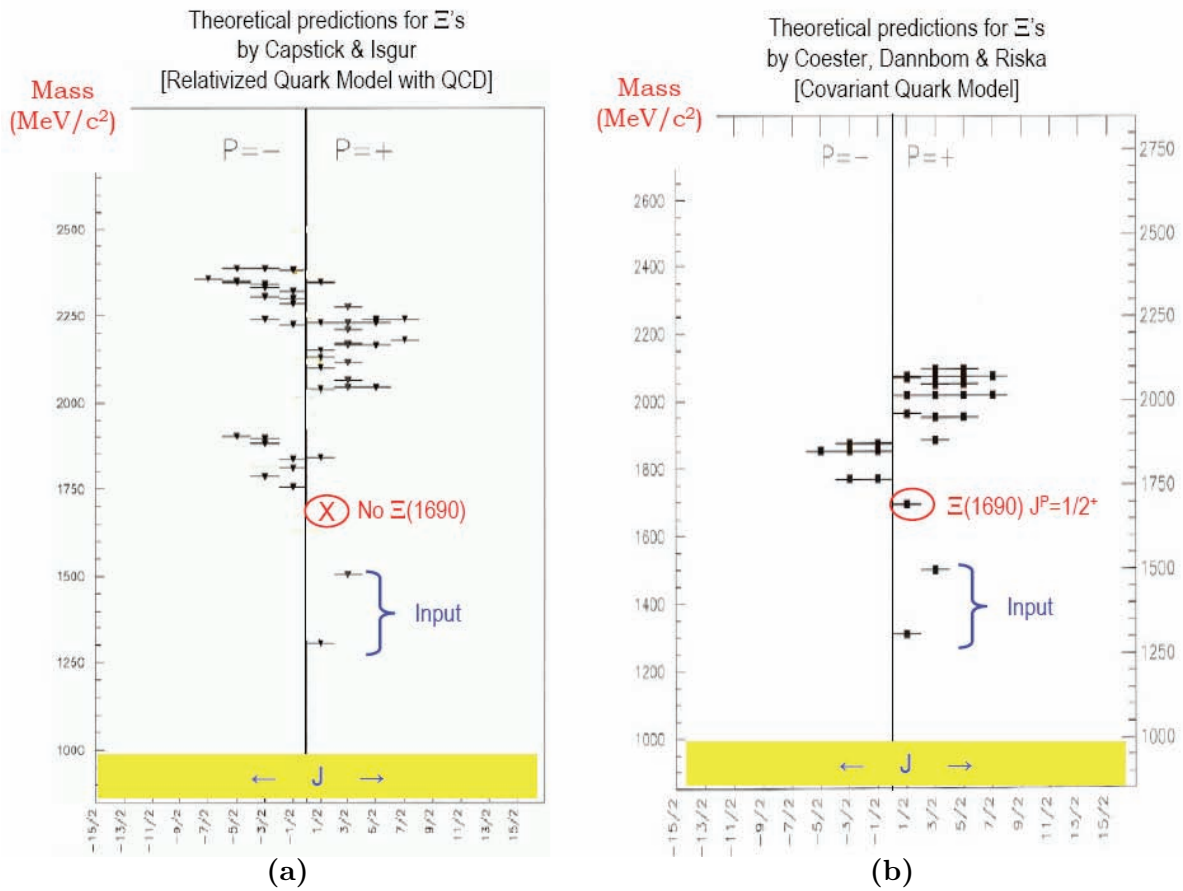

Figure 1.11: An example of discrepancies between covariant quark models. (a) The predictions by Captick and Isgur [25] miss the $\Xi(1690)$. (b) The model obtained by Coester, Dannbom and Riska [26] predicts the existence of the $\Xi(1690)$ with spin 1/2 and positive parity.

1.6 Thesis Content

In this thesis, studies of hyperon and hyperon resonance production in charm baryon decays at *BABAR* are presented.

An overview of the *BABAR* detector and the SLAC PEP-II asymmetric-energy e^+e^- collider is given in chapter 2. In chapter 3, the procedures followed in selecting the data samples used in the analyses described in chapters 4, 5, and 6 are explained. The analysis detailed in chapter 4 consists of a measurement the spin of the Ω^- using two-body decays of the Ξ_c^0 and Ω_c^0 [28, 29]. In chapter 5, these analysis procedures are extended to three-body final states, and properties of the $\Xi(1690)^0$ are extracted from a detailed isobar[15] model analysis of the $\Lambda_c^+ \to \Lambda\bar{K}^0K^+$ Dalitz plot [30]. In chapter 6, similar techniques are used to study $\Xi(1530)^0$ production in Λ_c^+ decay and the amplitude structure of the $\Xi^-\pi^+$ system [29]. Conclusions and future possibilities are discussed in chapter 7. Detailed explanations of efficiency-correction procedures and the formalism used in the analyses are presented in Appendices A-E.

---

[15]The term "isobar model" has become part of the jargon related to the analysis of three-body states. It originated in 1957 in a paper [S. J. Lindenbaum and R. M. Sternheimer, Phys. Rev. **105**, 1874 (1957)] analyzing data on reactions of the type $\pi N \to \pi\pi N$ obtained using the high-energy pion beams made available by the Brookhaven Cosmotron. At lower energies such data were adequately described by the Fermi (i.e. phase space) model, but this was not the case in the new higher energy region. An "isobar model" was proposed instead, in which an excited isobaric state of the nucleon (i.e. an N^*) was produced and then decayed via $N^* \to N\pi$, and this provided a better description of the data. In later papers this isobar model was extended to include additional non-N^* amplitudes [M.G. Olsson and G. B. Yodh, Phys. Rev. **145**, 1309 (1966)], and subsequent partial wave analyses (PWA) of reactions of the type $\pi N \to \pi\pi N$ also incorporated resonances (isobars) in the $\pi\pi$ system. Eventually this approach was extended to PWA such as that of the $K\pi\pi$ system produced in $KN \to K\pi\pi N$ reactions, and to the analyses of Dalitz plots resulting from charm meson decay to three pseudoscalar mesons, among others. The term "isobar model" is thus meant to convey the idea of an analysis of a three-body state in terms of a superposition of quasi-two-body amplitudes; it certainly has nothing to do with weather maps!

CHAPTER 2
PEP-II AND THE *BABAR* DETECTOR

2.1 Brief Description of the Collider

The primary goal of the *BABAR* detector at the SLAC PEP-II asymmetric-energy e^+e^- collider is to study CP-violating asymmetries in the decay of B mesons to CP eigenstates. The design of the detector makes it also suitable to contribute to many other physics topics such as precise measurements of the decays of charm hadrons and τ leptons, charm meson and baryon spectroscopy, etc., as well as the search for rare processes that become accessible with high luminosity.

The PEP-II asymmetric e^+e^- collider illustrated in Fig. 2.1. operates at 10.58 GeV nominal center-of-mass energy, the energy necessary to produce the $\Upsilon(4S)$ which decays almost entirely to B meson pairs. Approximately 10% of the data are taken 40 MeV below the $\Upsilon(4S)$ energy in order to study continuum events (ie. $e^+e^- \to q\bar{q}$), which contribute background to the B meson analyses.

The accelerator has asymmetric beam energies, with a 9 GeV electron beam colliding head on with a 3.1 GeV positron beam, which results in a boost, $\beta\gamma = 0.56$, of the $\Upsilon(4S)$ resonance in the direction of the electron beam in the laboratory frame.

This boost insures significant separation of the B meson decay vertices, allowing the determination of their relative decay times and the measurement of the time dependence of $B^0\overline{B}^0$ oscillations [31]. This requires events in which one B meson decaying to a CP eigenstate is fully reconstructed (into typically two or more

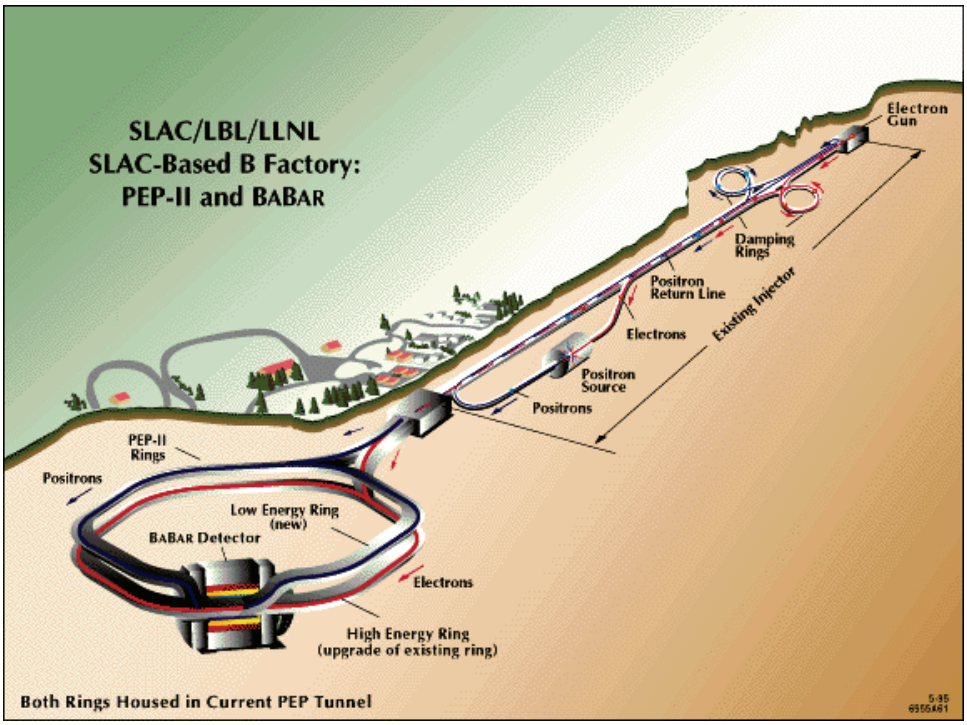

Figure 2.1: The PEP-II storage ring facility. Bunches are accelerated in the SLAC Linear Accelerator and injected into the storage rings in order to collide at the *BABAR* detector, located as shown at IR2.

charged particles and one or two π^0's), and the other B meson is identified (tagged) as a B^0 or $\overline{B}^0$ by its decay products; e.g. a charged lepton, or other flavor-identifying final state particles. Combining these requirements with the branching fractions for B mesons to CP eigenstates of typically $10^{-3} - 10^{-6}$, places stringent requirements on the detector, which should have [32]:

- a large and uniform acceptance down to small polar angles relative to the boost direction;
- excellent reconstruction efficiency for charged particles down to 60 MeV/c lab.

momentum and for photons to 20 MeV lab. energy;

- very good momentum resolution in order to separate small signals from background;
- excellent energy and angular resolution for the detection of photons from π^0 and η^0 decays, and from radiative decays in the lab. energy range from 20 MeV to 4 GeV;
- very good vertex resolution, both transverse and parallel to the beam direction;
- efficient electron and muon identification, with low misidentification probabilities for hadrons; this feature is crucial for tagging the B flavor, for the reconstruction of charmonium states, and is also important for the study of decays involving leptons;
- efficient and accurate identification of hadrons over a wide range of momenta for B flavor-tagging, and for the reconstruction of exclusive states; e.g. modes such as $B^0 \to K^{\pm}\pi^{\mp}$ or $B^0 \to \pi^+\pi^-$, as well as charm meson and τ decays;
- a flexible and selective trigger system with built-in redundancy;
- low-noise electronics and a reliable, high bandwidth data-acquisition and control system;
- detailed continuous monitoring and automated calibration;
- an online computing and network system which can control, process, and store the expected high volume of data;
- and detector components which can tolerate significant radiation doses and operate reliably under high-background conditions.

Runs 1-6 have been very successful with a total integrated luminosity[1] of 408.21 fb^{-1} delivered by PEP-II, of which 392.76 fb^{-1} has been recorded by *BABAR* as of Feb 2, 2007 (Fig. 2.2). In addition to this, PEP-II has achieved a maximum instantaneous luminosity of $\sim 1.2 \times 10^{34}$ $\text{cm}^{-2}\text{s}^{-1}$, which is approximately four times larger than originally designed.

To date ~400 million $B\bar{B}$ pairs have been produced, so that the goal of operating machine and detector in factory mode has been convincingly realized, with much more production to come.

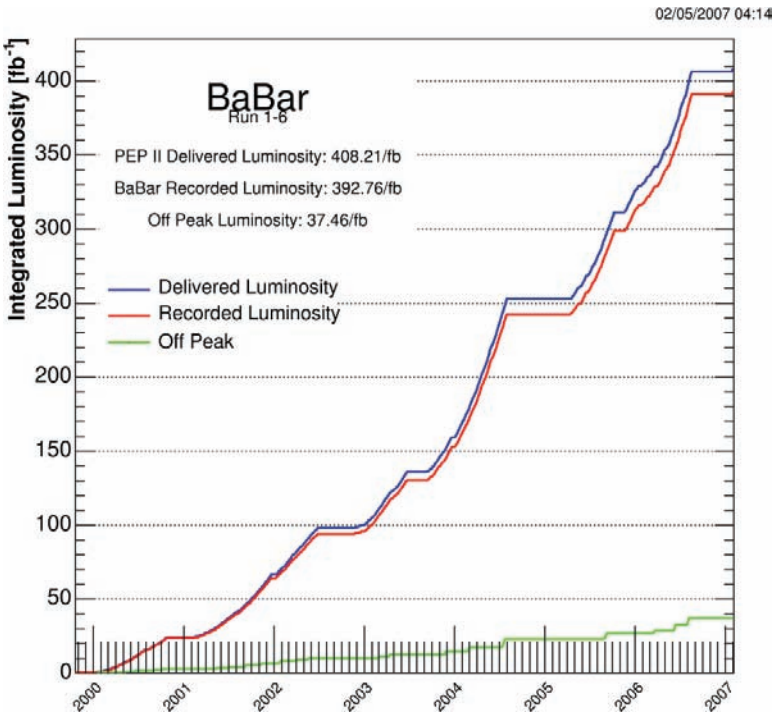

Figure 2.2: Integrated PEP-II-delivered and BaBar recorded luminosities

[1]For a process of cross section σ fb and integrated luminosity L fb^{-1}, $N = L \times \sigma$ events of that type have been produced over the running period.

2.2 Overview of the Detector

The detector illustrated in fig. 2.3, is composed of several sub-detectors each of which is responsible for fulfilling one or more of the physics requirements outlined in section 2.1.

The tracking system consists of a five-layer double-sided-readout silicon vertex detector (SVT) and a 40-layer drift chamber (DCH). Both devices also provide particle identification (PID) information through measurements of specific ionization energy loss (dE/dx). The drift chamber is surrounded by the DIRC, a detector of internally reflected Cherenkov light, which is the primary source of charged particle identification at high momentum. These systems are enclosed in a CsI(Tl) electromagnetic calorimeter (EMC) which is used for photon and neutral hadron detection and $e^{\pm}$ identification. The assembly is mounted within a solenoidal superconducting coil which provides a 1.5 T magnetic field approximately in the direction of the e^{-} collision axis. The last layer of the detector consists of the instrumented flux return (IFR), which incorporates resistive plate chambers as well as limited streamer tubes to serve as a muon and neutral hadron detection system. Further details of the *BABAR* detector and reconstruction software are given elsewhere [32]. The trigger, data acquisition and data monitoring systems are controlled by online software.

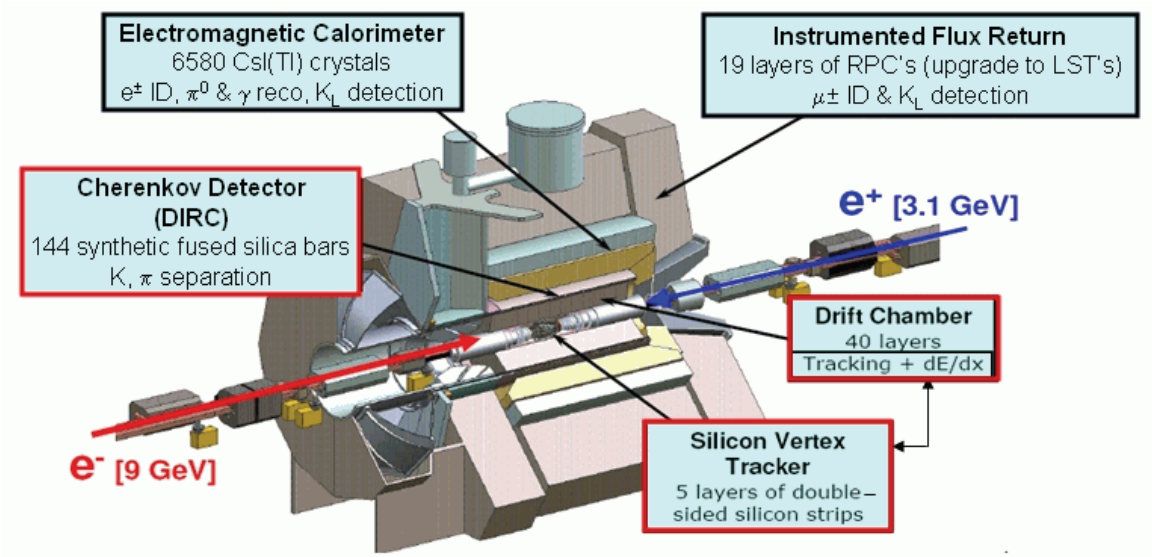

Figure 2.3: A representation of the *BABAR* detector. Starting at the collision axis and radially moving outward, the detector components shown are the Silicon Vertex Tracker (SVT), the Drift CHamber (DCH), the Detector of Internally Reflected Cherenkov Radiation (DIRC) particle identification system, the ElectroMagnetic Calorimeter(EMC), and the Instrumented Flux Return (IFR) housing the muon and neutral hadron detector. Some of the beamline magnets (namely, Q1, Q2 and Q4) near the interaction region are shown as they aid the production of the high luminosity required at PEP-II.

2.3 Silicon Vertex Tracker (SVT)

The Silicon Vertex Tracker (SVT) was designed for very high precision measurement of azimuthal (ϕ) and longitudinal (z) coordinates on the trajectories of charged particles just outside the beampipe[2].

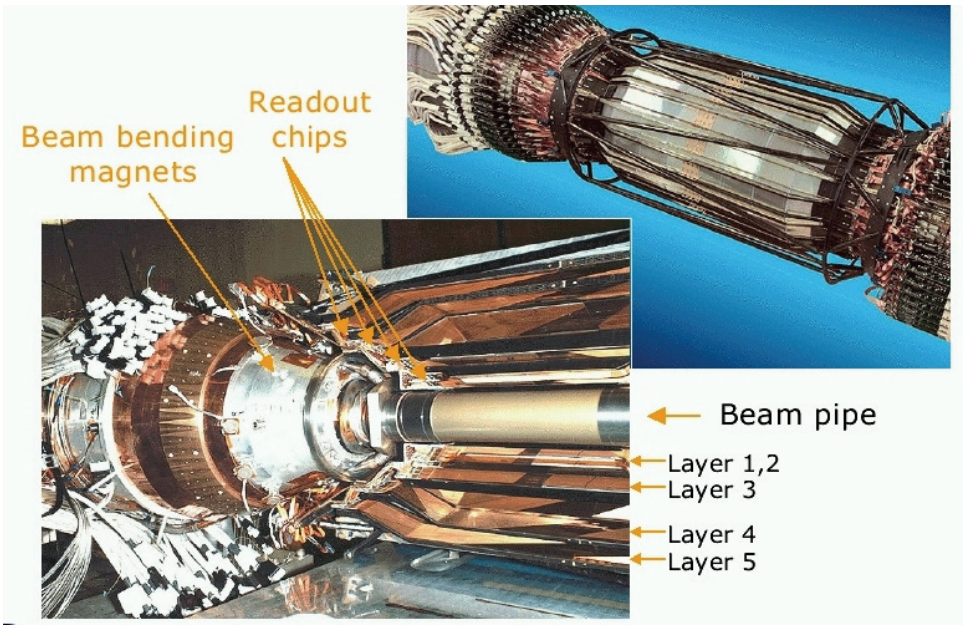

Figure 2.4: The partially assembled SVT, showing the positioning of the silicon wafers around the IP region, and the B1 bending magnets

The SVT consists of five layers of double-sided silicon micro-strip detectors that are pitched at $\sim$ 20-50 microns, depending on function (i.e. whether measuring ϕ or z) and layer number. Layers 1-3 occupy a radial range from $\sim$ 3 to $\sim$ 6 cm,

[2]The beampipe in essence consists of 2 Beryllium cylinders with a layer of cooling water in between. The inner cylinder (2.4976 cm inner radius, 2.5824 cm outer radius) is the actual beampipe and the outer cylinder is the water jacket (2.7345 cm inner radius, 2.8346 cm outer radius).

with each layer forming a hexagonal cylinder coaxial with the beampipe axis. Layers 4 and 5 are in the radial range from $\sim$ 12 - $\sim$ 15 cm, in 16- and 18-sided polygon configurations with innovative lamp-shade structures fore and aft. The detector is divided vertically into $x > 0$ and $x < 0$ "clamshells". Fig. 2.4 shows the beampipe in the process of being captured by the $x > 0$ clamshell. The second picture in Fig. 2.4 shows the completed detector mounted between the B1 magnets to which the SVT carbon fibre support frame is attached.

The outer two layers provide coordinates which are linked with coordinate information from the Drift Chamber (DCH) in the *BABAR* charged track reconstruction software, to produce very accurate information on position, direction and momentum for charged particles produced in PEP II e^+e^- collisions.

In addition to providing coordinate measurements, the SVT strip clusters associated with a charged particle track provide specific ionisation (dE/dx) information by means of time-over-threshold measurements. After calibration these are equivalent to measurements of energy deposition in the silicon as a result of ionisation of the medium. Since the number of samples used in calculating dE/dx for a given track is quite small (typically ~ 6) the resolution is not particularly good ($\sim$ 18% of dE/dx).

The decision to build a five-layer SVT was driven by the idea that the SVT system should be capable of performing stand-alone track-finding. The thinking was that three layers are needed to define a candidate helix, a fourth layer is required for corroboration, and a fifth layer is necessary in order to compensate for inefficiency, etc. In practice, this works quite well, and pion tracks of transverse momenta from $\sim$100

down to $\sim$50 MeV/c can be found with reasonable efficiency. Above $\sim$100 MeV/c, the DCH track-finding takes over for the most part, although higher momentum tracks which interact or decay between the outer radius of the SVT and the inner radius of the drift chamber can still be found by the SVT track reconstruction software. This capability is particularly relevant for physics analyses such as those involving $D^*(2010)$ production and decay to $D^0\ \pi^{\pm}$, since the $\pi^{\pm}$ produced tend to have rather low lab. momentum.

The SVT stand-alone track-finding capability is also of great relevance to the so-called Global Alignment (GA) of the *BABAR* detector. In order to satisfy earthquake safety requirements, the Support Tube containing the SVT may not be attached directly to the DCH. However, it is subject to thermal, mechanical and magnetic stresses, the last because it contains the B1 and Q1 permanent magnet machine elements. This causes the position and orientation of the SVT to vary slightly over time w.r.t. the DCH, which defines the *BABAR* coordinate system. The SVT coordinate system is mapped into the DCH system by means of a set of GA parameters which define a rigid body translation and rotation. This set of six parameters is obtained for each run number during data-taking by matching an ensemble of charged tracks, each of which is reconstructed separately in the SVT and DCH coordinate frames, at the wall of the Support Tube. By means of these GA parameters, local SVT measurements are converted to the DCH coordinate system for use in the general track reconstruction software.

Finally, the z coordinate measurement precision in the SVT is at least an

order of magnitude better than that which can be obtained from the DCH because of the small wire angle values in the stereo layers of the latter. It follows that the dip angle (essentially dz/dr) for a charged track is defined almost entirely by the SVT z measurements on the track. This of course has important consequences for the total momentum of the track, but it also has a significant impact on the particle identification capability of the DIRC. The latter is very sensitive to the position and direction in three dimensions of a charged particle trajectory at entry to the relevant quartz bar, and in this sense the coordinate measurements provided by the SVT play a crucial role in reliable particle identification as well as in precision vertexing.

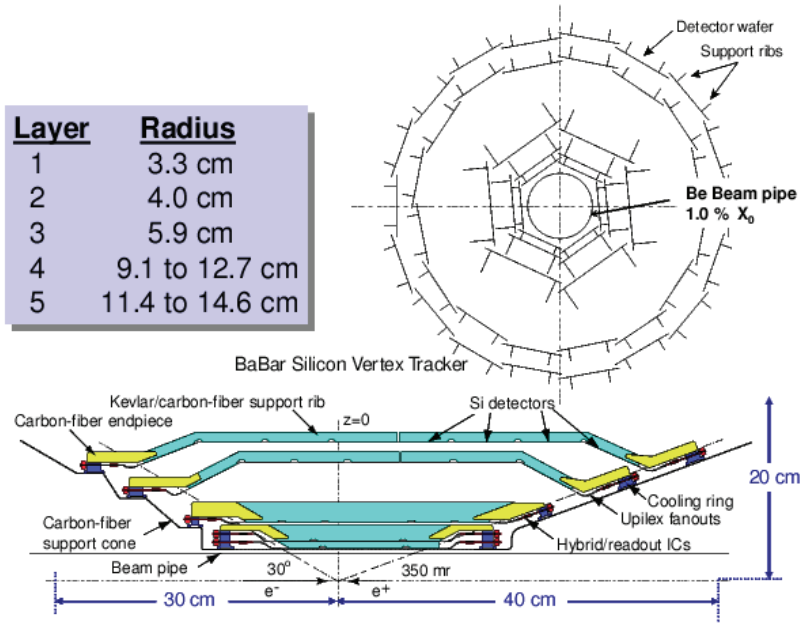

Figure 2.5: Schematic view of the SVT

2.4 Drift Chamber (DCH)

The Drift Chamber (DCH) is the main charged particle tracking device in *BABAR*, and as such must provide efficient pattern recognition capability and high precision transverse momentum (p_T) and position measurements over its large fiducial region. At the same time it is expected to yield corresponding measurements of specific ionization (dE/dx) of sufficient quality as to contribute significantly to the process of charged particle identification in *BABAR*. In addition, the DCH serves to define the *BABAR* coordinate system.

The DCH is a large cylindrical tracking volume of internal length 276.4 cm oriented within the cryostat of the *BABAR* superconducting magnet such that its axis coincides to a good approximation with the axis of the ∼1.5 T magnetic field. The

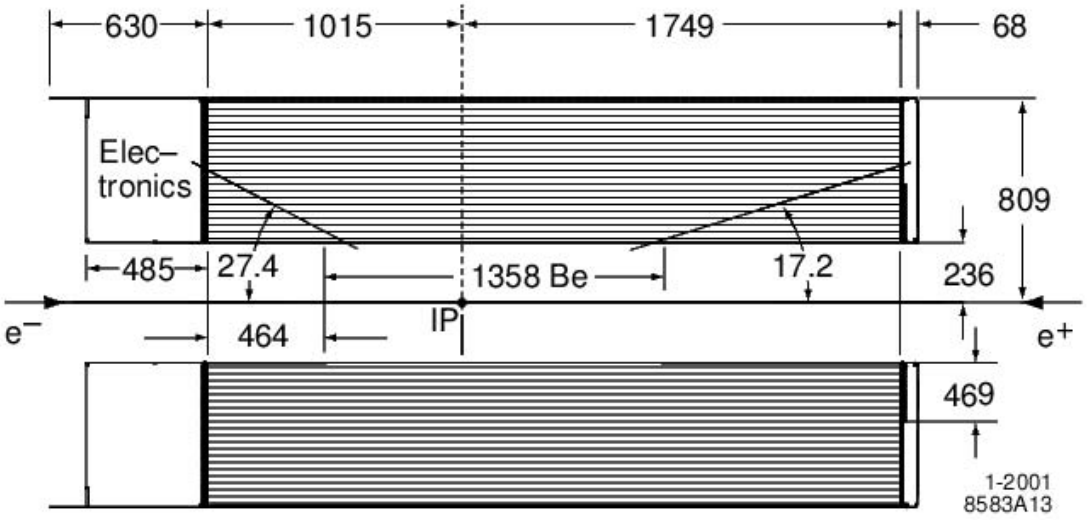

Figure 2.6: Drift Chamber Side View [32], dimensions in mm. The interaction point (IP) is not located in the center of the chamber, but rather is offset to the left by ∼ 37 cm in order to optimize C.M. acceptance, given the asymmetric beam energies.

inner cylinder, which can be seen in Fig. 2.7 during DCH stringing at TRIUMF, consists of fore and aft sections of Al of 5 mm thickness, internal radius 23.6 cm, and a low-mass central section of Be of thickness 1 mm and internal radius 23.8 cm whose length is defined by the tracking fiducial region. The inside and outside surfaces of the Be section are coated with BR127 anti-corrosion paint, which contains sodium chromate, hence the greenish color visible in Fig. 2.7. The Al endplates are 24 mm thick, but the forward endplate is thinned to 12 mm thickness beyond radius $\sim$47 cm in order to reduce the amount of material in front of the Electromagnetic Calorimeter (EMC) endcap. All of the front-end electronics used to read out the DCH data is mounted on the rear endplate. The outer cylinder is composed of a hexagonal Nomex foam structure contained within carbon fiber skins, each of which is clad in Al foil in order to provide r.f. shielding.

The chamber is strung with 7104 gold-coated tungsten-rhenium sense wires of 20 micron diameter; the field and clearing wires are of gold-coated Al, 120 micron in diameter, while the guard wires have the same composition but are of diameter 80 micron; there are 28768 wires in total, and the stringing operation required 15 weeks. The sense wire pattern forms 40 approximately cylindrical layers (the stereo layers cannot define a cylindrical surface), with radially-sequential groups of four layers clustered to form 10 superlayers. The field wires are arranged to create the approximately hexagonal drift cell pattern illustrated in Fig. 2.7 for the four innermost superlayers; the lines connecting the field wires are drawn merely to illustrate the relevant drift cell boundaries. The individual cells have radial height $\sim$1.2 cm and

azimuthal width ∼1.8-1.9 cm, so that the maximum drift distance is ∼9 mm, which corresponds to a drift time of ∼600 nsec. The time-to-distance calibration then yields position resolution of ∼100 microns over most of the drift cell, although this degrades to more than 200 microns close to the sense wire and near the cell boundary. The individual superlayers provide axial (A) or stereo (U or V) information. From the innermost superlayer (minimum radius ∼26 cm, 96 cells per layer) to the outermost (maximum radius ∼78 cm, 256 cells per layer) the sequence is AUVAUVAUVA, and the values of the stereo angle increase in magnitude from ∼2.6 deg. to ∼4.3 deg. with increasing radius.

The gas mixture used was chosen to minimize multiple scattering, and hence to optimize transverse momentum resolution. A mixture consisting of 80% He and 20% isobutane by volume satisfied this requirement while providing a level of performance which compares favorably to those obtained in the past for the more traditional argon-based gas mixtures. The DCH was designed to operate at a high-voltage value of 1960 V with no water vapor added to the gas mixture. However, after a near-disastrous high-voltage accident during commissioning, this was reduced to 1900 V for the period October, 1999 to July, 2000. During this time, a loss of track-finding efficiency was observed for tracks at near normal incidence to the DCH sense wires, for which saturation effects are maximal. The high-voltage was increased therefore to 1930 V in January, 2001, and the DCH has operated at this voltage ever since. At the same time it was decided to add 3500 ppm of water vapor to the gas mixture in order to reduce the probability of electrical discharge.

The *BABAR* coordinate system[3] is defined by the DCH. Horizontal (x) and vertical (y) axes are specified in terms of the nominal positions of the holes in the DCH endplates into which the sense-wire feed-throughs are inserted. It should be noted that the actual hole positions relative to nominal were surveyed by means of a Coordinate Measuring Machine at the factory of the manufacturer, and that these corrections are incorporated when specifying the end-locations of each individual sense wire. At assembly, care was taken to align these two sets of axes, and to ensure that the line connecting their origins was normal to the surfaces of both plates. This line then specifies the z-axis of the *BABAR* coordinate system, and its direction is chosen to coincide to a good approximation with the axis of the *BABAR* magnetic field, with positive z in the direction of the field. In the collider hall, this is also the approximate direction of the high energy (e^-) beam; the orientation of the DCH is then such that the chosen y direction points upward toward the roof, and the x-direction is in the horizontal plane pointing outward from the center of the PEP II rings. The origin of the coordinate system along the z-axis is then chosen to be located at 37 cm in the negative z direction relative to the center of the magnet cryostat. This defines the Interaction Point (IP in Fig. 2.6), and is the nominal point at which the e^- and e^+ beams collide. This choice of coordinate system matches the asymmetric detector configuration, which compensates for the energy asymmetry between the colliding beams in such a way as to yield approximately symmetric detector acceptance in the center-of-mass frame. Systematic studies making use of charged particle trajectories

[3]Right-handed coordinate system.

in this coordinate system are then used to transform local measurements in the other detector subsystems into this DCH frame (e.g. the GA transformation described in Section 2.2).

Typically a charged particle track traversing the full radial extent of the DCH will have ∼36 DCH coordinate measurements associated with its trajectory. If the track originated within the PEP II beampipe, ∼10 SVT coordinates will also be associated with this track. In order to extract precise momentum and position information from these measurements, they are incorporated into a Kalman filter [33] fit which takes into account variation of the magnetic field with position, multiple scattering and energy loss in the materials of the *BABAR* detector traversed, and how these corrections depend on the mass hypothesis being made concerning the identity of the charged particle. The momentum resolution which results from this process can be extracted directly from cosmic ray data. Cosmic rays which enter the DCH preferentially in the upper half of the chamber, pass close to the collision region within the beampipe, and exit through the bottom half of the DCH, can be reconstructed separately as upper DCH and lower DCH tracks. By comparing the upper and lower DCH versions of the same track, estimates of transverse momentum resolution, $\mathrm{dp}_T/\mathrm{p}_T$, can be obtained from actual DCH and SVT measurements (as opposed to Monte Carlo simulation). The momentum resolution dependence on p_T obtained in this way can be parametrized by [32]:

$$\frac{\mathrm{dp}_T}{\mathrm{p}_T} = (0.45 + 0.13 \times \mathrm{p}_T)\% \tag{2.1}$$

with p_T in GeV/c. The first term represents the multiple scattering limit, while the

second term results if the precision of the measurement of the sagitta of the curved trajectory in the transverse (i.e. x-y) plane remains constant while the sagitta itself decreases as $1/p_T$. It follows that the resolution varies from $\sim$0.5% at $\sim$ 0.5 GeV/c to $\sim$ 1% at 5 GeV/c. This is in excellent agreement with the design objective, and reflects the high quality of *BABAR* charged track reconstruction. It is this quality which yields the excellent invariant mass and vertex precision necessary for precision measurements performed at *BABAR*.

In addition to providing coordinate information through drift-time measurement, the DCH also provides specific ionization (dE/dx) information by means of the pulse-height recorded simultaneously for the relevant sense wire. After calibration, this measures the ionization energy loss in the DCH cell in question, and, when normalized to unit path length, provides a local dE/dx sampling. Since such samples follow a Landau distribution, they will not yield a reliable estimate of the most-probable dE/dx value if simply averaged; it is the most-probable value which exhibits a Bethe-Bloch dependence on velocity, and hence yields particle identification information. In order to obtain a reliable estimate of the most-probable dE/dx value for the track in question, the 20% of dE/dx samples with the largest values are discarded, and the mean value for the remaining samples is calculated. This removes the so-called "Landau tail", and the resulting "80% Truncated Mean" provides a good estimate of the most-probable dE/dx value. For a typical track with $\sim$36 samples, $\sim$29 are used to obtain the dE/dx estimate. A single sample provides an estimate with $\sim$42% resolution, and so the resolution in dE/dx would be expected to be $42/\sqrt{29-1}$ $\sim$7.9%

of dE/dx for a typical track. The DCH provides very high quality energy-loss information which thus permits excellent mass discrimination for charged particle tracks with lab. momentum below ~ 1.2 GeV/c.

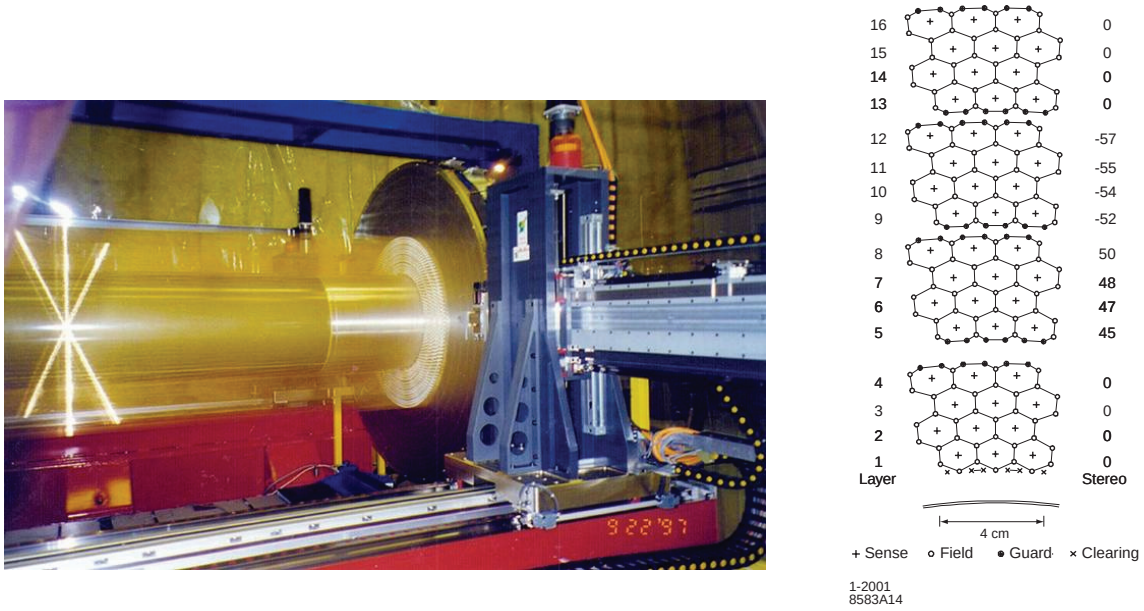

Figure 2.7: The DCH: (left) a robot was used to string the DCH, (right) the DCH drift cell design.

2.5 Detector of Internally Reflected Cherenkov Radiation (DIRC)

Distinguishing hadrons from leptons over a large range of solid angle and momentum is an essential requirement for meeting the physics objectives of *BABAR*. In particular, measurements of CP violation require particle identification (PID), both to reconstruct exclusive final states and to tag the quark content of B decays. Information from the SVT, DCH, EMC, and the IFR is used to identify electrons and muons and contributes to hadron identification. However, an additional dedicated particle identification system is essential to distinguish charged pions from kaons for momenta greater than $\sim$0.6 GeV/c, and from protons for momenta above $\sim$1.2 GeV/c as this is required to obtain efficient tagging and event reconstruction. In order to meet this requirement, a DIRC system is incorporated into the barrel region of the detector. It is azimuthally symmetric w.r.t. the z-axis, and its coverage extends in lab. polar angle from 25.5° to 141.4°; in azimuth, it covers $\sim$92% of 2π, since there are small gaps in coverage between the bar boxes.

The DIRC is an internal reflection imaging device that uses 144 synthetic fused silica bars arranged in a 12-sided polygon around the beam line as illustrated in Fig. 2.8. This maximizes azimuthal coverage, simplifies construction, and minimizes edge effects.

For sufficiently fast charged particles, some part of the Cherenkov radiation cone emitted by the particle ($\Theta_c(E) = \cos^{-1}[1/n\beta]$, with n $\sim$1.473) is captured by internal reflection in the bar and transmitted to the photon detector array located at

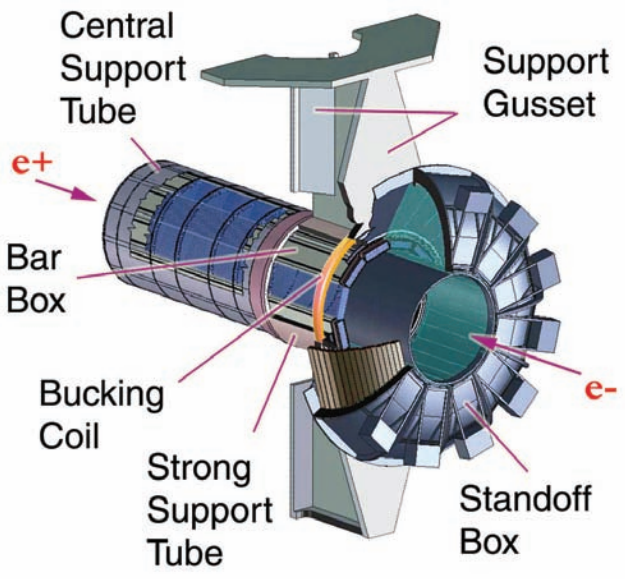

Figure 2.8: An illustration of the DIRC [32] particle identification system. The DIRC comprises 144 thin fused silica bars positioned in a 12-sided cylindrical polygon parallel to the beam-pipe. The cylinder of the DIRC is cantilevered off the standoff box (SOB). Therefore, the SOB acts as a support structure and houses the water used to direct the light from the quartz bars to the photomultiplier tubes.

the backward end of the detector. (Forward-going light is first reflected from a mirror located at the end of the bar.) The high optical quality of the quartz, along with rigorous specifications of squareness, flatness and polish of the bar surfaces, preserves the angle of the emitted Cherenkov light and minimizes absorption. The measurement of this angle, in conjunction with knowledge of the track angle and momentum from the drift chamber, allows a determination of the particle mass. An advantage of the DIRC for an asymmetric collider is that the high momentum tracks are boosted forward, which gives a much higher light yield than for particles at normal incidence. This is due to two effects: the longer path length in the quartz and a larger fraction

of the produced light being internally reflected in the bar.

Each quartz bar is 1.7 cm thick, 3.5 cm wide, and 490 cm long, and is constructed by glueing four shorter bars end-to-end. The total radial space occupied by the DIRC, including quartz thickness, sagitta from the polygonal shape, mechanical supports, and a 1 cm clearance on each side, is 10 cm. This material represents 0.19 X_0 (radiation length) at normal incidence. An effort has been made to minimize both the radial thickness and the amount of material, since these increase the size and cost of the barrel EMC while degrading its performance.

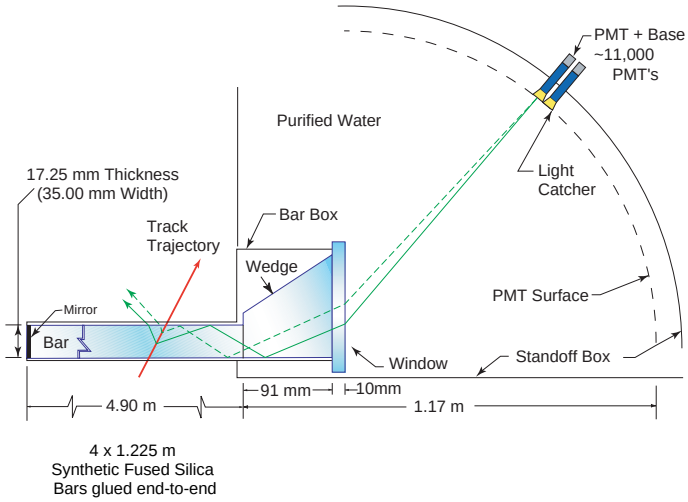

Figure 2.9: Shown is a schematic of a single quartz bar in the DIRC detector illustrating the principle of the detector [32]. As a particle enters the quartz bar, a Cherenkov cone is created which then propagates to the end of the bar and onto the PMT detector surface.

Fig. 2.9 illustrates the principle of the DIRC. A quartz "wedge" is glued to

the readout end of each bar. This reflects the lower Cherenkov ring image onto the upper one, moving it inside the PMT acceptance. The wedge is a 9.1 cm long block of quartz with the same width as the bars, and a trapezoidal profile, 2.7 cm high at the bar end and 7.9 cm high where it is glued to the quartz window which provides the interface to the water-filled standoff-box (SOB). Total internal reflection on all sides of the quartz wedge provides nearly loss-free transmission.

Within the water, the Cherenkov cone image is allowed to expand in diameter and is then detected by an array of $\sim$11,000 conventional 2.5 cm-diameter photomultiplier tubes located on the exterior of the tank. They are organized in a close-packed array at a distance of about 120 cm from the end of the radiator bars. Light-catcher attachments provide increased light-collection efficiency. Water is used because if pure it has good transmission properties for the Cherenkov spectrum detected by the PMTs, has a similar refractive index to that of quartz, a good match in dispersion, and it is also inexpensive.

The phototubes, together with modular bases, are located in a gas-tight volume as protection against helium leaks from the drift chamber. The photo-detection surface approximates a partial cylindrical section in elevation and a toroid when viewed from the end. To maintain good PMT single photon efficiency, the SOB is surrounded by a steel box which, along with a bucking coil, provides adequate magnetic shielding for the phototubes.

2.6 ElectroMagnetic Calorimeter (EMC)

The Electromagnetic Calorimeter (EMC) is designed to detect electromagnetic showers with excellent energy and angular resolution over the 20 MeV to 4 GeV energy range. This capability allows the detection of photons from secondary hadronic decays and radiative and electromagnetic processes (along with n's and hadronic showers from K_L^0's). By means of electron identification, the EMC contributes to J/ψ and τ reconstruction, along with flavor identification of neutral B-mesons via semi-leptonic decays.

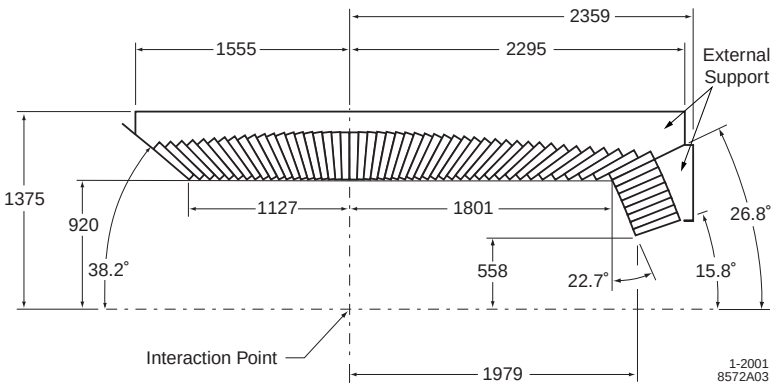

Figure 2.10: A longitudinal cross-section of the EMC (only the top half is shown) indicating the arrangement of the 56 crystal rings. The detector is symmetric around the z-axis. All dimensions are given in mm.

The EMC consists of a cylindrical barrel (5760 crystals), and a conical forward endcap (820 crystals). A longitudinal cross section of the EMC indicating the arrangement of the 56 crystal rings, is shown in Fig. 2.10. The detector is symmetric around the z-axis, its coverage extends in lab. polar angle from 15.8° to 140.8° (90%

in the C.M. system) and over the full azimuth.

Thallium-doped caesium iodide (CsI(Tl)) scintillating crystals (Fig. 2.11), have a short radiation length (1.85 cm) allowing for shower containment at *BABAR* energies with a relatively compact design. Their high light yield and emission spectrum permit efficient use of silicon photodiodes which operate well in magnetic fields. These are coupled to the back surface of the crystals with a polystyrene plate.

To enable the calorimeter to make an accurate measurement of the energy of the particles at the time of creation, and due to the sensitivity of the π^0 efficiency to the minimum detectable photon energy, it is important to keep the amount of material in front of the EMC to the lowest possible level, so as to reduce the chance of pre-shower and γ conversions. The barrel and the outer five rings of the endcap have $\sim 0.3-0.6\ X_0$ of material in front of the crystal faces. The three innermost rings of the endcap are shadowed by the SVT support structure (although the main crystal support structure is at the rear of the crystal to minimize material) and electronics as well as the B1 bending dipole, resulting in up to $3X_0$ for the innermost ring. The principal purpose of the two innermost rings is to enhance shower containment for particles close to the acceptance limit.

Figure 2.11: A thallium-doped Caesium Iodide [CsI(Tl)] Crystal.

2.7 Instrumented Flux Return (IFR)

Surrounding the EMC is a large iron yoke that is instrumented to provide muon and hadron identification. The iron structure also provides the external flux return for the magnetic field from the superconducting solenoid. The primary purpose of the IFR is to identify muons; this information can then be used in the same way as that for electrons identified with the EMC. The IFR can also be used in K_L^0 reconstruction by detecting the appearance of neutral energy, with the corresponding position in the IFR then providing a direction vector to be matched to the missing momentum vector in an exclusive final state. The IFR can also be used as a tail catcher for electromagnetic or hadronic showers not fully contained in the EMC.

The IFR, illustrated in Fig. 2.12 consists of 18 layers of steel, of increasing thickness from 2 cm at the inner layer to 10 cm at the outer layer, which screen out pions by preventing "punch through". Single gap resistive plate chambers (RPC's) are inserted between the steel absorber plates, and these detect streamers from ionizing particles via external capacitive readout strips. The planar RPC's (Fig. 2.12) consist of two bakelite sheets separated by a 2-mm-wide gap kept uniform by polycarbonate spacers. There are 19 layers of RPC's in the barrel section and 18 in the end doors.

Unfortunately, the performance of the original RPC's declined unexpectedly and steadily soon after *BABAR* turned on in 1999. The Forward end door RPCs were replaced in the summer of 2002, and the barrel RPCs needed to be replaced with Limited Streamer Tube (LST) technology before efficiency reaches unacceptable levels. LST's were placed in the top and bottom sextants of the hexagon during the

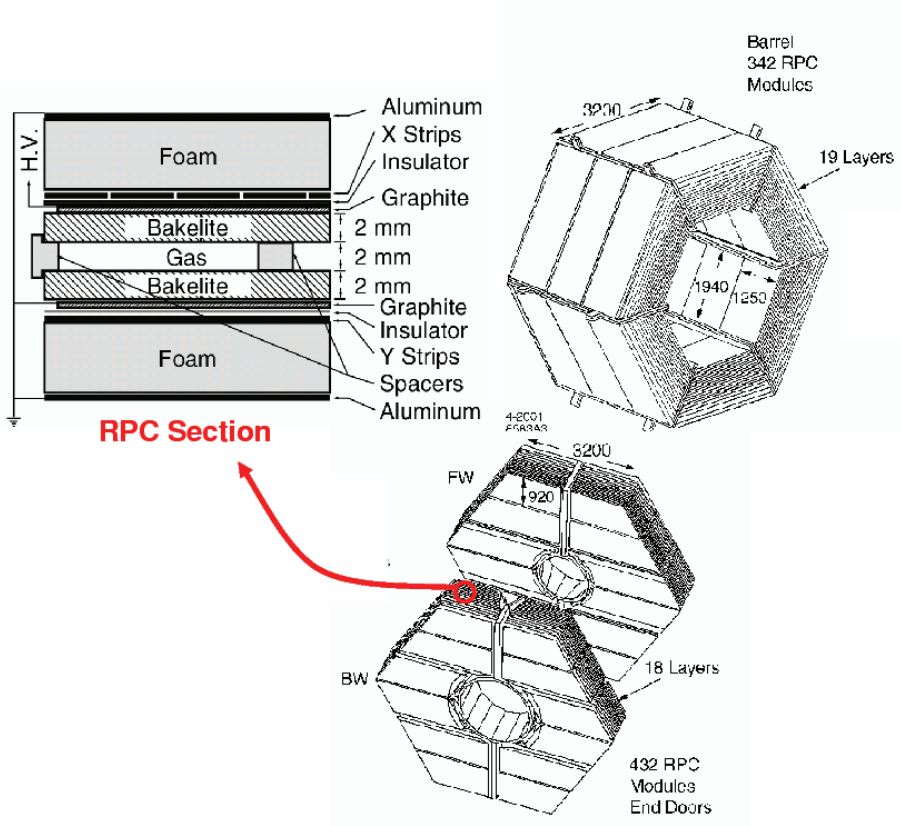

Figure 2.12: Diagram showing the Instrumented Flux Return (IFR) [32]. Resistive Plate Chambers are inserted between the many iron plates that serve as the magnet flux return to detect muons and showers from neutral hadrons.

down time in 2004, and the replacement was completed in 2006 for the remaining four sextants, which are at an angle and therefore required a more lengthy installation process. The LST's have been essential in restoring *BABAR* 's muon identification capability, and efficiency levels greater than 90% should be attainable as a result of this complex and demanding upgrade effort.

2.8 The Magnets

The primary magnet is a superconducting solenoid with a nominal 1.5 T field strength and a field uniformity of $\sim 2\%$ in the tracking region. The conductor is made of superconducting Niobium Titanium (NbTi) cable which operates at a temperature of 20K. Due to the low temperature required for the operation of the superconducting magnet, a surrounding cryogenic system is also necessary.

The Samarium Cobalt (SmCo) permanent magnets used to focus the two particle beams and bend them into head-on collision are located very near to the interaction region ($\pm$20cm in z), thus allowing for accurate positioning and steering just prior to collision. The resulting transverse beam size at the interaction point is $6.2(\text{y}) \times 155(\text{x})\mu\text{m}$.

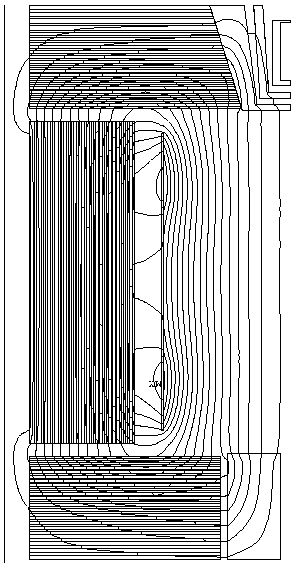

Figure 2.13: The Magnetic Field

2.9 Electronics, Trigger and Data Acquisition System

The electronics, trigger, data acquisition, and online computing represent a collection of tightly coupled hardware and software systems designed to maximize the acceptance of physics events of interest with high efficiency.

Front-End Electronics (FEE) assemblies, located directly on the detector, perform signal processing tasks followed by transfer of data to the Data Acquisition System (DAQ) via optical fibre. Each FEE consists of an amplifier, a digitizer, a trigger latency buffer and an event buffer for storing data prior to transfer to the DAQ.

The *BABAR* trigger is designed to accept physics events of interest with high efficiency while rejecting background, thereby reducing the flow of data to a manageable rate for storage. A trigger efficiency greater than 99% for $B\bar{B}$ events is necessary for CP violation studies. The trigger is implemented in two stages: the Level 1 hardware trigger is designed to retain nearly all physics events, at an output rate of $\lesssim 2$ kHz, while rejecting background. The Level 3 trigger software algorithms then select events of interest at an output rate limited to 120 Hz. At design luminosity beam-induced background rates are typically about 20 KHz for at least on track in the DCH with transverse momentum greater than 120 MeV/c^2 or at least one EMC cluster with $E > 100$ MeV.

Data retrieved from the subsystems are collected by the "front-end" electronics. Selected data from the DCH, EMC and IFR are then used to form Level 1 (L1) trigger "primitives"; these are the raw data such as track transverse momentum from the DCH, energy deposited in the EMC and clusters in the IFR. The maximum Level

1 response latency is 12 μs.

The DCH track primitives are formed from track segments by the Track Segment Finding (TSF) modules. These modules also classify the quality of track segments. From the TSF modules, the data are sent to the Binary Link Tracker (BLT), which forms complete tracks from the segments; these tracks are required either to reach the outer layer of the DCH and be present in at least eight of the ten DCH superlayers, or to penetrate to the middle layer of the DCH. Tracks are then further classified depending on how far they have penetrated into the DCH. EMC primitives are formed using data collected from the 280 towers from the barrel and the endcap calorimeter (which are divided into 7×40 and 8×3 regions in θ and ϕ respectively). The energy is then summed over θ for each ϕ region and compared to various thresholds. The IFR primitives are used to identify di-muon and cosmic ray events. These are defined by *OR* signals of all ϕ read-out strips in eight layers in each sector, where a sector is one of ten regions of the IFR (six barrel sextants, four half end doors). A trigger object is formed when four out of the eight trigger layers have hits within a time window of 134 ns.

These data are then passed through the Global Trigger, where a decision is made to accept or reject the event based on predetermined logic and prescaling rates (the logic and rates are not fixed and are highly configurable). A L1 signal is sent through the Read Out Modules (ROMs) back to the "front-end" where the data are finally extracted. These data are then shipped to the event builder ROMs which assemble the event so that it can be processed by Level 3 (L3) trigger farm nodes and

other "Online Event Processing" nodes assigned to monitoring tasks.

The L3 trigger, a software implementation, further classifies data coming from Level 1. Level 3 output lines can be prescaled to reduce the rate at which certain processes are recorded; for example Bhabha scattering events are required for calibration and luminosity measurements, but not at the rate at which they occur, and so prescaling is applied. In order to allow calculations of efficiency some events that do not pass Level 3 are accepted anyhow at a certain prescaled rate. These events are known as "L1 Pass-Through" events. Events which pass the L3 Trigger are sent to the logging manager which writes the data to an eXtended Tagged Container (XTC). Each XTC file represents a single "run", typically 1 hour of continuous data acquisition time. At the end of a run, the XTC file is archived and made available for further processing.

An intermediate Level 2 trigger has not been implemented in *BABAR*, even with increased data rates and higher luminosity, because the L3 capacity is easily able to handle the observed rates.

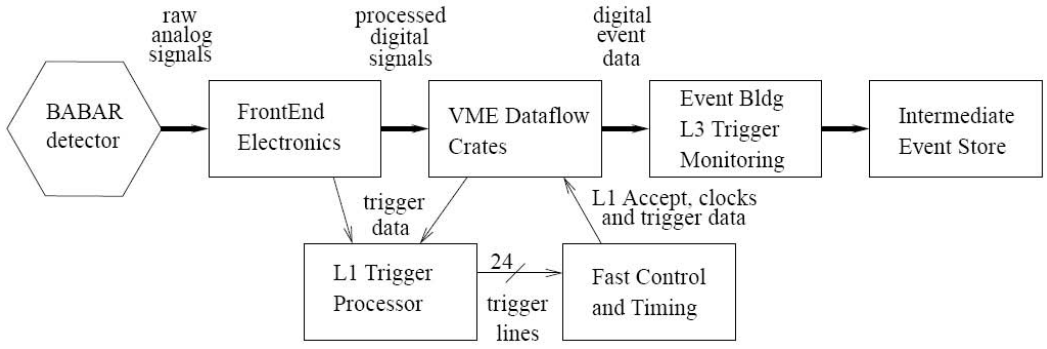

Figure 2.14: Schematic diagram of the Data Acquisition System.

A schematic diagram of the DAQ is shown in Fig. 2.14. Following the initial processing of the raw detector output by the subsystem Front End Electronics the digitized signals are sent over fast optic fibre links to VME dataflow crates containing the dataflow ROMs. For all systems except the EMC, the ROMs contain Triggered Personality Cards (TPCs), meaning that the signals are only collected from the FEE on receipt of a Level 1 Accept (L1A) signal from the Fast Control and Timing System (FCTS). For the EMC however, the ROMs connected to the FEE contain Untriggered Personality Cards (UPCs), meaning that the signals are continuously received from the FEE, processed and, on receipt of an L1A, passed to another TPC ROM. The TPC ROMs run subsystem specific software that performs feature extraction (FEX) in an attempt to isolate signals and suppress background and noise. The ROMs and other boards in the dataflow crates are configurable on a run by run basis. This is achieved by using the configuration database, in which system-specific conguration objects are stored. The data are then passed to the Online Event Processing (OEP) farm for further processing by the Level 3 Trigger and data quality monitoring. Events passed by Level 3 (XTC files) are then picked up by the Online Prompt Reconstruction (OPR) farms. Information on detector conditions, such as temperature, voltages, gas supply and humidity, are extracted from the ROMs and placed in the conditions database for later use in the event reconstruction by OPR. The XTC file data are then sent to the Prompt Calibration (PC) farm, and then to Event Reconstruction (ER) at which time the events are sequentially calibrated and reconstructed using algorithms, and then written into the event store.

CHAPTER 3
EVENT SELECTION PROCEDURE

3.1 General Description

The data samples used in the analyses presented in this thesis were collected with the *BABAR* detector at the PEP-II asymmetric-energy e^+e^- collider at center-of-mass energies 10.58 (at the $\Upsilon(4S)$ resonance) and 10.54 GeV (below the $\Upsilon(4S)$ production threshold).

Although *BABAR* was primarily intended to be a B-meson factory, it is also an excellent charm hadron factory. The present data sample (corresponding to an integrated luminosity of 390 fb^{-1}) contains over 400 M $\Upsilon(4S) \to B\bar{B}$ events and over 1200 M $e^+e^- \to q\bar{q}$ ($q = c, s, u, d$) events out of which 500 M are $e^+e^- \to c\bar{c}$ reactions. The relevant production cross sections at $\sqrt{s} = m(\Upsilon(4S))$ are listed in Table 3.1 [34].

The *BABAR* detector has excellent resolution as can be seen from the Λ and K_S[1]

Table 3.1: The $e^+e^- \to q\bar{q}$ production cross sections at $\sqrt{s} = m(\Upsilon(4S))$.

$e^+e^- \to$	cross section (nb)
$b\bar{b}$	1.05
$c\bar{c}$	1.30
$s\bar{s}$	0.35
$u\bar{u}$	1.39
$d\bar{d}$	0.35

($q = b, c, s, u, d$)

[1]Neutral kaons decay weakly into CP eigenstates ($CP|K^0 >= |\bar{K}^0 >$). The CP-even eigenstate, which decays to two pions, may written to a good approximation (assuming a

invariant mass distributions of Fig. 3.1, with 0.1 and 0.4 MeV/c^2 histogram bins, respectively.

Furthermore very high statistics charm baryon production and decay such as $\Lambda_c^+ \to pK^-\pi^+$ and $\Lambda_c^+ \to pK_S$, and fair statistics in rare decay modes (such as $\Lambda_c^+ \to \Sigma^0 K_S K^+$) are available (Fig. 3.1)[50].

The large samples of charm baryon two-body and quasi-two-body decays available at *BABAR*, as well as accessibility to rare decay modes with reasonable statistics, provides an excellent opportunity to study hyperons and hyperon resonances with high precision, and three such analyses constitute the work to be described in this thesis. The present chapter is devoted to a description of the selection procedures employed to obtain the relevant data samples, and the corresponding analyses are presented in detail in chapters 4, 5, and 6.

The selection of charm baryon candidates requires the sequential reconstruction of initial and intermediate state candidates using four-momentum addition of tracks. Particle identification (PID) selectors [35] based on specific energy loss (dE/dx) and Cherenkov angle measurements have been used to identify proton, pion and kaon final tracks. Each intermediate state candidate is required to have its invariant mass within a $\pm 3\sigma$ mass window centered on the fitted peak position of the relevant distribution, where σ is the mass resolution obtained from a fit to the mass spectrum. In all cases, the fitted peak mass is consistent with the expected value [22], and the

negligible amount of CP violation) $|K_S^0> = \frac{1}{\sqrt{2}}\left(|K^0> + |\bar{K}^0>\right)$, while the CP-odd eign-state, $|K_L^0> = \frac{1}{\sqrt{2}}\left(|K^0> - |\bar{K}^0>\right)$, decays to three pions. Therefore, in the study of $\Lambda_c^+ \to \Lambda \bar{K}^0 K^+$, the $\bar{K}^0$ is reconstructed as a K_S.

intermediate state invariant mass is then constrained to this value, with corresponding vertex fit probability required to be greater than 0.001. Due to the fact that each weakly-decaying intermediate state (i.e. the K_S and hyperons) is long-lived, the signal-to-background ratio is improved by imposing a vertex displacement[2] criterion (in the direction of the momentum vector). In order to further enhance signal-to-background ratio, a selection criterion is imposed on the center-of-mass momentum, p^*, of the parent charm baryon, since it is found empirically that combinatorial background is reduced significantly w.r.t. signal at higher p^* values. The use of charge conjugate states is implied for all studies presented in this thesis.

3.2 Selection of $\Xi_c^0 \to \Omega^- K^+$ and $\Omega_c^0 \to \Omega^- \pi^+$ Events

The data samples used for this analysis correspond to a total integrated luminosity of 116 fb^{-1} and 230 fb^{-1} for $\Xi_c^0 \to \Omega^- K^+$ and $\Omega_c^0 \to \Omega^- \pi^+$, respectively.

The selection of Ξ_c^0 and Ω_c^0 candidates requires the intermediate reconstruction of events consistent with $\Omega^- \to \Lambda K^-$ and $\Lambda \to p \pi^-$; PID selectors are used to identify the proton and the kaon tracks and the pion daughter of the Ω_c^0, while the pion daughter of the Λ is reconstructed as a charged track with no additional particle identification needed.

The weak decays of the Ω^- and Λ lead to an event topology represented schematically in Fig. 3.2; the lifetime of the charm baryon is so short that there is no significant displacement of its decay point w.r.t. the e^+e^- collision axis. The

[2]The distance between the production and decay vertex position.

signal-to-background ratio is improved by imposing vertex displacement criteria on the Ω^- and Λ decay points. The distance between the $\Omega^- K^+$ or $\Omega^- \pi^+$ vertex and the Ω^- decay vertex, when projected onto the plane perpendicular to the collision axis, must exceed 1.5 mm in the Ω^- direction. The distance between the Ω^- and Λ decay vertices is required to exceed 1.5 mm in the direction of the Λ momentum vector. In order to further enhance signal-to-background ratio, a selection criterion is imposed on the center-of-mass momentum, p^*, of the charm baryon: $p^* > 1.8$ GeV/c for Ξ_c^0 and $p^* > 2.5$ GeV/c for Ω_c^0 candidates. In addition, a minimum laboratory momentum requirement of 200 MeV/c is imposed on the π^+ daughter of the Ω_c^0 in order to reduce combinatorial background level due to soft pions.

The Λ invariant mass spectrum obtained from an inclusive 1.2 fb^{-1} data subsample is shown in Fig. 3.3. The invariant mass distribution (in data) of Ω^-'s produced from Ξ_c^0 decay, for the Ξ_c^0 mass signal region of Fig. 3.5, is shown in Fig. 3.4. As can be seen from this distribution, the Ω^- spectrum is almost completely free of background.

The invariant mass spectra of Ξ_c^0 and Ω_c^0 candidates in data are shown before efficiency correction in Figs. 3.5(a) and (b), respectively [28]. The signal yields (770$\pm$33 Ξ_c^0 and 159$\pm$17 Ω_c^0 candidates) are obtained from fits with a double Gaussian (Ξ_c^0) or single Gaussian (Ω_c^0) signal function and a linear background function. The corresponding average selection efficiencies obtained from Monte Carlo simulations are 14.7% and 15.8%, respectively.

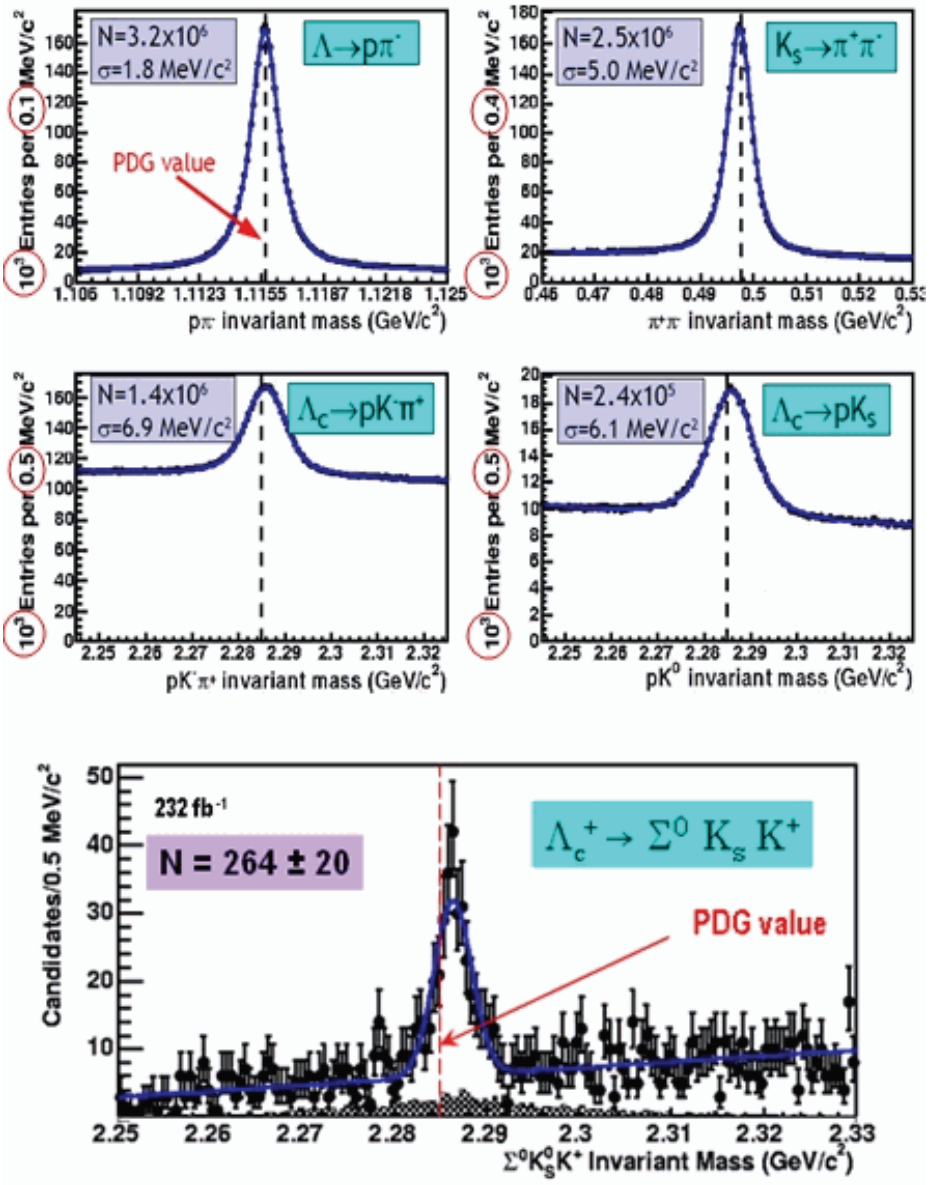

Figure 3.1: The invariant mass spectra of Λ, K_S and Λ_c^+ candidates produced inclusively [50].

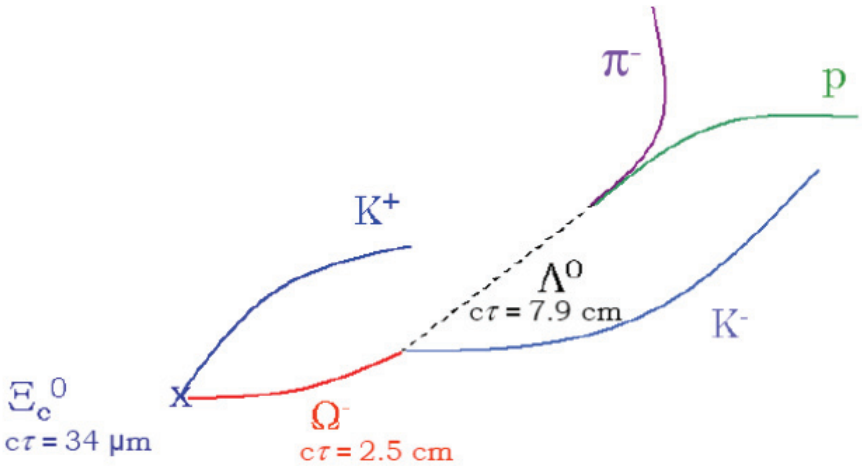

Figure 3.2: Sketch of the decay topology for $\Xi_c^0 \to \Omega^- K^+$; $\Omega^- \to \Lambda K^-$; $\Lambda \to p\pi^-$.

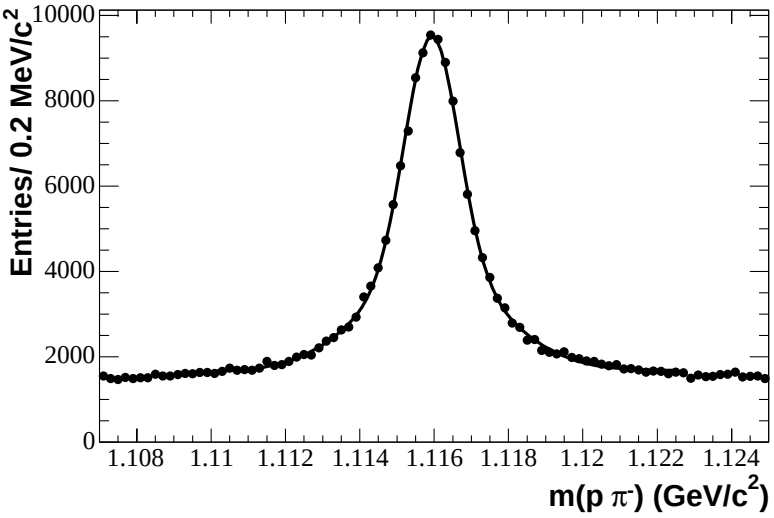

Figure 3.3: The uncorrected Λ invariant mass spectrum in $\sim$1.2 fb^{-1} of data. Superimposed on the distribution is a fit with a double Gaussian function with a common mean and a linear polynomial to parametrize the signal and background, respectively.

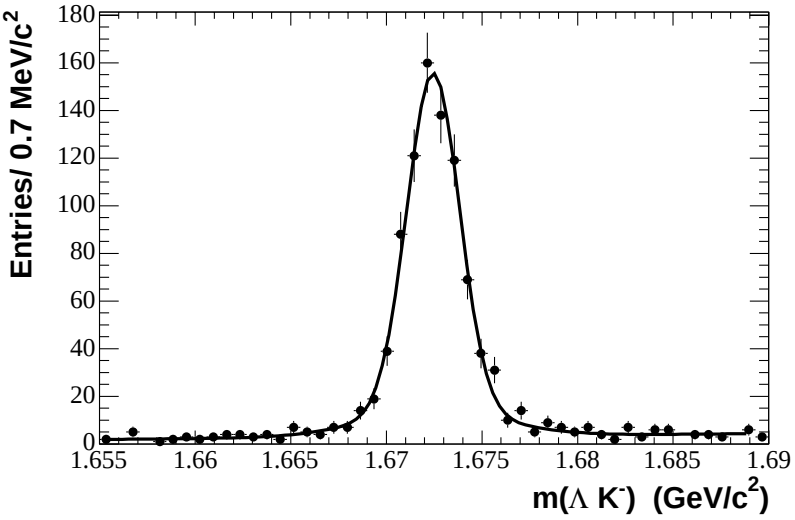

Figure 3.4: The uncorrected Ω^- invariant mass spectrum corresponding in $\sim 100\ \mathrm{fb}^{-1}$ data. Superimposed on the distribution is a fit with a double Gaussian function with a common mean and a linear polynomial to parametrize the signal and background, respectively.

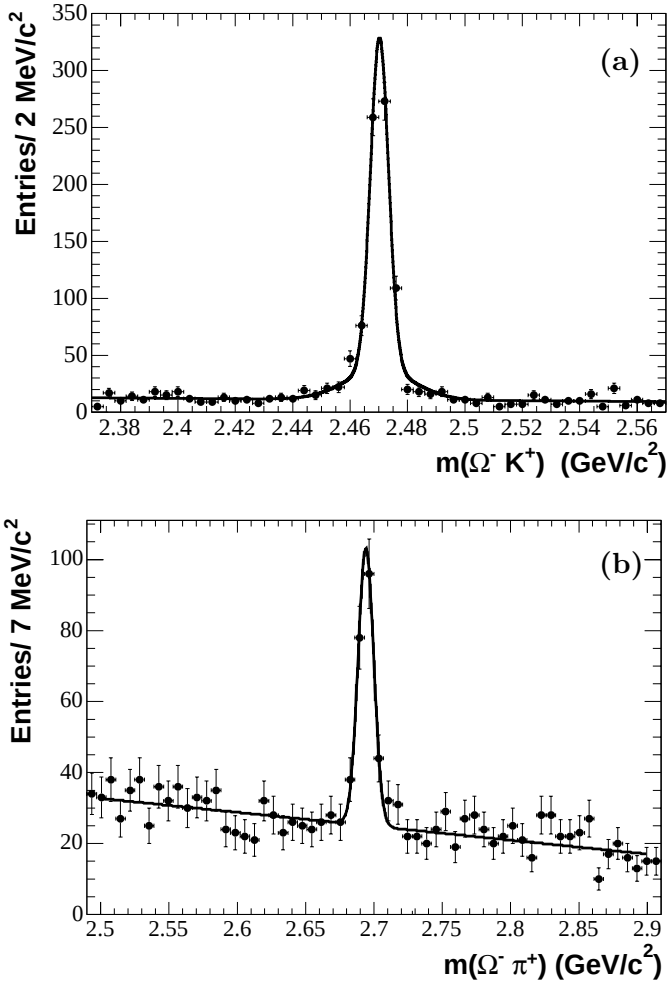

Figure 3.5: The uncorrected $\Omega^- K^+$ (a) and $\Omega^- \pi^+$ (b) invariant mass spectra in data. (a) The signal yield is obtained from an unbinned maximum likelihood fit to the invariant mass spectrum, with a double Gaussian and a linear function to fit the signal and background, respectively. The total yield is 770 ± 33; the narrow and wide Gaussians have respective widths 3.2 ± 0.2 and 11.8 ± 2.2 MeV/c^2; the χ^2/NDF is 80/49. (b) The signal yield is obtained from a fit with a single Gaussian signal distribution over a linear background function. The yield is 159 ± 17; the Gaussian width is 5.69 ± 0.79 MeV/c^2; the χ^2/NDF is 45/53.

3.3 Selection of $\Lambda_c^+ \to \Lambda \bar{K}^0 K^+$ Events

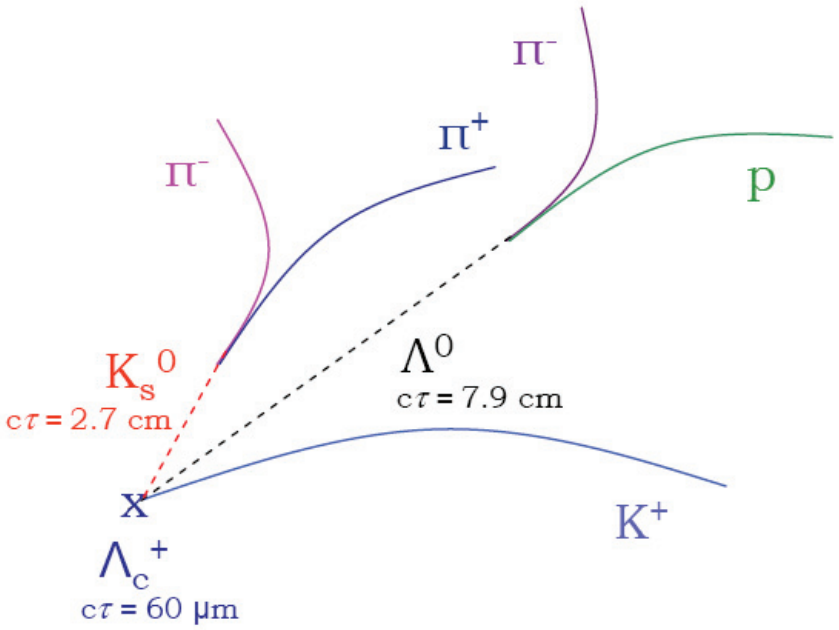

Figure 3.6: Sketch of the decay topology for $\Lambda_c^+ \to \Lambda \bar{K}^0 K^+$; $\Lambda \to p\pi^-$; $K_S \to \pi^+\pi^-$.

The data sample used for this analysis corresponds to a total integrated luminosity of about 200 fb^{-1}, and the relevant event topology is as shown schematically in Fig. 3.6. The selection of Λ_c^+ candidates requires the intermediate reconstruction of oppositely-charged track pairs consistent with $\Lambda \to p\,\pi^-$ and $K_S \to \pi^+\,\pi^-$ decays. The Λ and K_S candidates are then vertexed with a positively charged kaon track to form a Λ_c^+ candidate. In the reconstruction, proton and kaon candidates are required to satisfy PID criteria. The pion daughter of the Λ is reconstructed as a charged track. The signal-to-background ratio is improved by requiring that the Λ and K_S

decay vertex be separated from the event primary vertex by at least of 2.0 mm and 1.0 mm, respectively, in the flight direction of the Λ or K_S. In order to further enhance the signal-to-background ratio the center-of-mass momentum, p^*, of the Λ_c^+ is required to be greater than 1.5 GeV/c.

The invariant mass spectrum of Λ_c^+ candidates satisfying these selection criteria is shown before efficiency-correction in Fig. 3.7. A signal yield of 2930 ± 105 candidates is obtained from a fit to the invariant mass spectrum with a double Gaussian signal function and a linear background.

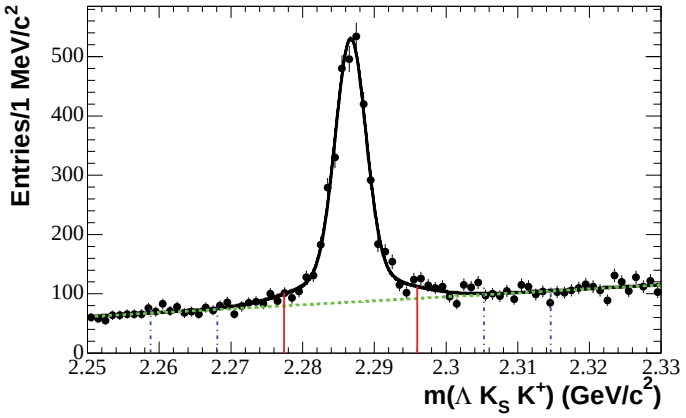

Figure 3.7: The invariant mass distribution of uncorrected $\Lambda K_S K^+$ candidates in data. The superimposed curve corresponds to a binned χ^2 fit which uses a double Gaussian signal function and a linear background parametrization denoted by the dashed line. The vertical lines delimit the signal region used in this analysis (solid) and the corresponding mass-sideband regions (dotted). The total yield is 2930 ± 105; the narrow and wide Gaussians have respective widths 2.1 ± 0.1 and 7.2 ± 0.2 MeV/c^2, corresponding to an r.m.s. of 4.2 ± 0.6 MeV/c^2 and an HWMH of ~ 3.1 MeV/c^2; the χ^2/NDF is 72.2/72.

3.4 Selection of $\Lambda_c^+ \to \Xi^-\pi^+K^+$ Events

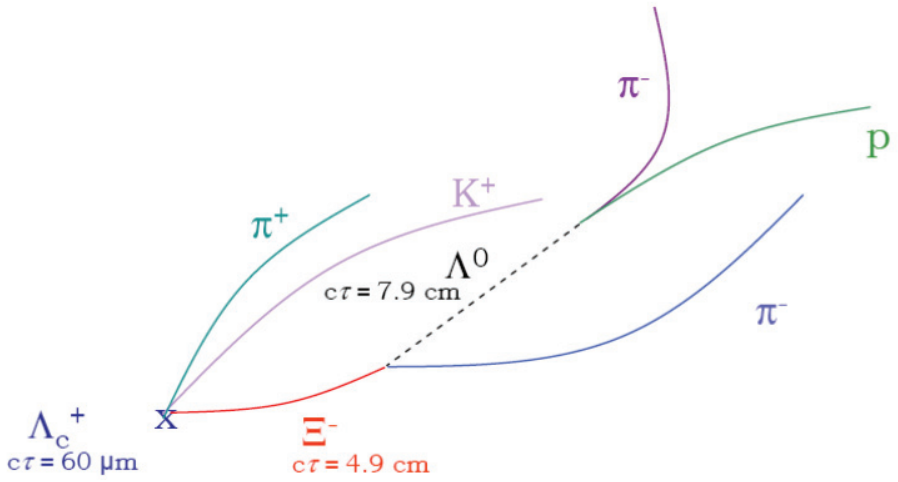

Figure 3.8: Sketch of the decay topology for $\Lambda_c^+ \to \Xi^-\pi^+K^+$; $\Xi^- \to \Lambda\pi^+$; $\Lambda \to p\pi^-$.

The data sample used for this analysis corresponds to a total integrated luminosity of about 230 fb^{-1}, and the relevant event topology is as shown schematically in Fig. 3.8. The selection of Λ_c^+ candidates requires the intermediate reconstruction of oppositely-charged track pairs consistent with $\Lambda \to p\,\pi^-$ and subsequently, the vertexing of the Λ candidate with a π^- to form a $\Xi^- \to \Lambda\pi^-$ candidate. The Ξ^- and π^+ candidates are vertexed with a positively charged kaon track to form a Λ_c^+ candidate. In the reconstruction, proton and kaon candidates are required to satisfy PID criteria, the pion daughter of the Λ is reconstructed as a charged track, as before.

The distance between the $\Xi^-K^+\pi^+$ vertex and the Ξ^- decay vertex, when projected onto the plane perpendicular to the collision axis, must exceed 1.5 mm in the Ξ^- direction. The distance between the Ξ^- and Λ decay vertices is required

to exceed 1.5 mm in the direction of the Λ momentum vector. The invariant mass distribution of uncorrected $\Xi^- \to \Lambda\pi^+$ candidates in $59\,\mathrm{fb}^{-1}$ is shown in Fig. 3.9. For illustration purposes, a fit with a double Gaussian on a linear background is overlaid.

In order to improve the purity of the sample the center-of-mass momentum, p^*, of the Λ_c^+ is required to be greater than 2.0 GeV/c.

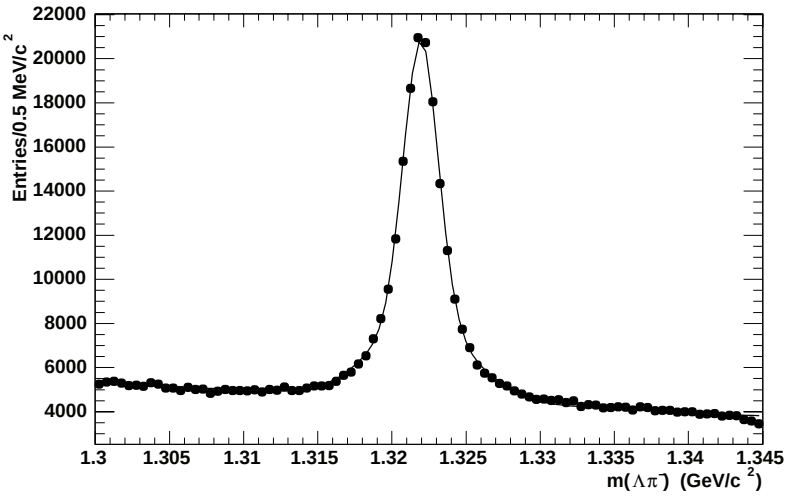

Figure 3.9: The invariant mass distribution of uncorrected $\Xi^- \to \Lambda\pi^+$ candidates in $59\,\mathrm{fb}^{-1}$ of data. For illustration purposes, a fit with a double Gaussian on a linear background is overlaid.

The invariant mass spectrum of Λ_c^+ candidates satisfying these selection criteria is shown before efficiency-correction in Fig. 3.10. A signal yield of 13035 ± 163 candidates is obtained from a fit to the invariant mass spectrum with a double Gaussian signal function and a linear background.

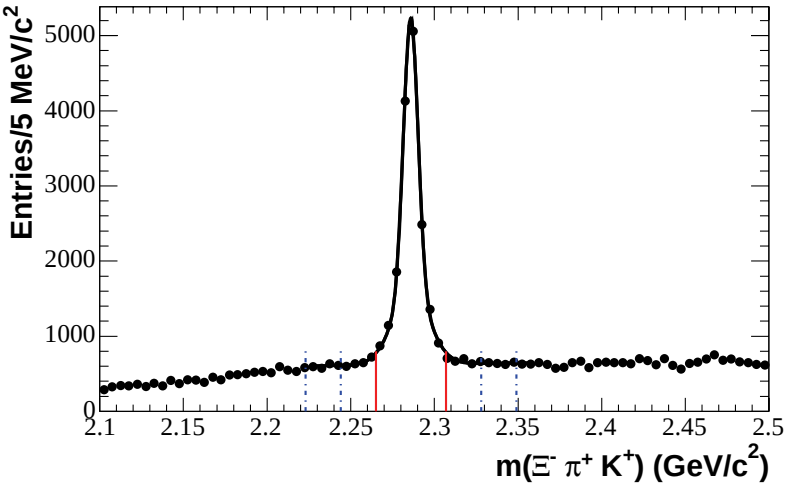

Figure 3.10: The invariant mass distribution of uncorrected $\Lambda_c^+ \to \Xi^-\pi^+K^+$ candidates in data. The superimposed curve corresponds to a binned χ^2 fit which uses a double Gaussian signal function and a linear background parametrization denoted by the dashed line. The vertical lines delimit the signal region used in this analysis (solid) and the corresponding mass-sideband regions (dotted). The total yield is 13035 ± 163; the narrow and wide Gaussians have respective widths 3.5 ± 0.1 and 9.5 ± 0.3 MeV/c^2, corresponding to an r.m.s. of 4.2 ± 0.5 MeV/c^2 and an HWMH of ~ 7.5 MeV/c^2; the χ^2/NDF is 19.6/20.

CHAPTER 4
MEASUREMENT OF THE SPIN OF THE Ω^- HYPERON

As discussed in chapter 1, although the existence of the Ω^- has been known since 1964, although it is firmly believed that it has spin $J = 3/2$, the spin value has never been established experimentally. It has been shown that $J \geq 3/2$ [14, 15, 16], but values greater than 3/2 have never been ruled out. The analyses presented in this chapter, based on the assumption that the ground-state charm baryons have spin 1/2 establish unequivocally that the Ω^- does indeed have spin 3/2.

Measurements of the Ω^- spin are obtained using Ω^- samples from the decay of Ξ_c^0 and Ω_c^0 charm baryons. The primary Ω^- sample is obtained from the decay sequence $\Xi_c^0 \to \Omega^- K^+$, with $\Omega^- \to \Lambda K^-$, while a much smaller sample resulting from $\Omega_c^0 \to \Omega^- \pi^+$, with $\Omega^- \to \Lambda K^-$ is used for corroboration. It is assumed that each charm baryon type has spin 1/2 and, as a result of its inclusive production, that it is described by a diagonal spin projection density matrix. The analysis does not require that the diagonal matrix elements be equal.

4.1 Predicted Angular Distributions for Charm Baryon Spin 1/2

The helicity formalism [36, 37] is applied in order to examine the implications of various Ω^- spin hypotheses for the angular distribution of the Λ from Ω^- decay.

By choosing the quantization axis along the direction of the Ω^- in the charm baryon rest-frame, the Ω^- inherits the spin projection of the charm baryon, since

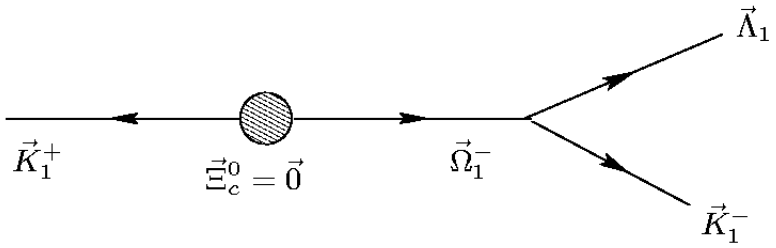

a) All decay products in the Ξ_c^0 rest-frame.

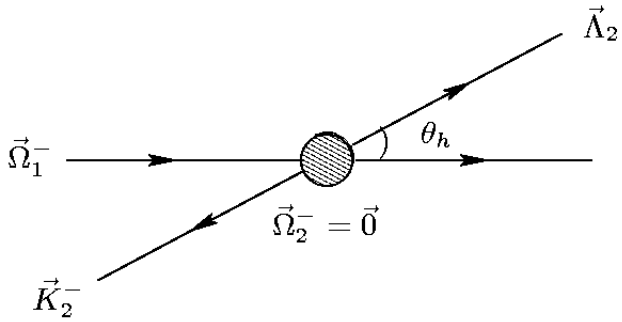

b) All decay products in the Ω^- rest-frame;
in this frame, $\vec{\Omega}_1^- \to \vec{\Omega}_2^- = \vec{0}$, $\vec{\Lambda}_1 \to \vec{\Lambda}_2$, $\vec{K}_1^- \to \vec{K}_2^-$.

Figure 4.1: Schematic definition of the helicity angle θ_h in the decay chain $\Xi_c^0 \to \Omega^- K^+$, $\Omega^- \to \Lambda K^-$; as shown in b) θ_h is the angle between the Λ direction in the Ω^- rest-frame and the Ω^- direction in the Ξ_c^0 rest-frame.

any orbital angular momentum in the charm baryon decay has no projection in this direction. It follows that, regardless of the spin J of the Ω^-, the density matrix describing the Ω^- sample is diagonal, with non-zero values only for the $\pm 1/2$ spin projection elements, i.e. the helicity λ_i of the Ω^- can take only the values $\pm 1/2$. Since the final state Λ and K^- have spin values 1/2 and 0, respectively, the net final state helicity λ_f also can take only the values $\pm 1/2$. The helicity angle θ_h is then defined as the angle between the direction of the Λ in the rest-frame of the Ω^- and the quantization axis (Fig. 4.1). The probability for the Λ to be produced with Euler angles $(\phi, \theta_h, 0)$ with respect to the quantization axis is given by the square of the amplitude ψ, characterizing the decay of an Ω^- with total angular momentum J and helicity λ_i to a 2-body system with net helicity λ_f,

$$\psi = A^J_{\lambda_f} D^{J\,*}_{\lambda_i \lambda_f}(\phi, \theta_h, 0), \tag{4.1}$$

where the transition matrix element $A^J_{\lambda_f}$ represents the coupling of the Ω^- to the final state, $D^J_{\lambda_i \lambda_f}$ is a Wigner D-function [38], and the $*$ denotes complex conjugation; $A^J_{\lambda_f}$ does not depend on λ_i because of rotational invariance (Wigner-Eckart theorem [39]). The angular distribution of the Λ is then given by the total intensity,

$$I \propto \sum_{\lambda_i, \lambda_f} \rho_{i\,i} \left| A^J_{\lambda_f} D^{J\,*}_{\lambda_i \lambda_f}(\phi, \theta_h, 0) \right|^2, \tag{4.2}$$

where the $\rho_{i\,i}$ $(i = \pm 1/2)$ are the diagonal density matrix elements inherited from the charm baryon, and the sum is over all initial and final helicity states.

Using this expression, the Λ angular distributions integrated over ϕ are ob-

tained for spin hypotheses $J_\Omega = 1/2$, $3/2$, and $5/2$, respectively:

$$dN/d\cos\theta_h \propto 1 + \beta\cos\theta_h \tag{4.3}$$

$$dN/d\cos\theta_h \propto 1 + 3\cos^2\theta_h + \beta\cos\theta_h(5 - 9\cos^2\theta_h) \tag{4.4}$$

$$dN/d\cos\theta_h \propto 1 - 2\cos^2\theta_h + 5\cos^4\theta_h + \beta\cos\theta_{\rm h}(5 - 26\cos^2\theta_h + 25\cos^4\theta_h), \tag{4.5}$$

where the coefficient of the asymmetric term

$$\beta = \left[\frac{\rho_{1/2\,1/2} - \rho_{-1/2\,-1/2}}{\rho_{1/2\,1/2} + \rho_{-1/2\,-1/2}}\right]\left[\frac{\left|A^J_{1/2}\right|^2 - \left|A^J_{-1/2}\right|^2}{\left|A^J_{1/2}\right|^2 + \left|A^J_{-1/2}\right|^2}\right]$$

may be non-zero as a consequence of parity violation in charm baryon and Ω^- weak decay[1]. The derivations of Eqs. 4.3, 4.4 and 4.5 are presented in detail in Appendix A.

4.2 Exclusive Ω^- Production in $\Xi_c^0 \to \Omega^- K^+$ Decay

In this analysis, measurements of the Ω^- spin are obtained using Ω^- samples from the decay of Ξ_c^0 and Ω_c^0 charm baryons inclusively produced in e^+e^- collisions at center-of-mass energies 10.58 and 10.54 GeV. The selection of these data samples has been described in chapter 3, section 3.2. The primary Ω^- sample is obtained from the decay sequence $\Xi_c^0 \to \Omega^- K^+$, with $\Omega^- \to \Lambda K^-$.

[1]Eqs. 4.3 and 4.4 are the distributions considered in connection with the discovery of the $\Delta(1232)$ resonance [40], generalized to account for parity violation.

4.2.1 Treatment of Background

The $\cos\theta_h(\Lambda)$ distribution is divided into ten intervals of equal size ranging from -1 to +1. For each interval, the $\Omega^- K^+$ invariant mass spectrum (cf. Fig. 3.5 (a)) from data is fitted with a double Gaussian signal function and linear background function, with the RMS fixed to the line shape obtained from the fit to the mass spectrum for the full range of $\cos\theta_h(\Lambda)$ described previously (section 3.2). Each fitted yield gives the background subtracted content of that interval of the $\cos\theta_h(\Lambda)$ spectrum. The fitted invariant mass spectrum for each interval is shown in Fig. 4.2 and the corresponding fit parameters are included in Table 4.1.

Table 4.1: The parameter values obtained from unbinned maximum likelihood fits to the Ξ_c^0 invariant mass for the individual intervals of $\cos\theta_h(\Lambda)$.

$\cos\theta_h(\Lambda)$ Interval	Uncorrected Yield	Fit χ^2/NDF	Fit Prob.	Efficiency-Corrected Yield
(-1.0, -0.8)	112.4 ± 11.2	39.4/49	0.86	805.3 ± 80.4
(-0.8, -0.6)	100.6 ± 10.9	43.7/49	0.72	713.5 ± 77.3
(-0.6, -0.4)	76.5 ± 9.4	45.2/49	0.67	537.2 ± 66.1
(-0.4, -0.2)	48.2 ± 7.6	62.0/49	0.12	335.5 ± 53.0
(-0.2, 0.0)	36.4 ± 6.7	29.5/49	0.99	250.7 ± 46.0
(0.0, 0.2)	46.3 ± 7.5	49.0/49	0.51	315.1 ± 50.8
(0.2, 0.4)	58.8 ± 8.5	49.1/49	0.50	396.3 ± 57.5
(0.4, 0.6)	66.1 ± 8.7	34.5/49	0.95	441.4 ± 58.3
(0.6, 0.8)	89.0 ± 9.8	58.9/49	0.18	588.4 ± 64.8
(0.8, 1.0)	138.7 ± 12.4	51.5/49	0.41	908.4 ± 81.5

The resulting background-subtracted uncorrected $\cos\theta_h(\Lambda)$ distribution shown in Fig. 4.3 is fitted using a parameterization of the form $\alpha(1+3\cos^2\theta_h)$, corresponding

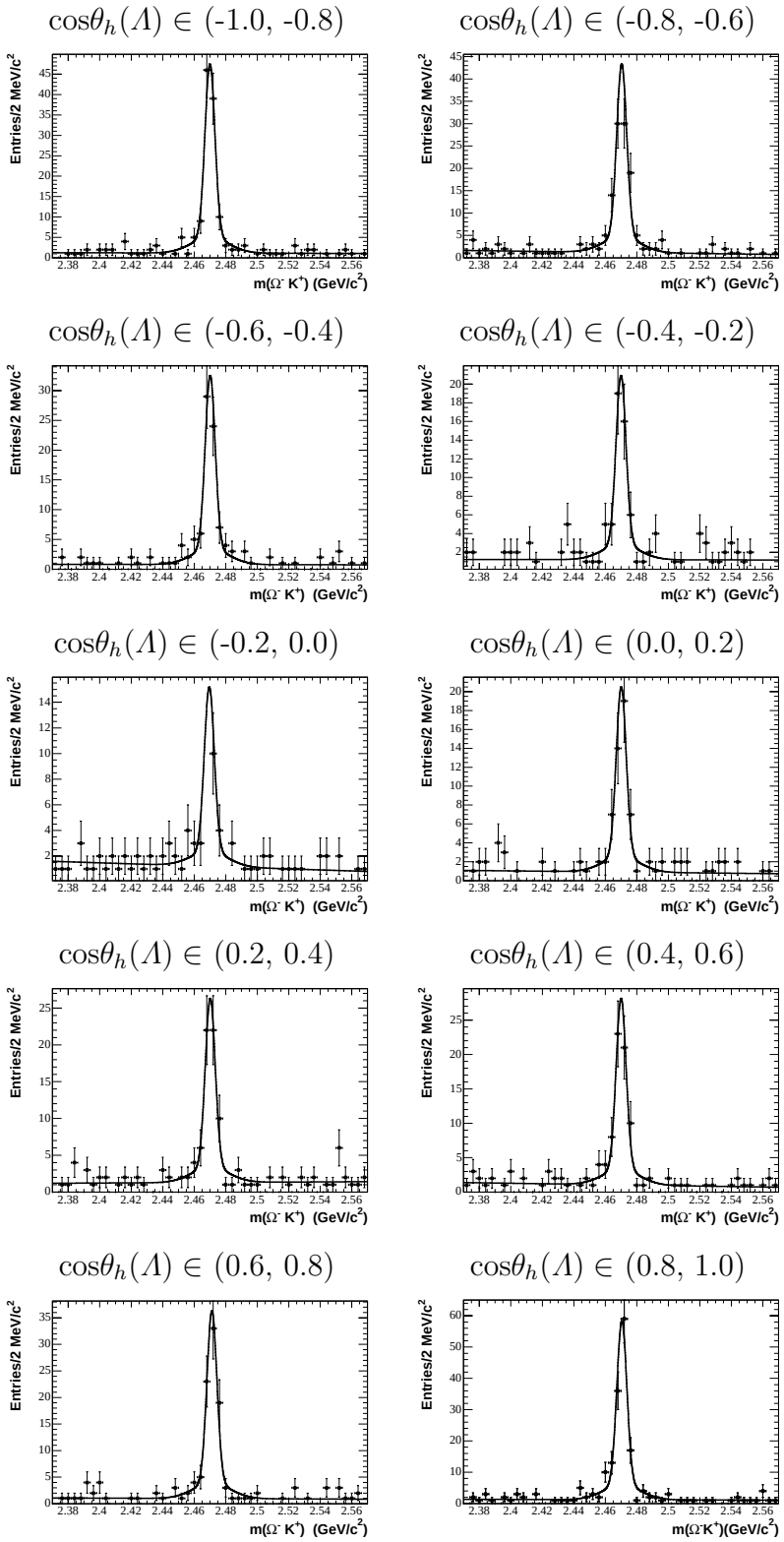

Figure 4.2: The invariant mass distribution of Ξ_c^0 candidates for each interval of $\cos\theta_h(\Lambda)$; the curves correspond to the fits described in the text.

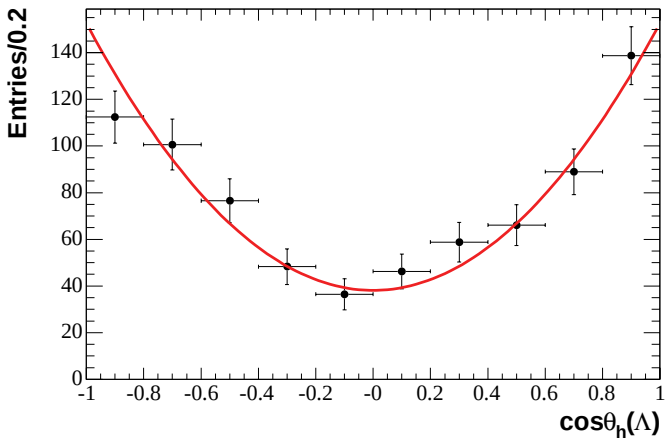

Figure 4.3: The background-subtracted uncorrected cos$\theta_h(\Lambda)$ distribution.

to a spin-3/2 hypothesis for the Ω^- and a spin-1/2 hypothesis for the Ξ_c^0 [40]. This fit has a χ^2 probability of 65% with $\chi^2/NDF = 6.9/9$, even though the distribution has not yet been efficiency-corrected.

4.2.2 Efficiency-corrected $\Omega^- \to \Lambda K^-$ Decay

Angular Distribution

The cos$\theta_h(\Lambda)$ distribution is expected to be symmetric about zero. However, the distribution seen in data has a predominant asymmetry in the region $|\cos\theta_{\rm h}(\Lambda)| > 0.8$. This effect is studied using a signal Monte Carlo (MC) sample of $\Omega^- \to \Lambda^0 K^-$ continuum events. An asymmetry similar to that observed in data, is apparent in the helicity angular distribution of truth-matched reconstructed signal MC events shown in Fig. 4.4. In contrast, for generated events (Fig. 4.5), it is symmetric.

In Figs. 4.6 and 4.7 scatter plots of the cosine of the angle between the $K^{+,-}$ and the lab z-axis (cos$\delta_{1,2}$) versus the cosine of the opening angle between the parent

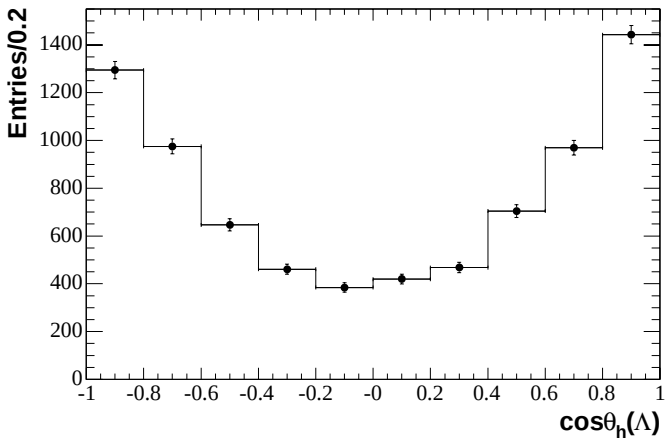

Figure 4.4: Truth-matched reconstructed Signal MC cos$\theta_h(\Lambda)$ distribution weighted by 1+3cos$\theta^2(\Lambda)$.

baryon (Ξ_c^0, Ω^-) and its decay kaon (cos$\alpha_{1,2}$) are shown. There is an empty band in cosδ in the reconstructed spectra, corresponding to the effect of detector acceptance. Due to this effect, the reconstructed distribution suffers from a loss of events in the region where the parent baryon and its daughter kaon are almost collinear. This however, is not the case for the generated spectrum. This loss of reconstructed events in the region cos$\delta_1 < 0.98$ and cos$\alpha_2 < 0.99$ induces an asymmetry in the backward end of the helicity cosine distribution. In order to further establish this point, it is required that cos$\delta_1 < 0.98$ and cos$\alpha_2 < 0.99$ in the reconstructed and generated spectra. As can be seen from Fig. 4.8, where the generated distribution is scaled to that of the reconstructed truth-matched distribution, this criterion induces an asymmetry in the generated spectrum similar to that in the reconstructed one.

Based on this MC study, it is clear that the spectrum in data can be corrected by obtaining the MC efficiency as a function of cos$\theta_h(\Lambda)$. The truth-matched

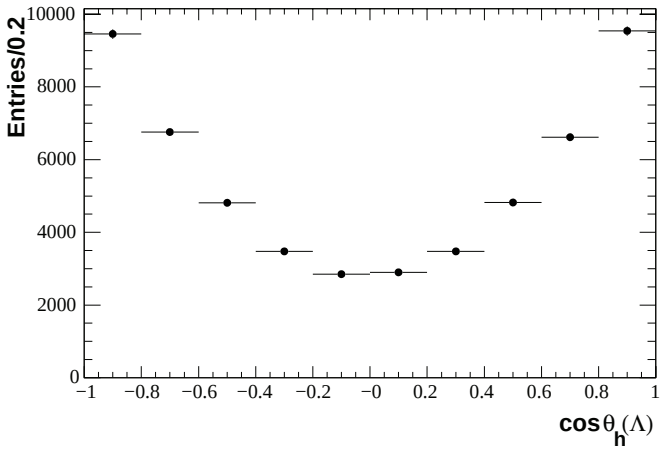

Figure 4.5: Generated signal MC $\cos\theta_h(\Lambda)$ distribution weighted by $1+3\cos\theta^2(\Lambda)$.

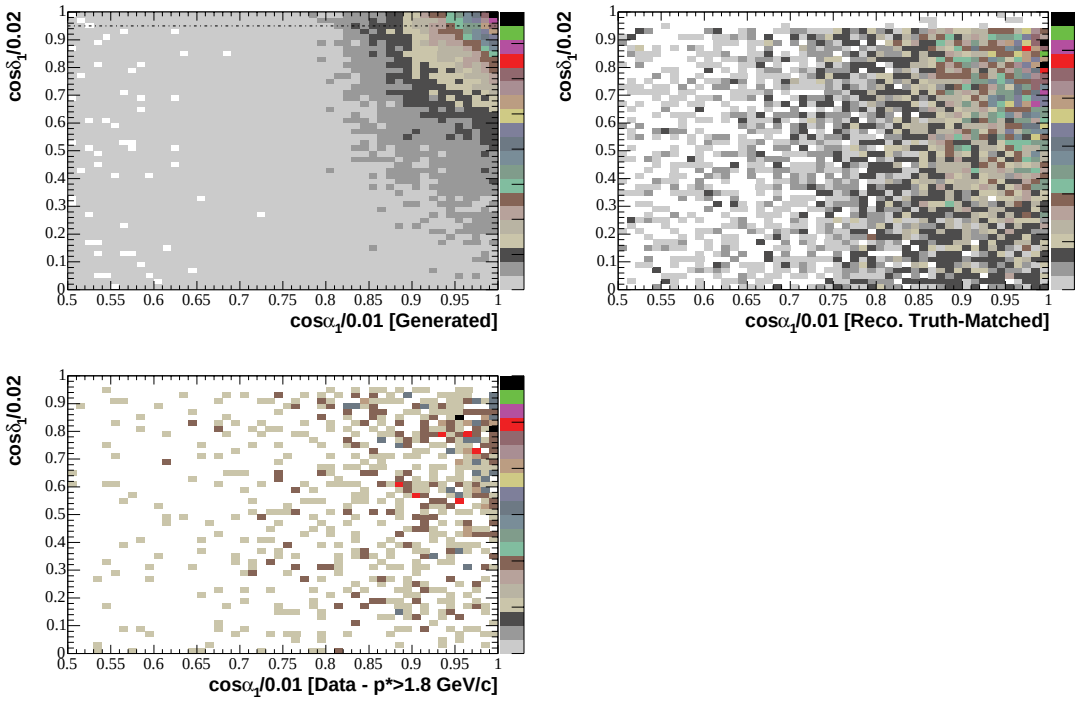

Figure 4.6: The scatter plots of the cosine of the angle between the K^+ and the lab z-axis ($\cos\delta_1$) versus the cosine of the opening angle between the Ξ_c^0 and its decay kaon ($\cos\alpha_1$).

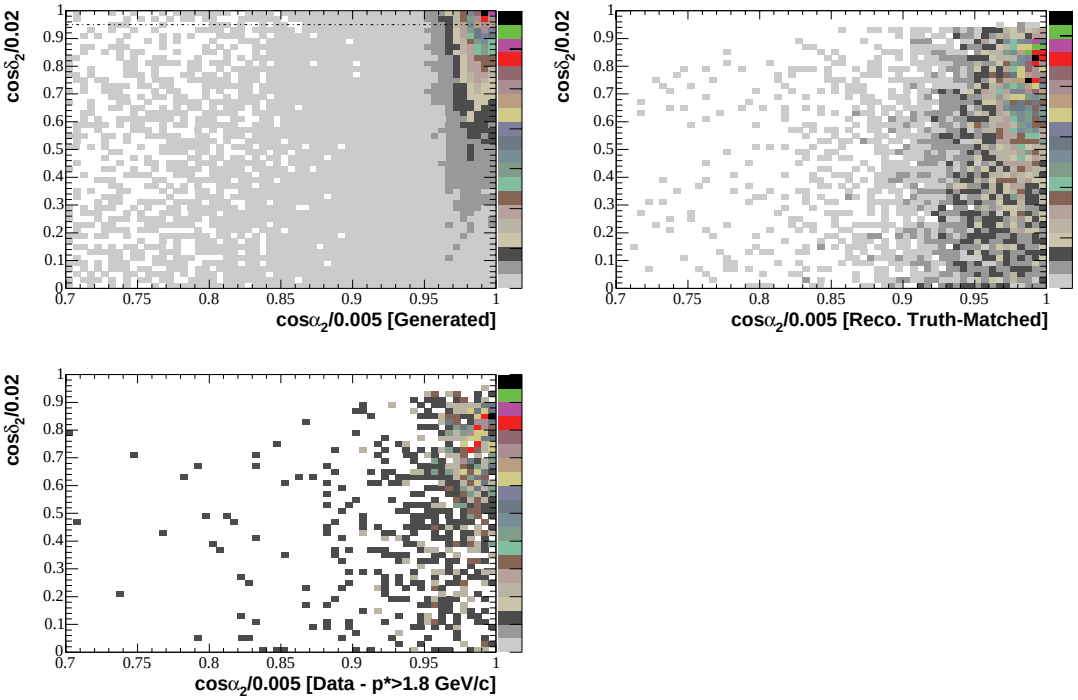

Figure 4.7: The scatter plots of the cosine of the angle between the K^- and the lab z-axis (δ_2) versus the opening cosine of the angle between the Ω^- and its decay kaon ($\cos\alpha_2$).

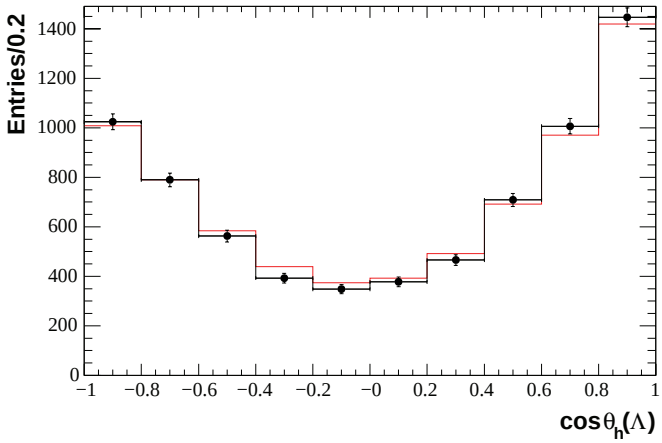

Figure 4.8: The reconstructed (red lines) and generated (black dots) MC distributions satisfying $\cos\delta_1 < 0.98$ and $\cos\alpha_2 < 0.99$.

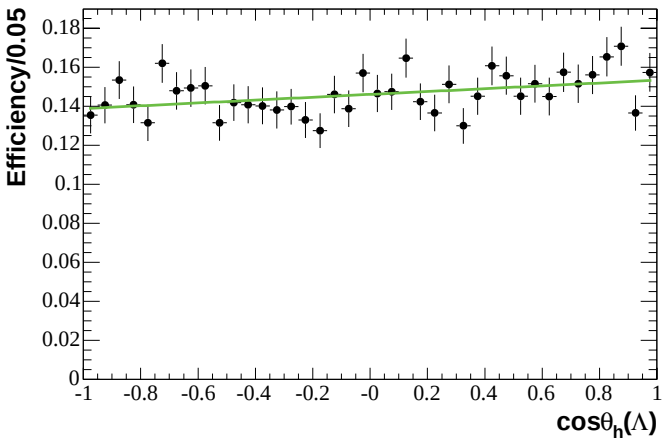

Figure 4.9: The Signal MC efficiency as a function of $\cos\theta_h(\Lambda)$.

distribution of signal MC satisfying the selection criteria is plotted in 40 intervals of $\cos\theta_h(\Lambda)$. In Signal MC, the helicity cosine distribution is generated flat; however, all angular effects cancel in the ratio of reconstructed to generated events. Similarly, the generated $\cos\theta_h(\Lambda)$ distribution in the region $p* > 1.8$ GeV/c is plotted in 40 intervals of $\cos\theta_h(\Lambda)$. The efficiency in each interval is obtained as the ratio of the reconstructed to generated event numbers in that interval. The efficiency is fit with a linear function and the efficiency at the center of each interval of $\cos\theta_h(\Lambda)$ is obtained from the efficiency parametrization shown in Fig. 4.9. The fit to the efficiency distribution has a χ^2 probability of 41% with $\chi^2/NDF = 39.4/38$, and the average value is about 15%.

4.3 Results of Fits to the Efficiency-Corrected Data

Figure 4.10 shows the efficiency-corrected $\cos\theta_h(\Lambda^0)$ distribution. The yield and its uncertainty after corrections is listed in Table 4.1 for each interval.

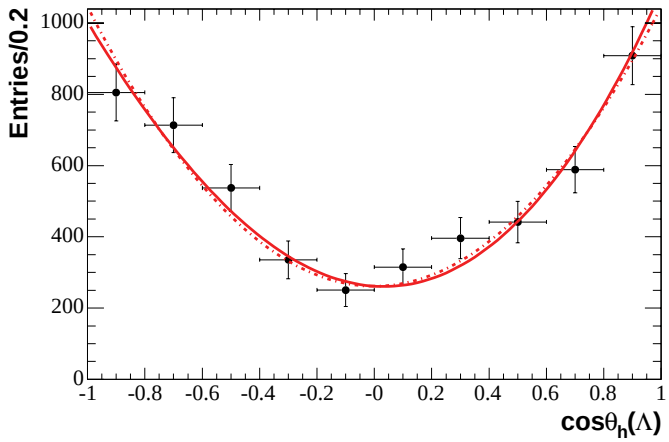

Figure 4.10: The efficiency-corrected $\cos\theta_h$ distribution for $\Xi_c^0 \to \Omega^- K^+$ data. The dashed curve corresponds to expression (2), which allows for a possible asymmetry through the parameter β. The solid curve represents the fit to the data with $\beta = 0$.

The chi-squared probability values for fits to the angular distribution functions given in section 4.1 are given in Table 4.2. The dashed curve corresponds to a fit of the $J_\Omega = 3/2$ parameterization of Eq. 4.4 and yields $\beta = 0.04 \pm 0.06$. Since the fit probability is good (64%), this indicates that the data show no significant asymmetry and so β is set to 0. The solid curve represents the fit to the data with $\beta = 0$ and actually yields a slightly better probability because of the extra degree of freedom.

The efficiency-corrected $\cos\theta_h(\Lambda)$ distribution with fits corresponding to Eqs. 4.3 and 4.5 is shown in Fig. 4.11. The solid (dashed) line represents the expected distribution for $J_\Omega = 1/2$ with $\beta = 0$ ($\beta \neq 0$), while the solid (dashed) curve corresponds to $J_\Omega = 5/2$ with $\beta = 0$ ($\beta \neq 0$); the fit results are indicated in Table 4.2, and the corresponding fit probabilities are extremely small.

The forward-backward asymmetry $A = \frac{F-B}{F+B}$, of the efficiency-corrected $\cos\theta_h(\Lambda)$

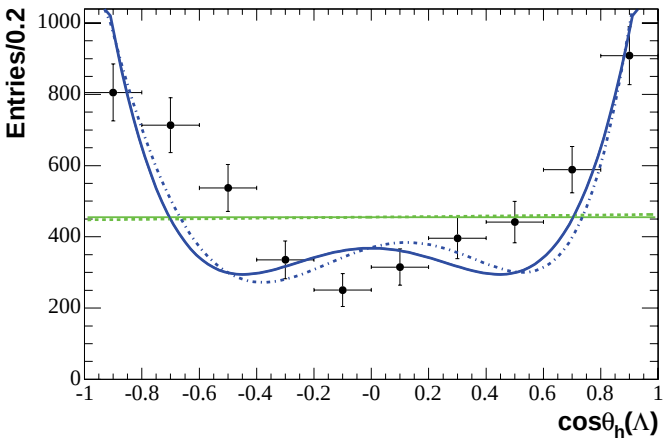

Figure 4.11: The efficiency-corrected $\cos\theta_h$ distribution for $\Xi_c^0 \to \Omega^- K^+$ data. The solid (dashed) line represents the expected distribution for $J_\Omega = 1/2$ with $\beta = 0$ ($\beta \neq 0$), while the solid (dashed) curve corresponds to $J_\Omega = 5/2$ with $\beta = 0$ ($\beta \neq 0$).

Table 4.2: The fit probabilities corresponding to Ω^- spin hypotheses 1/2, 3/2 and 5/2, assuming $J_{\Xi_c} = 1/2$.

J_Ω	Fit χ^2/NDF	Fit probability	Comment
1/2	100.4/9	1×10^{-17} ($\beta = 0$)	Fig. 4.11, solid line
1/2	100.4/8	3×10^{-18} ($\beta = 0.02 \pm 0.11$)	Fig. 4.11, dashed line
3/2	6.5/9	0.69 ($\beta = 0$)	Fig. 4.10, solid curve
3/2	6.1/8	0.64 ($\beta = 0.04 \pm 0.06$)	Fig. 4.10, dashed curve
5/2	47.6/9	3×10^{-7} ($\beta = 0$)	Fig. 4.11, solid curve
5/2	45.3/8	3×10^{-7} ($\beta = 0.12 \pm 0.08$)	Fig. 4.11, dashed curve

distribution of Fig. 4.10, where B and F represent the number of signal events satisfying $\cos\theta_h(\Lambda) \leq 0$ and $\cos\theta_h(\Lambda) \geq 0$, respectively, is 0.001 ± 0.019. This value shows quantitatively that the distribution has no significant asymmetry and corroborates the results given by the fits of of Figs. 4.10 and 4.11.

Clearly, the only viable possibility is that the Ω^- has spin 3/2, provided the

Ξ_c^0 has spin 1/2.

For Ω^- spin greater than 5/2, the predicted angular distributions peak even more strongly at $\cos\theta_h(\Lambda) \sim \pm 1$, and have $2J_\Omega - 2$ turning points, and so such values may be discounted.

4.4 Exclusive Ω^- Production in $\Omega_c^0 \to \Omega^-\pi^+$ Decay

The Ω^- spin measurement obtained from the $\Xi_c^0 \to \Omega^- K^+$ sample is corroborated using a much smaller data sample resulting from $\Omega_c^0 \to \Omega^-\pi^+$, with $\Omega^- \to \Lambda K^-$.

The Ω_c baryon is presumed to belong to the **6** representation of an $SU(3)$ $J^P = 1/2^+$ multiplet; as a result the angular distribution of Ω's produced exclusively from the decay of this charm baryon is expected to be $\alpha(1 + 3\cos^2\theta_h)$.

Due to the limited statistics, a mass-sideband subtraction method is used to extract the number of signal events in each interval of $\cos\theta_h(\Lambda)$. The Ω_c^0 signal region corresponds to the mass range 2.677 to 2.711 GeV/c^2; the left and right mass-sideband regions are defined as (2.643, 2.660) GeV/c^2 and (2.728, 2.745) GeV/c^2, respectively (cf. Fig. 3.5 (b)).

Figure 4.12 shows the uncorrected $\cos\theta_h(\Lambda)$ distribution. The curve shown corresponds to a fit of the function $\alpha(1 + 3\cos^2\theta_h)$ with $\chi^2/NDF = 7.3/9$ and a probability of 61%.

The efficiency as a function of $\cos\theta_h(\Lambda)$ shown in Fig. 4.13 is obtained from Signal MC and is parameterized with a fourth order polynomial; the fit has χ^2/NDF

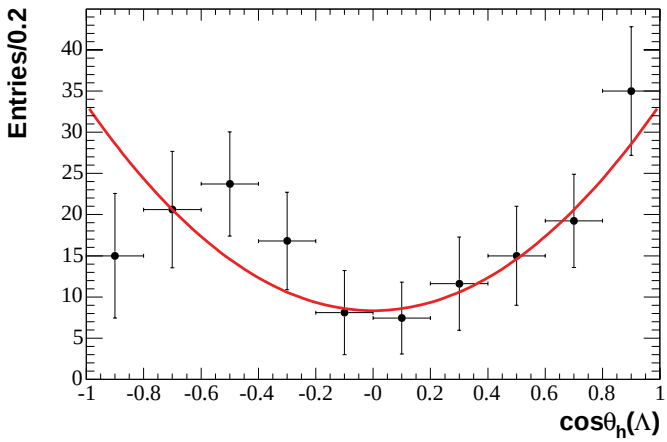

Figure 4.12: The mass-sideband-subtracted uncorrected $\cos\theta_h(\Lambda)$ distribution in data for the Ω_c^0 signal events.

of 61.5/91 and a corresponding probability of 90%.

After correcting the spectrum by the efficiency calculated in each bin from the parametrization obtained from the MC, the distribution shown in Fig. 4.14 is obtained; it is consistent with the helicity cosine distribution hypothesis for a spin 1/2 to 3/2 transition. The fit to the corrected distribution with a function $\alpha(1 + 3\cos\theta_h^2(\Lambda))$ has a χ^2/NDF of 6.5/9 and a probability of 69%. Although, when letting the β parameter free in the fit for the parametrization corresponding to the spin 3/2 hypothesis for the Ω^- (as done in section 4.3), $\beta = 0.4 \pm 0.2$ is obtained; the calculated value for the forward-backward asymmetry is $A = \frac{F-B}{F+B} = 0.013 \pm 0.058$, which corroborates the previously established observation that the angular distribution is symmetric.

The chi-squared probability values for fits to the angular distribution functions of Eqs. 4.3 and 4.5 with $\beta = 0$ are given in Table 4.3.

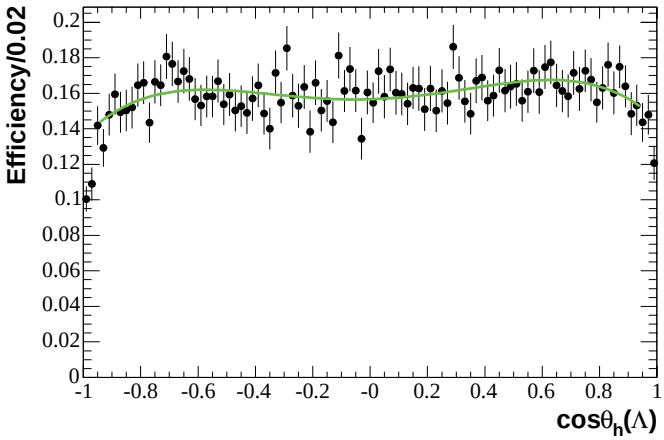

Figure 4.13: The detection efficiency for $\Omega_c^0 \to \Omega^-\pi^+$ as a function of $\cos\theta_h(\Lambda)$; the curve is obtained from the fit of a fourth-order polynomial to the measured values.

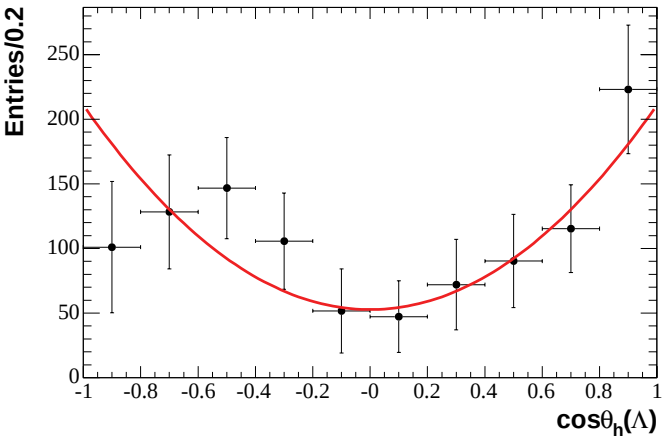

Figure 4.14: The efficiency corrected $\cos\theta_h(\Lambda)$ distribution in data for the Ω_c^0 signal events using the mass-sideband-subtraction method; the curve corresponds to a fit of the function $\alpha(1 + 3\cos^2\theta_{\rm h}(\Lambda))$ to the data points.

Table 4.3: The fit probabilities corresponding to Ω^- spin hypotheses 1/2, 3/2 and 5/2, assuming $J_{\Omega_c} = 1/2$ and $\beta = 0$.

J_Ω	Fit χ^2/NDF	Fit probability	Comment
1/2	14.6/9	0.10	Fig. 4.15, solid line
3/2	6.5/9	0.69	Fig. 4.14, solid curve
5/2	13.1/9	0.16	Fig. 4.15, dashed curve

The lack of statistics in this mode compared to the $\Xi_c^0 \to \Omega^- K^+$ sample, is such that the uncertainty in the fits is much larger. Thus, the fit probability assuming that the Ω_c^0 has spin 1/2, and the Ω^- has spin 3/2 does not differ as strongly from the other hypotheses considered as for $\Xi_c^0 \to \Omega^- K^+$. Nevertheless, it is clear that if the Ω_c^0 has spin 1/2, spin value of 3/2 is preferred for the Ω^-.

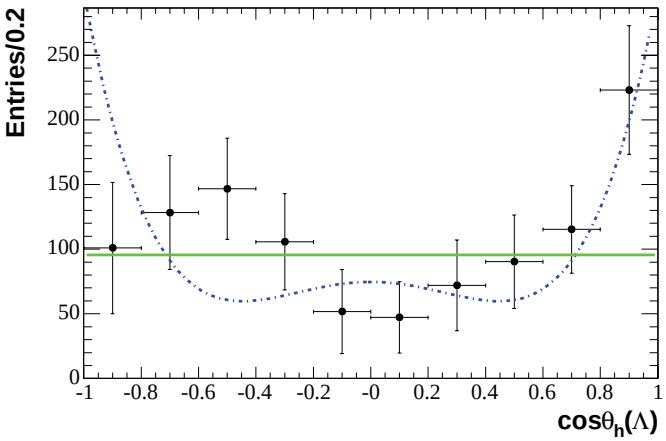

Figure 4.15: The efficiency corrected $\cos\theta_h(\Lambda)$ distribution in data for the Ω_c^0 signal events using the mass-sideband-subtraction method; the curves correspond to the fits described in the text.

4.5 The Use of Legendre Polynomial Moments in Spin Determination

For Ω^- spin J, the angular distributions obtained in the previous section can be written (after efficiency-correction and background subtraction):

$$\frac{dN}{d\cos\theta_h} = N\left[\sum_{l=0}^{l_{max}} \langle P_l \rangle P_l\left(\cos\theta_h\right)\right], \tag{4.6}$$

where $l_{max} = 2J-1$, and if l is odd $\langle P_l \rangle = 0$. The normalized Legendre Polynomials satisfy

$$\int_{-1}^{1} d\cos\theta_h \mathrm{P}_i\left(\cos\theta_h\right) \mathrm{P}_j\left(\cos\theta_h\right) = \delta_{i\,j}; \tag{4.7}$$

so that

$$\int_{-1}^{1} \frac{dN}{d\cos\theta_h} P_l\left(\cos\theta_h\right) d\cos\theta_h = \mathrm{N}\langle \mathrm{P}_l \rangle \approx \sum_{\mathrm{j}=1}^{\mathrm{N}} \mathrm{P}_l\left(\cos\theta_{h_j}\right) \tag{4.8}$$

Each assumption for J defines l_{max}, so that $\langle P_l \rangle = 0$ for $l > l_{max}$ and $\langle P_l \rangle$ is calculable. The relation

$$\sum_{j=1}^{N} \frac{P_{l_{max}}\left(\cos\theta_{h_j}\right)}{\langle P_{l_{max}} \rangle} = N \tag{4.9}$$

implies that the number of Ω^- signal events in a given mass bin is obtained by giving each event, j, in that bin, a weight

$$w_j = \frac{P_{l_{max}}\left(\cos\theta_{h_j}\right)}{\langle P_{l_{max}} \rangle}. \tag{4.10}$$

In particular, for $J = 3/2$, giving each event a weight $w_j = \sqrt{10} P_2(\cos\theta_{h_j})$ projects the complete Ω^- signal, where the distribution of $N_i = \sum_j w_j$ is called the $\frac{P_L(\cos\theta_h)}{\langle P_{l_{max}} \rangle}$

moment distribution. In order to test the $J = 5/2$ hypothesis, each event is given a weight $w_j = \frac{7}{\sqrt{2}} P_4(\cos\theta_{h_j})$.

The effect of this weighting procedure on data is demonstrated by using the $\Xi_c^0 \to \Omega^- K^+$ candidate sample of Fig. 3.4(a), but with no p^* cut in order to increase the signal size. The corresponding $\Omega^- K^+$ invariant mass distribution is shown in Fig. 4.16, with signal and sideband regions as indicated, and the dependence of signal-efficiency on $\cos\theta_h(\Lambda)$ for this sample is a shown in Fig. 4.17.

Figures 4.18 and 4.20 show the Ω^- invariant mass distributions corresponding to the $\Xi_c^0 \to \Omega^- K^+$ mass-signal region ($2.452 < m < 2.488$ GeV/c^2) indicated Fig. 4.16. The solid histogram represents the efficiency-corrected (using the efficiency parametrization of Fig. 4.17), unweighted Ω^- mass spectrum, while the open circles represent the efficiency-corrected (Fig. 4.18(a)) $\sqrt{10}P_2(\cos\theta_h)$ and (Fig. 4.20) $7/\sqrt{2}P_4(\cos\theta_h)$ moments of the distribution. As expected, the $\sqrt{10}P_2(\cos\theta_h)$ moment projects out the Ω^- signal, whereas the $7/\sqrt{2}P_4(\cos\theta_h)$ moment does not.

Figure 4.18(b) shows the efficiency-corrected Ω^- mass spectrum corresponding to Ξ_c^0 low- and high-mass sideband regions (Fig. 4.16), each of width 6-σ (i.e. $2.398 < m < 2.434$ and $2.506 < m < 2.542$ GeV/c^2, respectively). The peak indicates that the Ξ_c^0 mass-sidebands contain real Ω^- events. However, since these Ω^-'s are not produced from *real* Ξ_c^0 candidates, the corresponding $\sqrt{10}P_2(\cos\theta_h(\Lambda))$ moment distribution has no structure. Thus, the effect of weighting each event j by the factor $(< P_2 >)^{-1} P_2(\cos\theta_j)$ is to project away background candidates from the invariant mass spectrum.

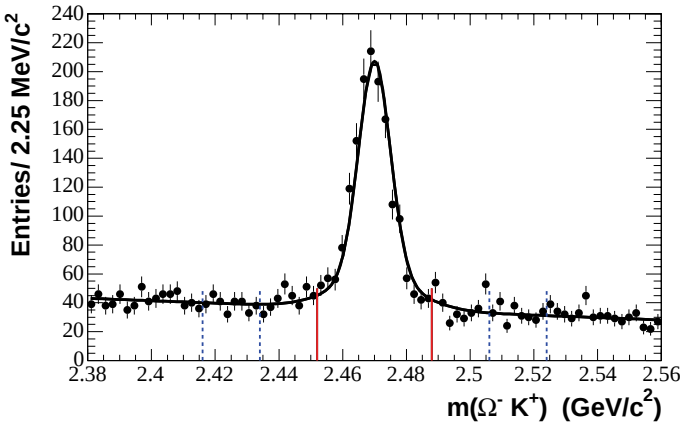

Figure 4.16: The $\Omega^- K^+$ invariant mass spectrum in data for Ξ_c^0 candidates with no p^* cut (c.f. Fig. 3.4(a)). The solid red lines delimit the selected signal region and the dotted blue lines, the low and high mass-sideband regions, used in the analysis. The superimposed curve represents a fit with a double Gaussian to parametrize the Ξ_c^0 signal and a linear function to describe the background lineshape. This fit ($\chi^2/NDF = 60.9/73$, prob=0.84) gives a total yield of 1153 ± 124 and an r.m.s. of 7.7 ± 0.8 MeV.

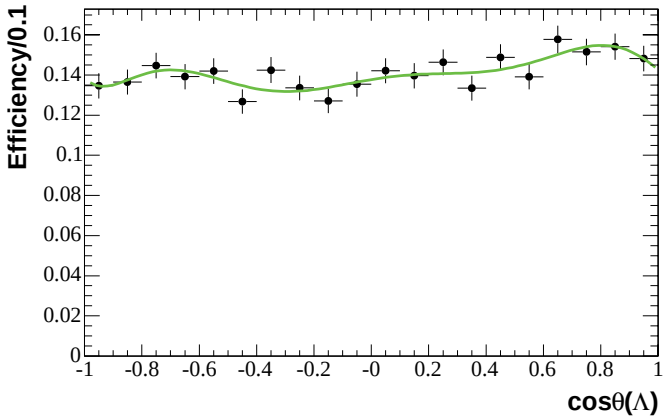

Figure 4.17: The efficiency calculated from $\Xi_c^0 \to \Omega^- K^+$ Signal Monte Carlo as a function of $\cos\theta_h(\Lambda)$. The superimposed green curve represents a fit to the distribution with an 8^{th} order polynomial function ($\chi^2/NDF = 12.6/11$ prob. $= 0.32$).

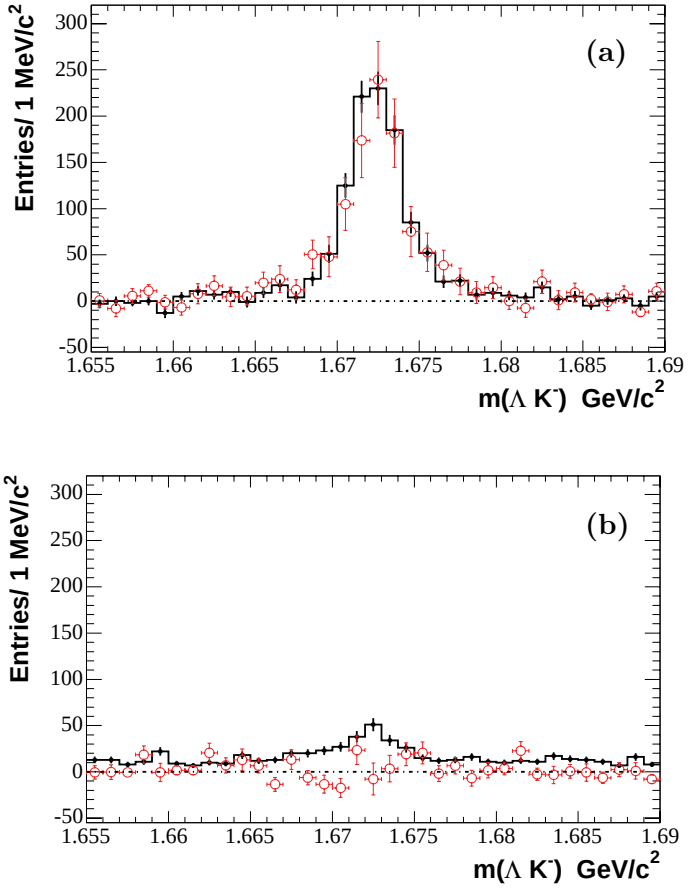

Figure 4.18: The efficiency-corrected normalized $\sqrt{10}P_2(\cos\theta_h(\Lambda))$ moment distributions (open circles) as a function of the Ω^- invariant mass obtained from $\Xi_c^0 \to \Omega^- K^+$ events corresponding to (a) the Ξ_c^0 mass-signal region, (b) the Ξ_c^0 mass-sideband regions (Fig. 4.16); the solid histogram shows the efficiency-corrected, unweighted Ω^- mass spectrum for (a) the mass-sideband-subtracted Ξ_c^0 mass-signal region, (b) the Ξ_c^0 mass-sideband regions . The histograms have been scaled by the overall efficiency factor of 0.14.

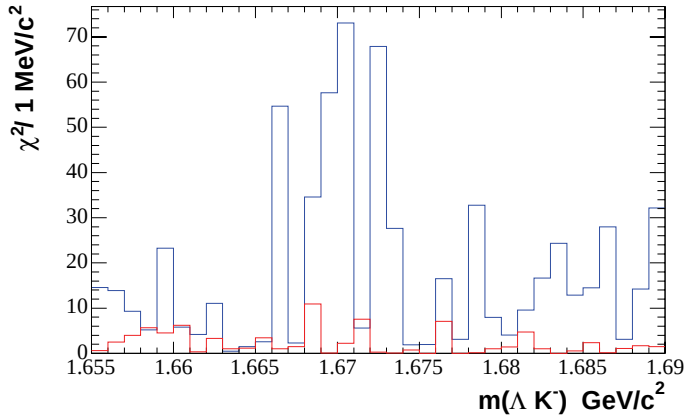

Figure 4.19: The χ^2 calculated between the unweighted Ω^- mass spectrum (solid histogram) and the normalized moment $\sqrt{10}P_2(\cos\theta_h(\Lambda))$ distribution (open circles) of Fig. 4.18; for the Ξ_c^0 signal region (red), and the Ξ_c^0 mass-sideband regions (blue).

A χ^2 is then computed between the Ω^- mass spectra (solid histograms) and the normalized moment distributions (open circles) of Figs. 4.18 and 4.20. The results are shown in Figs. 4.19 and. 4.21.

As expected, the χ^2 value for the Ξ_c^0 mass-sideband regions distributions is large, in particular in the signal region of the Ω^-, which corroborates the finding that these Ω^- candidates are not produced from Ξ_c^0 signal events. The χ^2 distribution obtained for the $7/\sqrt{2}P_4(\cos\theta_h(\Lambda))$ weighting is also very poor, as indicated by Fig. 4.21.

The use of Legendre polynomial moments illustrated here will prove to be useful in connection with the spin determination of hyperon resonances to be presented in chapters 5 and 6.

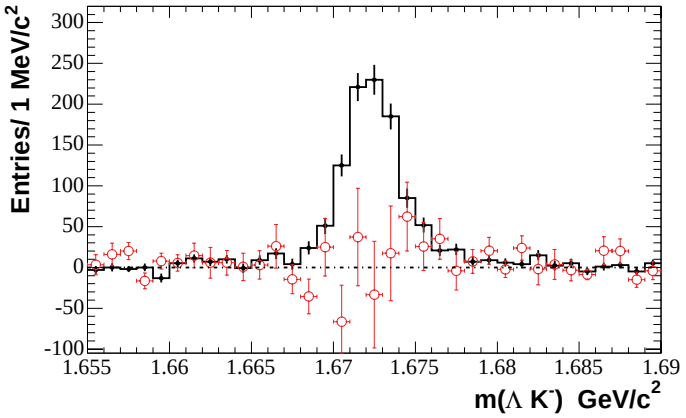

Figure 4.20: The efficiency-corrected normalized $7/\sqrt{2}P_4(\cos\theta_h(\Lambda))$ moment (open circles) as a function of the Ω^- invariant mass obtained from $\Xi_c^0 \to \Omega^- K^+$ events; the solid histogram shows the efficiency-corrected, unweighted Ω^- mass spectrum for the Ξ_c^0 mass-signal region, after mass-sideband-subtraction. The distributions have been scaled by the overall efficiency factor of 0.14.

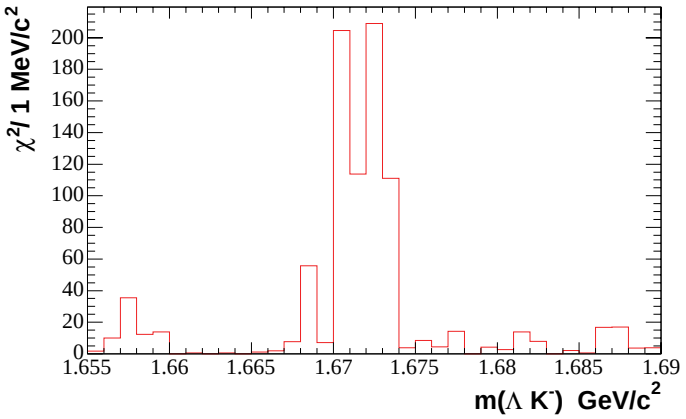

Figure 4.21: The χ^2 calculated between the unweighted Ω^- mass spectrum (solid histogram) and the $\frac{7}{\sqrt{2}}P_4(\cos\theta_h(\Lambda))$ weighted distribution (open circles) of Fig. 4.20.

4.6 The Implications of $J_{\Xi_c} = 3/2$

The analyses presented in the prior section of this chapter have relied on the assumption that the parent charm baryon has spin 1/2. The implications of charm baryon spin 3/2 for the spin of the Ω^- are now considered.

As the observed helicity cosine distribution has no forward-backward asymmetry, the Λ angular distributions for $J_{\Xi_c} = 3/2$ and different spin hypotheses for the Ω^- are (neglecting the asymmetric term):

$$J_\Omega = 1/2 \;\; : \;\; 1 \tag{4.11}$$

$$J_\Omega = 3/2 \;\; : \;\; (1 + 3\cos^2\theta_h) + 2x\,(1 - 3\cos^2\theta_h) \tag{4.12}$$

$$J_\Omega = 5/2 \;\; : \;\; (10\cos^4\theta_h - 4\cos^2\theta_h + 2) - x\,(25\cos^4\theta_h - 18\cos^2\theta_h + 1). \tag{4.13}$$

where, $x = \rho_{3/2} + \rho_{-3/2}$ and $Tr(\rho) = 1$. [The details of the derivations are given in Appendix A, section A.2.] Note that if $x = 0.5$ expressions 4.11 and 4.12 yield a flat distribution, and Eq. 4.13 becomes becomes

$$J_\Omega = 5/2 : -5\cos^4\theta + 10\cos^2\theta + 3,$$

i.e. for $J_\Omega = 5/2$, $x = 0.5$

$$\frac{dN}{\mathrm{d}\cos\theta_h} \propto -5\cos^4\theta_h + 10\cos^2\theta_h + 3, \tag{4.14}$$

which has a minimum at $\cos\theta_h = 0$, maxima at $\cos\theta_h = \pm 1$, as can be seen from Fig. 4.22. If x is allowed to vary, the best fit to the data has $x = 0.4$, which corresponds to

$$\frac{dN}{\mathrm{d}\cos\theta_h} \propto 1 + 2\cos^2\theta_h; \tag{4.15}$$

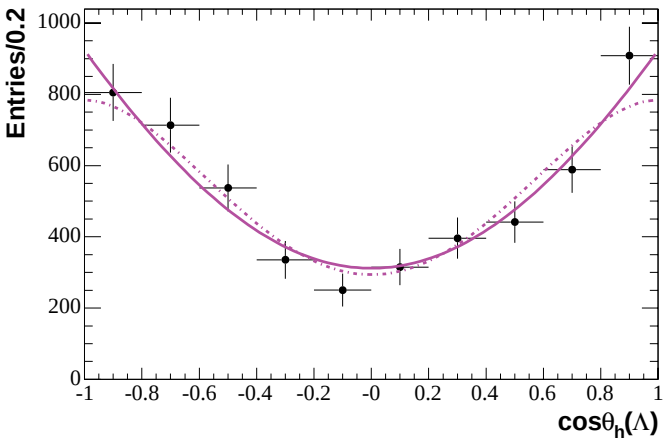

Figure 4.22: The efficiency-corrected $\cos\theta_h$ distribution for $\Xi_c^0 \to \Omega^- K^+$ data; the curves correspond to the possible distributions for $J_{\Xi_c} = 3/2$ and $J_\Omega = 5/2$ ($\beta = 0$). The solid curve corresponds to $\rho_{1/2} + \rho_{-1/2} = 0.4$, while the dashed curve corresponds to $\rho_{1/2} + \rho_{-1/2} = 0.5$.

the quartic term is thus cancelled. This fit is represented by the solid curve of Fig. 4.22; it has χ^2/NDF of 7.06/8 and a probability of 0.53. If it is assumed that the density matrix elements of the parent baryon are equally polulated, $x = 0.5$, and the fit (represented by the dashed curve in Fig. 4.22) has χ^2/NDF of 9.02/9 and a probability of 0.44. From this result, we conclude that although for $J_{\Xi_c} = 3/2$, the hypothesis $J_\Omega = 1/2$ is ruled out, and $J_\Omega = 3/2$ may reasonably be considered disfavored on the basis of the polarization study described in Appendix A, section A.3, the hypothesis $J_\Omega = 5/2$ is entirely acceptable.

4.7 Summary

In summary, the angular distribution of the decay products of Ω^- baryon, resulting from the Ξ_c^0 and Ω_c^0 decays is consistent with being of the form $\alpha(1+3\cos^2\theta_h)$.

This observation is consistent with spin assignments 1/2 for the Ξ_c^0 and the Ω_c^0 and 3/2 for the Ω^-. Spin values of 1/2 and 5/2 (obtained from Ξ_c^0 decays) for the spin of the Ω^- are excluded at the 99% confidence level.

If the spin of the Ξ_c^0 is 3/2, spin 1/2 for the Ω^- is excluded and spin 3/2 is disfavored on the basis of a polarization study. However, spin 5/2 yields perfectly acceptable fits to the observed angular distribution.

There are ongoing *BABAR* analyses which in principle provide direct information on charm baryon spin (e.g. $B \to \Lambda_c^+ \bar{p}$), but statistical limitations may prevent a definitive result in the near future.

CHAPTER 5
STUDY OF THE $\Xi(1690)^0$ RESONANCE PRODUCED IN $\Lambda_c^+ \to \Lambda \bar{K}^0 K^+$ DECAY

5.1 Extending the Ω^- Spin Formalism to Quasi-two-body Λ_c^+ Decay

In the present chapter, and in chapter 6, the two-body-decay formalism developed in chapter 4 in order to establish the spin of the Ω^- is extended to the study of charm baryon quasi-two-body decay modes of the type $\Lambda_c^+ \to K^+ \Xi^{*0}$, where Ξ^{*0} denotes a resonant Cascade state which decays strongly (i.e. has significant decay width) to a hyperon-pseudoscalar meson final state. As in chapter 4, it is assumed that the parent charm baryon, in this case the Λ_c^+, has spin 1/2. Parity is conserved in such Ξ^* decays so that, in the notation of chapter 4,

$$\left|A^J_{1/2}\right| = \left|A^J_{-1/2}\right|,$$

where J denotes the Ξ^* spin. As a consequence, the asymmetric terms in Eqs. 4.3-4.5 vanish (i.e. $\beta = 0$), and the expected angular distributions for Ξ^* spin 1/2, 3/2 and 5/2 are much simplified.

However, as is well known, there is no free lunch, and the analyses of interest are found to be rendered rather complex as a result of strong interaction effects in the three-body final states studied.

In chapter 6, the analysis is focused on the decay sequence $\Lambda_c^+ \to K^+ \Xi(1530)^0$, $\Xi(1530)^0 \to \Xi^- \pi^+$, however strong interaction $\Xi^- \pi^+$ amplitudes other than that responsible for the $\Xi(1530)$ are found to be present. These result in interference

effects which greatly complicate the understanding of the $\Xi(1530)$ although it turns out that they do exhibit behavior which is interesting in its own right.

The goals of the analysis described in the present chapter are to obtain precise values for the mass and width parameters of the $\Xi(1690)^0$, and to determine its spin via the decay sequence $\Lambda_c^+ \to K^+\Xi(1690)^0$, $\Xi(1690)^0 \to \Lambda\bar{K}^0$. In this case complications arise because the three-body final state $K^+\bar{K}^0\Lambda$ exhibits clear evidence for the presence of a sizeable contribution resulting from the process $\Lambda_c^+ \to a_0(980)^+\Lambda$ with $a_0(980)^+ \to K^+\bar{K}^0$. The amplitudes describing this decay interfere with those describing decay via $\Xi(1690)^0$, such that extraction of the properties of the latter requires an isobar model description of the entire Dalitz plot corresponding to the $\Lambda\bar{K}^0K^+$ final state.

5.2 Present Status of the $\Xi(1690)$

The $\Xi(1690)$ has been observed in its $\Lambda\bar{K}$, $\Sigma\bar{K}$ and $\Xi\pi$ decay modes with various degrees of certainty. However, its quantum numbers have not yet been measured. The first evidence for the $\Xi(1690)$ came from the observation of a threshold enhancement in the $\Sigma^{+,0}K^-$ mass spectrum produced in the reaction $K^-p \to (\Sigma^{+,0}K^-)K\pi$ at 4.2 GeV/c in a bubble chamber experiment [42]. There were also indications of signals in the $\Lambda\bar{K}^0$ and ΛK^- channels. Subsequently, the $\Xi(1690)^-$ was observed in a hyperon beam experiment at CERN, in which an enhancement around 1700 MeV/c^2 was seen in ΛK^- pairs diffractively produced by a 116 GeV/c Ξ^- beam [43, 44]. The $\Xi^-\pi^+$ decay mode of the $\Xi(1690)^0$ was first reported by the WA89 Collaboration on

the basis of a clear peak in the $\Xi^-\pi^+$ mass spectrum resulting from the interactions of a 345 GeV/c Σ^- beam in copper and carbon targets [45]. Evidence of $\Xi(1690)^0$ production in Λ_c^+ decay was reported by the Belle experiment, on the basis of 246 ± 20 $\Lambda_c^+ \to (\Sigma^+ K^-)K^+$ and 363 ± 26 $\Lambda_c^+ \to (\Lambda \bar{K}^0)K^+$ events [46].

5.3 Two-body Invariant Mass Projections

The present analysis concerns the Dalitz plot corresponding to $\Lambda_c^+ \to \Lambda \bar{K}^0 K^+$ decays with the aim of obtaining mass, width and spin information on the $\Xi(1690)^0$ via its $\Lambda \bar{K}^0$ decay mode. The sample of Λ_c^+ candidate events is selected as described previously in section 3.3, and results from a *BABAR* integrated luminosity of ~ 200 fb^{-1}.

Figures 5.1- 5.3 show the invariant mass projections in data. In (a) the black histogram represents the uncorrected (i.e. without efficiency-correction) invariant mass projection corresponding to the Λ_c^+ signal region, while the solid red and blue dots represent the uncorrected mass projections corresponding to the Λ_c^+ high- and low-mass sideband regions, respectively; (b) shows the uncorrected Λ_c^+ mass-sideband-subtracted invariant mass projection; and (c) shows the efficiency-corrected[1] Λ_c^+ mass-sideband-subtracted invariant mass spectrum. In each of Figs. 5.2 and 5.3, the threshold mass value has been subtracted from the invariant mass in order to show clearly the behavior near threshold.

The efficiency-corrected Λ_c^+ mass-sideband-subtracted $m(\Lambda K_S)$ distribution

[1]Each selected event is weighted by the inverse value of the relevant efficiency, which is parametrized as described in Appendix B.

(Fig. 5.1(c)) exhibits a clear peak which is consistent with the $\Xi(1690)^0$. The skewing of the peak toward high mass proves to be an important feature of the observed $\Xi(1690)^0$ lineshape. The Λ_c^+ mass-sideband-subtracted $m(K_S K^+)$ distribution (Fig. 5.2(c)) shows the accumulation of events near $K_S K^+$ threshold observed in the Dalitz plot of Fig. 5.6, discussed later in this section. The distribution turns over near threshold, but does not drop to zero as would be expected because of phase-space suppression. This indicates the presence of significant dynamical effects in the $\bar{K}^0 K^+$ system in this region, which, as described below in the analysis of the Dalitz plot, results from proximity to the $a_0(980)^+$ resonance mass position, and the existence of a significant $\Lambda_c^+ \to \Lambda a_0(980)^+$ decay mode.

There is no evidence for structure in the corrected ΛK^+ mass distribution of Fig. 5.3(c).

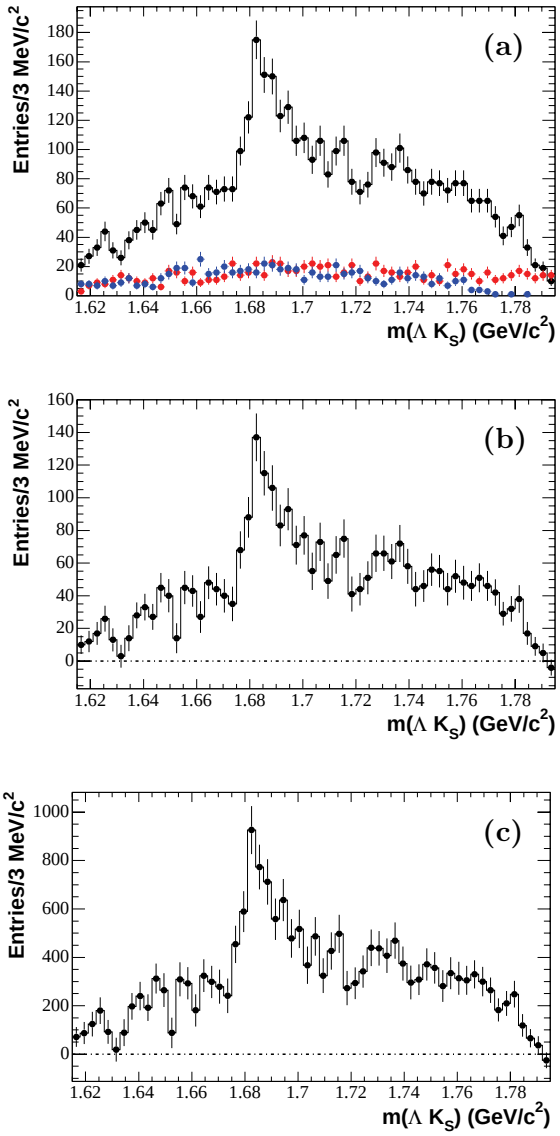

Figure 5.1: The ΛK_S invariant mass projection in data. In (a) the black histogram represents the uncorrected (i.e. without efficiency-correction) ΛK_S invariant mass projection corresponding to the Λ_c^+ signal region, and the solid red and blue dots represent the uncorrected ΛK_S mass spectrum corresponding to the Λ_c^+ high- and low-mass sideband regions, respectively; (b) shows the uncorrected Λ_c^+ mass-sideband-subtracted ΛK_S invariant mass projection, and (c) shows the efficiency-corrected Λ_c^+ mass-sideband-subtracted ΛK_S invariant mass projection.

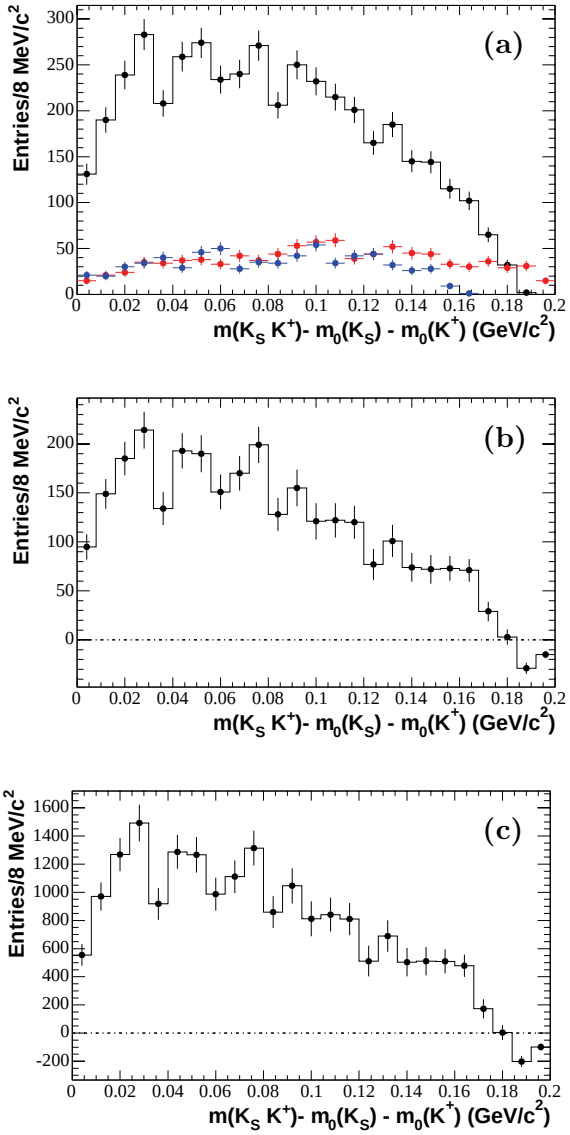

Figure 5.2: The K_SK^+ invariant mass projection in data. In (a) the black histogram represents the uncorrected K_SK^+ invariant mass projection corresponding to the Λ_c^+ signal region, and the solid red and blue dots represent the uncorrected K_SK^+ mass spectrum corresponding to the Λ_c^+ high- and low-mass sideband regions, respectively; (b) shows the uncorrected Λ_c^+ mass-sideband-subtracted K_SK^+ invariant mass projection, and (c) shows the efficiency-corrected Λ_c^+ mass-sideband-subtracted K_SK^+ invariant mass projection. In each figure, the K_SK^+ threshold mass value has been subtracted from the invariant mass in order to show clearly the behavior close to the $a_0(980)^+$ mass position.

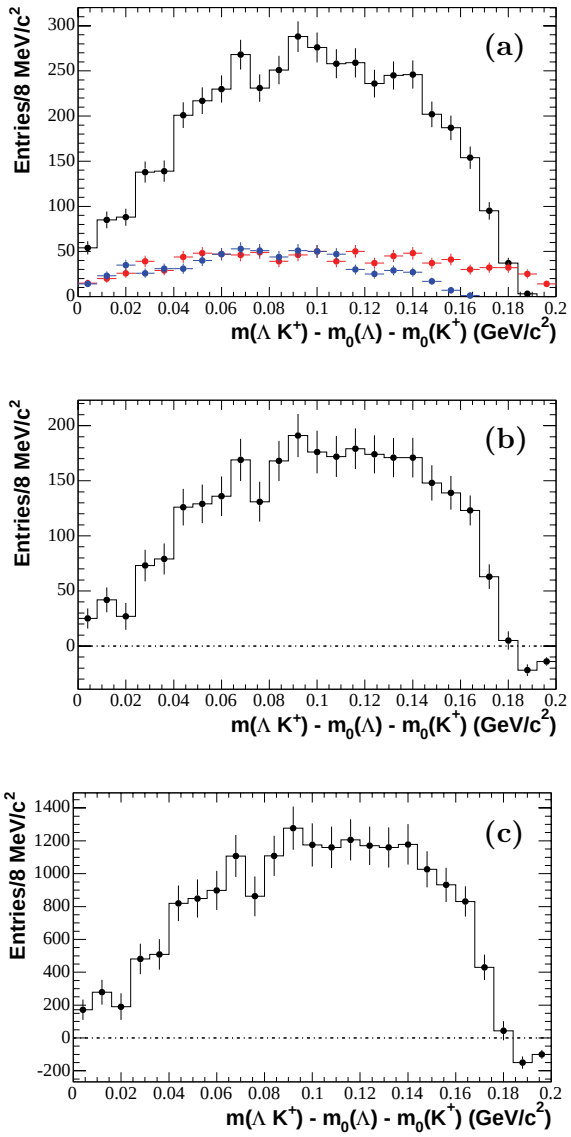

Figure 5.3: The ΛK^+ invariant mass projection in data. In (a) the black histogram represents the uncorrected ΛK^+ invariant mass projection corresponding to the Λ_c^+ signal region, and the solid red and blue dots represent the uncorrected ΛK^+ mass spectrum corresponding to the Λ_c^+ high- and low-mass sideband regions, respectively; (b) shows the uncorrected Λ_c^+ mass-sideband-subtracted ΛK^+ invariant mass projection, and (c) shows the efficiency-corrected Λ_c^+ mass-sideband-subtracted ΛK^+ invariant mass projection. In each figure, the ΛK^+ threshold mass value has been subtracted from the invariant mass in order to show clearly the behavior near threshold.

5.4 Legendre Polynomial Moments for the $\Lambda\bar{K}^0$ System

The procedures demonstrated in section 4.5 can be applied in the context of quasi-two-body decays to investigate hyperon resonance spin by obtaining the mass-dependent Legendre polynomial moment projections for the relevant mass spectrum. In order to test the hypothesis $J_{\Xi(1690)} = 3/2$, the weighted efficiency-corrected $m(\Lambda K_S)$ distribution is obtained for events in the Λ_c^+ signal region by assigning to each event i, a weight $w_i = \sqrt{10}P_2(\cos\theta_{\Lambda_i})$, where θ_Λ is defined for $\Xi(1690)$ decay just as illustrated in Fig. 4.1 for Ω^- decay. If the spin of the $\Xi(1690)$ were 3/2, as for the Ω^-, the effect would be to project away the background such that the number of weighted events would be consistent with the total number of signal events seen in Fig. 5.1 (c). Fig. 5.4 (a) shows the efficiency-corrected $\sqrt{10}P_2(\cos\theta_\Lambda)$ moment distribution as a function of $m(\Lambda K_S)$; clearly there is no evidence for such a signal in the $\Xi(1690)^0$ mass region. Similar conclusions are drawn from the distribution of the $7/\sqrt{2}P_4(\cos\theta(\Lambda))$ moment shown in Fig. 5.4 (b), and for those obtained for higher even-order Legendre polynomial moments (not shown).

This suggests that the spin of the $\Xi(1690)$ is 1/2, and leads to the expectation that the $\cos\theta_\Lambda$ distribution in data corresponding to the $\Xi(1690)^0$ signal region ($1.665 < m(\Lambda K_S) < 1.705$ GeV/c^2) should be flat. However, as shown in Fig. 5.5, this distribution is not at all flat, but exhibits an almost linear tripling of intensity as $\cos\theta_\Lambda$ increases from -1 to $+1$. In order to investigate this effect, the Dalitz plot for the decay $\Lambda_c^+ \to \Lambda\bar{K}^0K^+$ is next studied in detail.

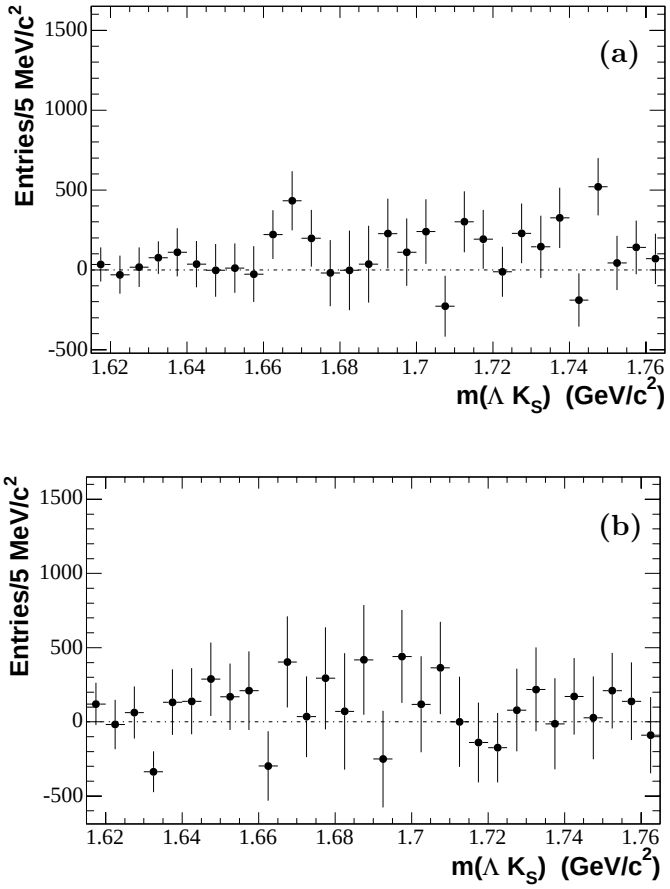

Figure 5.4: The efficiency-corrected moments as a function of $m(\Lambda K_S)$ corresponding to the Λ_c^+ signal region: (a) $\sqrt{10}P_2(\cos\theta_\Lambda)$ and (b) $7/\sqrt{2}P_4(\cos\theta_\Lambda)$.

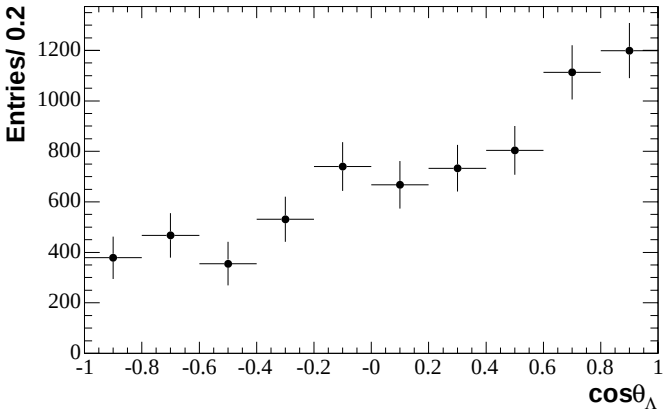

Figure 5.5: The efficiency-corrected, background-subtracted cosθ_Λ distribution in data for the Λ_c^+ signal region for 1.665< $m(\Lambda K_S)$ <1.705 GeV/c^2.

5.5 The Dalitz plot for $\Lambda_c^+ \to \Lambda \bar{K}^0 K^+$

Evidence for $a_0(980)^+$ Production

The Dalitz plot for $\Lambda_c^+ \to \Lambda \bar{K}^0 K^+$ signal candidates is shown, without efficiency-correction, in Fig. 5.6(a). A clear band is observed in the mass-squared region of the $\Xi(1690)^0$, together with an accumulation of events near $\bar{K}^0 K^+$ threshold at the upper boundary of the Dalitz plot; since the $a_0(980)^+$ is the only known $I = 1$ meson state in the accessible $\bar{K}^0 K^+$ mass range ($m(\bar{K}^0 K^+) < 1.17$ GeV/c^2), this is indicative of the occurrence of the weak decay $\Lambda_c^+ \to \Lambda a_0(980)^+$ where the $a_0(980)^+$ decays strongly into $\bar{K}^0 K^+$.

In contrast, the Dalitz plots corresponding to the Λ_c^+ mass-sideband regions (Fig. 5.6(b) and (c)) exhibit no structure.

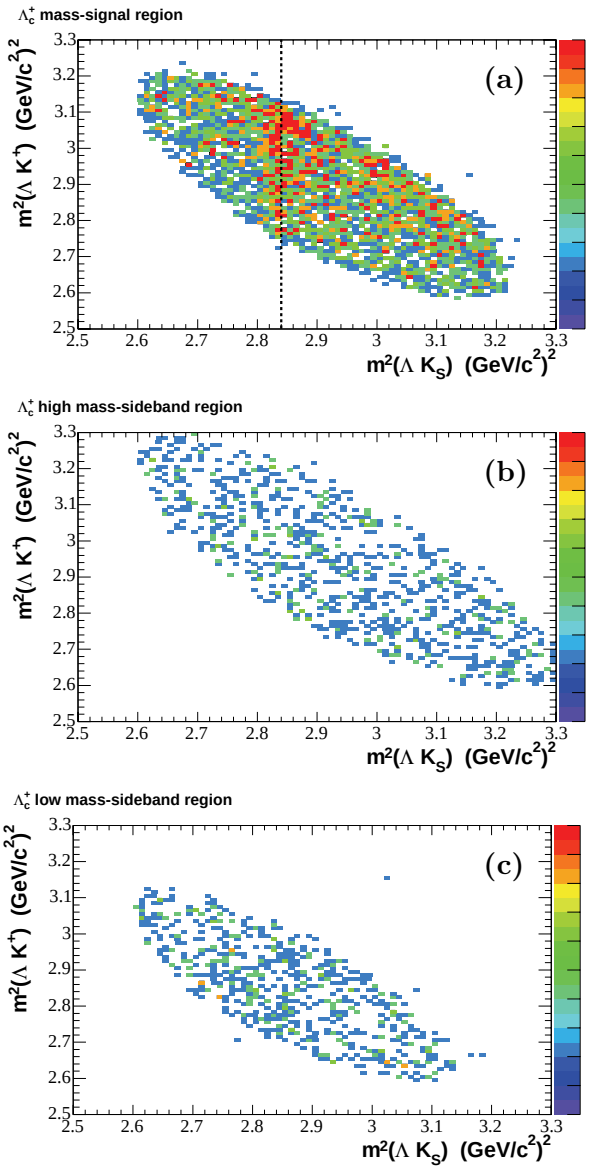

Figure 5.6: The Dalitz plots for $\Lambda_c^+ \to \Lambda \bar{K}^0 K^+$ candidates. The distribution in (a) is for the Λ_c^+ signal region, and those in (b) and (c) are for the Λ_c^+ high- and low-mass sideband regions indicated in Fig. 3.7.

5.6 Mass and Width Measurement of the $\Xi(1690)^0$ Assuming $J = 1/2$

The properties of the $\Xi(1690)^0$ are extracted from a two-dimensional fit to the rectangular Dalitz plot of $\cos\theta_\Lambda$ versus $m(\Lambda K_S)$ corresponding the Λ_c^+ signal region (Fig. 5.7).

The kinematics and phase-space properties of this type of plot are discussed at the beginning of Appendix B, and the simple procedure followed in order to represent the reconstruction efficiency at any point in the rectangular Dalitz plot is explained in detail also in this Appendix. This simple approach to efficiency parametrization readily lends itself to descriptions of the rectangular plots corresponding to the Λ_c^+ sideband regions, and thus by interpolation to a two-dimensional representation of the incoherent background contribution to the Λ_c^+ signal region of Fig. 5.7.

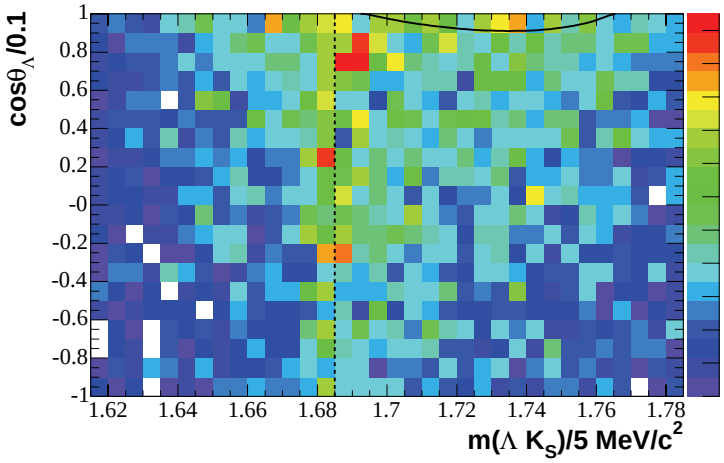

Figure 5.7: The rectangular Dalitz plot of $\cos\theta_\Lambda$ versus $m(\Lambda K_S)$ corresponding the Λ_c^+ signal region. The dashed line indicates the approximate $\Xi(1690)^0$ mass; the solid curve indicates the locus corresponding to the $a_0(980)$ central mass value of 999 MeV/c^2.

In the fit procedure described in the following sections, it is assumed first that the $\Xi(1690)$ has spin 1/2 [2], since this choice seems favored by the moments analysis of section 5.2.

The ingredients necessary in order to fit the data distribution of Fig. 5.7 are:

- an efficiency parametrization as a function of $m(\Lambda K_S)$ and $\cos\theta_\Lambda$
- after efficiency-correction, a description as a function of $m(\Lambda K_S)$ and $\cos\theta_\Lambda$ of the incoherent background present in the Λ_c^+ mass-signal region.
- a description of the dependence of the (ΛK_S) mass resolution on $m(\Lambda K_S)$.

These topics are discussed separately in sections 5.6.1-3 prior to a description of the actual fit procedure.

5.6.1 Efficiency Parametrization as a Function of $m(\Lambda K_S)$ and $\cos\theta_\Lambda$

The reconstruction and selection efficiency is determined from a simulated sample of $\Lambda_c^+ \to \Lambda\bar{K}^0K^+$ Monte Carlo (MC) events uniformly distributed on the Dalitz plot (i.e. a phase-space distribution). The procedure followed is described in detail in Appendix B. For a given mass interval in $m(\Lambda K_S)$, the angular dependence of the efficiency is described by an expansion in terms of Legendre polynomials, with $L = 6$, as follows:

$$E(\cos\theta_\Lambda, \mathrm{m}(\Lambda\mathrm{K_S})) = \mathrm{E_0(m)} + \mathrm{E_1(m)P_1}(\cos\theta_\Lambda) + ... + \mathrm{E_L(m)P_L}(\cos\theta_\Lambda). \qquad (5.1)$$

[2] The spin 3/2 and 5/2 hypotheses will be considered later.

The (ΛK_S) mass dependence of the coefficients $E_0, ...E_L$ is obtained by interpolation, so that the efficiency can be evaluated at any point in Fig. 5.7. Each selected event can then be weighted inversely according to its efficiency obtained from this parametrization, and in this way efficiency-corrected distributions are obtained.

The average efficiency is found to vary from $\sim$ 14% at ΛK_S threshold to $\sim$ 15.5% at the maximum accessible mass value, and the dependence on cosθ_Λ is very weak (see Appendix B), so that the net effect of efficiency-correction on the Dalitz plot analysis is quite small.

5.6.2 Background Parametrization as a Function of $m(\Lambda K_S)$ and cosθ_Λ

In order to fit the Dalitz plot of Fig. 5.7, the ΛK_S mass is restricted to the range $1.615 \leq m(\Lambda K_S) \leq 1.765$ GeV/c^2. This is done in order to accommodate the mass-smearing procedure described in the next section as it affects the fit to the data. The loss of integrated function contribution from the fit region $1.615 \leq m(\Lambda K_S) \leq 1.765$ GeV/c^2 due to smearing can then be compensated properly by the smeared contributions from the regions below 1.615 GeV/c^{2}and above 1.765 GeV/c^2.

This restriction of ΛK_S mass range has a small effect on the estimated background contribution in the Λ_c^+ signal region. This can be seen by comparing the Λ_c^+ candidate mass distribution before (Fig. 3.7) and after (Fig. 5.8) the restriction. The effect is to slightly reduce the slope of the background and the estimate of the number of background events in the signal region indicated in Fig. 5.8. The curve

in Fig. 5.8 results from a binned χ^2 fit using a double Gaussian signal function and linear background function. A similar fit to the distribution of Fig. 5.8, after the efficiency-correction procedure of section 5.6.1 has been applied, yields corrected estimates of 18810 ± 764 signal events and 9392 ± 237 background events in the signal region denoted by the solid vertical lines. The efficiency-corrected rectangular Dalitz plot for the background in the signal region which results from the high- and low-mass sideband regions (indicated by the dashed vertical lines in Fig. 5.8) is therefore normalized to 9392 events and then allowed to vary by ± 237 events in order to obtain estimates of systematic uncertainty in the mass and width parameter values of the $\Xi(1690)$ associated with the treatment of background.

The method chosen to parametrize the sideband rectangular Dalitz plots is very similar to that used to parametrize the efficiency.

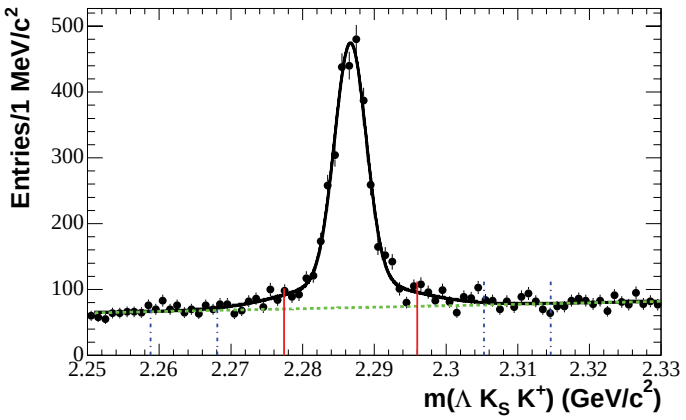

Figure 5.8: The invariant mass distribution of uncorrected $\Lambda K_S K^+$ candidates corresponding to the restriction $1.615 \leq m(\Lambda K_S) \leq 1.765$ GeV/c^2. The superimposed curve is explained in the text.

In a given $m(\Lambda\bar{K}^0)$ interval, the distribution of events in $\cos\theta_\Lambda$ may be described by the expression:

$$\frac{dN}{d\cos\theta_\Lambda} = N\left(< P_0 > P_0(\cos\theta_\Lambda) + < \mathrm{P_1} > \mathrm{P_1}(\cos\theta_\Lambda) + ... + < \mathrm{P_L} > \mathrm{P_L}(\cos\theta_\Lambda)\right), \quad (5.2)$$

where $\int_{-1}^{1} P_i(\cos\theta_\Lambda)\mathrm{P}_j(\cos\theta_\Lambda)\mathrm{d}\cos\theta_\Lambda = \delta_{ij}$ as previously, and N is the efficiency-corrected total number of events. The orthogonality of Legendre polynomials then yields

$$N < P_j >= \int_{-1}^{1} P_j(\cos\theta_\Lambda)\frac{\mathrm{dN}}{\mathrm{d}\cos\theta_\Lambda}\mathrm{d}\cos\theta_\Lambda. \quad (5.3)$$

The integral is approximated by

$$\sum_{i=1}^{N_{obs}} P_j(\cos\theta_{\Lambda_i})w_i,$$

where w_i is the weight due to efficiency-correction, and the index i runs over the observed events in this mass interval I, so that

$$N < P_j > \sim \sum_{i=1}^{N_{obs}} P_j(\cos\theta_{\Lambda_i})w_i. \quad (5.4)$$

The range of $m(\Lambda\bar{K}^0)$ from near threshold (1.615 GeV/c^2) to the upper limit (1.765 GeV/c^2) is divided into four equal intervals, for both the low- and high-mass Λ_c^+ sidebands; for each interval, the efficiency-corrected number of events, N, is obtained, and the coefficients $C_j = N < P_j > (j > 0)$ are calculated; it is found that $L = 4$ provides an adequate description of the data. The efficiency-corrected distributions and curves obtained using expression 5.2 are shown in Fig. 5.9 and Fig. 5.10 for the low- and high-mass sideband regions, respectively; the corresponding values of N and of the C_j coefficients are shown in Fig. 5.11.

The representation of the background distribution in the signal region is obtained by first of all averaging the low- and high-mass values for N and C_j shown in Fig. 5.11, to yield the average values, $< N >$ and $< C_j >$ plotted in Fig. 5.12. An interpolation procedure is then required to specify the $\cos\theta_\Lambda$ dependence at a particular ΛK_S mass value. For $< N >$, the data are well-represented by a quadratic function multiplied by a two-body phase space factor, as shown by the blue curve. For the coefficients $< C_j >$, quadratic fit functions are used in the primary analysis, and a linear interpolation procedure is used to study systematic uncertainties associated with this procedure. In each case, the integral over the rectangular Dalitz plot for $1.615 \leq m(\Lambda K_S) \leq 1.765$ GeV/c^2 of the resulting distribution is normalized to the estimated number of efficiency-corrected background events in the signal region, as indicated at the beginning of this section.

The outcome of this procedure is illustrated in Fig. 5.13. The black dots represent the averaged low- and high-mass sideband projections of the rectangular Dalitz plots, while the open blue (red) dots result from the quadratic (linear) interpolation procedure. Both procedures give almost indistiguishable results, and provide excellent representations of the averaged sideband behavior. There is no significant structure in either projection, and for $\cos\theta_\Lambda$, the observed oscillation above a flat distribution has a maximum amplitude of only $\sim 5\%$. Consequently, the corrections for this background behavior should have little impact on the outcome of the Dalitz plot analysis.

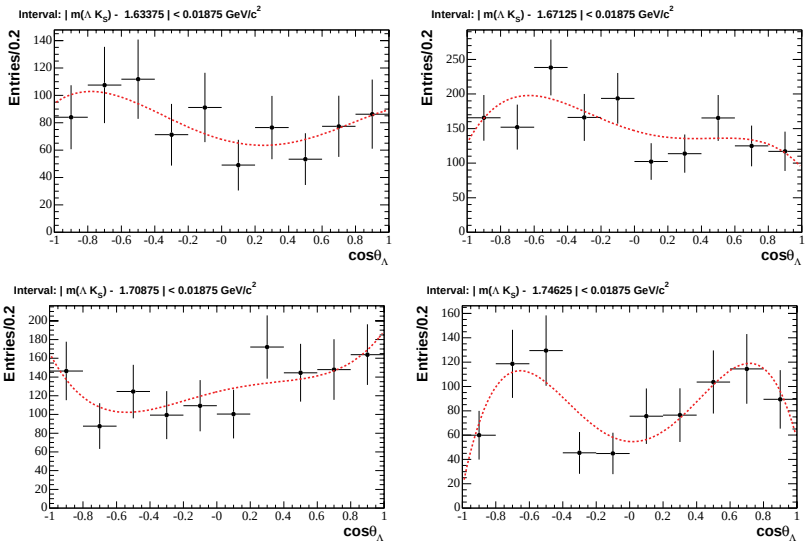

Figure 5.9: The efficiency-corrected $\cos\theta_\Lambda$ distributions corresponding to the four 37.5 MeV/c^2 intervals from $m(\Lambda K_S) = 1.615$ GeV/c^2 to $m(\Lambda K_S) = 1.765$ GeV/c^2 for the Λ_c^+ low-mass sideband region. Superimposed are curves representing the function $dN/d\cos\theta_\Lambda = \mathrm{N}\left(\frac{1}{2} + ...+ < \mathrm{P}_4(\mathrm{m}) > \mathrm{P}_4(\cos\theta_\Lambda)\right)$.

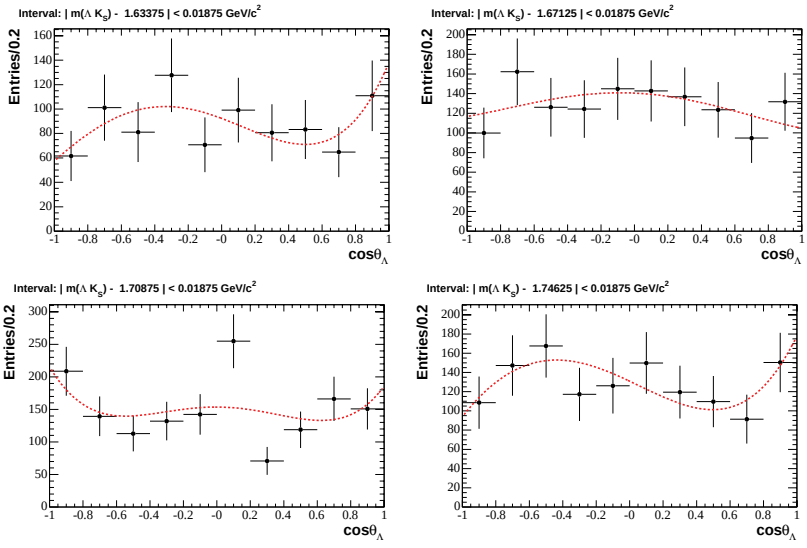

Figure 5.10: The efficiency-corrected $\cos\theta_\Lambda$ distributions corresponding to the four 37.5 MeV/c^2 intervals from $m(\Lambda K_S) = 1.615$ GeV/c^2 to $m(\Lambda K_S) = 1.765$ GeV/c^2 for the Λ_c^+ high-mass sideband region. Superimposed are curves representing the function $dN/d\cos\theta_\Lambda = \mathrm{N}\left(\frac{1}{2} + ...+ < \mathrm{P}_4(\mathrm{m}) > \mathrm{P}_4(\cos\theta_\Lambda)\right)$.

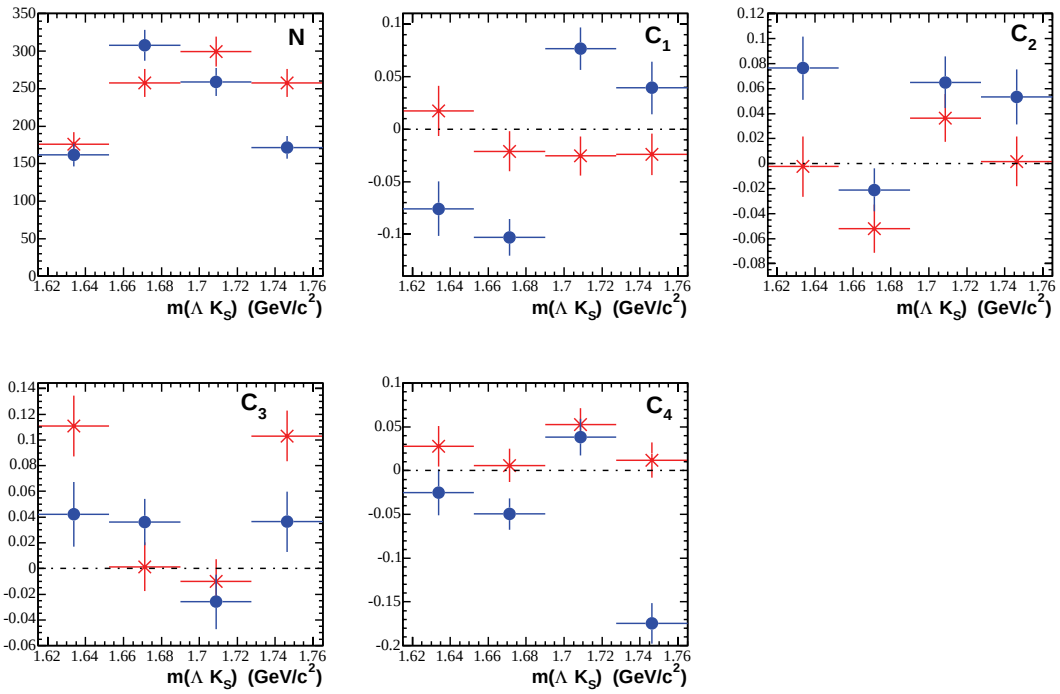

Figure 5.11: The values of N and C_j obtained from expression 5.4. The blue solid points correspond to the Λ_c^+ low-mass sideband region, the red crosses to the Λ_c^+ high-mass sideband region.

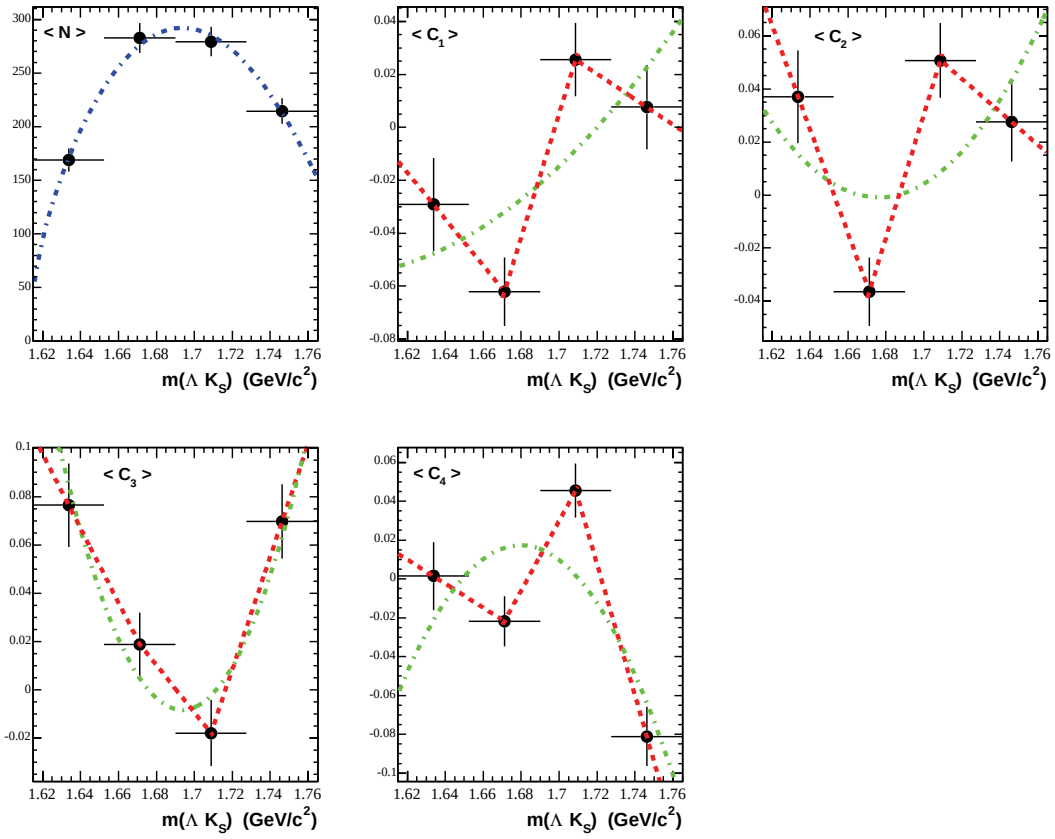

Figure 5.12: The average values of N and of the coefficients C_j obtained for the low- and high-mass sideband regions. For $< N >$, the curve is a fit with a second order polynomial multiplied by a two-body phase-space factor. For the coefficients $< C_j >$, the green curves represent fits to quadratic functions, and the red lines correspond to a simple linear interpolation between points.

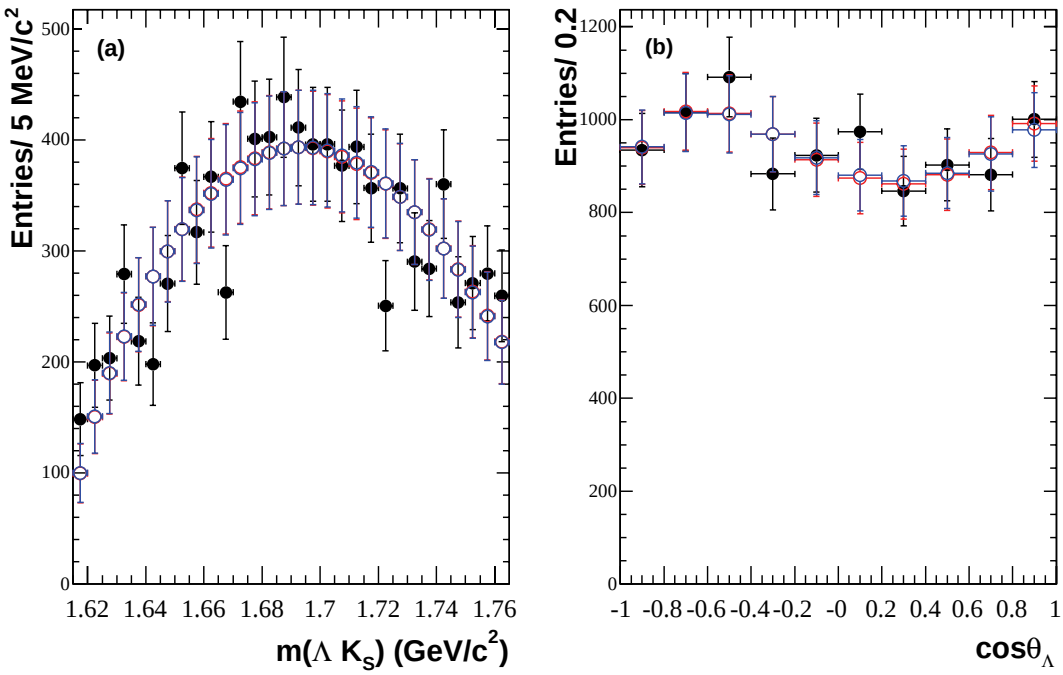

Figure 5.13: The averaged low- and high-mass sideband projections of the corresponding rectangular Dalitz plots (black dots) compared to the results of the quadratic (open blue dots) and linear (open red dots) interpolation procedures described in the text.

5.6.3 (ΛK_S) Mass Resolution Function Parametrization

For a narrow resonance such as the $\Xi(1690)$, the measurement of its mass and width may be sensitive to detector resolution effects; in particular the apparent width will tend to be larger than its true value. In addition, because of the fact that resolution tends to increase with Q-value [3], it is necessary to study the mass-dependence of the resolution function as a function of $m(\Lambda K_S)$. A parametrization of the resolution lineshape is obtained, and it will then be incorporated into the fit procedure used to measure the mass and width of the $\Xi(1690)$, in order to extract more precise values for these parameters.

The behavior of ΛK_S mass resolution is investigated using reconstructed truth-associated MC signal events. These events are divided into seven sub-samples corresponding to 20 MeV/c^2 intervals of reconstructed ΛK_S mass in the range $1.615-1.755$ GeV/c^2, and the distribution of (generated-reconstructed) mass is obtained for each sub-sample. Each distribution is well-described by a function composed of a core Gaussian and a wide Gaussian, both centered at zero mass difference. The results of fits using this functional form are summarized in Fig. 5.14. The mass dependence of the sigma of the core (wide) Gaussian in Fig. 5.14 (a) ((b)) shows the expected increase with increasing Q-value. The fractional yield associated with the wide Gaussian (Fig. 5.14 (c)) oscillates about a value of ~ 0.4, and so it was decided to fit for the average value and to fix the fractional yield to the fitted value (0.38 ± 0.03) obtained.

[3] Q-value is the difference between the invariant mass and its value at threshold.

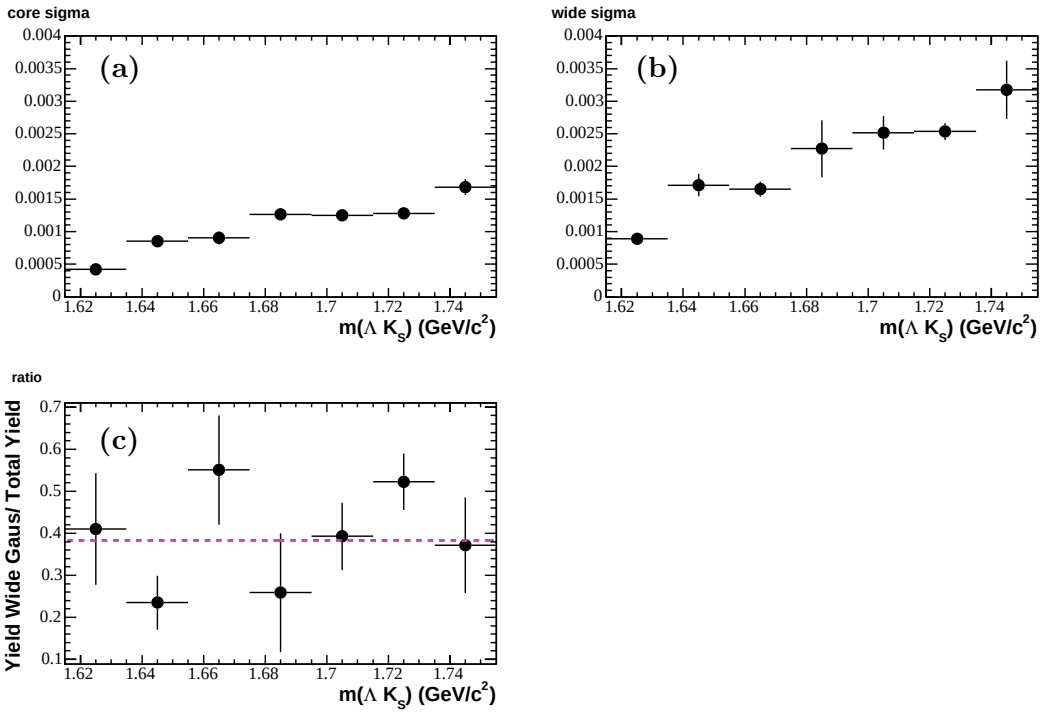

Figure 5.14: The $m(\Lambda K_S)$ dependence of the resolution function parameter values obtained from Signal MC events as described in the text. The fitted average value of the ratio of the yield of the wide Gaussian to the total yield (0.38±0.03) is represented by the dashed line in (c).

The fit procedure was then repeated with the ratio of the yield of the wide Gaussian to the total yield fixed to the value obtained from the fit shown in Fig. 5.14 (c), i.e. 0.38. The value of this ratio is subsequently varied by its uncertainty as part of the study of the systematic uncertainty due to the resolution function lineshape.

The new results are shown in Fig. 5.15 (a) and (b), and correspond to the fixed value of the yield ratio (Fig. 5.15 (c)). In order to interpolate the mass resolution dependence, the measured values of Figs. 5.15 (a), (b) are fit with second order polynomials, with the results shown by the curve in each figure. The net behavior

of the mass resolution is represented by calculating the half-width-at-half-maximum (HWHM) of the net fit function, and this behaves as shown in Fig. 5.15 (d).

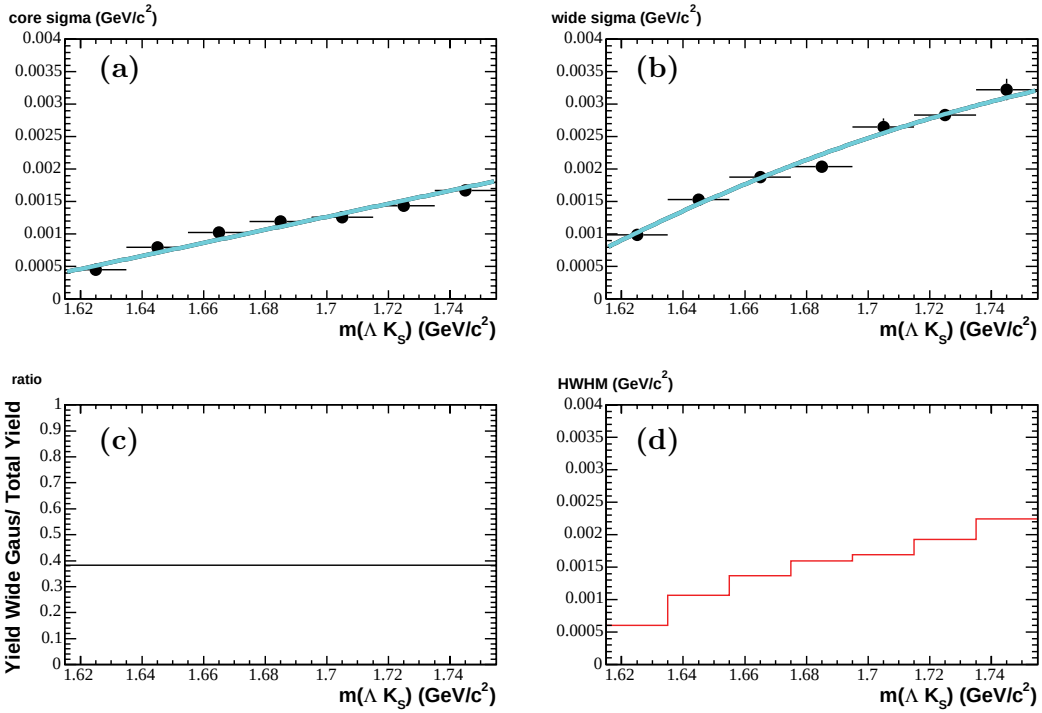

Figure 5.15: The resolution function parameters obtained using reconstructed Signal MC events as described in the text. The distributions of the narrow and wide sigmas are fitted to the second order polynomials represented by the curves in (a) and (b). The net HWHM behavior is shown in (d). A yield ratio of 0.38 is obtained, as shown in (c).

The following (ΛK_S)-mass-dependent parametrization of the resolution function is obtained in this way:

$$R = (1 - r)G(\sigma_1(m)) + rG(\sigma_2(m))$$

with $r = 0.38$; G is a Gaussian function centered at zero and

$$\sigma_1(m) \quad = -0.1042 + 0.1155\,m - 0.0315\,m^2$$

$$\sigma_2(m) \quad = -0.1647 + 0.1805\,m - 0.0483\,m^2,$$

where σ_1 and σ_2 represent the respective narrow and wide Gaussian r.m.s. deviation values, and $m = m(\Lambda K_S)$. At $m(\Lambda K_S) \sim 1.69$ GeV/c^2, the net resolution function has HWHM ~ 1.5 MeV/c^2.

A similar resolution function for cosθ_Λ has been calculated using reconstructed Signal MC events by taking the difference between the generated and reconstructed values of cosθ_Λ for truth-associated events. The distribution, shown in Fig. 5.16, is well represented by a triple Gaussian function. The HWHM for this fit function is 0.015, which is well below the interval size (0.2) in cosθ_Λ used in the fits to the rectangular Dalitz plot to extract the mass and width values of the $\Xi(1690)^0$. For this reason no cosθ_Λ smearing is incorporated in the fit procedure.

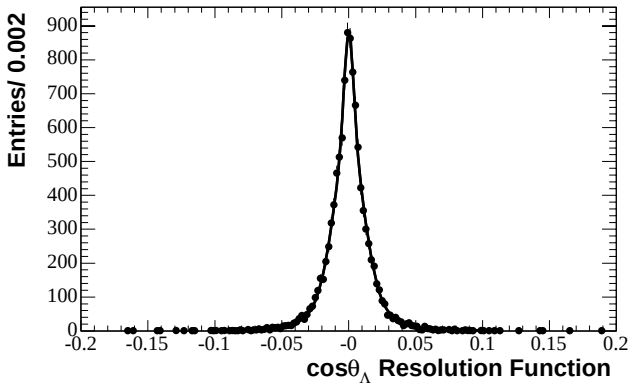

Figure 5.16: The cosθ_Λ resolution function obtained using reconstructed Signal MC events as described in the text. The superimposed lineshape consists of a triple Gaussian function with a common mean. This fit has a χ^2/NDF of 80.2/84 and a probability of 0.60, and the net fit function has a HWHM of 0.015.

5.6.4 Isobar Model Description of the $\Lambda_c^+ \to \Lambda \bar{K}^0 K^+$ Dalitz Plot

It is shown in the remainder of section 5.6 that a model incorporating the isobars characterizing $\Lambda a_0(980)^+$ and $\Xi(1690)^0 K^+$ decay of the Λ_c^+ gives an excellent description of the $\Lambda_c^+ \to \Lambda \bar{K}^0 K^+$ Dalitz plot. No additional isobars are needed in order to accurately model the data. As such, the analysis not only provides precise information on the properties of the $\Xi(1690)$, but also constitutes the first observation of the $\Lambda a_0(980)^+$ decay mode of the Λ_c^+ charm baryon [22].

The amplitude describing the $\Xi(1690)^0$ is chosen to be

$$A(\Xi[1690]) = \frac{1}{(m_0^2 - m^2) - i m_0 \Gamma(m)}, \tag{5.5}$$

where $m_0 = m(\Xi(1690)^0)$ and m is the ΛK_S invariant mass. Assuming that the ΛK_S system is in an S-wave state, and ignoring the contribution of other partial widths to the total width, the latter is described by

$$\Gamma(m) = \Gamma(m_0) \frac{q}{m} \frac{m_0}{q_0}, \tag{5.6}$$

where $\Gamma(m_0)$ is the total width parameter to be extracted from the data. It is assumed that the $\Xi(1690)^0$ is produced in an orbital angular momentum S-wave with respect to the recoil K^+, although P-wave is also allowed, and hence that no additional form factor describing Λ_c^+ decay to $\Xi(1690)^0 K^+$ is required. Effects due to possible P-wave production and/or decay are considered in the context of systematic error contributions (section 5.6.8).

The $a_0(980)$ is known to couple to both $\eta\pi$ and $\bar{K}K$, and is therefore charac-

terized by the following (Flatté) parametrization:

$$A(a_0[980]) = \frac{g_{\bar{K}K}}{m_a^2 - m_{\bar{K}K}^2 - ig_{\bar{K}K}^2\left(\rho_{\bar{K}K} + \frac{1}{r^2}\rho_{\eta\pi}\right)}. \tag{5.7}$$

In this expression, m_a and $m_{\bar{K}K}$ correspond to the mass of the $a_0(980)^+$ and of the $(\bar{K}^0K^+)$ system, respectively; $\rho_j(m) = 2q_j/m$ is the phase space factor for the decay into the two-body channel $j = \eta\pi, \bar{K}K$, and $r = g_{\bar{K}K}/g_{\eta\pi}$. It is assumed that the $a_0(980)^+$ is produced in an S-wave orbital angular momentum state with respect to the recoil Λ, although P-wave is also allowed, and hence that, as for the $\Xi(1690)^0K^+$ amplitude, no additional form factor describing the Λ_c^+ decay to the $\Lambda a_0(980)^+$ final state is required.

The $\Lambda a_0(980)^+$ and $\Xi(1690)^0K^+$ amplitudes describe transitions between the same initial and final state particles, and as such it is expected a priori that they should be added coherently (i.e. with the possibility of interference) in order to provide a description of the observed rectangular Dalitz plot intensity distribution.

In order to demonstrate experimentally the need for such coherence, an initial attempt is made to describe the Dalitz plot intensity using an incoherent superposition of the $\Xi(1690)^0K^+$ and $\Lambda a_0(980)^+$ contributions. The relevant distributions are calculated as described in Appendix C, sections C.1 and C.2, respectively, and, based on the moments analysis of section 5.4, it is hypothesized at present that the $\Xi(1690)$ has spin 1/2.

The Dalitz plot intensity, $I(m, \cos\theta_\Lambda)$, for the incoherent superposition may

then be written

$$I = pq|A|^2 \tag{5.8}$$

with

$$\begin{aligned} |A|^2 &= C\left[|p_0 A(\Xi[1690])|^2 + |A(a_0[980])|^2\right] \\ &= C\left[p_0^2 I_1 + g_{\bar{K}K}^2 I_2\right]; \end{aligned} \tag{5.9}$$

p_0 represents a constant relative strength of the amplitudes, C is a normalization constant, and

$$\begin{aligned} M_2 &= (m_a^2 - m_{\bar{K}K}^2) \\ G2 &= \rho_{\eta\pi} g_{\eta\pi}^2 + \rho_{\bar{K}K} g_{\bar{K}K}^2, \\ M_1 &= (m_0^2 - m^2), \\ G_1 &= m_0 \Gamma(m), \\ I_1 &= \frac{1}{M_1^2 + G_1^2}, \\ I_2 &= \frac{1}{M_2^2 + G_2^2}. \end{aligned} \tag{5.10}$$

The mass of the $(\bar{K}^0 K^+)$ system is a function of the kinematic variables of the rectangular plot (i.e. in the rest-frame of the $(\Lambda\bar{K}^0)$ system), and is given by:

$$m_{\bar{K}K} = \sqrt{m_{\bar{K}}^2 + m_K^2 + 2\left(E_{\bar{K}} E_K - qp'\cos\theta_\Lambda\right)}, \tag{5.11}$$

where q and p' correspond to the 3-momenta, in the $(\Lambda\bar{K}^0)$ rest-frame, of the Λ and K^+, respectively. Written explicitly in terms of m and $\cos\theta_\Lambda$, this becomes:

$$\begin{aligned} m_{\bar{K}K}^2 &= m_{\bar{K}}^2 + m_K^2 + \frac{\left(M_{\Lambda_c}^2 - (m_K^2 + m^2)\right)\left(m^2 + m_K^2 - m_\Lambda^2\right)}{2m^2} \\ &\quad + \cos\theta_\Lambda \left(\frac{2\mathrm{M}_{\Lambda_\mathrm{c}}}{\mathrm{m}}\right) \mathrm{pq}, \end{aligned} \tag{5.12}$$

where

$$p = \frac{\sqrt{\left(M_{\Lambda_c}^2 - (m_K + m)^2\right)\left(M_{\Lambda_c}^2 - (m_K - m)^2\right)}}{2M_{\Lambda_c}}$$

is the momentum of the K^+ in the Λ_c^+ rest-frame, and

$$q = \frac{\sqrt{(m^2 - (m_{\bar{K}} + m_\Lambda)^2)\,(m^2 - (m_{\bar{K}} - m_\Lambda)^2)}}{2m}$$

is the momentum of the Λ in the $\Lambda\bar{K}^0$ rest-frame.

The fit procedure followed is described in detail in sections 5.6.5 and 5.6.6 in conjunction with the Dalitz plot fits using a coherent amplitude superposition. At present, the results of applying that same procedure to the incoherent superposition are simply summarized in Fig. 5.17 and Table 5.1. Clearly, inclusion of the $a_0(980)^+$ contribution greatly improves the description of the $\cos\theta_\Lambda$ distribution, and of the non-resonant contribution to the ΛK_S mass distribution. The corresponding Dalitz plot fit probability is 14% which seems acceptable. However, the resulting $\Xi(1690)$ lineshape deviates systematically from the observed distribution. This is shown explicitly in Fig. 5.18, where the difference between the latter and the red histogram of Fig. 5.17 is plotted.

In the $\Xi(1690)$ region, the phase of the $a_0(980)^+$ amplitude of Eq. 5.7 should be approaching 180°. In the absence of any additional overall phase w.r.t. the $\Xi(1690)^0$ amplitude, interference would then be expected to yield a projected contribution to the ΛK_S mass distribution proportional to the real part of the $\Xi(1690)^0$ BW amplitude multiplied by (-1).

The curve superimposed on the distribution in Fig. 5.18 corresponds to just

such a projection, with $\Xi(1690)^0$ mass and width parameters fixed to the values of Table 5.1. The fact that this curve gives an adequate representation of the data is an indication that an improved description of the Dalitz plot can be obtained by using a coherent superposition of the $\Xi(1690)^0 K^+$ and $\Lambda a_0(980)^+$ amplitudes.

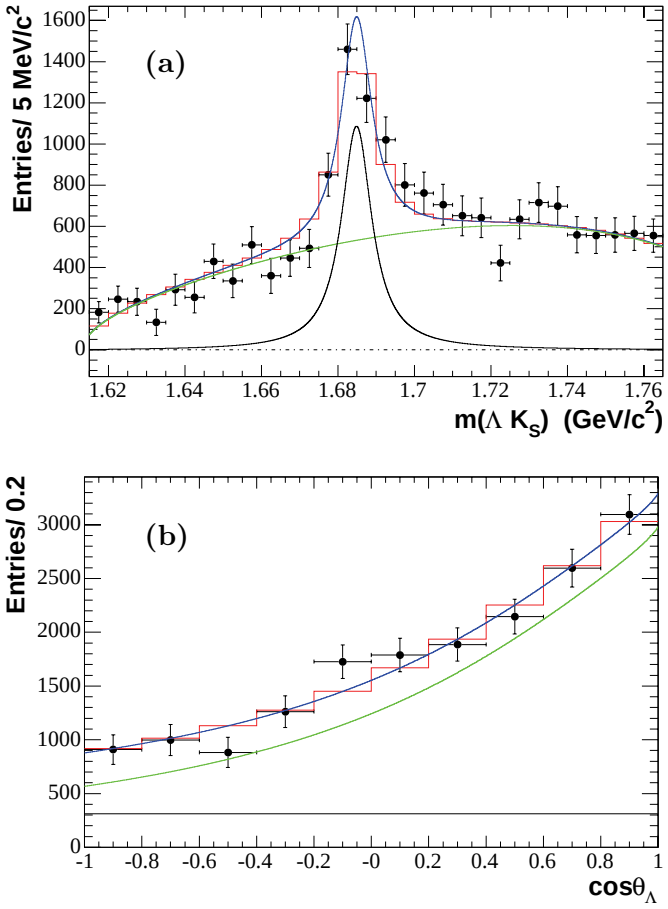

Figure 5.17: The projections of the efficiency-corrected, background-subtracted rectangular plot in data. The red histograms result from the fit function smeared by the mass resolution function. The blue curve corresponds to the fit function with resolution effects unfolded; the green and black curves represent the contributions to the total fit function from the $a_0(980)^+$ and the $\Xi(1690)^0$ amplitude squared, respectively.

Under the assumption of spin 1/2 for the $\Xi(1690)$, the total amplitude-squared characterizing the intensity at a point in the Dalitz plot has no additional angular structure due to $\Xi(1690)$ spin and is therefore a simple coherent superposition of the amplitudes of the $\Xi(1690)$ and $a_0(980)$, as shown in Appendix C, section C.3, i.e. in Eq. 5.8,

$$\begin{aligned} |A|^2 &= C\left(p_0^2 I_1 + g_{\bar{K}K}^2 I_2 \right. \\ &\left. +2p_0 g_{\bar{K}K} I_1 I_2 k\left[(M_1M_2 + G_1G_2)\cos\delta + (\mathrm{G_1M_2} - \mathrm{G_2M_1})\sin\delta\right]\right) \quad . \end{aligned} \tag{5.13}$$

where k is an effective scale factor and δ is an effective phase between the two amplitudes, and the other quantities are defined as in Eq. 5.8.

As discussed in Appendix C, section C.3, Lorentz boost effects between the Λ_c^+ and ΛK_S rest-frames are also taken into account through the use of the effective parameters k and δ. The impact on the interference term of Eq. 5.13 due to the associated Wigner rotations is expected to be small anyway, as discussed in section 5.8.

The ratio of coupling constants measured by the Crystal Barrel (CB) experi-

Table 5.1: The MIGRAD fit parameter values corresponding to Fig. 5.17.

Fit Parameter	Value
$\Xi(1690)$ Amplitude Relative Strength [MeV] (p_0)	26.7 ± 11.4
$\Xi(1690)$ Mass [MeV/c^2]	1685.0 ± 0.7
$\Xi(1690)$ Width [MeV]	9.7 ± 2.1
Overall Normalization Factor	1380.8 ± 1041.6
$g_{\bar{K}K}$ [MeV]	303.2 ± 138.0
Coupling Ratio Squared (r^2)	0.4 ± 0.3

Note: The likelihood value from Eq. 5.14 is 1562.5 for this fit.

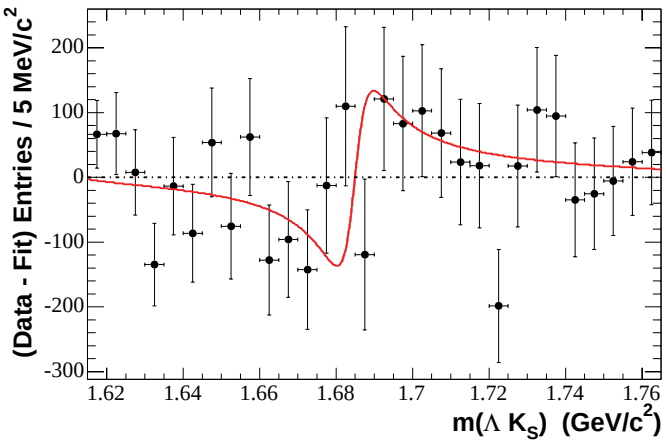

Figure 5.18: The difference between the mass projection of the efficiency-corrected, background-subtracted rectangular plot in data and the fit function smeared by mass resolution (histogram of Fig. 5.17 (a)). The curve superimposed corresponds to the real part of the Breit-Wigner function characterizing the amplitude of the $\Xi(1690)^0$, with the mass and width parameters fixed to the fit result of Table 5.1, but multiplied by (-1) to take account of the phase of the $a_0(980)^+$ (see text).

ment [48] is

$$\frac{g^2_{\bar{K}K}}{g^2_{\eta\pi}} = 1.03 \pm 0.14$$

where, $g_{\eta\pi} = 324 \pm 15$ MeV, and the value of the $a_0(980)$ mass obtained from this experiment is 999 ± 2 MeV/c^2.

In the fit procedure the ratio of coupling constants and the value of the $g_{\bar{K}K}$ coupling strength are free parameters. The mass of the $a_0(980)$ is fixed to the value obtained by the CB experiment, but is then varied by its uncertainty in order to obtain the related systematic error estimates. In addition, as part of the study of systematic uncertainties due to the Flatté parametrization parameter values, the ratio of coupling strengths is fixed to that from the CB experiment, and $g_{\bar{K}K}$ is allowed to be a free parameter in the fit.

5.6.5 (ΛK_S) Mass Resolution Smearing Procedure

As explained previously, it is important to incorporate (ΛK_S) mass resolution effects into the fit procedure, especially with regard to the measurement of the width of the $\Xi(1690)^0$. To this end, the (ΛK_S) invariant mass range is divided into 0.1 MeV/c^2 wide intervals from threshold to 1.78 GeV/c^2, and for each such interval the cosθ_Λ range is further divided into intervals of width 0.01. The fit function intensity value, $f(m(\Lambda K_S), \cos\theta_\Lambda)$, is evaluated in the middle of each of the resulting small boxes. The intensity per box is then smeared over the relevant intervals of (ΛK_S) mass, separately for the narrow and wide Gaussian of the resolution function. The relevant intervals are taken to be those within ± 6 standard deviations of the central box, each Gaussian being considered separately. The contribution to each individual $(m(\Lambda K_S), \cos\theta_\Lambda)$ interval used in the fit procedure (see Fig. 5.19) is then obtained as the difference in the Error Function[4] values at the mass limits of that interval. The smeared contributions are then accumulated for all $(m(\Lambda K_S), \cos\theta_\Lambda)$ intervals of the rectangular Dalitz plot used in the fit procedure.

5.6.6 The Binned Maximum Poisson Likelihood Fit

For the $\Lambda_c^+ \to \Lambda K_S K^+$ signal region, a grid is defined within the rectangular plot of $m(\Lambda K_S)$ versus cosθ_Λ (Fig. 5.19). This starts above threshold and ends below the maximum accessible ΛK_S mass because mass resolution smearing is incorporated

[4]For a Gaussian (with known σ) distributed measurement, the probability that the measured value x will fall within $\pm\delta$ of the true value μ is given by the Error Function, $erf\left(\frac{\delta}{\sqrt{2}\sigma}\right) = \frac{1}{\sqrt{2\pi}\sigma}\int_{\mu-\delta}^{\mu+\delta} e^{-(x-\mu)^2/2\sigma^2} dx$.

in the fit procedure. The range over which smearing is performed is from threshold to 1.780 GeV/c^2, and the grid is chosen interior to this region in order to avoid problems with the lowest and highest mass intervals. As shown in Fig. 5.19, the mass range from 1.615 GeV/c^2 to 1.765 GeV/c^2 is divided into 5 MeV/c^2 intervals, and each interval is further divided into intervals of cosθ_Λ, each of width 0.2. In performing the fits using the smeared fit function, it was decided to exclude the interval 1.615-1.620 GeV/c^2 in order to avoid any problems related to mass resolution.

The number of events indicated within each box of Fig. 5.19 corresponds to the Λ_c^+ signal region; the values range from 0 to 37, and it is this rather low occupancy which has motivated the Poisson probability approach to the fit to the rectangular plot.

Within the i^{th} box of the grid:

[i] N_i^{obs} events are observed, and these are composed of Λ_c^+ signal and background events;

[ii] each event has its own efficiency for the i^{th} box, ϵ, calculated as per section 5.6.1, so that the average efficiency for the i^{th} box, $< \epsilon >_i$, may be obtained as the inverse of the average efficiency weight

$$< \epsilon >_i = \frac{N_i^{obs}}{\sum_{j=1}^{N_i^{obs}} 1/\epsilon_j^i},$$

where ϵ_j^i is the efficiency for the j^{th} event in the i^{th} box; for the box with 0 events, the efficiency value for the center of the box is used;

[iii] the background parametrization (section 5.6.2) yields an estimate of the efficiency-

corrected number of events in the i^{th} box resulting from background, B_i; it follows that the expected number of *observed* background events in the i^{th} box can be estimated as

$$\mu_i^B = < \epsilon >_i B_i;$$

[iv] in a similar way, the signal function can be integrated over the i^{th} box (with or without mass smearing), to yield an efficiency-corrected signal estimate, S_i, and the expected number of *observed* signal events can be obtained similarly as

$$\mu_i^S = < \epsilon >_i S_i;$$

[v] it follows from this that the expected number of *observed* events in the i^{th} box is

$$\mu_i = \mu_i^S + \mu_i^B,$$

and that the Poisson probability for N_i^{obs} events to be observed is

$$p_i = e^{-\mu_i} \frac{(\mu_i)^{N_i^{obs}}}{(N_i^{obs})!}.$$

This treatment of the i^{th} box of Fig. 5.19 is illustrated graphically by Fig. 5.20.

The likelihood function describing the observed distribution of events over the grid is then given by the product of these probabilities for the range of bins of interest, i.e.

$$\mathcal{L} = \Pi_{i=1}^{N^{bins}} e^{-\mu_i} \frac{(\mu_i)^{N_i^{obs}}}{(N_i^{obs})!}.$$

The values of the parameters describing the signal function can then be estimated by maximizing this likelihood function. In practice, since the minimization routine

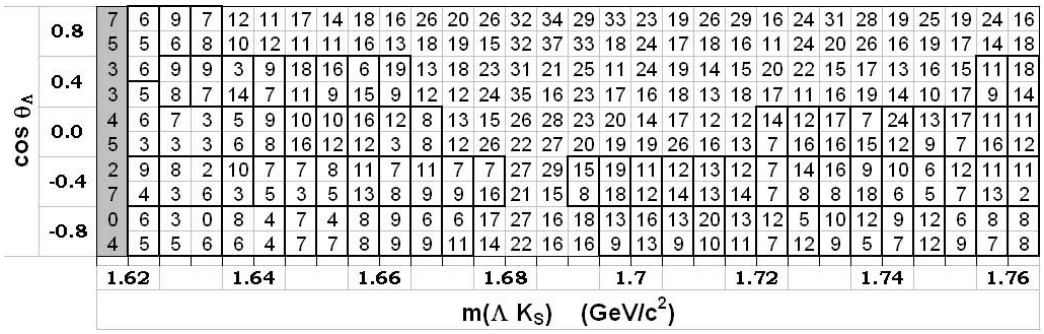

Figure 5.19: The rectangular plot of $m(\Lambda K_S)$ versus $\cos\theta_\Lambda$. The data are for the Λ_c^+ signal region, and the gray shaded area is excluded from the fits described in the text. The dark lines denote the fit regions which are combined for the purpose of chi-squared calculation (see the upper plot in Fig. 5.24).

MINUIT [41] is used to do this, it is actually the function $L = -2ln(\mathcal{L})$ which is minimized, where the explicit minus sign changes the process from maximization to minimization. The factor of 2 ensures that the errors are correctly estimated, as MINUIT estimates errors on the basis of a change in the function value of 1 unit with respect to the minimum value; this is fine for chi-squared minimization, but for a likelihood function the appropriate change is half a unit.

The function to be minimized is then:

$$L = -2 \sum_{i=1}^{N^{bins}} ln \left[e^{-\mu_i} \frac{(\mu_i)^{N_i^{obs}}}{(N_i^{obs})!} \right].$$

This simplifies to

$$L = 2 \left[\sum_{i=1}^{N^{bins}} \left[\mu_i - N_i^{obs} ln(\mu_i) \right] + ln\left(\Gamma(N_i^{obs} + 1) \right) \right].$$

Clearly, the last term is a constant, so that the final form of the function to be minimized is

$$L = 2 \sum_{i=1}^{N^{bins}} \left[\mu_i - N_i^{obs} ln(\mu_i) \right]. \tag{5.14}$$

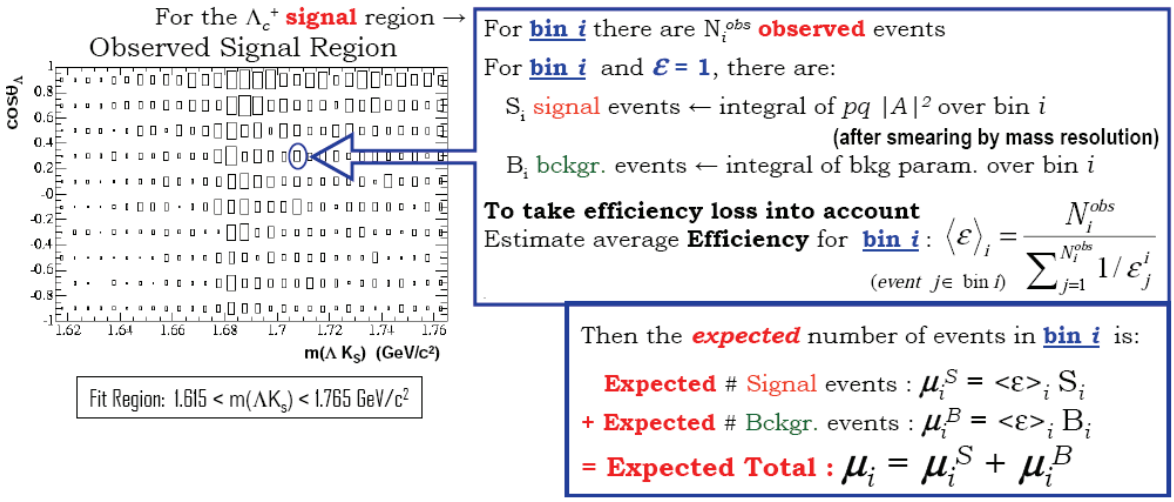

Figure 5.20: Illustration of the treatment of the i^{th} box in the Binned Maximum Poisson Likelihood procedure used to fit the Λ_c^+ signal region rectangular plot of $\cos\theta_\Lambda$ versus $m(\Lambda K_S)$.

In order to obtain an absolute assessment of goodness-of-fit a χ^2 value based on the fit function is calculated. Furthermore, in order to ensure that $\sqrt{N}$ provides a reasonable uncertainty estimate for a box containing N events, it is required that there be a minimum number of 10 observed events (corresponding to the Λ_c^+ signal region) in each box used in the χ^2 calculation. This requires a modification of the grid structure, and that indicated by the dark lines on Fig. 5.19, and shown explicitly in the upper plot of Fig. 5.24, has been chosen.

For each box of the original grid the efficiency-corrected signal function and background contributions are calculated and multiplied by the average efficiency for that box, as before, in order to obtain the expected number of observed events. These estimates can be added to provide estimates for combined boxes when required, and

a χ^2 function is defined as

$$\chi^2 = \sum_{j=1}^{N^{comb}} \left[\frac{N_j^{obs} - \mu_j^{combined}}{\sqrt{\mu_j^{combined}}} \right]^2 ,$$

where N^{comb} is the total number of boxes (combined and uncombined) used in the calculation, and is smaller than the number of boxes in the original grid of Fig. 5.19. The χ^2 can then be converted into a C.L. using $NDF = N^{comb} - 8$, where 8 is the number of free parameters used in the fit. For the grid shown in Fig. 5.19, the 290 boxes used in the likelihood fit yield $N^{comb} = 200$ for use in the χ^2 calculation.

5.6.7 Fit Results

Following the prescription of the previous section, the fit results given in Table 5.2 and shown in Fig. 5.21 are obtained. In Fig. 5.21 the solid dots represent the efficiency-corrected, background-subtracted distribution in data, where the background contribution was estimated following the procedures described in section 5.6.2. The red histograms represent the integrated fit function after mass resolution smearing. The blue curves correspond to the fit function with no resolution effects; the green, magenta and black curves represent the contributions to this total fit function from the $a_0(980)^+$ amplitude squared, the interference between the $a_0(980)^+$ and the $\Xi(1690)^0$ amplitudes, and the $\Xi(1690)^0$ amplitude squared, respectively. The likelihood value (Eq. 5.14) for this fit is 1550.4, and the corresponding χ^2/NDF is 188.4/192, which represents a C.L. of 56.4%.

The quality of the fit is demonstrated by the normalized residual distribution shown in Fig. 5.23. The distribution is centered at zero and is well-described by a

Gaussian with unit r.m.s. deviation, indicating that the fit is excellent.

A differential look at the χ^2 value is provided by the rectangular Dalitz plots of Fig. 5.24 for the Λ_c^+ signal region. The upper plot shows the event content of the boxes used to obtain the χ^2, while the lower plot shows the the χ^2 contribution from each individual box. Only four boxes yield contributions larger than 5 (c.f. Fig. 5.23), and these show no tendency to cluster in the (comparatively) high-population regions of the plot, i.e. there is no evidence of systematic deviation between the data and the fit result.

For comparison, the fit results obtained without mass resolution smearing are listed in Table 5.3. As expected this fit yields a width parameter value which is larger (by 0.9 MeV) than that of Table 5.2, while the other parameter values are unaffected, and the likelihood value is only very slightly worse.

The isobar description obtained for the Dalitz plot appears to be in qualitative agreement with that expected on the basis of the associated quark diagrams. Decay of the Λ_c^+ to $\Lambda a_0(980)^+$ would be characterized by the external spectator quark diagram of Fig. 1.9 (b), but for the transition $\Lambda_c^+ \to \Lambda$, and with the W coupling to an $a_0(980)^+$ instead of a π^+. A W-exchange diagram corresponding to Fig. 1.9 (a), but for the transition $\Lambda_c^+ \to \Xi(1690)^0$, would similarly characterize $\Lambda_c^+ \to \Xi(1690)^0 K^+$ decay. There are no obvious dynamical suppression mechanisms at work, other than the threshold mass of the $\Lambda\bar{K}^0$ system which excludes coupling to the $\Xi(1530)$.

It is interesting to compare the fit results obtained using the coherent and incoherent superposition of the $\Lambda a_0(980)^+$ and $\Xi(1690)^0 K^+$ amplitudes. The red his-

tograms representing the mass-integrated $\cos\theta_\Lambda$ distributions shown in Fig. 5.17(b) and Fig. 5.21(b) are almost identical. However, the $m(\Lambda K_S)$ projections of Fig. 5.17(a) and Fig. 5.21(a) exhibit significant differences in the $\Xi(1690)$ signal region. The systematic deviations discussed in section 5.6.4 and shown in Fig. 5.18 for the incoherent superposition are no longer apparent in Fig. 5.21 (a), where the $\Xi(1690)^0$ signal shape is well-reproduced. This is shown explicitly by the distribution of Fig. 5.22, where the systematic deviations between the data and the fit result seen Fig. 5.18 are no longer evident. The fit results summarized in Tables 5.1 and 5.2. indicate an associated likelihood function (Eq. 5.14) reduction of approximately 12 points, and although the fitted value of the width changes by only 0.4 MeV, use of the coherent superposition results in a decrease of the fitted mass value of 2.1 MeV/c^2. This is because, for overall relative phase $\sim 0^\circ$, the interference term is able to describe the skewing of the lineshape toward high mass, as discussed in conjunction with Fig. 5.18, whereas in the absence of interference, the entire fitted lineshape moves to a higher mass value in attempting to respond to the skewing and so improve the fit.

Although the systematic changes in the fitted $\Xi(1690)^0$ lineshape resulting from the use of the coherent amplitude superposition do not appear overly significant, the impact on the interpretation of the observed signal is in fact significant. The $\Xi(1690)^0$ signal represented by the black histogram in Fig. 5.17(a) has been reduced by $\sim 25\%$ in Fig. 5.21(a), the difference being absorbed by the $\Xi(1690)^0 K^+$-$\Lambda a_0(980)^+$ interference contribution generated in order to accommodate the skewing of the observed signal. It follows that the Λ_c^+ decay rate to $\Xi(1690)^0 K^+$ obtained

from a description of the final state Dalitz plot is significantly smaller than would be obtained from a fit to the mass projection using a BW signal function and an incoherent background function, as for Fig. 5.17(a), or as in the analysis of ref. [46]. However, the analysis presented to this point assumes that the $\Xi(1690)$ has spin 1/2. The discussion of Λ_c^+ decay rate needs to be revisited after investigation of the spin 3/2 and 5/2 hypotheses.

The differential chi-squared distribution of Fig. 5.24 demonstrates quite clearly that the fit quality is very good over the entire rectangular Dalitz plot, and in particular in the $\Xi(1690)$ signal region. This is shown explicitly in Fig. 5.25 for the signal region defined as $1.660 < m(\Lambda K_S) < 1.705$ GeV/c^2. In Fig. 5.25 the solid dots represent the efficiency-corrected, background-subtracted distribution in data, as before. The contributions to the total fit function (after mass resolution smearing), from the $a_0(980)^+$ amplitude squared (green curve), the interference term (magenta curve) and the $\Xi(1690)^0$ amplitude squared (black line) account for 59.7%, 11.8% and 28.5% of the total intensity (blue curve), respectively, and the latter provides an excellent description of the data in the $\Xi(1690)$ region.

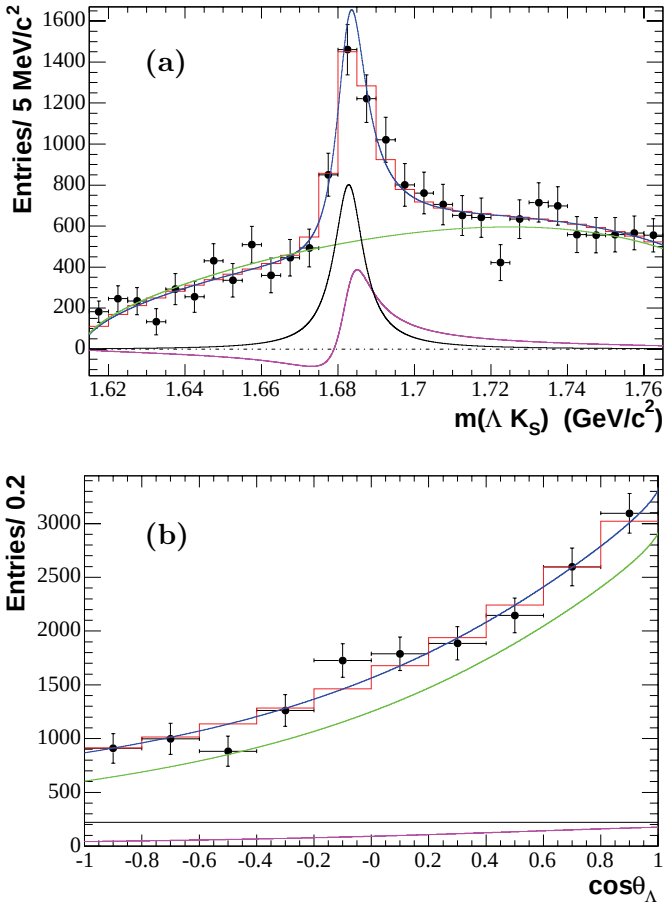

Figure 5.21: The projections of the efficiency-corrected, background-subtracted rectangular plot in data. The red histograms represent the integrated fit function after mass resolution smearing. The curves are described in the text.

Table 5.2: The MIGRAD fit parameter values corresponding to Fig. 5.21.

Fit Parameter	Value	Neg. Error	Pos. Error
$\Xi(1690)$ Ampl. Rel. Strength [MeV] (p_0)	24 ± 8	–	–
$\Xi(1690)$ Mass [MeV/c^2]	1682.9 ± 0.9	-0.9	+0.9
$\Xi(1690)$ Width [MeV]	9.3 ± 1.9	-1.7	+2.0
Effective Phase δ [rad.]	0.3 ± 0.5	-0.4	+0.6
Effective Scale k	0.4 ± 0.2	-0.2	+0.3
Overall Normalization Factor	1205 ± 726	–	–
$g_{\bar{K}K}$ [MeV]	349 ± 136	–	–
Coupling Ratio Squared (r^2)	0.5 ± 0.4	–	–

Note: The last two columns list the MINOS error estimates. The likelihood value (Eq. 5.14) for this fit is 1550.4, and the corresponding χ^2/NDF obtained as described in the text is 188.4/192.

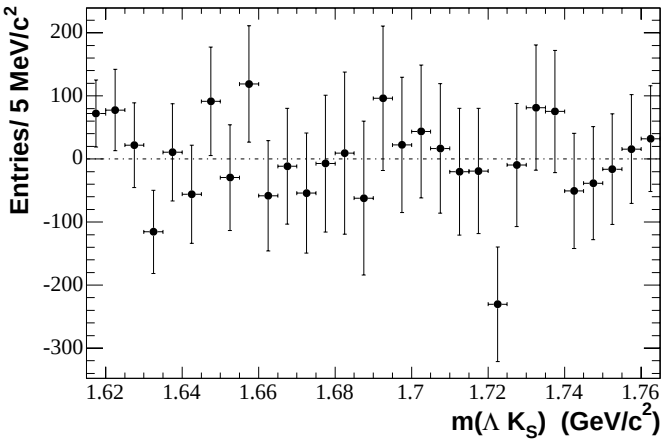

Figure 5.22: The difference between the mass projection of the efficiency-corrected, background-subtracted rectangular plot in data and the fit function smeared by mass resolution (histogram of Fig. 5.21).

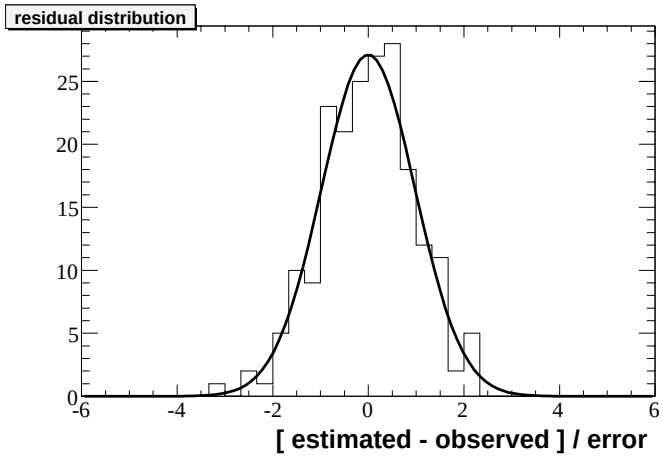

Figure 5.23: The normalized residual distribution $\Delta = \left[\frac{\mu_j^{combined} - N_j^{obs}}{\sqrt{\mu_j^{combined}}}\right]$, corresponding to the fit results of Fig. 5.21 and Table 5.2. Superimposed on the distribution is the result of a fit with a single Gaussian function with an r.m.s. value of 0.98±0.05 and a mean value of -0.02 ± 0.07, which is consistent with zero, as expected if the fit is unbiased.

Table 5.3: The MIGRAD fit parameter values obtained without mass resolution smearing.

Fit Parameter	Value
$\Xi(1690)$ Amplitude Relative Strength [MeV] (p_0)	25 ± 8
$\Xi(1690)$ Mass [MeV/c^2]	1682.9 ± 0.9
$\Xi(1690)$ Width [MeV]	10.2 ± 1.8
Effective Phase δ [rad.]	0.3 ± 0.5
Effective Scale k	0.4 ± 0.2
Overall Normalization Factor	1197 ± 714
$g_{\bar{K}K}$ [MeV]	349 ± 135
Coupling Ratio Squared (r^2)	0.5 ± 0.4

Note: The likelihood value from Eq. 5.14 is 1550.5 for this fit.

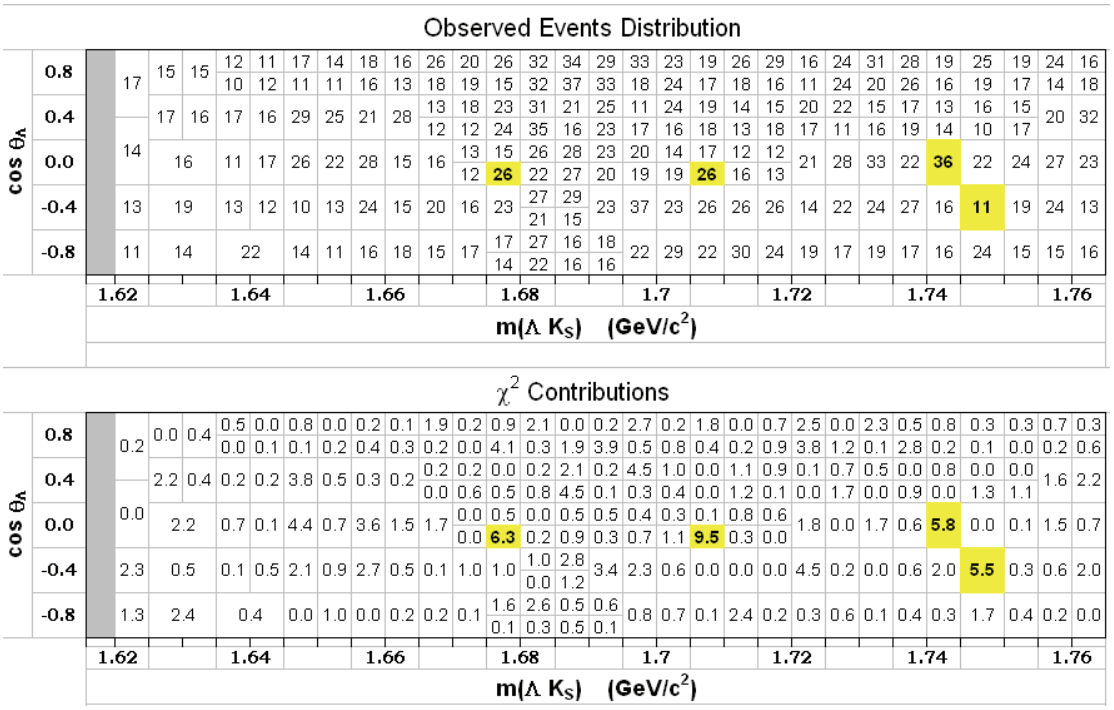

Figure 5.24: The rectangular plot of $m(\Lambda K_S)$ versus $\cos\theta_\Lambda$ for the Λ_c^+ signal region modified such that every box contains at least 10 events. The χ^2 contributions from the boxes of the rectangular plot. Boxes yielding χ^2 contributions exceeding 5 are highlighted in both plots.

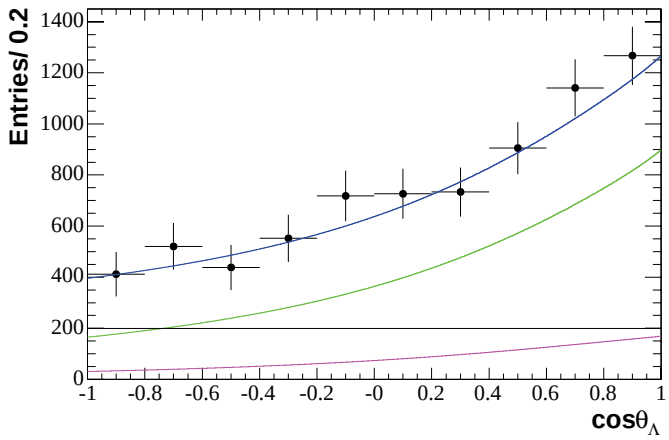

Figure 5.25: The cosθ_Λ projection of the efficiency-corrected, background-subtracted rectangular plot in data for the region $1.660 < m(\Lambda K_S) < 1.705$ GeV/c^2 (solid dots with error bars). The superimposed curves are explained in the text.

A further check of fit quality is provided by the efficiency-corrected, background-subtracted $m(K^+K_S)$ and $m(\Lambda K^+)$ distributions corresponding to the fitted region of the rectangular plot. These are shown by the solid dots with error bars in Figs. 5.26 (a) and (b), respectively. The color-coding in Fig. 5.26 is the same as in Fig. 5.25, and again the fit provides an excellent description of the data. The kinks in the curves, which are especially noticeable in Fig. 5.26 (b), are due to the restriction of $m(\Lambda K_S)$ to the range $1.620 - 1.765$ GeV/c^2 used in the fit [cf. Fig. 5.6 (a)].

A three-dimensional representation of the fit function intensity over the rectangular Dalitz plot is shown from two perpectives in Fig. 5.27. The pronounced ridge associated with $\Xi(1690)^0$ production is clear in both, while the left view exhibits a pronounced intensity decrease toward threshold on the low side of the ridge, and the right view shows the rise at high mass and cos$\theta_\Lambda \sim 1$ resulting from the presence of

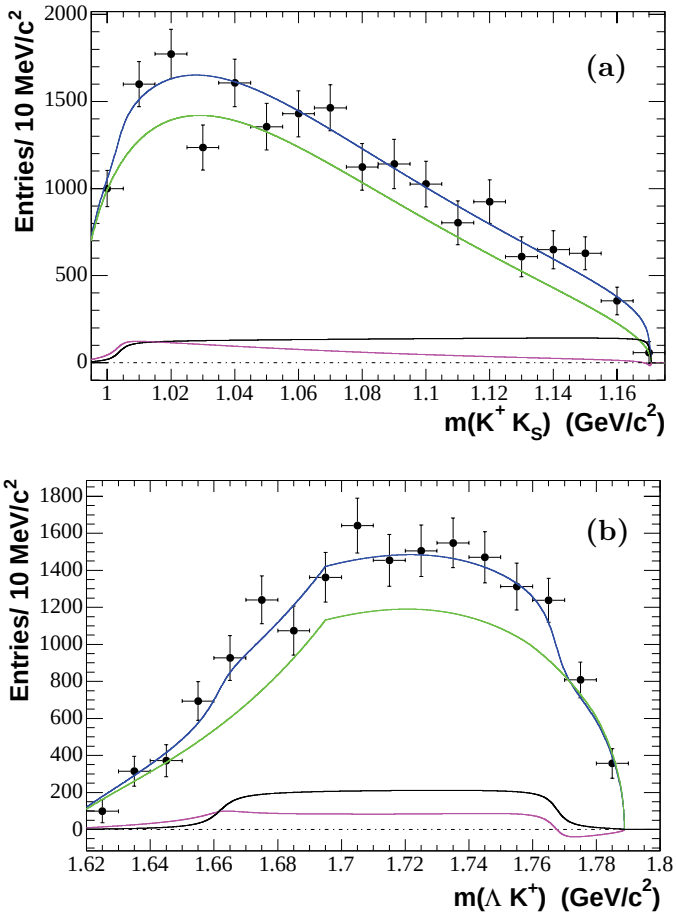

Figure 5.26: The efficiency-corrected, background-subtracted projections in data corresponding to the region $1.620 < m(\Lambda K_S) < 1.765$ GeV/c^2 (solid dots with error bars). (a) The $m(K^+K_S)$ projection. (b) The $m(\Lambda K^+)$ projection. The superimposed curves are explained in the text.

a significant $a_0(980)^+$ contribution on the high side of the ridge. The total fit function intensity distribution over the fit region of the rectangular plot, and its separate contributions are illustrated in the color contour plots of Figs. 5.28 and 5.29. In each figure, the upper left plot corresponds to the total intensity, the upper right plot results from the $\Lambda a_0(980)^+$ amplitude squared, the lower right is from the $\Xi(1690)^0 K^+$ amplitude squared, and the lower left represents the interference contribution; in the

latter, the white region denotes negative values resulting from destructive interference. In Fig. 5.28, each plot has its own intensity scale in order to make structure clear; in Fig. 5.29, all plots have the scale of the total intensity plot (upper left). Figures 5.28 and 5.29 illustrate quite clearly how important the inclusion of a coherent amplitude describing the $\Lambda a_0(980)^+$ decay mode is to a detailed understanding of the $\Lambda \bar{K}^0 K^+$ final state, and hence to precise extraction of the properties of the $\Xi(1690)^0$.

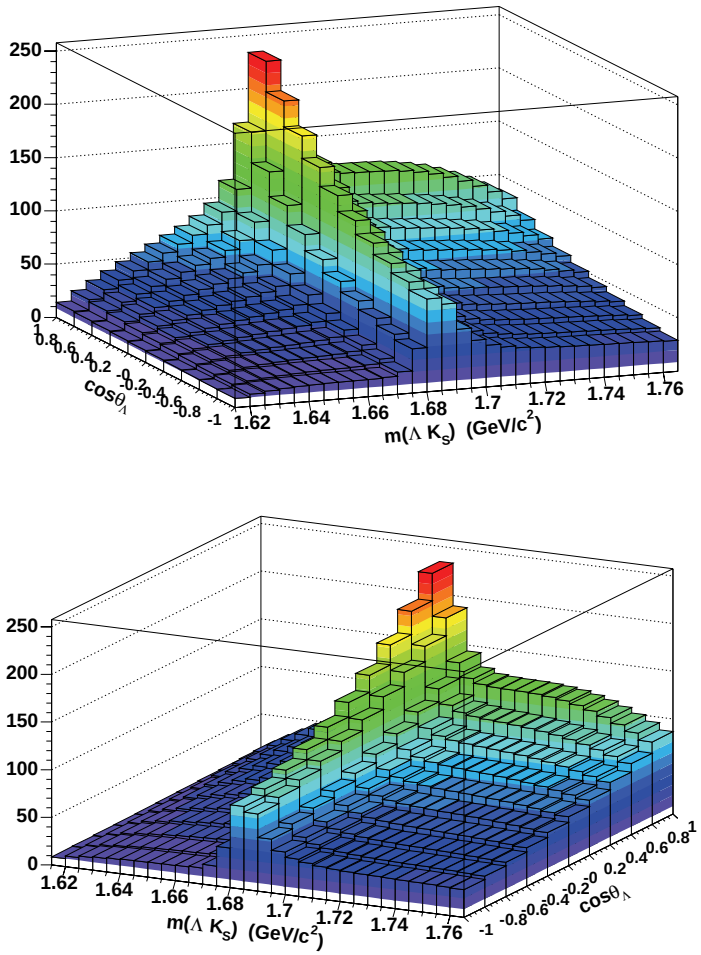

Figure 5.27: Three-dimensional representations of the fit function intensity distribution of the rectangular Dalitz plot.

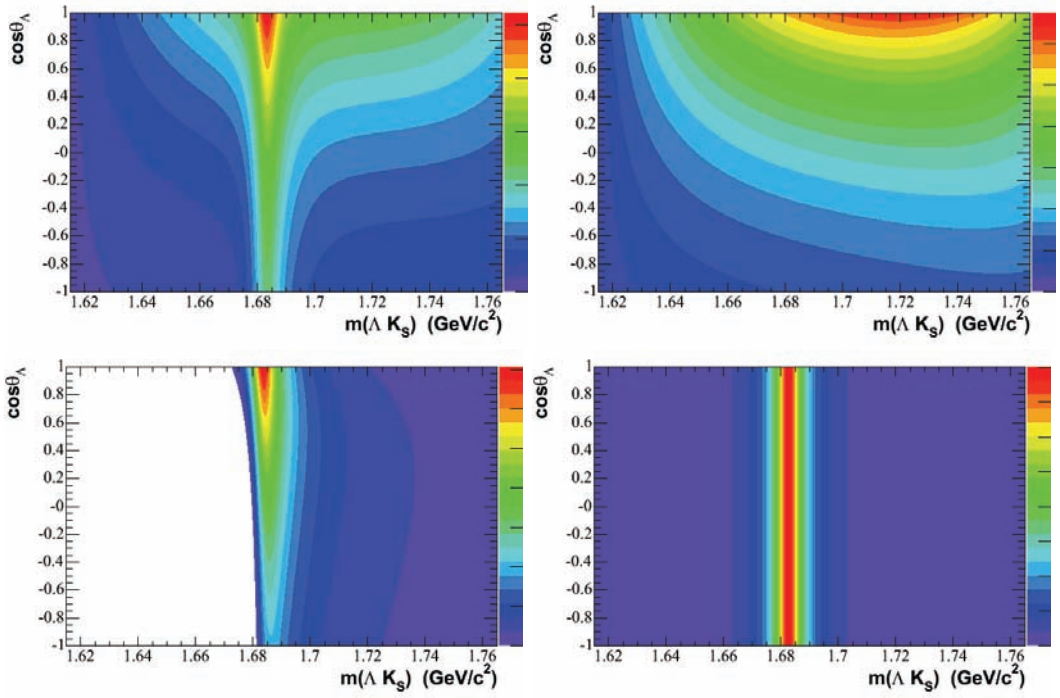

Figure 5.28: Contour plots representing total fit function intensity (top left) and the contributions from the $a_0(980)^+$ amplitude squared (top right), the interference between the $a_0(980)^+$ and the $\Xi(1690)^0$ amplitudes (bottom left), and the $\Xi(1690)^0$ amplitude squared (bottom right). Each plot has its own intensity scale, and the white area of the bottom left plot correspond to negative intensity, i.e. destructive interference.

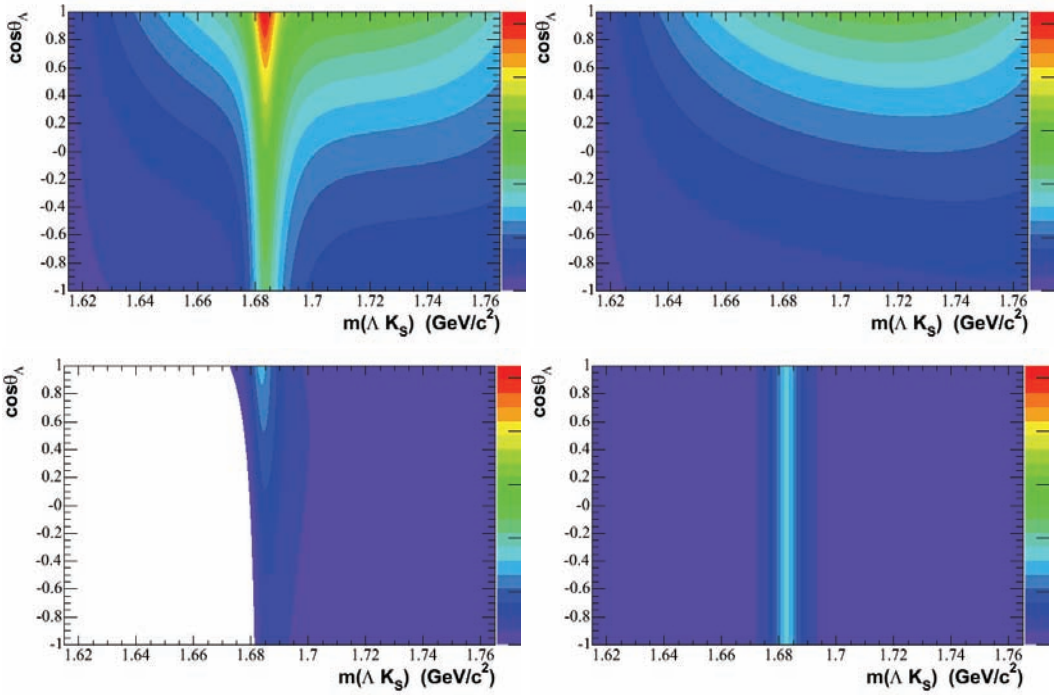

Figure 5.29: As for Fig. 5.28, except that all plots use the scale of the total intensity plot (upper left).

5.6.8 Study of Systematic Uncertainties

It proves to be the case that all of the sources of systematic error considered affect the parameter values only slightly if at all. Consequently, a conservative point of view is adopted, in that the largest measurement excursion in a given study is assigned as the related systematic estimate. The study of systematic error contributions to the measured values of $\Xi(1690)^0$ mass and width described in this section assumes spin 1/2 for the $\Xi(1690)$.

The fit procedure of the previous section is repeated using the background parametrization obtained by linear interpolation of the $< N >$ and $< C_i >$ coefficients plotted in Fig. 5.12 (dashed red lines). The new fit results indicate that there is no change in the mass value, but the width is changed by 0.2 MeV.

Next a systematic error due to the background normalization is assessed by varying the total number of background events by the one sigma uncertainty in the estimated number of events under the Λ_c^+ peak, as described in section 5.6.2. The results corresponding to the variations by this uncertainty yield no change in the $\Xi(1690)^0$ mass, and the larger change in width is only +0.1 MeV.

One the basis of these studies, the systematic error associated with the mass value is considered to be 0.0 MeV/c^2, while that associated with the width is conservatively estimated to be $\sqrt{(0.2)^2 + (0.1)^2}$ MeV, i.e. 0.2 MeV.

The fractional contribution of the wide Gaussian to the total resolution function is varied by its uncertainty, and the fit procedure repeated. The results of a $\pm 1\sigma$ variation indicate no change in mass value, and that the width value changes by 0.1

MeV at most. As a result, systematic uncertainly contributions of 0.0 MeV/c^2 and 0.1 MeV, respectively, are assigned.

The fit procedure was repeated using the modified efficiency parametrization described in Appendix B. The fitted mass and width values change by 0.1 MeV/c^2 and 0.1 MeV, respectively, and so these are assigned as the relevant systematic uncertainty values.

In the description of the isobar model in section 5.6.4 it was pointed out that, for the decay $\Lambda_c^+ \to \Xi(1690)^0 K^+$, the final state orbital angular momentum, L, could be 0 or 1, corresponding to S- and P-wave decay, respectively, and that the final state orbital angular momentum describing the ΛK_S system from $\Xi(1690)^0$ decay, l, can also take values 0 or 1, under the assumption of spin 1/2 for the $\Xi(1690)$. The choice of $L = 0$, $l = 0$, was made in fitting the rectangular Dalitz plot, and so in order to investigate systematic effects on the values of the mass and width parameters resulting from this choice, the other possibilities are now considered.

The values $L = 1$ and $l = 1$ imply the need for the inclusion of a P-wave centrifugal barrier factor[5] contribution describing the relevant decay. For P-wave,

[5]From the covariant description of the decay amplitudes, one obtains a mass-dependent expression for the width of the resonance. The width of the resonance proceeding via a partial wave of orbital angular momentum l is given by:

$$\Gamma(m) \approx \Gamma_0 \left(\frac{q}{q_0}\right)^{2l+1},$$

where, Γ_0 and q_0 are the width and 3-momentum of the resonance. This expression is only valid for low energies, and the case of a wave scattered far away from thresholds needs to be addressed using a more general description using centrifugal barrier factors. In the Classical picture for the scattering of a particle in spherically symmetric potential $U(r)$, the radial

this is done by introducing the factor

$$\frac{p}{\sqrt{1+R^2p^2}},$$

where R is the Blatt-Weisskopf radius [49], and p is the quasi-two-body momentum in the rest-frame of the decaying particle. Typically, $R \simeq 3$ GeV^{-1} (i.e. 0.6 fermi), and this is the value chosen in the present study. For $L = 1$, the effect is to introduce an additional factor $p/\sqrt{1+R^2p^2}$ in the numerator of Eq. 5.5, where p is the momentum of the bachelor K^+ in the Λ_c^+ rest-frame. For $l = 1$, the corresponding factor is

$$\frac{q}{\sqrt{1+R^2q^2}},$$

where q is the momentum of the Λ in the ΛK_S rest-frame. This factor also appears in the numerator of Eq. 5.5, but in addition, it causes modification of $\Gamma(m)$, which appears in the denominator. Equation 5.6 must then be written

$$\Gamma(m) = \Gamma(m_0)\frac{q}{m}\cdot\frac{m_0}{q_0}\cdot\left(\frac{q^2}{1+R^2q^2}\right)\cdot\left(\frac{1+R^2q_0^2}{q_0^2}\right), \tag{5.15}$$

since it is the square of the Blatt-Weisskopf factor which appears in the width. The results of fits to the Dalitz plot using the (L, l) combinations $(1, 0)$, $(1, 1)$ and $(0, 1)$

equation for $l > 0$,

$$\left(\frac{1}{2mr^2}\frac{d}{dr}\left(r^2\frac{d}{dr}\right) + \left[\frac{1}{2m} - \frac{l(l+1)}{2mr^2} - U(r)\right]\right)\psi(r) = 0,$$

contains an l-dependent centrifugal barrier term:

$$V_l = \frac{l(l+1)}{2mr^2}.$$

As the value of l increases, so does the centrifugal barrier, and therefore, the transition amplitude decreases. These centrifugal barrier factors (Blatt-Weisskopf damping functions) over an interaction of radius R are function of R, of the quasi-two-body momentum in the rest-frame of the decaying particle, and of the orbital angular momentum of the two-particle system (in the outgoing channel).

are then used to assign net systematic uncertainties of 0.2 MeV/c^2 and 0.1 MeV to the mass and width parameter values, respectively.

The uncertainties due to the coupling constants incorporated in the Flatté parametrization are studied by first fixing the square of their ratio (r^2) to the value obtained by the Crystal Barrel experiment. The fit results are quite consistent with those of Table 5.2, and the fit χ^2/NDF changes from 188.4/192 to 191.1/193, corresponding to a reduction in C.L. of $\sim 3.5\%$. The mass and width parameter values change by only +0.1 MeV/c^2 and +0.3 MeV, respectively.

Next, the value of the mass of the $a_0(980)$ is varied by the uncertainty determined by the Crystal Barrel experiment. Variations in this parameter by $\pm 1\sigma$ yield no change in the mass and width values, and so net uncertainties of 0.1 MeV/c^2 and 0.3 MeV are attributed to the choice of $a_0(980)^+$ parameter values.

Uncertainties due to detector effects are estimated from the study of systematic uncertainties in the mass measurement of the Λ_c^+ using $\Lambda_c^+ \to \Lambda K_S K^+$ and $\Lambda_c^+ \to \Sigma^0 K_S K^+$ decays [50]. This study found that the dominant systematic uncertainty in mass arose from the amount of material in the tracking volume and from the magnetic field strength, but that this effect was small for $\Lambda_c^+ \to \Lambda \bar{K}^0 K^+$ because of the limited phase space available in the decay. Because systematic uncertainties scale with Q-value, a reliable and conservative estimate of the uncertainty in the mass of the $\Xi(1690)^0$ (Q-value ~ 70 MeV/c^2) is obtained from the uncertainty due to detector effects in Λ_c^+ mass estimated for $\Lambda_c^+ \to \Lambda \bar{K}^0 K^+$ (Q-value ~ 180 MeV/c^2). This yields a systematic uncertainty estimate of ± 0.1 MeV/c^2 on the $\Xi(1690)^0$ mass. Since the

$\Xi(1690)^0$ has a small width, and the preceding is a mass scale effect, any impact on the width measurement can be ignored.

5.6.9 Summary of Systematic Uncertainties

Incorporating the systematic uncertainties summarized in Table 5.4, and ignoring, for the moment, spin assumptions other than 1/2, the following measured values for the mass and width parameters of the $\Xi(1690)^0$ resonance are obtained:

$$m(\Xi(1690)^0) = 1682.9 \pm 0.9\ (\text{stat.}) \pm 0.3\ (\text{syst.})\ \ \text{MeV/c}^2,$$

$$\Gamma(\Xi(1690)^0) = 9.3^{+2.0}_{-1.7}\ (\text{stat.}) \pm 0.4\ (\text{syst.})\ \ \text{MeV}.$$

These results represent a significant improvement in the precision to which these quantities are presently known [22].

Table 5.4: Summary of systematic uncertainty contributions.

Source	Estimated Systematic Uncertainty	
Background Normalization and	$\Xi(1690)^0$ Mass [MeV/c^2]	0.0
Parametrization	$\Xi(1690)^0$ Width [MeV]	$\pm$0.2
Resolution Function	$\Xi(1690)^0$ Mass [MeV/c^2]	0.0
Lineshape	$\Xi(1690)^0$ Width [MeV]	$\pm$0.1
Efficiency	$\Xi(1690)^0$ Mass [MeV/c^2]	$\pm$0.1
Parametrization	$\Xi(1690)^0$ Width [MeV]	$\pm$0.1
Orbital Ang. Momentum	$\Xi(1690)^0$ Mass [MeV/c^2]	$\pm$0.2
Variation	$\Xi(1690)^0$ Width [MeV]	$\pm$0.1
$a_0(980)^+$ Parameter	$\Xi(1690)^0$ Mass [MeV/c^2]	$\pm$0.1
Values	$\Xi(1690)^0$ Width [MeV]	$\pm$0.3
Detector	$\Xi(1690)^0$ Mass [MeV/c^2]	$\pm$0.1
Effects	$\Xi(1690)^0$ Width [MeV]	0.0
Total Systematic	$\Xi(1690)^0$ Mass [MeV/c^2]	$\pm$0.3
Uncertainty	$\Xi(1690)^0$ Width [MeV]	$\pm$0.4

The change in mass value (-2.1 MeV/c^2) in going from the incoherent to the coherent amplitude superposition procedure in fitting the rectangular Dalitz plot, discussed in section 5.6.7, is much larger than the net systematic uncertainty resulting from the studies described in section 5.6.8. This is not treated as a source of systematic uncertainty, since the coherent treatment is considered to be the correct one, both from the standpoint of Quantum Mechanics, and on the basis of experimentally observed structures in many other Dalitz plots. For example, the *BABAR* Dalitz plots for $D^0 \to K_S K^+ K^+$ decay [51] and for $D^0 \to K_S \pi^+ \pi^-$ decay [52] exhibit quite dramatic interference effects, and even in chapter 6 of this thesis there is clear evidence of interference between the S- and P-wave amplitudes describing the $\Xi^- \pi^+$ system in the vicinity of the $\Xi(1530)^0$ resonance. The corresponding change in width (-0.4 MeV) is also not considered to be a source of systematic uncertainty for the same reasons.

5.7 Dalitz Plot Analyses for $\Xi(1690)$

Spin 3/2 and 5/2

For $\Xi(1690)$ spin J, and a corresponding definition of the helicity angle of the Λ in the ΛK_S rest-frame, the expected distributions in cosθ_Λ for J =3/2, and 5/2 are described by Eqs. 5.16 and 5.17, respectively.

$$\begin{aligned} I &= pq\, C \left[p_0^2 I_1 \left(\frac{3\cos^2\theta_\Lambda + 1}{4} \right) + \frac{g_{\bar{K}K}^2 I_2}{2} \right. \\ &+ \left. \frac{k}{\sqrt{2}} (\cos\theta_\Lambda)\, p_0 g_{\bar{K}K} I_1 I_2 \left[(M_1 M_2 + G_1 G_2)\cos\delta + (\mathrm{G_1 M_2} - \mathrm{G_2 M_1})\sin\delta \right] \right] \end{aligned} \tag{5.16}$$

$$I = pq\,C\left[p_0^2 I_1\,3\left(\frac{5\cos^4\theta_\Lambda - 2\cos^2\theta_\Lambda + 1}{8}\right) + \frac{g_{\bar{K}K}^2 I_2}{2}\right. \tag{5.17}$$
$$\left. + \frac{\sqrt{3}k}{4}\left(3\cos^2\theta_\Lambda - 1\right) p_0 g_{\bar{K}K} I_1 I_2 \left[(M_1M_2 + G_1G_2)\cos\delta + (\mathrm{G_1M_2} - \mathrm{G_2M_1})\sin\delta\right]\right]$$

The details of the derivations are given in Appendix C, section C.3, where it is pointed out that the effective scale parameter, k, and the effective phase parameter, δ, incorporate any Lorentz boost effects, as discussed previously with regard to Eq. 5.13.

For $J = 3/2$, the orbital angular momenta L and l discussed in section 5.6.8, lead to P- or D-wave [49] centrifugal barrier contributions to the $\Xi(1690)^0$ amplitudes, while for $J = 5/2$, D- or F-wave contributions need to be incorporated. For the fits described in the present section $(L, l) = (1, 1)$ barrier factors were used for $J = 3/2$, and $(L, l) = (2, 2)$ for $J = 5/2$. The other possible combinations were not tried since the fit results differed only slightly from those with $(L, l) = (0, 0)$, and since the corresponding studies of $J = 1/2$ systematic uncertainty indicate that only small changes would be expected.

The fit procedures used in testing the $J = 1/2$ hypothesis for the spin of the $\Xi(1690)$ were repeated for $J = 3/2$ using the intensity distribution representation of Eq. 5.16. The results are shown in Fig. 5.30 and summarized in Table 5.5. The fit has $\chi^2/NDF = 234.3/192$, which corresponds to a C.L. of 1.9%. The mass of the $\Xi(1690)^0$ increases by 2 MeV/c^2, while the width decreases by 0.5 MeV, mainly because of the inclusion of the P-wave barrier factors. The quadratic nature of the $\Xi(1690)^0$ intensity contribution to the $\cos\theta_\Lambda$ distribution (Fig. 5.30 (b)) seems to

result in the fit being systematically above the data for $\cos\theta_\Lambda < -0.4$, and the smallness of the $\Xi(1690)K^+ - \Lambda a_0(980)^+$ interference contribution results in a systematic failure to reproduce the skewing toward high mass of the $\Xi(1690)$ signal in Fig. 5.30 (a). This is shown explicitly in Fig. 5.31, which shows behavior very similar to that of Fig. 5.18, corresponding to the incoherent amplitude superposition discussed in section 5.6.4.

Table 5.5: The MIGRAD fit parameter values corresponding to Fig. 5.30 for $J = 3/2$.

Fit Parameter	Value
$\Xi(1690)$ Ampl. Rel. Strength [MeV] (p_0)	425 ± 91
$\Xi(1690)$ Mass [MeV/c^2]	1684.9 ± 0.8
$\Xi(1690)$ Width [MeV]	8.8 ± 2.1
Effective Phase δ [rad.]	-2.7 ± 1.1
Effective Scale k	0.2 ± 0.2
Overall Normalization Factor	4871 ± 1094
$g_{\bar{K}K}$ [MeV]	234 ± 30
Coupling Ratio Squared (r^2)	0.2 ± 0.1

Note: The likelihood value (Eq. 5.14) for this fit is 1592.0, and the corresponding χ^2/NDF obtained as described in the text is 234.3/192.

The low C.L. for the fit, and the observed systematic deviations in the $\cos\theta_\Lambda$ and $m(\Lambda K_S)$ distributions, indicate that the spin 3/2 hypothesis for the $\Xi(1690)$ is clearly disfavored.

In a similar way, the intensity distribution of Eq. 5.17 is used to test the hypothesis that the $\Xi(1690)$ has spin 5/2. The results are shown in Fig. 5.32 and summarized in Table 5.6. This fit has $\chi^2/NDF = 210.3/192$ and a C.L. of 17.4%,

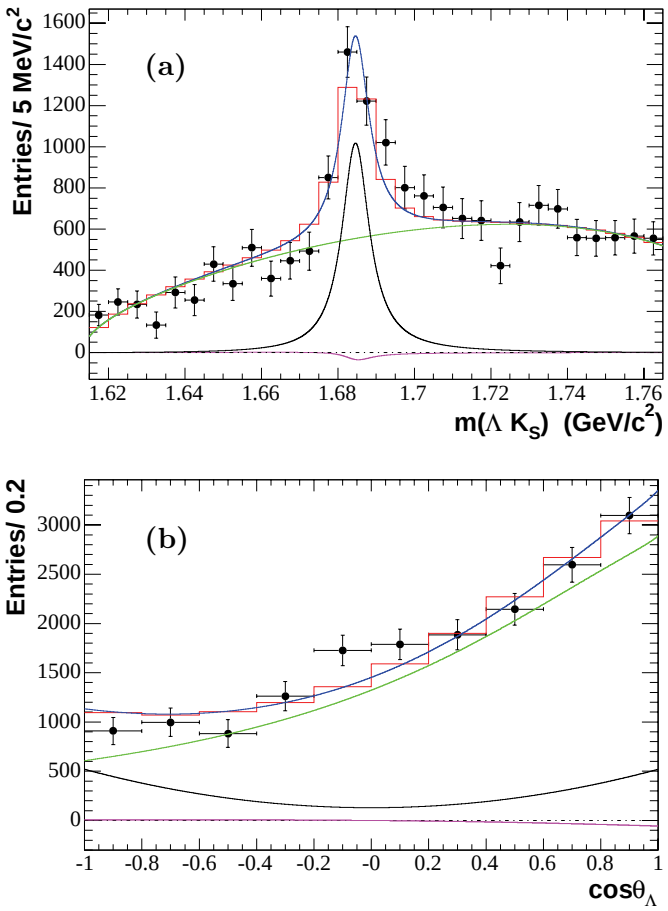

Figure 5.30: The projections of the efficiency-corrected, background-subtracted rectangular plot in data. The solid histogram corresponds to the fit function (smeared by resolution) corresponding to $J = 3/2$. The superimposed curves are as for $J = 1/2$ (see text).

which represents a significant improvement over that obtained for $J = 3/2$, but is significantly poorer than for $J = 1/2$ (56.4%). The $\cos\theta_\Lambda$ distribution is well-described (Fig. 5.32 (b)), but the systematic failure to describe the skewing of the $\Xi(1690)^0$ signal toward high mass is still present (Figs. 5.32 (a) and 5.33), and this is the primary cause of the rather low C.L. value. The results of the fits to the rectangular Dalitz plot for $\Xi(1690)$ spin hypotheses 1/2, 3/2 and 5/2 are summarized in Table 5.7.

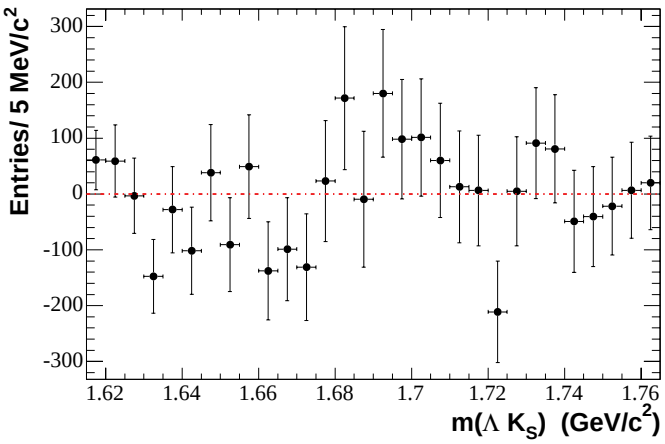

Figure 5.31: The difference between the data points and the fit function smeared by mass resolution (solid histogram) of Fig. 5.30.

Table 5.6: The MIGRAD fit parameter values corresponding to Fig. 5.32 for $J = 5/2$.

Fit Parameter	Value
$\Xi(1690)$ Ampl. Rel. Strength [MeV] (p_0)	2981 ± 612
$\Xi(1690)$ Mass [MeV/c^2]	1684.9 ± 0.8
$\Xi(1690)$ Width [MeV]	9.0 ± 2.0
Effective Phase δ [rad.]	2.4 ± 0.2
Effective Scale k	0.9 ± 0.2
Overall Normalization Factor	5198 ± 1210
$g_{\bar{K}K}$ [MeV]	219 ± 29
Coupling Ratio Squared (r^2)	0.2 ± 0.1

Note: The likelihood value (Eq. 5.14) for this fit is 1570.8, and the corresponding χ^2/NDF obtained as described in the text is 210.3/192.

It is concluded that the data are consistent with spin $J = 1/2$ and that $J = 3/2$ is clearly disfavored. The quadratic nature of the helicity angular distribution of the

interference term for $J = 5/2$ is such that the $\cos\theta_\Lambda$ distribution is well-reproduced. However, the fit fails to reproduce the skewing of the $\Xi(1690)$ signal (Figs. 5.32 (a) and 5.33).

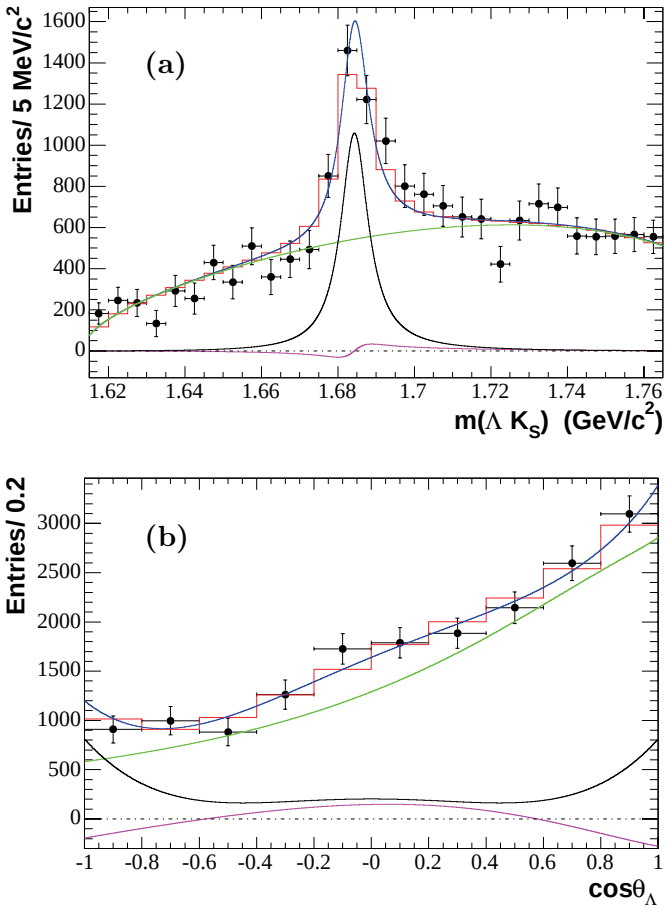

Figure 5.32: The projections of the efficiency-corrected, background-subtracted rectangular plot in data. The solid histogram corresponds to the fit function (smeared by resolution) corresponding to $J = 5/2$. The superimposed curves are as for $J = 1/2$ (see text).

It follows that, although the $J = 5/2$ C.L. is acceptable, the latter systematic failure makes it appear that this hypothesis is unlikely to be correct. This point

of view is reinforced by the analysis to be described in chapter 6, which, although model-dependent, provides additional evidence in favor of spin 1/2 (and even negative parity) for the $\Xi(1690)$. Finally, theoretical models [25, 26] typically do not predict the existence of $J = 5/2$ Cascade resonances at mass values below 1.7 GeV/c^2.

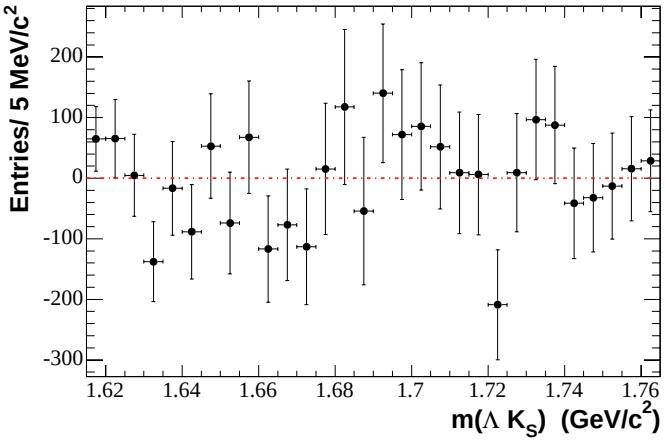

Figure 5.33: The difference between the data points and the fit function smeared by mass resolution (solid histogram) of Fig. 5.32.

Table 5.7: A summary of the fits to the rectangular Dalitz plot for $\Xi(1690)$ spin values 1/2, 3/2 and 5/2 (MIGRAD errors).

$\Xi(1690)$ Spin	m[$\Xi(1690)$] [MeV/c^2]	$\Gamma[\Xi(1690)]$ [MeV]	k	δ [rad]	χ^2/NDF	C.L. (%)
1/2	1682.9 ± 0.9	9.3 ± 1.9	0.4 ± 0.2	0.3 ± 0.5	188.4/192	56.4 [52.9]
3/2	1684.9 ± 0.8	8.8 ± 2.1	0.2 ± 0.2	-2.7 ± 1.1	234.3/192	1.9 [1.0]
5/2	1684.9 ± 0.8	9.0 ± 2.0	0.9 ± 0.2	2.4 ± 0.2	210.3/192	17.4 [12.2]

Note: If the parameter r^2 is fixed at the Crystal Barrel central value (1.03), the C.L. values indicated in parentheses are obtained.

5.8 Comments Concerning Lorentz Boost Effects

As discussed in Appendix C, section C.3, the interference term between the amplitudes describing Λ_c^+ decay to $\Xi(1690)^0 K^+$ and $\Lambda a_0(980)^+$ is affected, in principle, by the transformation of the latter from the rest-frame of the Λ_c^+ to the rest-frame of the $\Lambda\bar{K}^0$ system, This involves an initial rotation to a new spin quantization axis, shown as the z-axis in Fig. 5.34. As a result of the boost, the new direction if the Λ is rotated by the angle ω (the Wigner rotation angle) relative to its direction in the Λ_c^+ rest-frame, as shown in the figure.

If the Λ had momentum $\mathbf{q}^*$ and helicity λ in the Λ_c^+ rest-frame, the boost

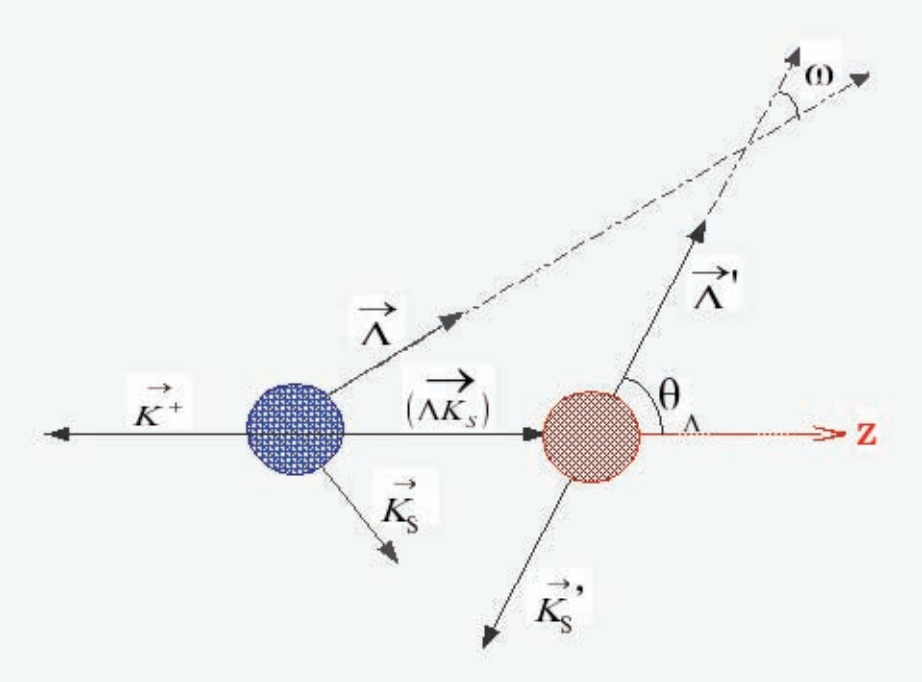

Figure 5.34: Illustration of the angle ω.

operator $U(L)$ would modify the amplitude describing the Λ as follows:

$$U(L)\varphi_{\mathbf{q}^*,\lambda} = \sum_{\lambda'=-s}^{+s} \varphi_{\mathbf{q},\lambda'} d^s_{\lambda'\,\lambda}(\omega),$$

where $\mathbf{q}$ is the Λ momentum in the ΛK_S rest-frame, s is the spin of the Λ, and λ' can take the values $\pm 1/2$. Explicitly, e.g. for $\lambda = 1/2$

$$\varphi_{\mathbf{q}^*,1/2} \rightarrow \varphi_{\mathbf{q},1/2}\cos(\omega/2) + \varphi_{\mathbf{q},-1/2}\sin(\omega/2), \tag{5.18}$$

so that in general the boost transforms a Λ helicity state in the Λ_c^+ rest-frame into a linear superposition of the two possible helicity states in the ΛK_S rest-frame according to Eq. 5.18.

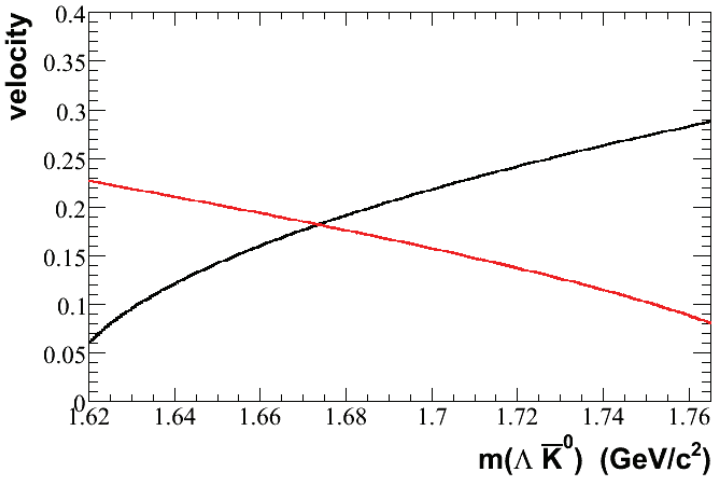

Figure 5.35: Representation of the behavior of β^* (red curve) and β (black curve) with ΛK_S mass (see text).

To illustrate what this implies for the analysis of $\Lambda_c^+ \rightarrow K^+ K_S \Lambda$ decay, con-

sider the particular case in which the final state particles are collinear in the Λ_c^+ rest-frame [i.e. $\cos\theta_\Lambda = \pm 1$ using the Dalitz plot variable].

For $\cos\theta_\Lambda = +1$

$$\mathbf{q}^* = \gamma^*(\mathbf{q} + \beta^* E) = \gamma^* E(\beta + \beta^*) \tag{5.19}$$

And for $\cos\theta_\Lambda = -1$

$$\mathbf{q}^* = \gamma^*(-\mathbf{q} + \beta^* E) = \gamma^* E(-\beta + \beta^*) \tag{5.20}$$

in an obvious notation.

If $\mathbf{q}^*$ and the Λ spin projection in the Λ_c^+ rest-frame are both in the $+z$ direction (Fig. 5.34), then the helicity in this frame is $+1/2$ for $\cos\theta_\Lambda = +1$ and for $\cos\theta_\Lambda = -1$. From Eq. 5.20, the latter requires $\beta^* > \beta$, i.e. low ΛK_S mass. The boost to the ΛK_S rest-frame reverses the direction of the Λ but not of its spin, so that for $\beta^* > \beta$ the Λ has helicity -1/2 in the ΛK_S frame. This behavior is represented correctly by Eq. 5.18; for $\cos\theta_\Lambda = +1$, $\omega = 0$ and the Λ helicity is unaltered by the transformation; for $\cos\theta_\Lambda = -1$, $\omega = \pi$ and the Λ helicity is flipped to -1/2. The ΛK_S mass value below which the helicity flips for $\cos\theta_\Lambda = -1$ can be read off from Fig. 5.35. The red curve represents the behavior of β^* with ΛK_S mass, and the black curve similarly represents β. For $m(\Lambda K_S) < 1.673$ GeV/c^2, $\beta^* > \beta$ and the Λ helicity will be flipped according to Eq. 5.18. For higher mass values, and for all masses at $\cos\theta_\Lambda = +1$, the Λ helicity will not change as a result of the boost. From Fig. 5.35, the velocity values involved for the present analysis are small. Clearly, the angle ω depends on the Dalitz plot position. The distribution of $\cos\omega$ for the efficiency-corrected Dalitz plot population is shown in Fig. 5.36, and the strong peaking at $\cos\omega \sim 1$ indicates that

Wigner rotation effects should be small. This can be seen more clearly in Fig. 5.37, where the distribution of cosω/2 values is shown in three regions of ΛK_S mass [Note that the y-axis scale is the same on each plot]. In appendix C, section C.3, it is asserted that small effects due to Wigner rotation will be absorbed in the effective parameters k and δ, whose values are treated as constants over the Dalitz plot. The rotation angle ω depends on position in the plot, and so it would be expected that the differential χ^2 distribution (Fig. 5.24) might show evidence of bias if this assertion were wrong. There is no such indication.

To investigate this further, the normalized residuals of Fig. 5.23 are plotted separately in Fig. 5.38 for the Dalitz plot regions indicated in the caption. Each distribution is consistent with a Gaussian centered at zero, and with unit r.m.s. deviation value, so that again there is no evidence of bias. On this basis, it is concluded that the treatment of Lorentz boost effects discussed in Appendix C is entirely consistent with the observed Dalitz plot distribution at the present statistical level.

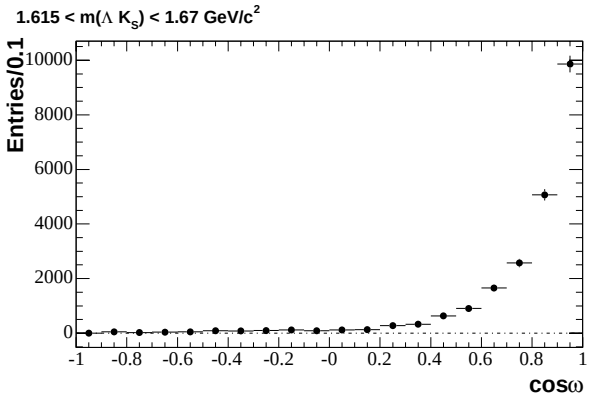

Figure 5.36: The Λ_c^+ mass-sideband-subtracted, efficiency-corrected cosω distribution in data, corresponding to the mass region $1.615 < m(\Lambda K_S) < 1.765$ GeV/c^2.

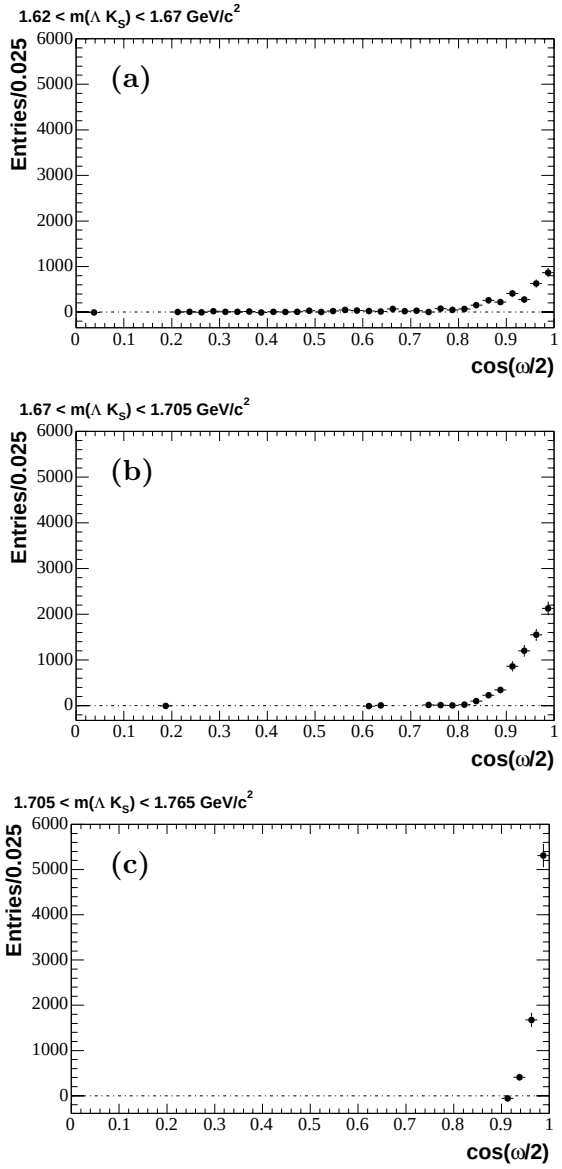

Figure 5.37: The Λ_c^+ mass-sideband-subtracted, efficiency-corrected $\cos(\omega/2)$ distribution in data, corresponding to the mass regions (a) $1.62 < m(\Lambda K_S) < 1.67$ GeV/c^2 (low mass region), (b) $1.67 < m(\Lambda K_S) < 1.705$ GeV/c^2 ($\Xi(1690)^0$ signal region), (c) $1.705 < m(\Lambda K_S) < 1.765$ GeV/c^2 (high mass region).

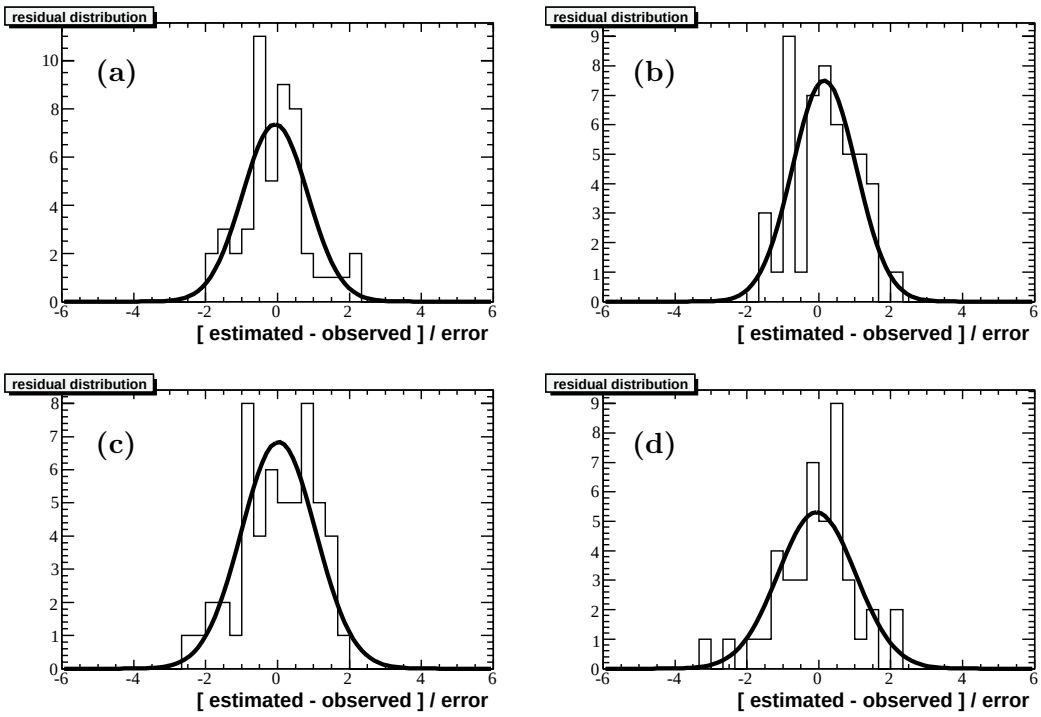

Figure 5.38: The normalized residual distribution $\Delta = \left[\frac{\mu_j^{combined} - N_j^{obs}}{\sqrt{\mu_j^{combined}}}\right]$, corresponding to (a) $1.625 < m(\Lambda K_S) < 1.7$ GeV/c^2 and $\cos\theta_\Lambda > 0.2$, (b) $m(\Lambda K_S) > 1.7$ GeV/c^2 and $\cos\theta_\Lambda > 0.2$, (c) $1.625 < m(\Lambda K_S) < 1.7$ GeV/c^2 and $\cos\theta_\Lambda < 0.2$. (d) $m(\Lambda K_S) > 1.7$ GeV/c^2 and $\cos\theta_\Lambda < 0.2$, Superimposed on each distribution is a single Gaussian function centered at zero with an r.m.s. deviation value of 1.0.

5.9 Conclusions

A simple isobar model treatment of the $K^+K_S\Lambda$ Dalitz plot has shown clear evidence for the existence of the decay modes $\Lambda_c^+ \to \Xi(1690)^0 K^+$ and $\Lambda_c^+ \to \Lambda a_0(980)^+$, the latter for the first time.

Information on the spin of the $\Xi(1690)^0$, and values of its mass and width parameters have been extracted from fits to the observed rectangular Dalitz plot using a model based on the coherent superposition of amplitudes describing the Λ_c^+ isobar decay modes.

For $\Xi(1690)$ spin 1/2, the fit is excellent (C.L.=56.4%), and the following mass and width parameter values have been obtained:

$$m(\Xi(1690)^0) = 1682.9 \pm 0.9\ (\text{stat.}) \pm 0.3\ (\text{syst.})\ \ \text{MeV/c}^2,$$

$$\Gamma(\Xi(1690)^0) = 9.3^{+2.0}_{-1.7}\ (\text{stat.}) \pm 0.4\ (\text{syst.})\ \ \text{MeV}.$$

For spin 3/2, the fit is poor (C.L.=1.9%) and there are systematic failures in the description of the resulting $\cos\theta_\Lambda$ and $m(\Lambda K_S)$ projections.

For spin 5/2, the fit is acceptable (C.L.=17.4%), but again there are systematic deviations from the observed $\Xi(1690)^0$ lineshape in the region of high mass, where interference with the $\Lambda a_0(980)^+$ amplitude seems important.

For spin 3/2 and 5/2, the fitted mass value is found to be higher by 2 MeV/c^2 than that for spin 1/2, and that for the width, 0.3-0.5 MeV lower. The mass shift is much larger than the systematic uncertainty estimated for the spin 1/2 hypothesis, but since spin 3/2 is clearly disfavored, and spin 5/2 also yields an inferior description of the data, this difference is not considered to provide a convincing measure of

systematic uncertainty.

CHAPTER 6
THE PROPERTIES OF THE $\Xi(1530)^0$ FROM $\Lambda_c^+ \to \Xi^-\pi^+K^+$ DECAY

The $\Xi(1530)$ is the only Cascade resonance whose properties are reasonably well understood. It decays $\sim 100\%$ to $\Xi\pi$ and $< 4\%$ to $\Xi\gamma$ [22], and its mass and width have been measured and are well known [22]. A spin-parity analysis of data produced in a bubble chamber by means of the reactions $K^-p \to \Xi(1530)^{0,-}K^{0,+}$ carried out by Schlein et *al.* [53] showed that $J^P = 3/2^+$ (i.e. P-wave) or $J^P = 5/2^-$ (i.e. D-wave) was favored, and that the data were consistent with $J \geq 3/2$; however, they state that spin $> 3/2$ is not required, and on this basis conclude that $J^P = 3/2^+$. Similar conclusions were drawn by Button-Schafer et *al.* [54] in their spin-parity analysis of $K^-p \to \Xi(1530)^{0,-}K^{0,+}$ and $K^-p \to \Xi(1530)^{0,-}K^{+,0}\pi^{0,+}$ events. Both experiments rule out $J = 1/2$ but their claim that $J > 3/2$ is not required is the basis for the conclusion that $J^P = 3/2^+$. The present analysis establishes spin 3/2 and hence establishes positive parity, based on the analyses of refces. [53, 54]. As in chapter 5, the Ω^- spin analysis procedures are extended to the context of Λ_c^+ quasi-two-body decay, in the present instance to the process $\Lambda_c^+ \to (\Xi^-\pi^+)K^+$, for which the $\Xi^-\pi^+$ invariant mass distribution exhibits a dominant $\Xi(1530)^0$ signal.

6.1 Two-body Invariant Mass Projections

The uncorrected $\Xi^-\pi^+$ invariant mass projections for the data sample selected as described in section 3.4 are shown in Fig. 6.1 (a). The distribution for $\Lambda_c^+ \to \Xi^-\pi^+K^+$ signal events corresponds to the black points, while the high and low

$\Xi^-\pi^+K^+$ mass-sidebands are shown in red and blue, respectively, where the Λ_c^+ signal and sideband regions used in this analysis are those indicated in Fig. 3.10. The uncorrected Λ_c^+ mass-sideband-subtracted $\Xi^-\pi^+$ invariant mass projection (Fig. 6.1 (b)) shows a strong signal due to the $\Xi(1530)^0$ resonance. The size of the peak clearly indicates that the decay $\Lambda_c^+ \to \Xi^-\pi^+K^+$ is dominated by $\Lambda_c^+ \to \Xi(1530)^0K^+$.

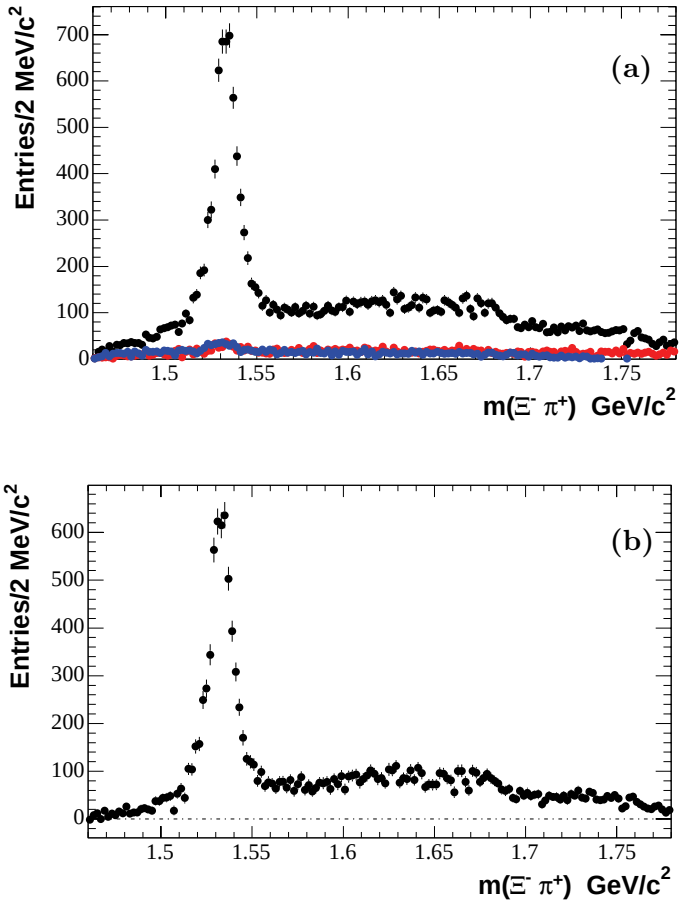

Figure 6.1: The uncorrected $\Xi^-\pi^+$ invariant mass projection in data. (a) The distribution for $\Lambda_c^+ \to \Xi^-\pi^+K^+$ signal events corresponds to the black points. The high and low $\Xi^-\pi^+K^+$ mass-sidebands are shown in red and blue, respectively. (b) The uncorrected Λ_c^+ mass-sideband subtracted $\Xi^-\pi^+$ invariant mass projection.

The uncorrected Λ_c^+ mass-sideband subtracted $\Xi^- K^+$ invariant mass projection shown in Fig. 6.2 (b) has a double-peak structure which is due to the reflection of the structure in the $\Xi(1530)^0$ region, as can be seen from Figs. 6.3 and 6.4(a) in the next section.

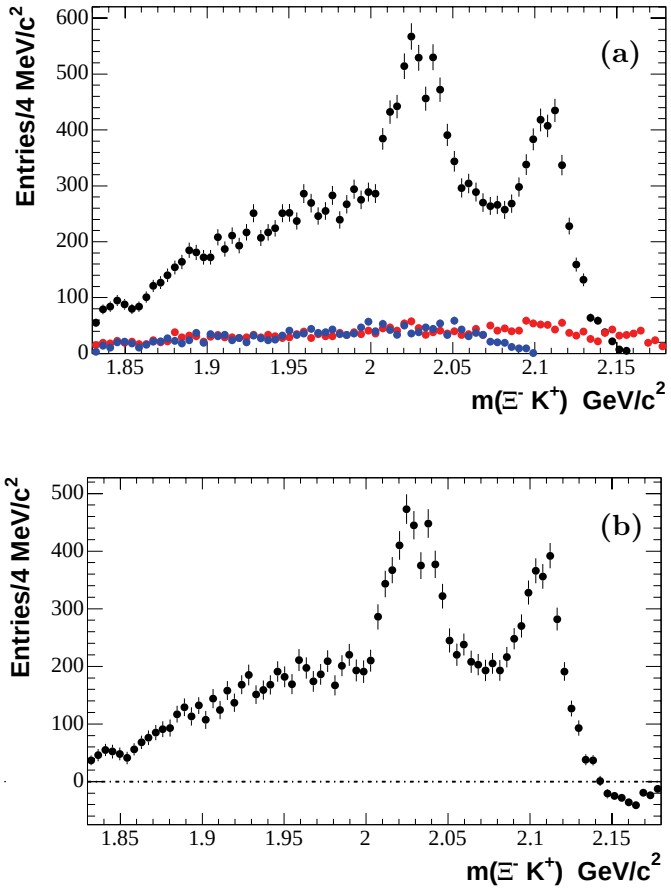

Figure 6.2: The uncorrected $\Xi^- K^+$ invariant mass projection in data. (a) The distribution for $\Lambda_c^+ \to \Xi^- \pi^+ K^+$ signal events corresponds to the black points. The high and low $\Xi^- \pi^+ K^+$ mass-sidebands are shown in red and blue, respectively. (b) The uncorrected Λ_c^+ mass-sideband subtracted $\Xi^- K^+$ invariant mass projection.

6.2 The Dalitz Plot for $\Lambda_c^+ \to \Xi^-\pi^+K^+$

The Dalitz plot (Fig. 6.3 (a)) shows evidence for only one resonant structure. A clear band can be seen at the nominal mass squared of the $\Xi(1530)^0$, indicating dominance of the contribution from $\Lambda_c^+ \to \Xi(1530)^0 K^+$, where $\Xi(1530)^0 \to \Xi^-\pi^+$ by strong decay.

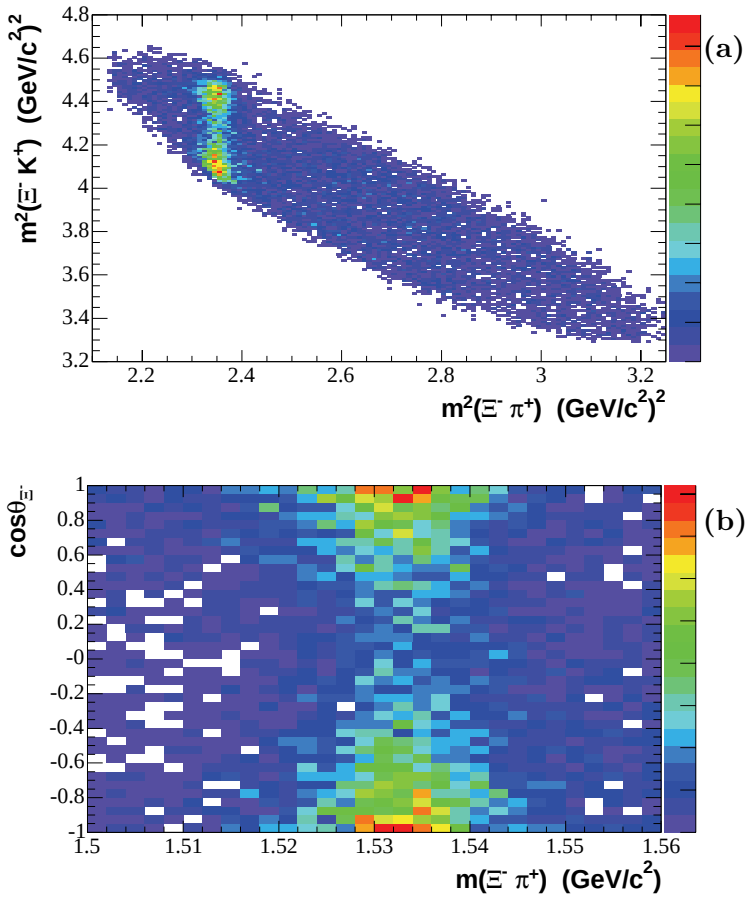

Figure 6.3: The Dalitz Plot for $\Lambda_c^+ \to \Xi^-\pi^+K^+$. (a) The Dalitz plot of the Ξ^-K^+ versus the $\Xi^-\pi^+$ invariant mass-squared distribution corresponding to the Λ_c^+ signal region. (b) The corresponding rectangular Dalitz plot for the $\Xi(1530)^0$ mass region.

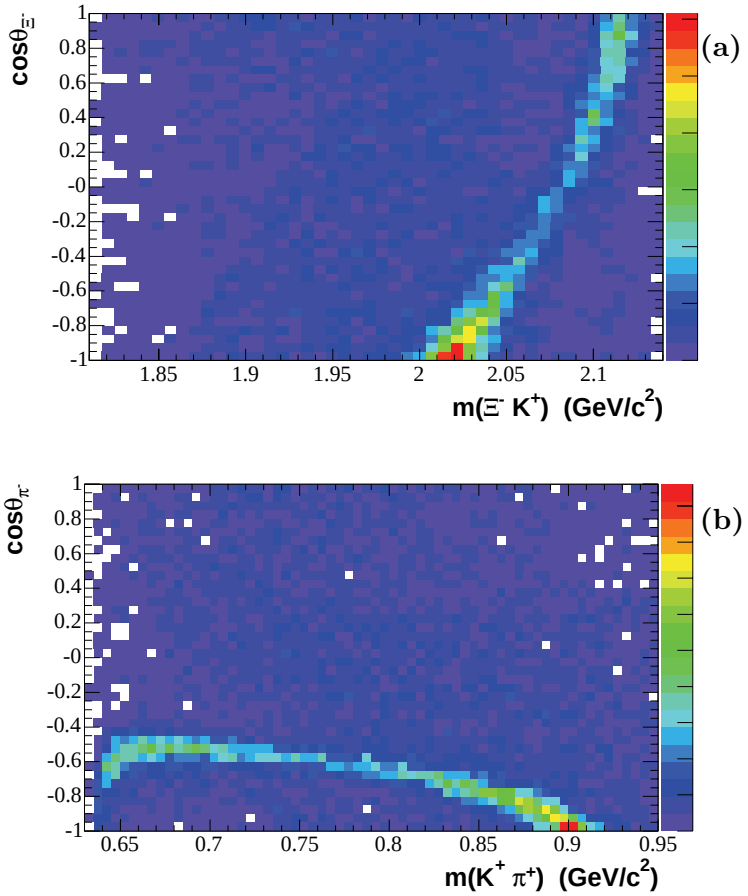

Figure 6.4: Rectangular Dalitz plots corresponding to the Λ_c^+ signal region. (a) The rectangular plot of Ξ^- helicity angle cosine versus $\Xi^- K^+$ invariant mass distribution. (b) The rectangular plot of π^- helicity angle cosine versus the $K^+\pi^+$ system invariant mass distribution.

Figures 6.3 (b) and 6.4 (a) show the rectangular plots of Ξ^- helicity angle cosine as a function of the invariant mass of the $\Xi^-\pi^+$ and $\Xi^- K^+$ systems, while Fig. 6.4 (b) is the corresponding plot of the π^- helicity angle cosine as a function of the invariant mass of the $\pi^+ K^+$ system. These scatter-plots correspond the the Λ_c^+ signal region.

Figure 6.5 shows Fig. 6.4 (a) with the maximum of the color scale set to

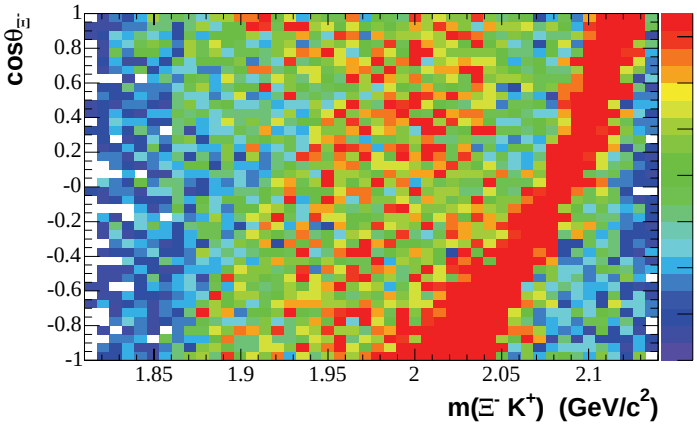

Figure 6.5: The rectangular plot of Ξ^- helicity angle cosine versus the Ξ^-K^+ system invariant mass distribution corresponding to the Λ_c^+ signal region (Fig. 6.4 (a)) with the maximum of the color scale set to 10 counts in order to enhance any structure in low-occupancy regions of the plot.

10 in order to enhance possible patterns in low occupancy regions by reducing the intensity scale. A resonant contribution in Ξ^-K^+ would be observed as a band at a particular mass on this plot. The absence of any such structure is consistent with the fact that the only resonant contribution to the Dalitz plot appears to be associated with the $\Xi^-\pi^+$ system (but see section 6.6). Fig. 6.4 (a) shows quite clearly that the peaks in $\Xi^-\pi^+$ invariant mass near 2.0 and 2.1 GeV/c^2 are associated with the regions cos$\theta_{\Xi^-} \sim \pm 1$ in the $\Xi(1530)^0$ region of Fig. 6.3 (b). Finally, as expected for an $I = 3/2$ system, the $K^+\pi^+$ invariant mass distribution shows no evidence of structure other than that resulting from reflection of the $\Xi(1530)$ region (Fig. 6.4 (b)).

6.3 $\Xi(1530)$ Spin Determination

It follows from the previous section that the decay $\Lambda_c^+ \to \Xi^-\pi^+K^+$ seems to proceed predominantly through the quasi-two-body decay $\Lambda_c^+ \to \Xi(1530)^0K^+$, and as such it is analogous to the decay $\Xi_c^0 \to \Omega^-K^+$ analyzed in chapter 4. For $\Xi(1530)^0$ spin J, and a corresponding definition of the helicity angle of the Ξ^- in the $\Xi^-\pi^+$ rest-frame, Eqs. 4.3, 4.4, and 4.5 describe the expected distributions in $\cos\theta_{\Xi^-}$ for J =1/2, 3/2, and 5/2, respectively. However, since $\Xi(1530)^0 \to \Xi^-\pi^+$ is a strong decay, parity is conserved, with the consequence that

$$\left|A^J_{1/2}\right| = \left|A^J_{-1/2}\right|,$$

in the notation of chapter 4, with the result that $\beta = 0$, i.e. the asymmetric terms in Eqs. 4.3-4.6 are absent in the case of $\Xi(1530)^0$ decay.

Following the event weighting procedure of section 4.5, spin information for the $\Xi(1530)$ is obtained using Legendre polynomial moments. After the efficiency-correction procedure described in Appendix D, the $\sqrt{10}P_2(\cos\theta_{\Xi^-})$ moment of the $\Xi^-\pi^+$ system invariant mass distribution for the Λ_c^+ signal region shown in Fig. 6.6 (a) indicates that spin 3/2 is clearly favored, as almost all of the $\Xi(1530)$ signal is retained, while the $7/\sqrt{2}P_4(\cos\theta_{\Xi^-})$ moment (Fig. 6.7 (a)) is consistent with being flat implying that spin 5/2 is completely ruled out.

As can be observed from Figs. 6.6 (b),(c) and 6.7 (b),(c), the corresponding Λ_c^+ mass-sideband distributions are consistent with zero and can therefore be ignored in the weighting procedure.

Figure 6.8 shows a comparison on the same y-axis scale of the $\sqrt{10}P_2(\cos\theta_{\Xi^-})$

and $7/\sqrt{2}P_4(\cos\theta_{\Xi^-})$ moments for the $\Xi^-\pi^+$ system invariant mass distribution corresponding to the Λ_c^+ signal region. As previously stated, the multiplicative coefficient is necessary in order to project the total number of signal events. As seen in Fig. 6.8 (a), the $\sqrt{10}P_2(\cos\theta_{\Xi^-})$ moment projects the $\Xi(1530)$ signal, whereas the $7/\sqrt{2}P_4(\cos\theta_{\Xi^-})$ moment has no structure whatsoever. The moments for $L > 4$ also show no structure, so that it can be concluded that the $\Xi(1530)^0$ does indeed have spin 3/2. This establishes positive parity, as discussed above, so that the $\Xi(1530)^0$ corresponds to a resonant P-wave amplitude in the $\Xi^-\pi^+$ system.

If the Dalitz plot were dominated solely by the resonant channel $\Lambda_c^+ \rightarrow \Xi(1530)^0 K^+$, then the $\sqrt{10}P_2(\cos\theta_{\Xi^-})$ moment would project the entire $\Xi(1530)$ signal extracted by sideband subtraction from Fig. 6.9. Fig. 6.10 shows the difference between the $\sqrt{2}P_0(\cos\theta_{\Xi^-})$ and $\sqrt{10}P_2(\cos\theta_{\Xi^-})$ moments after mass-sideband-subtraction (since the Λ_c^+ mass-sidebands of the $\sqrt{2}P_0(\cos\theta_{\Xi^-})$ have structure) and efficiency-correction.

Instead of the expected smooth behavior, the distribution of Fig. 6.10 shows a dip in the vicinity of the $\Xi(1530)$ mass; this extends even to negative intensity values, which indicates that the $\sqrt{10}P_2(\cos\theta_{\Xi^-})$ projection of $\Xi(1530)$ events generates an overestimate of the signal by ∼15-20%. This challenges the assumption that a single wave may be used to characterize the $\Xi^-\pi^+$ system, and suggests the presence of other amplitudes contributing to the $\Xi(1530)$ region of the Dalitz plot.

Further evidence of results from an examination of the $\cos\theta_{\Xi^-}$ distribution corresponding to the $\Xi(1530)^0$ signal region. The Λ_c^+ mass-sideband-subtracted $\cos\theta_{\Xi^-}$

distribution corresponding to the $\Xi(1530)^0$ signal region (Fig. 6.11) exhibits an obvious quadratic behavior, clearly indicating that the spin of the $\Xi(1530)$ is not 1/2. The function $\alpha\,(1+3\cos^2\theta)$ corresponding to $J=3/2$ for the $\Xi(1530)^0$ fits the data best, although the deviations of the data from the curve are obvious, and the fit C.L. is only 0.0003 (Table 6.1). The fit with the parametrization corresponding to $J=5/2$ is extremely poor, with C.L. 6×10^{-44} (Table 6.1), as would be expected from the projection of Fig. 6.8 (b). In addition, the distribution of Fig. 6.11 exhibits clear signs of forward-backward asymmetry.

The above symptoms suggest that a description of the $\Xi(1530)^0$ region in terms of a single $\Xi^-\pi^+$ amplitude corresponding to a resonant structure is something of an over-simplification. Small additional $\Xi^-\pi^+$ amplitudes need to be incorporated if a quantitative understanding is to be achieved, since their contributions may be amplified through interference with the large Breit-Wigner (BW) amplitude describing the $\Xi(1530)$. A first attempt at a more general amplitude representation is described in the following sections of this chapter.

Table 6.1: The fit probabilities corresponding to $\Xi(1530)$ spin hypotheses 3/2 and 5/2, assuming $J_{\Lambda_c}=1/2$.

$J_{\Xi(1530)}$	Fit χ^2/NDF	Fit probability	Comment
3/2	47.7/19	0.0003	Fig. 6.11, solid curve
5/2	258.3/19	6×10^{-44}	Fig. 6.11, dashed curve

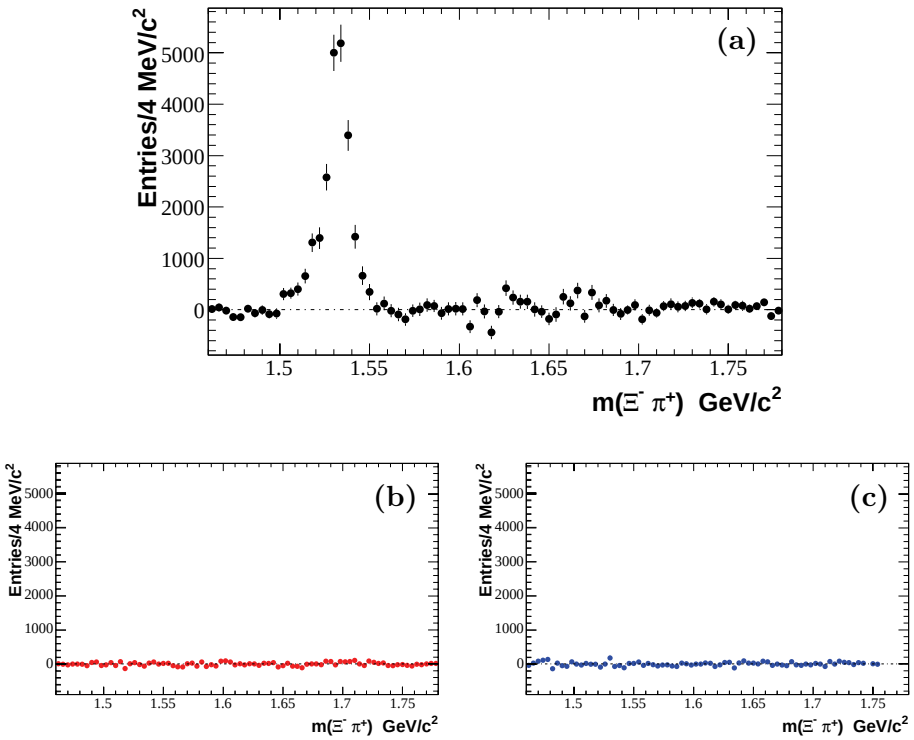

Figure 6.6: The efficiency-corrected $\sqrt{10}P_2(\cos\theta_{\Xi^-})$ moments of the $\Xi^-\pi^+$ system invariant mass distribution corresponding to (a) the Λ_c^+ signal region, (b) and (c) the high and low Λ_c^+ mass-sideband regions, respectively.

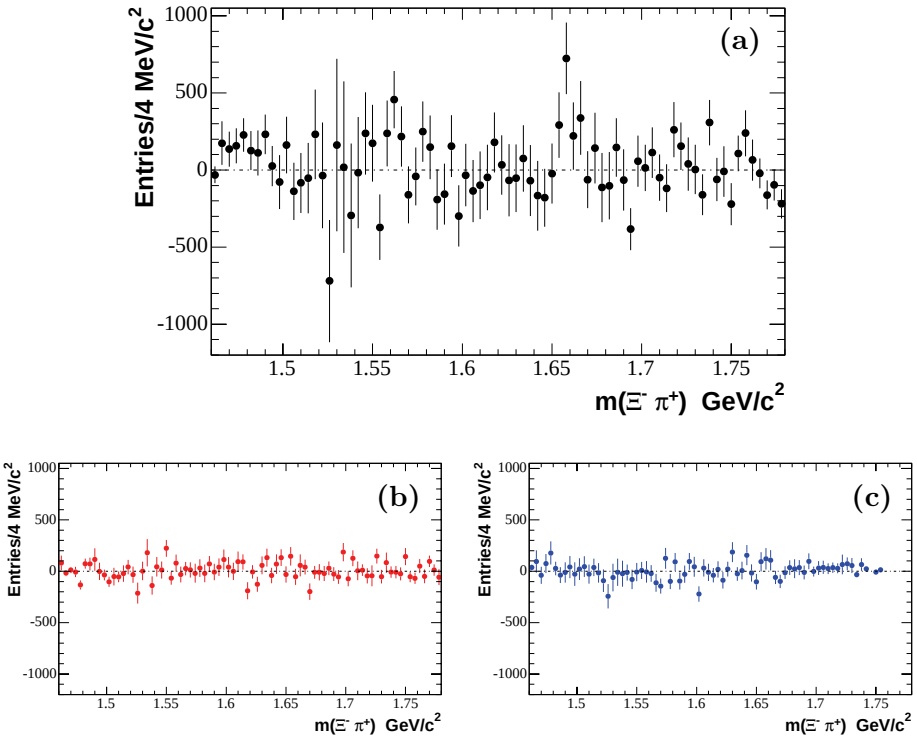

Figure 6.7: The efficiency-corrected $7/\sqrt{2}P_4(\cos\theta_{\Xi^-})$ moments of the $\Xi^-\pi^+$ system invariant mass distribution corresponding to (a) the Λ_c^+ signal region, (b) and (c) the high and low Λ_c^+ mass-sideband regions, respectively.

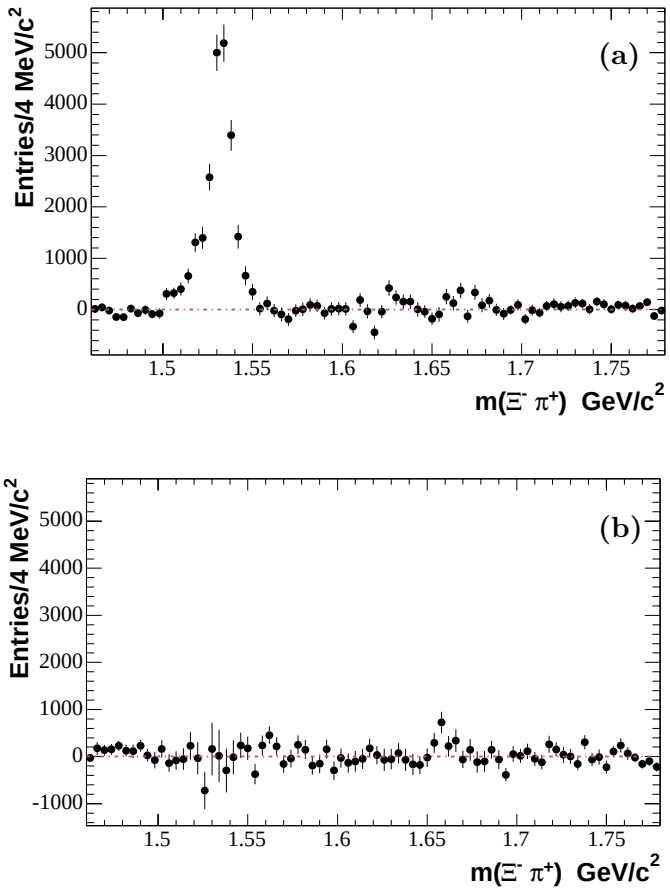

Figure 6.8: The efficiency-corrected moments of the $\Xi^-\pi^+$ system invariant mass distribution corresponding to the Λ_c^+ signal region: (a) $\sqrt{10}P_2(\cos\theta_{\Xi^-})$ and (b) $7/\sqrt{2}P_4(\cos\theta_{\Xi^-})$.

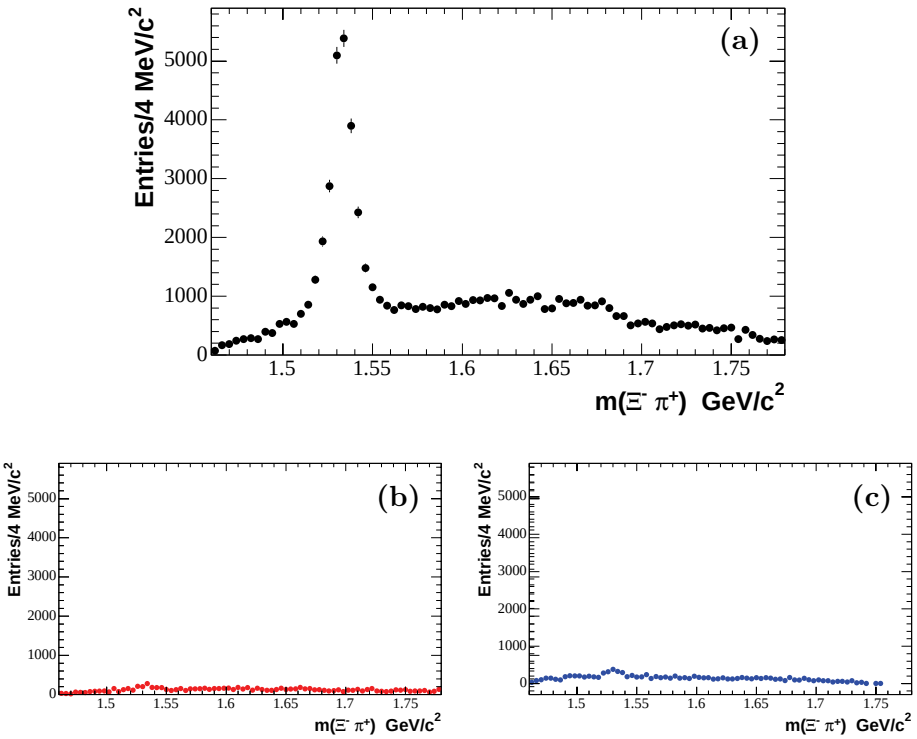

Figure 6.9: The efficiency-corrected $\sqrt{2}P_0(\cos\theta_{\Xi^-})$ moments of the $\Xi^-\pi^+$ system invariant mass distribution corresponding to (a) the Λ_c^+ signal region, (b) and (c) the high and low Λ_c^+ mass-sideband regions, respectively.

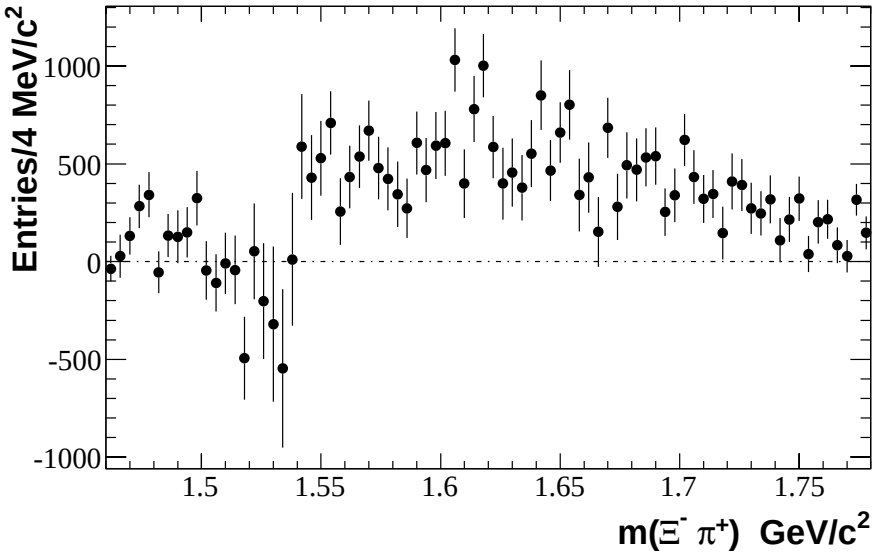

Figure 6.10: The Λ_c^+ mass-sideband-subtracted $\sqrt{2}P_0(\cos\theta_{\Xi^-}) - \sqrt{10}\mathrm{P}_2(\cos\theta_{\Xi^-})$ moment of the $\Xi^-\pi^+$ system invariant mass distribution, after efficiency-correction.

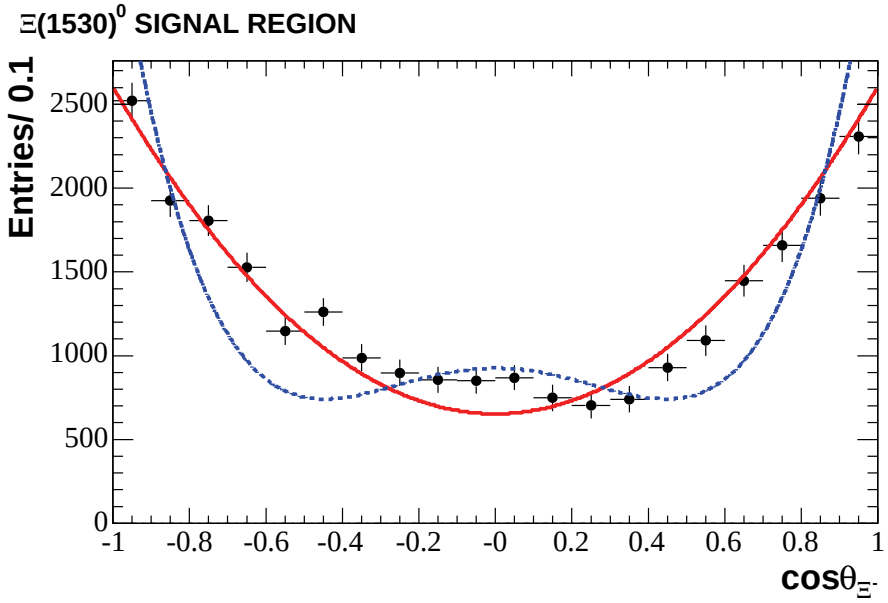

Figure 6.11: The efficiency-corrected $\cos\theta_{\Xi^-}$ distribution for $\Lambda_c^+ \to \Xi^-\pi^+K^+$ data. The black dots correspond to the $\Xi(1530)^0 \to \Xi^-\pi^+$ mass signal region. The red (blue) curve corresponds to the parametrization of the $\Xi(1530)$ angular distribution for the assumption of *pure* spin 3/2 (5/2).

6.4 Legendre Polynomial Moment Analysis

6.4.1 Evidence for $\Xi(1530)$ Phase Motion

Strong interactions in the $(\Xi^-\pi^+)$ system may give rise to interference between the resonant P-wave $\Xi(1530)$ amplitude and other $(\Xi^-\pi^+)$ amplitudes. Evidence for interference is seen in the behavior of the $P_1(\cos\theta_{\Xi^-})$ moment of the $\Xi^-\pi^+$ system as a function of invariant mass. The distribution shown in Fig. 6.12 is consistent with the interference pattern resulting from the rapid oscillation due to $\Xi(1530)$ P-wave Breit-Wigner (BW) phase motion in the presence of an amplitude with slowly varying phase.

The oscillatory pattern seen in Fig. 6.12 (a) corresponding to the Λ_c^+ signal region distribution is not observed in the spectra corresponding to the high and low Λ_c^+ mass-sideband regions (Fig. 6.12 (b),(c)), which demonstrates clearly that the pattern observed is indeed due to $\Xi(1530)$ phase-motion in events produced from signal Λ_c^+ candidates and not simply an artifact of combinatorial background.

The $P_1(\cos\theta_{\Xi^-})$ moment for $m(\Xi^-\pi^+) < 1.58$ GeV/c^2 behaves very much like the real part of the $\Xi(1530)$ BW amplitude (see Fig. 6.13 (b)), which suggests that the phase of the amplitude yielding the interference effect is close to zero. The proximity of the $\Xi^-\pi^+$ threshold, and the fact that the interference is seen in the $P_1(\cos\theta_{\Xi^-})$ moment suggest very strongly that the effect is due primarily to an S-wave $\Xi^-\pi^+$ amplitude (see Eq. 6.2 below).

6.4.2 Interpretation of the Observed $\Xi(1530)$

Phase Motion

Based on the discussion of section 6.4.1, a simple model incorporating only S- and P- wave $\Xi^-\pi^+$ amplitudes is considered, and the following intensity distribution is obtained (see Appendix E):

$$I(\cos\theta) = \frac{\left|\mathrm{S}^{1/2}\right|^2 + \left|\mathrm{P}^{1/2}\right|^2}{2} + \left|\mathrm{P}^{3/2}\right|^2 \left(\frac{3\cos^2\theta + 1}{4}\right) + \mathrm{Re}\left(\mathrm{S}^{1/2}\mathrm{P}^{3/2\,*}\right)\sqrt{2}\cos\theta \qquad (6.1)$$
$$- \left(\rho_{1/2\,1/2} - \rho_{-1/2\,-1/2}\right)\left[Re\left(S^{1/2}P^{1/2\,*}\right)\cos\theta + \mathrm{Re}\left(\mathrm{P}^{1/2}\mathrm{P}^{3/2\,*}\right)\left(\frac{3\cos^2\theta - 1}{\sqrt{2}}\right)\right],$$

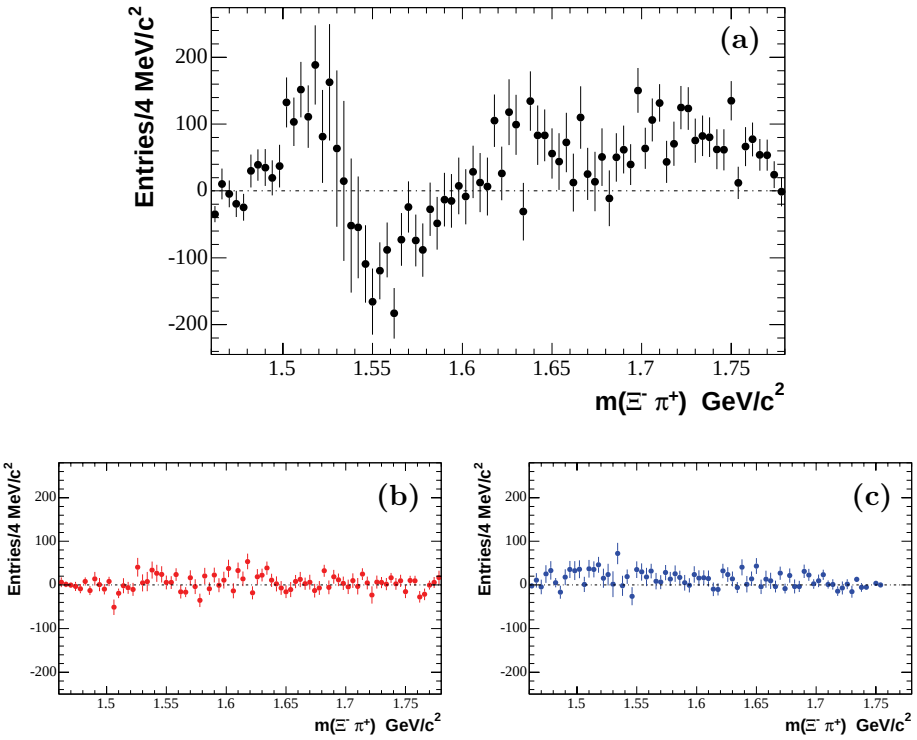

Figure 6.12: The efficiency-corrected $P_1(\cos\theta_{\Xi^-})$ moments of the $\Xi^-\pi^+$ system invariant mass distribution corresponding to (a) the Λ_c^+ signal region, (b) and (c) the high and low Λ_c^+ mass-sideband regions, respectively.

where $\theta = \theta_{\Xi^-}$ for convenience. If, it is assumed that the density matrix elements are equal,

$$\begin{aligned} I(\cos\theta) &= \left[\left|S^{1/2}\right|^2 + \left|P^{1/2}\right|^2 + \left|P^{3/2}\right|^2\right] \frac{1}{\sqrt{2}} P_0(\cos\theta) \\ &+ \left|P^{3/2}\right|^2 \frac{1}{\sqrt{10}} P_2(\cos\theta) \\ &+ Re\left(S^{1/2} P^{3/2\,*}\right) \sqrt{\frac{2}{3}} P_1(\cos\theta), \end{aligned} \tag{6.2}$$

so that the presence of a $P_1(\cos\theta)$ term results from interference between the $S^{1/2}$ and $P^{3/2}$ amplitudes. The orthogonality of the Legendre polynomial functions implies

$$I = \frac{dN}{d\cos\theta} = \langle P_0 \rangle P_0(\cos\theta) + ... + \langle \mathrm{P_2} \rangle \mathrm{P_2}(\cos\theta)$$

where,

$$\langle P_i \rangle = \int_{-1}^{1} P_i(\cos\theta) \mathrm{dN/d\cos\theta d\cos\theta} \sim \sum_j P_i(\cos\theta_\mathrm{j})$$

are the background (i.e. Λ_c^+ mass-sidebands)-subtracted, efficiency-corrected Legendre polynomial averages, and the summation is over the events in the mass interval considered.

It follows that the relationship between the Legendre polynomial moments and the underlying $\Xi^-\pi^+$ amplitudes is given by the system of equations:

$$\langle P_0 \rangle = \frac{1}{\sqrt{2}} \left(\left|S^{1/2}\right|^2 + \left|P^{1/2}\right|^2 + \left|P^{3/2}\right|^2\right) \tag{6.3}$$

$$\langle P_1 \rangle = \sqrt{\frac{2}{3}} Re\left(S^{1/2} P^{3/2\,*}\right) \tag{6.4}$$

$$\langle P_2 \rangle = \frac{1}{\sqrt{10}} \left|P^{3/2}\right|^2. \tag{6.5}$$

In this simple model, Eq. 6.4 demonstrates explicitly that the structure in the $P_1(\cos\theta)$ moment results from interference between the $S^{1/2}$ amplitude and the

dominant $P^{3/2}$ amplitude. This qualitatively describes the observed behavior in the vicinity of the $\Xi(1530)^0$ resonance, where the $P^{3/2}$ amplitude is undergoing a rapid BW phase motion, provided the phase of the $S^{1/2}$ amplitude is moving slowly.

If this amplitude behavior continued to higher $\Xi^-\pi^+$ mass, the $P_1(\cos\theta)$ moment would asymptotically approach zero from negative values as the $\Xi(1530)^0$ phase approached π. Instead, the $P_1(\cos\theta)$ moment passes through zero at $m(\Xi^-\pi^+) \sim 1.6$ GeV/c^2, and remains positive thereafter. This indicates that the $S^{1/2}$ phase is increasing substantially with increasing mass, reaching $\sim 90^\circ$ at ~ 1.6 GeV/c^2 (hence $Re\left(S^{1/2}P^{3/2\,*}\right) \sim 0$), and continues to increase beyond this point, hence the positive values of the $P_1(\cos\theta)$ moment (i.e. the $S^{1/2}$ phase is "catching up" on the $P^{3/2}$ phase). At the same time the $S^{1/2}$ amplitude must be increasing in magnitude in order to yield a significant $P_1(\cos\theta)$ moment, since $\left|P^{3/2}\right|^2$ is consistent with zero for mass values greater than ~ 1.56 GeV/c^2 (Fig. 6.8 (a) and Eq. 6.5). This suggests that the broad, non-$\Xi(1530)^0$ component of the $\Xi^-\pi^+$ invariant mass distribution of Fig. 6.9 (a) results primarily from the $\left|S^{1/2}\right|^2$ contribution to Eq. 6.3, although here it must be assumed that the $\left|P^{1/2}\right|^2$ makes no large contribution to the intensity. The latter assumption cannot be tested in the context of the model, since the three equations, Eqs.6.3-6.5, are insufficient to define the four unknowns involved ($\left|S^{1/2}\right|^2$, $\left|P^{1/2}\right|^2$, $\left|P^{3/2}\right|^2$, and the cosine of the $S^{1/2} - P^{3/2}$ relative phase angle).

In this model of an increasingly significant $S^{1/2}$ amplitude at higher $\Xi^-\pi^+$ mass, the detailed behavior of the intensity distribution in the vicinity if the $\Xi(1690)^0$ is of interest. This is shown in Fig. 6.13 (a), where the lower plot provides a closer

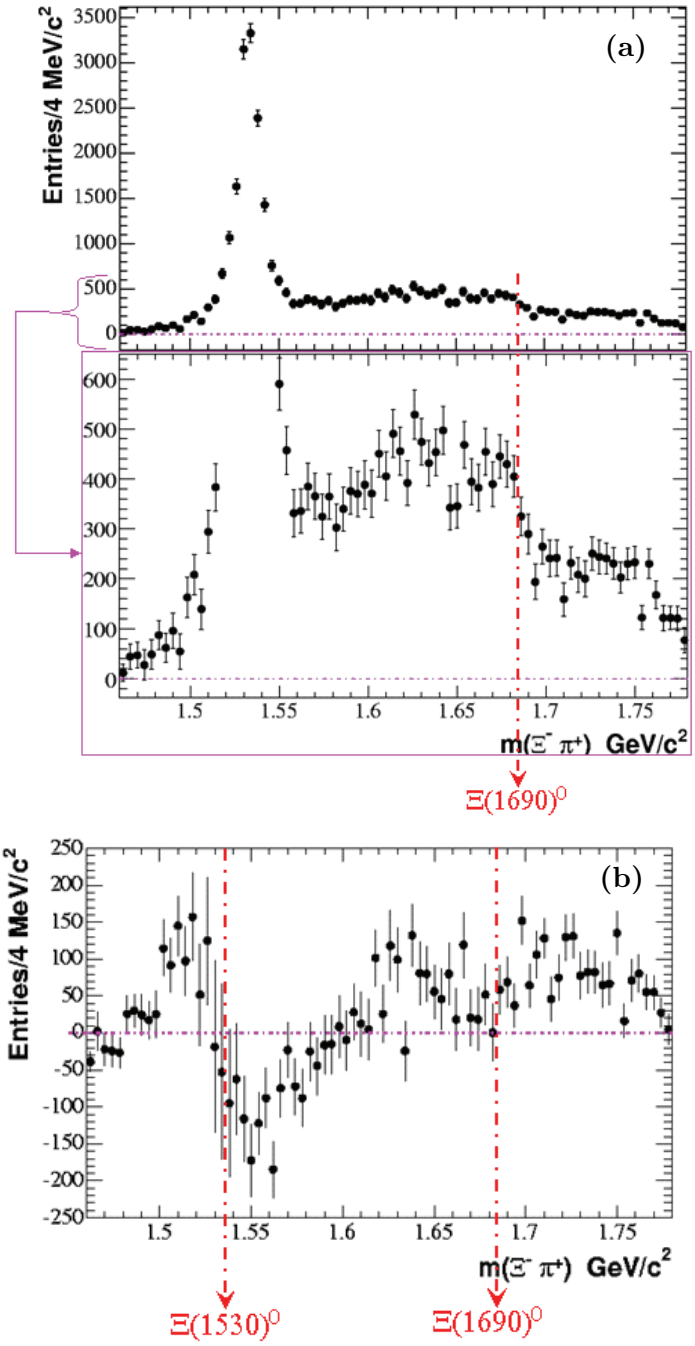

Figure 6.13: The efficiency-corrected Λ_c^+ mass-sideband-subtracted moments of the $\Xi^-\pi^+$ system invariant mass distribution corresponding to the Λ_c^+ signal region, with the nominal $\Xi(1530)^0$ and $\Xi(1690)^0$ mass values indicated by the red dot-dashed vertical lines: (a) $P_0(\cos\theta_{\Xi^-})$ and (b) $P_1(\cos\theta_{\Xi^-})$.

look at the high mass region. There is a sharp decrease in intensity by a factor of ~ 2 just at the $\Xi(1690)^0$ mass position. A hyperon beam experiment at CERN [45] has in fact observed a small $\Xi(1690)^0$ signal in the inclusive $\Xi^-\pi^+$ invariant mass distribution; this is accompanied by a much larger $\Xi(1530)^0$ signal (Fig. 6.14). The ratio of production cross sections (with decay to $\Xi^-\pi^+$) is $\sim 2\%$, so that in the present analysis it is reasonable to expect a small $\Xi(1690)^0$ contribution to the $\Xi^-\pi^+$ invariant mass distribution in the presence of a large $\Xi(1530)^0$ signal. It might be expected that such a contribution would appear as a peak rather than a dip. However,

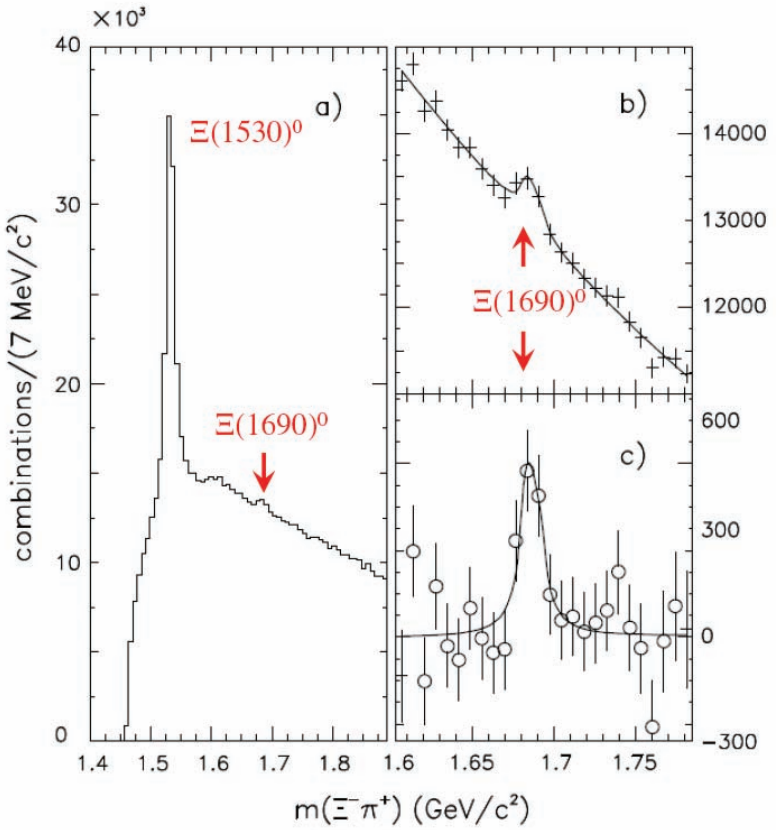

Figure 6.14: Evidence for the decay $\Xi(1690)^0 \rightarrow \Xi^-\pi+$ obtained in the inclusive $\Xi^-\pi^+$ invariant mass distribution from a hyperon beam experiment at CERN [45].

the presence of a dip leads to an intriguing possibility as to the parity of the $\Xi(1690)^0$. If, as discussed above, the non-$\Xi(1530)^0$ part of the $\Xi^-\pi^+$ invariant mass distribution results from a slowly-increasing $S^{1/2}$ amplitude whose phase passes through 90° at $\sim$ 1.6 GeV/c^2, then the subsequent coherent addition of an $S^{1/2}$ $\Xi(1690)$ resonant amplitude can yield the observed dip structure. This is illustrated schematically by the Argand diagram cartoon in Fig. 6.15. The steady counter-clockwise rotation of the $S^{1/2}$ wave vector would result in small amplitude and phase values in the $\Xi(1530)^0$ region, and the region near the top of the circle would correspond to $m(\Xi^-\pi^+) \sim 1.6$ GeV/c^2 since the relative $S^{1/2} - P^{3/2}$ phase would then be $\sim$ 90°, i.e. such that $Re\left(S^{1/2}P^{3/2*}\right) \sim 0$ as observed (Fig. 6.12 (a)).

The coherent addition of a narrow inelastic BW amplitude, represented by the circle, would cause the magnitude of the net $S^{1/2}$ amplitude to be reduced, and thus generate the observed dip in the intensity distribution. The mass dependence of

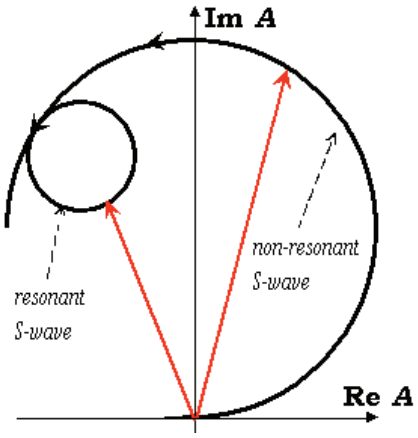

Figure 6.15: Cartoon of an Argand diagram illustrating a possible cause for the dip in the $\Xi^-\pi^+$ invariant mass distribution due to the presence of the $\Xi(1690)^0 \to \Xi^-\pi^+$.

the $P_1(\cos\theta)$ moment shown in Fig. 6.13 (b), and that of the non-$\Xi(1530)$ intensity distribution of Fig. 6.13 (a) show striking similarities to the corresponding behavior observed in the analysis of the $K^-\pi^+$ elastic scattering from the LASS spectrometer experiment at SLAC [55]. This is illustrated by means of Fig. 6.16 and 6.17 [56]. In Fig. 6.16, the quantity plotted is proportional to the interference between the $I = 1/2$ $K^-\pi^+$ S- and P- wave amplitudes resulting from the LASS analysis. As such it exactly parallels Eq. 6.4 and the $P_1(\cos\theta)$ moment of Fig. 6.13 (b). For the latter, the oscillation in the $\Xi(1530)$ region is very similar to that in the $K^*(892)$ resonance region of Fig. 6.16, and the subsequent mass dependence up to $\sim$ 1.63 GeV/c^2 behaves just like that obtained for $K^-\pi^+$ up to $m(K^-\pi^+) \sim 1.3$ GeV/c^2. The $K^-\pi^+$ S-wave amplitude and phase results from LASS are shown in Figs. 6.17 (a)

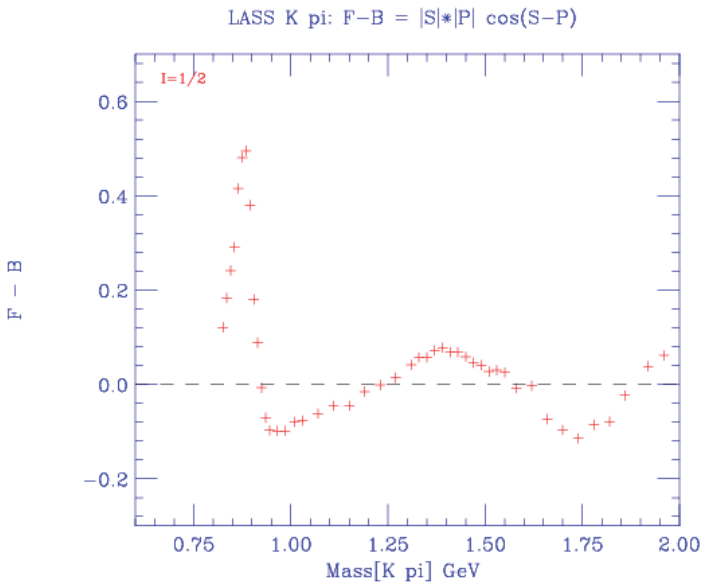

Figure 6.16: The $K^-\pi^+$ mass dependence of the forward-backward asymmetry resulting from the $I = 1/2$ $S - P$ wave interference obtained using the results from the LASS analysis of $K^-\pi^+$ elastic scattering [55].

and (b), respectively. To a very good approximation, the S-wave amplitude is purely elastic up to $K\eta'(958)$ threshold, and the fitted curves shown satisfy this behavior. There is a slow but steady increase in amplitude and phase up to $m(\Xi^-\pi^+) \sim 1.3$

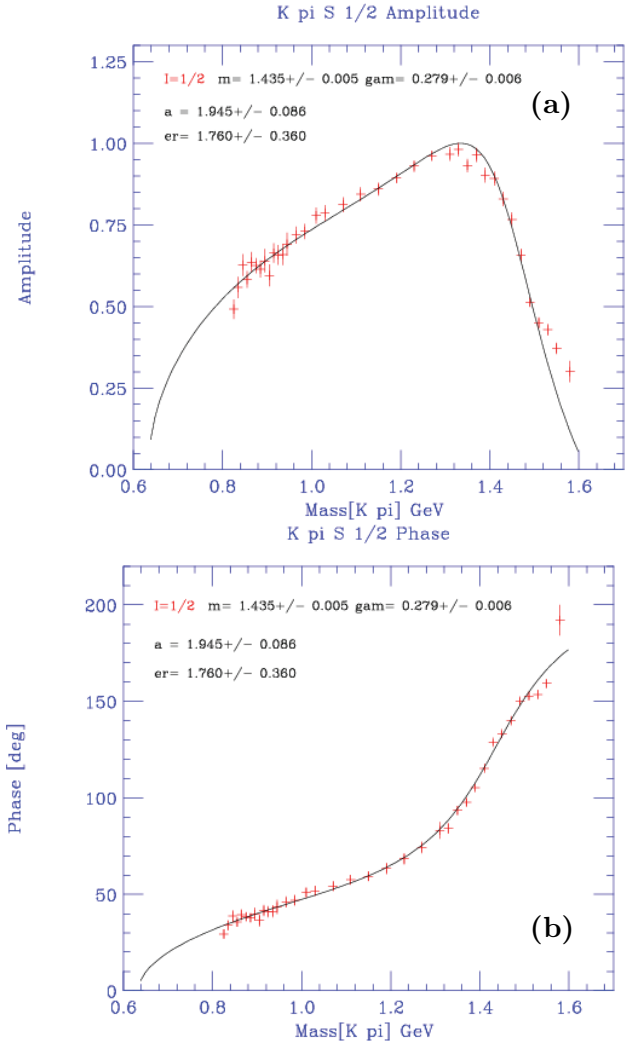

Figure 6.17: The $K^-\pi^+$ mass dependence of the forward-backward asymmetry resulting from the $I = 1/2$ S-wave $K^-\pi^+$ (a) scattering amplitude, and (b) phase, from the LASS experiment [55]; the curves result from a fit to the coherent superposition of elastic effective range and $K_0^*(1430)$ BW resonance amplitudes.

GeV/c^2, which is represented by an effective range parametrization[1].

At this point the phase relative to the P-wave is $\sim 90°$, so that the interference term plotted in Fig. 6.16 passes through 0 and the amplitude is near the top of the associated Argand diagram. A similar interpretation of the observed $\Xi^-\pi^+$ behavior below ~ 1.63 GeV/c^2 leads to a representation of the $S^{1/2}$ amplitude in this region by the large circle in Fig. 6.15. The rapid increase in $K^-\pi^+$ S-wave phase thereafter is due to the coherent addition of an elastic BW amplitude representing the $K_0^*(1430)$ resonance. Since the net $K^-\pi^+$ S-wave amplitude was at the top of the Argand plot, the onset of resonance causes the net amplitude to decrease rapidly, as shown in Fig. 6.16 (a), so that the resonance reveals itself via a rapid decrease in intensity rather than the normal BW peak. This known behavior of the $K^-\pi^+$ system prompts the suggestion that the dip in the $\Xi^-\pi^+$ mass distribution in the $\Xi(1690)$ region may be of similar origin. If so, the effect should be less dramatic, because the $\Xi(1690)$

[1]The following expression for the scattering S-wave amplitude was originally due to Bethe:

$$f(q) = \frac{1}{-a^{-1} + \frac{1}{2}r_0 q^2 - iq}\,,$$

where a is the scattering length, and r_0 the effective range. From

$$f(q) = \frac{e^{i\delta} sin\delta}{q} = \frac{1}{qcot\delta - iq}\,,$$

the phase shift formula

$$qcot\delta = -\frac{1}{a} + \frac{1}{2}r_0 q^2$$

is obtained. Applying the Optical Theorem on the effective range parametrization yields the total cross section expression $\sigma_t = 4\pi a^2$, at threshold, as expected from the Black Disk approximation.

resonance is inelastic, hence the schematic representation of its BW amplitude by a small circle in the cartoon of Fig. 6.15.

If the dip observed in Fig. 6.13 (a) does in fact result from the coherent addition of a $\Xi(1690)^0$ resonant amplitude to a slowly-varying $S^{1/2}$ $\Xi^-\pi^+$ amplitude, it may be inferred that the $\Xi(1690)$ has negative parity, and in addition that the conclusion of chapter 5 to the effect that the spin of the $\Xi(1690)$ is 1/2 is correct.

The behavior of the $P_1(\cos\theta)$ moment for $m(\Xi^-\pi^+)$ above ~ 1.63 GeV/c^2 is rather puzzling in light of the interpretation of the dip in the mass spectrum at ~ 1.68 GeV/c^2. The cartoon of Fig. 6.15 would indicate that the net $S^{1/2}$ amplitude and phase should not change dramatically in this region, and yet the moment seems to decrease almost to zero near the $\Xi(1690)$, before increasing again at higher mass. It does not seem possible to explain such behavior in a model requiring only $S^{1/2}$ and $P^{3/2}$ amplitudes. However, in section 6.5 where the inclusion of D-wave amplitudes is discussed, a correction to the $P_1(\cos\theta)$ moment which removes a $P-D$ interference contribution results in a moment contribution from $S^{1/2} - P^{3/2}$ interference which behaves smoothly with mass (Fig. 6.20), so that the problem is resolved.

6.4.3 Amplitude Analysis Assuming S and P Waves

It was pointed out in section 6.4.2 that Eqs. 6.3-6.5 cannot be solved in general. Nevertheless, Eq. 6.4 does provide a direct measure of $S^{1/2} - P^{3/2}$ interference, and similarly, Eq. 6.5 measures $\left|P^{3/2}\right|^2$. Substituting the latter into Eq. 6.3 then measures $\left|S^{1/2}\right|^2 + \left|P^{1/2}\right|^2$. The results obtained by following such a pro-

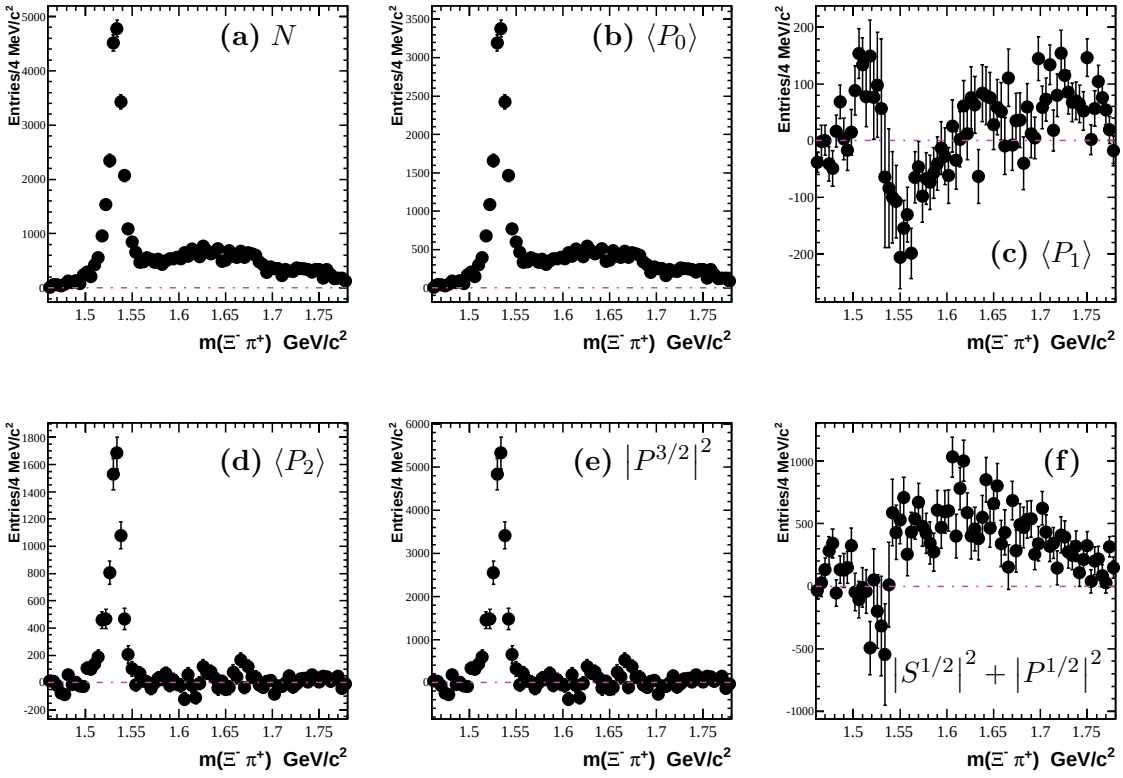

Figure 6.18: The results of an amplitude analysis assuming S and P waves. (a)-(d) The efficiency-corrected Λ_c^+ mass-sideband-subtracted $\Xi^-\pi^+$ mass spectrum and moment distributions; (e) the efficiency-corrected mass-sideband subtracted magnitude squared of the $P^{3/2}$-wave; (f) the corresponding $\left|S^{1/2}\right|^2 + \left|P^{1/2}\right|^2$ distribution.

cedure are summarized in Fig. 6.16. The mass spectrum is shown in Fig. 6.18 (a), while the moment distributions corresponding to Eqs. 6.3, 6.4 and 6.5 are shown in Figs. 6.18 (b),(c) and (d), respectively. The resulting behavior of the $P^{3/2}$ intensity is shown in Fig. 6.18 (e), and that for the sum $\left|S^{1/2}\right|^2 + \left|P^{1/2}\right|^2$ is in Fig. 6.18 (f). The latter distribution would be expected to behave smoothly with mass in the $\Xi(1530)^0$ region. Not only is this not the case, but the observed dip extends to negative (i.e. unphysical) intensity values. This is the same behavior discussed previously regarding

Fig. 6.10, and demonstrates quite explicitly that a simple $S-P$ wave model cannot describe the data in the $\Xi(1530)^0$ region. As a consequence, any attempt at extracting quantitative information concerning $S^{1/2}-P^{3/2}$ relative phase behavior in this region is pointless.

6.5 Legendre Polynomial Moment Analysis Incorporating *D* Wave

The results of the previous sections suggest that $\Xi^-\pi^+$ amplitudes of orbital angular momentum beyond P-wave are necessary to a description of the observed moments. In turn, this would imply the existence of structure in at least one $P_L(\cos\theta)$ moment with $L > 2$.

The formalism is therefore extended to include D-wave amplitude contributions, and this is described in detail in Appendix E. The presence of a $D^{5/2}$ amplitude might reveal itself through a $P_3(\cos\theta)$ moment resulting from $P^{3/2}-D^{5/2}$ interference, or even through a $P_4(\cos\theta)$ moment if its intensity is sufficiently strong. The mass dependence of the $P_3(\cos\theta)$ moment is shown in Fig. 6.19, and, within the statistical uncertainties, it seems to be systematically positive in the $\Xi(1530)^0$ region and negative between 1.6 and 1.7 GeV/c^2. However, the $P_4(\cos\theta)$ moment, shown earlier in Fig. 6.7, shows no clear systematic deviations from zero, indicating that any $D^{5/2}$ amplitude must be quite small.

The $P_i(\cos\theta)$ moment ($i = 5, ..., 9$) mass dependences show no clear systematic deviations from zero, indicating that amplitudes beyond D-wave are absent.

Assuming S, P, and D wave contributions to the $\Xi^-\pi^+$ system, the following intensity distribution is calculated (Appendix E):

$$
\begin{aligned}
I \;=\; & \frac{\left|S^{1/2}\right|^2 + \left|P^{1/2}\right|^2}{2} + \left[\left|P^{3/2}\right|^2 + \left|D^{3/2}\right|^2\right]\left(\frac{3\cos^2\theta + 1}{4}\right) \\
& + \left|D^{5/2}\right|^2 3\left(\frac{5\cos^4\theta - 2\cos^2\theta + 1}{8}\right) \\
& + \left[Re\left(S^{1/2}P^{3/2\,*}\right) + Re\left(P^{1/2}D^{3/2\,*}\right)\right]\sqrt{2}\cos\theta \\
& + Re\left(S^{1/2}D^{5/2\,*}\right)\sqrt{3}\left(\frac{3\cos^2\theta - 1}{2}\right) \\
& + Re\left(P^{3/2}D^{5/2\,*}\right)\sqrt{6}\cos^3\theta
\end{aligned}
\tag{6.6}
$$

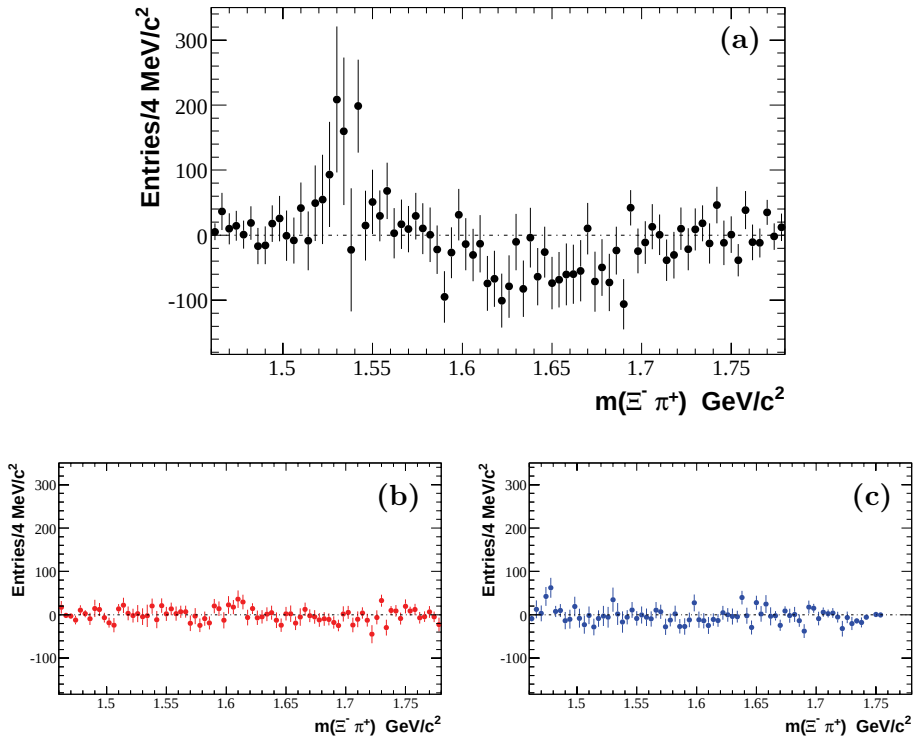

Figure 6.19: The efficiency-corrected $P_3(\cos\theta_{\Xi^-})$ moments as a function of $(\Xi^-\pi^+)$ invariant mass distribution for (a) the Λ_c^+ signal region, (b) and (c) the high and low Λ_c^+ mass-sideband regions, respectively.

$$
\begin{aligned}
-\left(\rho_{1/2\,1/2}-\rho_{-1/2\,-1/2}\right) \quad & \left[\left(Re\left(S^{1/2}P^{1/2\,*}\right)+Re\left(P^{3/2}D^{3/2\,*}\right)\left(\frac{9\cos^2\theta-5}{2}\right)\right.\right. \\
& \left.+Re\left(P^{1/2}D^{5/2\,*}\right)\sqrt{3}\left(\frac{5\cos^2\theta-3}{2}\right)\right)\cos\theta \\
& +\left(Re\left(S^{1/2}D^{3/2\,*}\right)+Re\left(P^{1/2}P^{3/2\,*}\right)\right)\left(\frac{3\cos^2\theta-1}{\sqrt{2}}\right) \\
& \left.+Re\left(D^{3/2}D^{5/2\,*}\right)\sqrt{3}\left(\frac{15\cos^4\theta-12\cos^2\theta+1}{2\sqrt{2}}\right)\right],
\end{aligned}
$$

so that,

$$
N=\int_{-1}^{1} I d\cos\theta=\left|\mathrm{S}^{1/2}\right|^2+\left|\mathrm{P}^{1/2}\right|^2+\left|\mathrm{P}^{3/2}\right|^2+\left|\mathrm{D}^{3/2}\right|^2+\left|\mathrm{D}^{5/2}\right|^2,
$$

as expected. In terms of normalized Legendre polynomials, and assuming that the density matrix elements are equal, this becomes (Appendix E):

$$
\begin{aligned}
I \;=\; & \frac{P_0(\cos\theta)}{\sqrt{2}}\left(\left|S^{1/2}\right|^2+\left|P^{1/2}\right|^2+\left|P^{3/2}\right|^2+\left|D^{3/2}\right|^2+\left|D^{5/2}\right|^2\right) \\
& +P_1(\cos\theta)\left(\frac{2}{\sqrt{3}}\left[\mathrm{Re}\left(\mathrm{S}^{1/2}\mathrm{P}^{3/2\,*}\right)+\mathrm{Re}\left(\mathrm{P}^{1/2}\mathrm{D}^{3/2\,*}\right)\right]+\frac{6}{5}\mathrm{Re}\left(\mathrm{P}^{3/2}\mathrm{D}^{5/2\,*}\right)\right) \\
& +\frac{P_2(\cos\theta)}{\sqrt{10}}\left(\left|P^{3/2}\right|^2+\left|D^{3/2}\right|^2+\frac{8}{7}\left|D^{5/2}\right|^2+\sqrt{20}Re\left(S^{1/2}D^{5/2\,*}\right)\right) \qquad (6.7) \\
& +\frac{4}{5}\sqrt{\frac{3}{7}}P_3(\cos\theta)\mathrm{Re}\left(\mathrm{P}^{3/2}\mathrm{D}^{5/2\,*}\right)+\frac{\sqrt{2}}{7}\mathrm{P}_4(\cos\theta)\left|\mathrm{D}^{5/2}\right|^2.
\end{aligned}
$$

The orthogonality of the Legendre polynomial functions implies

$$
I=\frac{dN}{d\cos\theta}=\langle P_0\rangle P_0(\cos\theta)+...+\langle \mathrm{P}_4\rangle \mathrm{P}_4(\cos\theta),
$$

and the relationship between the Legendre polynomial moments and the magnitudes of the contributing waves is given by the system of equations:

$$\langle P_0 \rangle = \frac{1}{\sqrt{2}} \left(\left|S^{1/2}\right|^2 + \left|P^{1/2}\right|^2 + \left|P^{3/2}\right|^2 + \left|D^{3/2}\right|^2 + \left|D^{5/2}\right|^2 \right) \quad (6.8)$$

$$\langle P_1 \rangle = \left(\frac{2}{\sqrt{3}} \left[Re\left(S^{1/2} P^{3/2\,*}\right) + Re\left(P^{1/2} D^{3/2\,*}\right) \right] + \frac{6}{5} Re\left(P^{3/2} D^{5/2\,*}\right) \right) \quad (6.9)$$

$$\langle P_2 \rangle = \sqrt{10} \left(\left|P^{3/2}\right|^2 + \left|D^{3/2}\right|^2 + \frac{8}{7} \left|D^{5/2}\right|^2 + \sqrt{20} Re\left(S^{1/2} D^{5/2\,*}\right) \right) \quad (6.10)$$

$$\langle P_3 \rangle = \frac{4}{5} \sqrt{\frac{3}{7}} Re\left(P^{3/2} D^{5/2\,*}\right) \quad (6.11)$$

$$\langle P_4 \rangle = \frac{\sqrt{2}}{7} \left|D^{5/2}\right|^2 \quad (6.12)$$

In general, this set of equations cannot be solved, since there are more unknowns than measureables. Additional measured quantities might be obtained by incorporating polarization measurements from the decay of the Ξ^- to $\Lambda\pi^-$, but no attempt has been made to develop the necessary formalism, and so a complete analysis is beyond the scope of the present study. Any such analysis would require the full statistics of the final *BABAR* data set, anticipated to correspond to an integrated luminosity of ~ 800 fb^{-1}, and so is set aside for the time being.

In spite of this, some useful observations can be made concerning the potential effects of extending the analysis of the $\Xi^-\pi^+$ system to include D-wave contributions. Clearly, the interference term between the $P^{3/2}$ and $D^{5/2}$ amplitudes can account for the structure observed in the mass dependence of the $P_3(\cos\theta)$ moment (Eq. 6.11), while the absence of any clear $P_4(\cos\theta)$ moment indicates that $\left|D^{5/2}\right|$ must be rather small (Eq. 6.12). The $P^{3/2} - D^{5/2}$ interference term also contributes to the $P_1(\cos\theta)$ moment, and so Eq. 6.9 may be used in conjunction with Eq. 6.9 to obtain

$$\left[Re\left(S^{1/2} P^{3/2\,*}\right) + Re\left(P^{1/2} D^{3/2\,*}\right) \right] = \frac{\sqrt{3}}{2} \langle P_1 \rangle - \frac{3\sqrt{7}}{4} \langle P_3 \rangle. \quad (6.13)$$

If the contribution from $P^{3/2} - D^{5/2}$ interference is small, the quantity on the right-hand side of Eq. 6.13 should provide an improved estimate of the behavior resulting from the $S^{1/2} - P^{3/2}$ interference. This quantity is plotted in Fig. 6.20. The interference pattern in the $\Xi(1530)^0$ region is preserved, and the behavior in the $\Xi(1690)^0$ region seems more compatible with the idea of a $\Xi(1690)^0$ BW amplitude adding coherently to a broad non-resonant $S^{1/2}$ amplitude, as discussed previously in section 6.4.2 with regard to Fig. 6.13 (b).

Finally the contributions to Eq. 6.10 beyond the $\left|P^{3/2}\right|^2$ may explain why the $P_2(\cos\theta_{\Xi^-})$ moment in the $\Xi(1530)^0$ region yields a larger signal than that observed in the mass distribution (of Fig. 6.10). Any contributions from $\left|D^{3/2}\right|^2$ and $\left|D^{5/2}\right|^2$ will tend to cancel in the distribution of Fig. 6.10, but the $S^{1/2} - D^{5/2}$ interference term has no counterpart in Eq. 6.8, and if positive will yield a $P_2(\cos\theta_{\Xi^-})$ moment larger

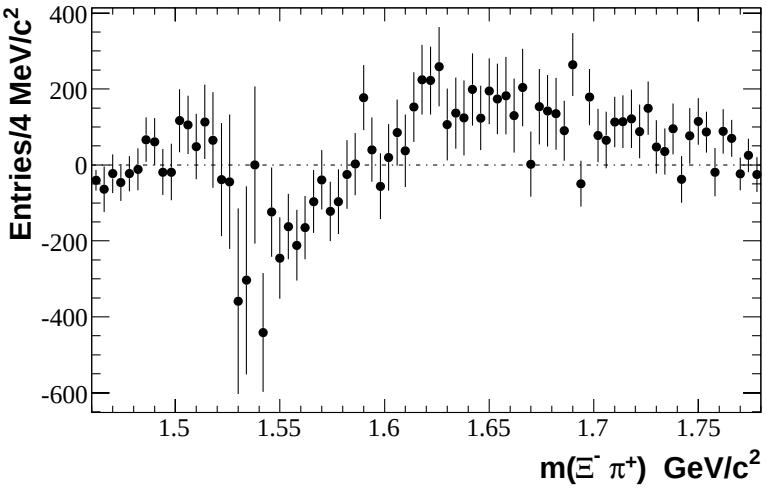

Figure 6.20: The efficiency-corrected $(\sqrt{3}/2)P_1(\cos\theta_{\Xi^-})$- $3\sqrt{7}/4P_3(\cos\theta_{\Xi^-})$ moment of the $\Xi^-\pi^+$ system invariant mass distribution, corresponding to the Λ_c^+ signal region.

than for a pure $P^{3/2}$ amplitude. In addition, a careful examination of the $P_2(\cos\theta_{\Xi^-})$ moment distribution (Fig. 6.6) indicates a lineshape which seems skewed toward low mass instead of toward high mass, as expected for a P-wave BW amplitude. This skewing might be the result of $S^{1/2} - D^{5/2}$ interference, and it is primarily for this reason that no attempt has been made so far to fit Fig. 6.6 in order to extract mass and width parameter values for the $\Xi(1530)^0$.

However, if this reasoning were correct, integration over $\cos\theta$ should remove the interference contribution and yield an invariant mass distribution described by Eq. 6.8, such that the $\Xi(1530)^0$ signal should be well-described by a Breit-Wigner lineshape with known mass and width parameter values [22].

Quantitative comparisons between the $\Xi(1530)$ $P_2(\cos\theta_{\Xi^-})$ moment projection and the expected lineshape, and between the $\Xi(1530)$ signal in the invariant mass distribution and the expected lineshape are presented, and their implications discussed, in section 6.6.

6.6 Implications of Fits to the $\Xi(1530)^0$ Lineshape

The mass and width parameter values for the $\Xi(1530)^0$ are 1531.80 ± 0.32 MeV/c^2 and 9.1 ± 0.5 MeV, respectively [22]. As discussed previously, it would be expected that the $P_2(\cos\theta_{\Xi})$ moment distribution might project the pure P-wave Breit-Wigner lineshape of the $\Xi(1530)^0$, although close inspection of Fig. 6.8 (a) suggests otherwise. In order to quantify this observation, the $P_2(\cos\theta_{\Xi})$ moment shown by the black dots in Fig. 6.21 (a), is fit with a P-wave relativistic BW amplitude

squared multiplied by the usual $p \cdot q$ phase space factor. A P-wave Blatt-Weisskopt Barrier Factor (BF) [49] with radius $R = 3$ GeV^{-1} is used to describe production and decay, and initially mass and width are fixed to the PDG values [22]. Mass smearing is carried out as for the $\Xi(1690)^0$ fits in chapter 5, and the fit yields the red histogram of Fig. 6.21 (a); Fig. 6.21 (b) shows the behavior of the difference between data and histogram in Fig. 6.21 (a). The discrepancies are large, and $\chi^2/NDF = 172.7/48$ (C.L. $= 6 \times 10^{-16}$). The effect of fitting for the mass and width parameter values is shown in Fig. 6.22. The fit values are 1533.5 ± 0.3 MeV/c^2 and 10.2 ± 0.6 MeV, and $\chi^2/NDF = 127.9/46$ (C.L. $= 1 \times 10^{-9}$). Clearly, both fits are very poor.

In section 6.5 it was speculated that the deviation from the expected lineshape might be due to $S^{1/2} - D^{5/2}$ wave interference within the $\Xi^-\pi^+$ system. If this were the case, the effect should integrate away in the invariant mass distribution, so that much better fits to the lineshape should be obtained there. The results of such fits corresponding to Fig. 6.21 (mass and width fixed) and Fig. 6.22 (mass and width free) are shown in Fig. 6.23 and 6.24, respectively. In each case, the background is represented by a third-order polynomial multiplied by the $p \cdot q$ phase space factor. The fit in Fig. 33 ($\chi^2/NDF = 447.5/44$; C.L. $= 0.0$) is much worse than that in Fig. 31, while that in Fig. 34 is only slightly better $\chi^2/NDF = 70.0/42$; C.L. $= 4 \times 10^{-3}$) than that of Fig. 32. For the fit of Fig. 34 (a), the mass and width parameter values obtained are 1534.4 ± 0.1 MeV/c^2 and 13.2 ± 0.5 MeV, respectively, in significant disagreement with the PDG values [22]. Quite clearly, the expected improvement in fit quality is not realized. The conclusion to be drawn would seem to be that this is

the result of overlap with some structure in the $K^+\pi^+$ and/or Ξ^-K^+ systems just as described in chapter 5 for the $\Lambda\bar{K}^0K^+$ final state, and that the distorted lineshape is not due to interference effects within the $\Xi^-\pi^+$ system itself.

As commented previously, Fig. 6.4 shows no indication of structure in either system, and certainly nothing would be expected in $K^+\pi^+$ since this system has

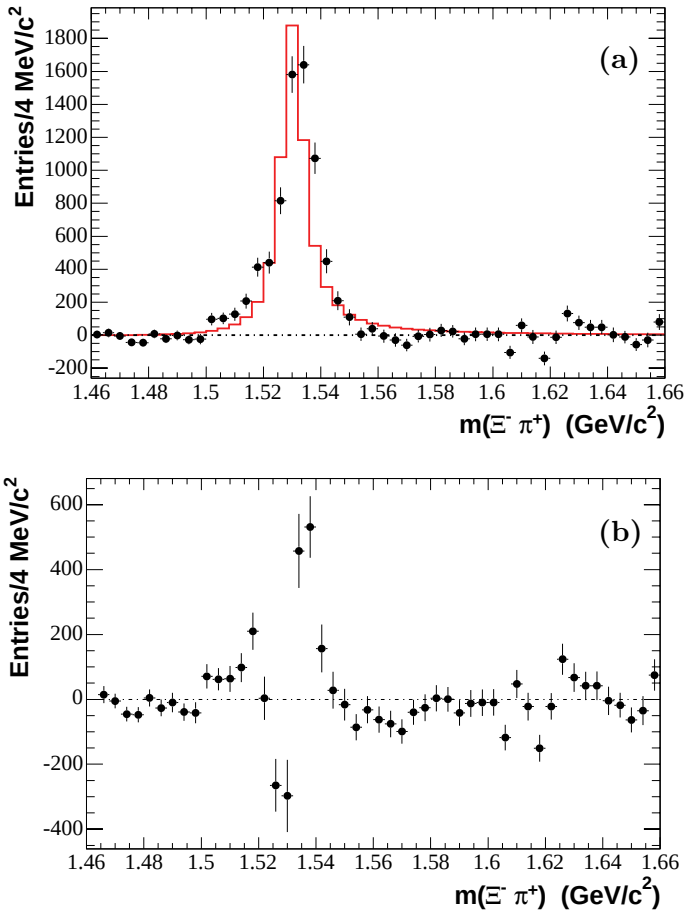

Figure 6.21: The result of the fit described in the text to the $P_2(\cos\theta_\Xi)$ moment. (a) The efficiency-corrected, Λ_c^+ mass-sideband-subtracted $P_2(\cos\theta_{\Xi^-})$ moment distribution for the $\Xi^-\pi^+$ system, corresponding to the Λ_c^+ signal region (solid dots). The red histogram corresponds to the fit described in the text with $\Xi(1530)^0$ mass and width fixed at the PDG values [22]. (b) The difference between the data points and the histogram of (a).

$I = 3/2$. The $\Xi^- K^+$ system might have contributions from Λ or Σ resonant states, and indeed branching fractions of a few percent are quoted for the $\Lambda(2100)$ and $\Sigma(2030)$ [22]. These overlap with the $\Xi(1530)^0$ region (cf. Fig. 6.4 (a)), but both have $J = 7/2$, and so would be expected to yield sharp peaks for $\cos\theta_\Xi \sim 1$ in Fig. 6.4 (a). There is no indication of such behavior.

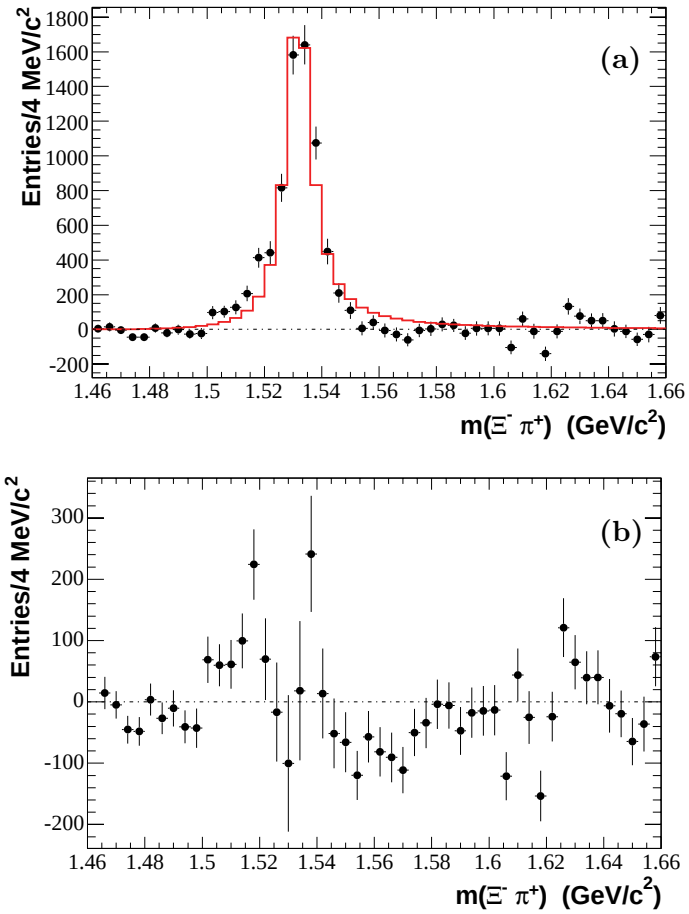

Figure 6.22: The result of the fit described in the text to the $P_2(\cos\theta_\Xi)$ moment. (a) The efficiency-corrected, Λ_c^+ mass-sideband-subtracted $P_2(\cos\theta_{\Xi^-})$ moment distribution for the $\Xi^-\pi^+$ system, corresponding to the Λ_c^+ signal region (solid dots). The red histogram corresponds to the fit described in the text with $\Xi(1530)^0$ mass and width parameters free. (b) The difference between the data points and the histogram of (a).

In order to make a more quantitative search for structure in the Ξ^-K^+ system, the $P_1(\cos\theta_{\Xi^-})$ - $P_4(\cos\theta_{\Xi^-})$ moment distributions are shown in Fig. 6.25 (a)-(d), respectively. The onset of dramatic structure at ~ 2 GeV/c^2 is due to overlap with the $\Xi(1530)^0$ (cf. Fig. 6.4 (a)), and it is very difficult to understand the extent to which this might be influenced by the presence of interfering Ξ^-K^+ amplitude

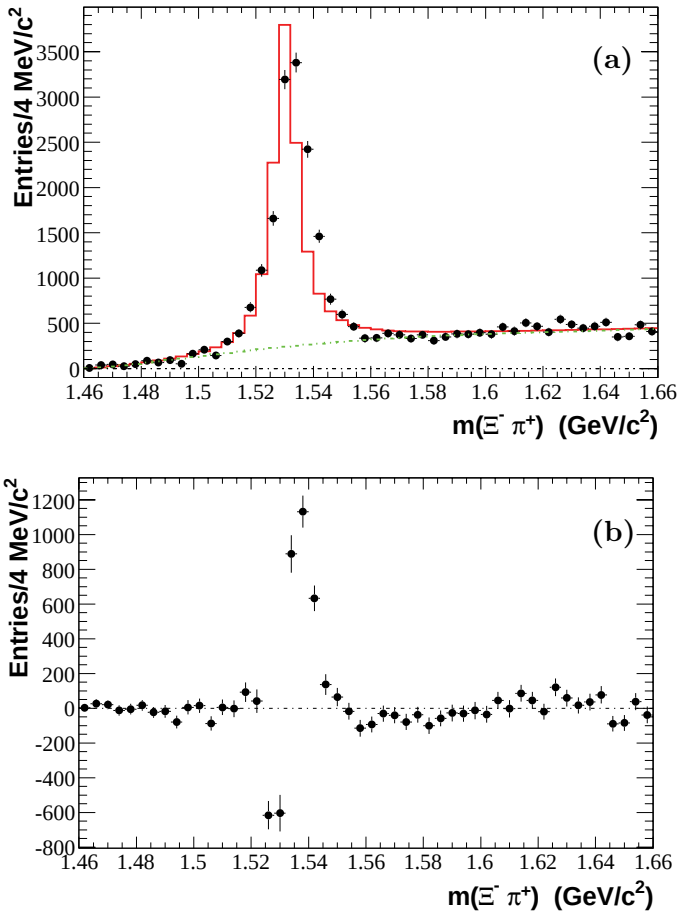

Figure 6.23: The result of the fit described in the text to the $P_0(\cos\theta_\Xi)$ moment. (a) The efficiency-corrected, Λ_c^+ mass-sideband-subtracted $P_0(\cos\theta_{\Xi^-})$ moment distribution for the $\Xi^-\pi^+$ system, corresponding to the Λ_c^+ signal region (solid dots). The red histogram corresponds to the fit described in the text with $\Xi(1530)^0$ mass and width fixed at the PDG values [22]; the green curve represents the polynomial background. (b) The difference between the data points and the histogram of (a).

contributions. For mass values less than 2 GeV/c^2, the $P_2(\cos\theta_{\Xi^-})$ moment indicates the possibility of a signal peaking at ~ 1.88 GeV/c^2. Taken at face value, this together with the absence of structure in the $P_4(\cos\theta_{\Xi^-})$ moment distribution, would suggest the presence of a $J = 3/2$ state in this region, and in fact the PDG lists the $\Lambda(1890)$ as a four-star state with mass ~ 1.89 GeV/c^2, width ~ 100 MeV and $J^P = 3/2^+$ [22].

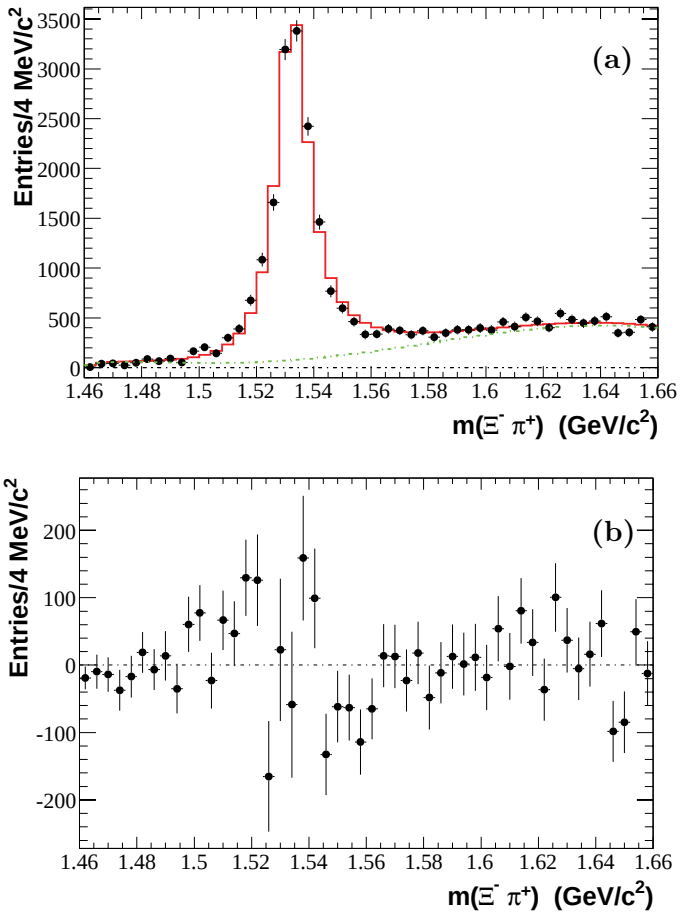

Figure 6.24: The result of the fit described in the text to the $P_0(\cos\theta_\Xi)$ moment. (a) The efficiency-corrected, Λ_c^+ mass-sideband-subtracted $P_0(\cos\theta_{\Xi^-})$ moment distribution for the $\Xi^-\pi^+$ system, corresponding to the Λ_c^+ signal region (solid dots). The red histogram corresponds to the fit described in the text with $\Xi(1530)^0$ mass and width parameters free; the green curve represents the polynomial background. (b) The difference between the data points and the histogram of (a).

No branching fraction to $\Xi^- K^+$ is listed.

At the present level of statistics, no definite conclusion can be drawn as to the presence of a $\Lambda(1890)$ contribution to the Dalitz plot intensity. However, the observed $P_2(\cos\theta_{\Xi^-})$ moment distribution does support the possibility that there may be small $\Xi^- K^+$ amplitudes present in the region of overlap with the $\Xi(1530)^0$ whose impact on the decay angular distribution and lineshape of the latter may be greatly enhanced as a result of interference with the much stronger $\Xi(1530)^0$ amplitude. It seems very difficult to understand the observed characteristics of the $\Xi(1530)$ signal without appeal to such a possibility.

The underlying quark diagrams involved are very similar to those describing

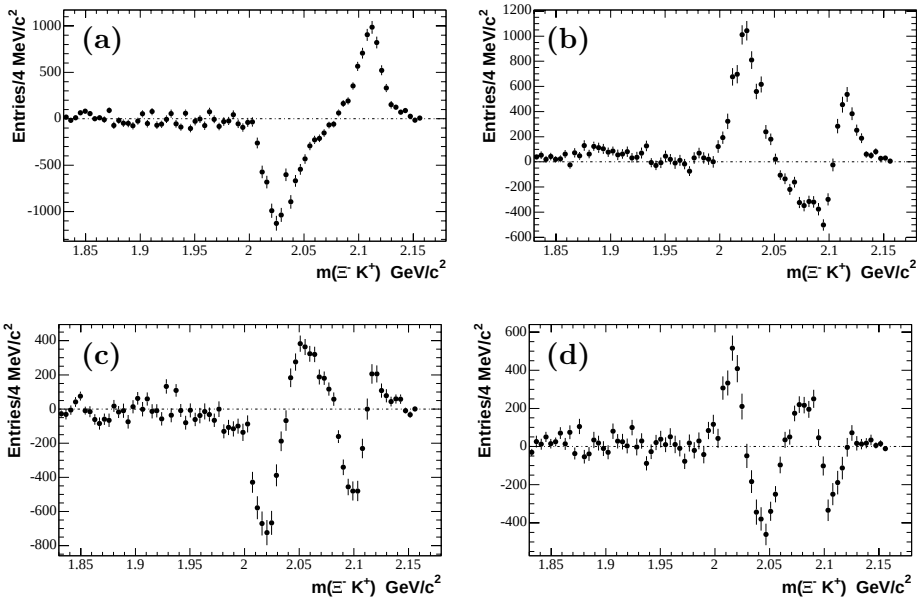

Figure 6.25: The efficiency-corrected $P_i(\cos\theta_{\Xi^-})$ moments of the $(\Xi^- K^-)$ system invariant mass distribution corresponding to the Λ_c^+ signal region: (a) $i = 1$, (b) $i = 2$, (c) $i = 3$, (d) $i = 4$.

$\Lambda_c^+ \to \Lambda \bar{K}^0 K^+$. The $\Xi(1530)$ mode would be characterized by a W-exchange diagram corresponding to Fig. 1.9 (a), while decay to an excited Λ or Σ^0 state would be described by an external spectator quark diagram corresponding to Fig. 1.9 (b). As for $\Lambda_c^+ \to \Lambda \bar{K}^0 K^+$, there are no obvious suppression mechanisms, other than the rather high threshold mass of the $\Xi^- K^+$ system, which as a result involves a mass region within which very little is known about Λ of Σ states which couple to $\Xi^- K^+$.

6.7 Conclusions

A moments analysis of the $\Xi^-\pi^+$ system resulting from data on the decay $\Lambda_c^+ \to \Xi^-\pi^+ K^+$ has established quite clearly that the $\Xi(1530)$ hyperon resonance has spin 3/2. In conjunction with previous analyses [53, 54], this also definitively establishes positive parity, and hence that the $\Xi(1530)$ is a $P^{3/2}$-wave resonance.

However, comparison of the $P_2(\cos\theta_{\Xi^-})$ moment to the $\Xi^-\pi^+$ mass distribution and fits to the angular decay distribution in the $\Xi(1530)$ region, indicate that it is necessary to include other $\Xi^-\pi^+$ amplitudes in order to obtain a complete description of the data.

The observation of a $P_1(\cos\theta_{\Xi^-})$ moment exhibiting oscillatory behavior in the $\Xi(1530)^0$ region indicates the need for an $S^{1/2}$ amplitude, and at the same time provides first evidence for the expected rapid BW phase motion of the $P^{3/2}$ $\Xi(1530)^0$ amplitude.

The behavior of the $\Xi^-\pi^+$ mass distribution in the vicinity of the $\Xi(1690)^0$ suggests the possibility that the BW amplitude describing the $\Xi(1690)^0$ may be

adding coherently to a broad $S^{1/2}$ amplitude describing the non-$\Xi(1530)^0$ part of the spectrum to yield a significant intensity decrease. If this interpretation is correct, the implication is that the $\Xi(1690)^0$ has negative parity, and the conclusion of chapter 5 to the effect that it has spin 1/2 is reinforced. It will be of great interest to revisit this point when the full *BABAR* data set is in hand.

A description in terms of just $S^{1/2}$ and $P^{3/2}$ amplitudes has been shown to be inadequate. It appears that D-wave contributions are required, but an analysis involving S-, P- and D- waves is beyond the reach of an angular-moment-based study, and would require that polarization moments be incorporated. In such a model, distortion of the $\Xi(1530)^0$ lineshape obtained by means of the $P_2(\cos\theta_{\Xi^-})$ moment projection might result from $S-D$ wave interference, and indeed attempts to fit this distribution give very poor results. However, such interference effects should integrate away in the $\Xi^-\pi^+$ invariant mass distribution, but the anticipated improvements in fits to the resulting $\Xi(1530)^0$ lineshape are not realized. This suggests that there may be Ξ^-K^+ amplitude contributions which overlap with the $\Xi(1530)^0$ region and distort the expected mass and angular distributions through interference effects similar to those found in the analysis of the $\Lambda\bar{K}^0K^+$ final state. The presence of a possible signal corresponding to the $\Lambda(1890)$ lends some support to such a picture, but much more data would be required in order to undertake a serious investigation of this possibility.

CHAPTER 7
CONCLUSIONS

The B-factory Experiment at SLAC was conceived as a means of investigating CP-Violation in the decay of B mesons. As a by-product, large numbers of charm particles are produced, and in particular charm baryons which decay to final states containing hyperons and hyperon resonances are reconstructed at a reasonable statistical level. The goal of this thesis has been to make use of such two-body and quasi-two-body charm baryon decay processes to investigate the properties of some of the hyperon and hyperon resonances involved. Analyses of the Ω^-, the $\Xi(1690)^0$ and the $\Xi(1530)^0$ have been presented in chapters 4, 5, and 6, respectively, and the main results are summarized in section 7.1. It should be emphasized that in each analysis, it has been assumed that the parent charm baryon has spin 1/2. In section 7.2, the possibilities for future analyses in the same vein are considered briefly.

7.1 Summary of Results

The angular distributions of the decay products of the Ω^- baryon resulting from Ξ_c^0 and Ω_c^0 decays are well-described by a function $\propto (1 + 3\cos^2\theta_h)$. These observations are consistent with spin assignments 1/2 for the Ξ_c^0 and the Ω_c^0, and 3/2 for the Ω^-. Values of 1/2 and greater than 3/2 for the spin of the Ω^- yield C.L. values significantly less than 1% when spin 1/2 is assumed for the parent charm baryon.

The properties of the $\Xi(1690)^0$ are extracted from a detailed isobar model

analysis of the $\Lambda_c^+ \to \Lambda \bar{K}^0 K^+$ Dalitz plot, and first evidence for the $\Lambda a_0(980)^+$ decay mode of the Λ_c^+ is presented. The hypothesis that the spin of the $\Xi(1690)$ resonance is 1/2 yields an excellent description of the data, and under this assumption the following mass and width parameter values of the $\Xi(1690)^0$ are obtained:

$$\begin{aligned} m(\Xi(1690)^0) &= 1682.9 \pm 0.9\ (\text{stat.}) \pm 0.3\ (\text{syst.})\ \ \text{MeV/c}^2, \\ \Gamma(\Xi(1690)^0) &= 9.3^{+2.0}_{-1.7}\ (\text{stat.}) \pm 0.4\ (\text{syst.})\ \ \text{MeV}. \end{aligned}$$

A spin value of 3/2 is clearly disfavored, and although spin 5/2 results in an acceptable fit probability, the fit exhibits a systematic failure to reproduce the observed $\Xi(1690)$ lineshape.

The properties of the $\Xi(1530)^0$ are studied using the decay $\Lambda_c^+ \to \Xi^- \pi^+ K^+$. The spin of the $\Xi(1530)$ is established for the first time to be 3/2, and first evidence of $\Xi(1530)$ Breit-Wigner phase motion is demonstrated. Structure in the $\Xi^-\pi^+$ mass distribution in the vicinity of the $\Xi(1690)^0$ may be interpreted as indicating that the $\Xi(1690)$ has negative parity, but such a conclusion is highly model-dependent. Attempts at obtaining mass and width parameter values for the $\Xi(1530)$ by fitting the $\Xi^-\pi^+$ mass distribution and the $P_2(\cos\theta)$ moment fail badly. This is interpreted as indicating the presence of interference effects related to structure in the $\Xi^- K^+$ system, although no clear evidence for such effects can be seen in the data. For the present the cause of these failures must remain something of a mystery.

7.2 Future Possibilities

If all goes as planned, the final *BABAR* data set should represent an increase by at least a factor of four over the data samples analyzed in this thesis.

Under the assumption that the ground state charm baryons have spin 1/2, the analysis of chapter 4 would not benefit directly from this statistical increase, since spin 3/2 is already well-established. However, the increase would benefit analyses in progress now which are attempting to use B decay processes (e.g. $B^0 \to \bar{p}\Lambda_c^+$) to establish charm baryon spin, since these analyses are statistically challenged at present.

The statistical increase should be of considerable help to the analysis of chapter 5, since it would be hoped that the skewing of the $\Xi(1690)^0$ lineshape toward high-mass would be more clearly defined, and that as a result the preference for spin 1/2 would be more convincingly established, since it appears that the spin 3/2 and 5/2 hypotheses are unable to reproduce this feature.

It is not clear that a significant increase in statistics could resolve the problems with the $\Xi(1530)^0$ lineshape discussed in chapter 6, since it has not been possible to define the source of the problem as yet, i.e. the problem is conceptual rather than statistical at present. The small signal in the $P_2(\cos\theta_\Xi)$ moment distribution for the $\Xi^- K^+$ system would certainly benefit from a significant increase in statistics, and if it could be established that this were indeed due to production of the $\Lambda(1890)$, it would strengthen the case that the difficulties in the $\Xi(1530)^0$ region result from structure in the 2-2.1 GeV/c^2 region in $\Xi^- K^+$ mass.

In the region of $\Xi^-\pi^+$ mass near the $\Xi(1690)^0$, a large increase in the available data sample would certainly help decide whether the observed dip structure can be attributed to the coherent addition of the $\Xi(1690)^0$ amplitude to a slowly-varying S-wave amplitude, thereby confirming the favored spin 1/2 assignment and establishing negative parity for the $\Xi(1690)$.

The use of charm baryon decay Dalitz plot analysis to provide a window on hyperon resonance spectroscopy, as developed in this thesis, can be extended to many similar three-body final states.

The decay sequence $\Lambda_c^+ \to \Lambda a_0(980)^+$, $a_0(980)^+ \to \eta\pi^+$ would provide direct evidence for the existence of this decay mode, and studies of the $\Lambda\eta$ system, and of the $\Lambda\pi^0$ system in $\Lambda_c^+ \to \Lambda\pi^0\pi^+$, would be highly relevant to the interpretation (and confirmation) of the possible $\Lambda(1890)$ signal in $\Lambda_c^+ \to (\Xi^-K^+)\pi^+$, since $\Lambda\eta$ has $I = 0$ and $\Lambda\pi^0$ has $I = 1$.

A preliminary look at the final state $\Lambda K_S\pi^+$ aimed at investigating $\Xi_c^+ \to \Lambda\bar{K}^0\pi^+$ has revealed clear evidence of the Cabibbo-suppressed decay $\Lambda_c^+ \to \Lambda K^*(892)^+$, and this constitutes the first evidence for this decay mode [22].

All of these final states can be investigated with the final state Λ replaced by a Σ^0. The threshold mass for the $\Sigma^0\bar{K}^0$ system is 1690.3 MeV/c^2, which is above the central mass value of the $\Xi(1690)^0$ reported in this thesis. However, for $\Lambda_c^+ \to \Sigma^0\bar{K}^0K^+$, the Q-value is only 102.5 MeV/c^2, so that overlap between the $\Xi(1690)^0K^+$ and $\Sigma^0a_0(980)^+$ amplitudes would be greater, and hence could affect the observed lineshape more. It would be very interesting to investigate the $\Sigma^0\bar{K}^0$

threshold region with the final *BABAR* statistics.

The only interesting Λ_c^+ three-body decay mode involving the Ξ^- is that to the $\Xi^-\pi^+K^+$ final state, and that has been discussed at length in chapter 6 of this thesis.

There are some interesting possibilities with regard to final states containing a Σ^+. It should be possible to reconstruct the Σ^+ in its $p\pi^0$ decay mode [46], although there are difficulties with the precision to which the decay point can be found. Decay modes of the Λ_c^+ to final states such as $\Sigma^+K^-K^+$, $\Sigma^+K_SK_S$, $\Sigma^+\pi^-\pi^+$, $\Sigma^+\pi^0\pi^0$ (conceptually), $\Sigma^+\pi^0\eta$ and even $\Sigma^+\eta\eta$ could be explored (by some unsuspecting new graduate student) for further information on the $\Xi(1690)$ and on possible Λ and Σ excited states recoiling against a π or η.

For the Ξ_c^+, there is a prediction [57] that no decay to $\Xi(1530)$ should be observed. A preliminary investigation of $\Xi_c^+ \to \Xi^-\pi^+\pi^+$ seems to confirm this. There is no corresponding prediction concerning the $\Xi(1690)^0$, but interestingly enough the data on $\Xi_c^+ \to \Lambda\bar{K}^0\pi^+$ show no evidence of $\Xi(1690)$ production. Detailed investigation of these final states, and also of the final states $\Sigma^0\bar{K}^0\pi^+$, $\Sigma^+K^-\pi^+$, $\Sigma^+\bar{K}^0\pi^0$ and $\Sigma^+\bar{K}^0\eta$ would be of interest.

For the Ξ_c^0, there is no similar prediction, and indeed an initial look at the Dalitz plot for $\Xi_c^0 \to \Lambda K^-\pi^+$ has revealed a rich, but very complicated structure. Resonance bands corresponding to $\bar{K}^*(892)^0$, $\Sigma(1385)^+$, $\Xi(1820)^-$ and $\Xi(1690)^-$ are quite clear, and there may be further activity in the $K^-\pi^+$ system near 1.4 GeV/c^2. The Dalitz plot is small, and so these bands overlap in general, resulting in fairly clear

interference effects. This decay mode may provide information on the $\Xi(1690)^-$, but the Dalitz plot analysis required will be rather complicated. Other Ξ_c^0 decays which may prove interesting involve the final states $\Lambda\bar{K}^0\pi^0$, $\Lambda\bar{K}^0\eta$ and the corresponding states in which the Λ is replaced by a Σ^0. Investigation of decay modes involving a Σ^+ (e.g. final states $\Sigma^+K^-\pi^0$, $\Sigma^+\bar{K}^0\pi^-$, $\Sigma^+K^-\eta$) or a Ξ^- (e.g. final states $\Xi^-\pi^+\pi^0$, $\Xi^-\pi^+\eta$) may also prove fruitful, but the relevant data have not yet been selected for study.

After the successful two-body analysis of the Ω^- presented in chapter 4 of this thesis, it was at first thought to be a straight-forward matter to extend the approach to quasi-two-body charm baryon decay in order to define the properties of the relevant hyperon resonances. In the case of the $\Xi(1690)^0$ analysis presented in chapter 5, it soon became evident that this was not the case, and that it was necessary to take account of other quasi-two-body amplitudes by means of an isobar-model description of the entire Dalitz plot. Similarly, in the analysis of chapter 6, it at first appeared that a simple quasi-two-body approach to the $\Xi(1530)^0$ production would be sufficient. However, even there it appears that a broader treatment of the Dalitz plot is required. Such an approach is significantly more complicated, but does provide the possibility that much more will be learned about the hyperon (and meson) resonance structures involved. The use of charm baryon decay developed in this thesis has opened a new window on this spectroscopy and, as discussed above, there will be many more opportunities to extend such studies to the plethora of charm baryon three-body decay modes accessible in the final *BABAR* data set.

APPENDIX A
TWO-BODY DECAY HELICITY FORMALISM

Consider the decay chain of a spin 1/2 charm baryon to a hyperon and a pseudo-scalar meson; where the primary hyperon decays to a secondary hyperon and a pseudo-scalar meson. The analyzer for the angular analysis of the decay products is well-defined: the quantization axis is chosen as the direction of the primary hyperon in the charm baryon rest-frame.

A.1 Helicity Angular Distribution For Charm Baryon

Spin Assumption $J = 1/2$

If the spin of charm baryon is 1/2, (along the quantization axis) its spin projections are $m = \pm 1/2$. As there is no angular momentum projection with respect to the quantization axis, the primary hyperon is produced with helicity $\lambda_i \pm 1/2$ according to the spin projection of the charm baryon:

$$m = +1/2 \implies \lambda_i = +1/2$$

$$m = -1/2 \implies \lambda_i = -1/2.$$

In this study the value of 1/2 for the spin of the secondary hyperon (i.e. the Λ) is well-established, so that the the final helicity values in the decay sequence are $\lambda_f \pm 1/2$. Using the Jackson phase conventions, the probability for the secondary hyperon to emerge with Euler angles $(\phi, \theta, 0)$ with respect to the quantization axis, is the square of the amplitude characterizing the decay of a particle with total angular momentum J and helicity λ_i to a 2-body system with net final helicity λ_f in the

primary hyperon rest-frame:

$$\begin{aligned} A &= \langle \phi, \theta, \lambda_f, 0 | U | J, \lambda_i \rangle \\ &= \langle \phi, \theta, \lambda_f, 0 | J, \lambda_i; \lambda_f, 0 \rangle \langle J, \lambda_i; \lambda_f, 0 | U | J, \lambda_i \rangle \\ &= A_{\lambda_f} D^{J*}_{\lambda_i \lambda_f}(\phi, \theta, 0), \end{aligned}$$

where $A_{\lambda_f} = \langle J, \lambda_i; \lambda_f, 0 | U | J, \lambda_i \rangle$ gives the coupling to the final helicity states (U is the time-evolution operator that propagates the initial state through the interaction); and $D^{J*}_{\lambda_i \lambda_f}(\phi, \theta, 0)$ are the matrix elements of the rotation operator $R(\phi, \theta, 0) = e^{-i\phi J_z} e^{-i\theta J_y} e^{-i0 J_z} = e^{-i\phi J_z} e^{-i\theta J_y}$ used to transform the two-particle basis states $|\phi, \theta, \lambda_f, 0\rangle$ into the the total angular momentum helicity basis.

Thus, the angular distribution for this decay chain is:

$$\begin{aligned} I &\propto \sum_{\lambda_{i,k}, \lambda_f} \rho_{ik} \left| A^J_{\lambda_f} \right|^2 D^{J*}_{\lambda_i \lambda_f}(\phi, \theta_h, 0) D^{J}_{\lambda_k \lambda_f}(\phi, \theta_h, 0) \\ &\propto \sum_{\lambda_i, \lambda_f} \rho_i \left| A^J_{\lambda_f} D^{J*}_{\lambda_i \lambda_f}(\phi, \theta_h, 0) \right|^2 . \end{aligned}$$

where $\rho_i \equiv \rho_{i\,i}$ ($i = \pm 1/2$) are the diagonal density matrix elements inherited from the charm baryon, and the sum is over all initial and final helicity states. Because the charm baryon is produced inclusively, we assume that the off-diagonal terms, $\rho_{i\,k}$, of its density matrix are zero. In order that the angular distribution be properly normalized such that it integrates to 1, it needs to be multiplied by the factor $2/(2J+1)$, so that

$$\begin{aligned}\frac{dN}{d\cos\theta} &= (2J+1)\frac{N}{2}\sum_{\lambda_i,\lambda_f}\rho_i\left|A_{\lambda_f}D^{J*}_{\lambda_i\lambda_f}(\phi,\theta,0)\right|^2 \\ &= (2J+1)\frac{N}{2}\left(|A_{1/2}|^2(\rho_{1/2}|D^{J*}_{1/2,1/2}(\phi,\theta,0)|^2+\rho_{-1/2}|D^{J*}_{-1/2,1/2}(\phi,\theta,0)|^2)\right. \\ &+ \left.|A_{-1/2}|^2(\rho_{1/2}|D^{J*}_{1/2,-1/2}(\phi,\theta,0)|^2+\rho_{-1/2}|D^{J*}_{-1/2,-1/2}(\phi,\theta,0)|^2)\right).\end{aligned}$$

With $D^{J*}_{\lambda_i,\lambda_f}(\phi,\theta,0)=e^{i\phi}d^J_{\lambda_i,\lambda_f}(\theta)$, we obtain:

$$\begin{aligned}\frac{dN}{d\cos\theta} &= N\frac{2J+1}{2}\left[|A_{1/2}|^2(\rho_{1/2}|d^J_{1/2,1/2}(\theta)|^2+\rho_{-1/2}|d^J_{-1/2,1/2}(\theta)|^2)\right. \\ &+ \left.|A_{-1/2}|^2(\rho_{1/2}|d^J_{1/2,-1/2}(\theta)|^2+\rho_{-1/2}|d^J_{-1/2,-1/2}(\theta)|^2)\right].\end{aligned}$$

The calculation of the angular distributions corresponding to the hypotheses spin J =1/2, 3/2, and 5/2, for the primary hyperon requiresb the Wigner d-functions $d^J_{\pm1/2,\pm1/2}; J=1/2,...5/2$. The d-functions for $J=1/2,3/2$ are listed in the PDG book (p 295):

$$\begin{aligned}d^{1/2}_{1/2,1/2}(\theta) &= \cos\frac{\theta}{2} \\ d^{1/2}_{1/2,-1/2}(\theta) &= -\sin\frac{\theta}{2} \\ d^{3/2}_{1/2,1/2}(\theta) &= \frac{3\cos\theta-1}{2}\cos\frac{\theta}{2} \\ d^{3/2}_{1/2,-1/2}(\theta) &= -\frac{3\cos\theta+1}{2}\sin\frac{\theta}{2}\end{aligned}$$

The d-functions for $J=5/2$ can be easily computed using the recurrence

relation:

$$d^{J+1}_{M_1,M_2}(\theta) = \frac{(J+1)(2J+1)}{\sqrt{((J+1)^2-M_1^2)((J+1)^2-M_2^2)}} \times \left[\left(\cos\theta - \frac{\mathrm{M_1M_2}}{\mathrm{J(J+1)}}\right) d^J_{M_1,M_2}(\theta) - \frac{\sqrt{(J^2-M_1^2)(J^2-M_2^2)}}{J(2J+1)} d^{J-1}_{M_1,M_2}(\theta)\right].$$

Therefore,

$$d^{J+1}_{1/2,1/2}(\theta) = \frac{(J+1)(2J+1)}{((J+1)^2-1/4)} \times \left[\left(\cos\theta - \frac{1}{\mathrm{4J(J+1)}}\right) d^J_{1/2,1/2}(\theta) - \frac{(J^2-1/4)}{J(2J+1)} d^{J-1}_{1/2,1/2}(\theta)\right];$$

$$d^{J+1}_{1/2,-1/2}(\theta) = \frac{(J+1)(2J+1)}{((J+1)^2-1/4)} \times \left[\left(\cos\theta + \frac{1}{\mathrm{4J(J+1)}}\right) d^J_{1/2,-1/2}(\theta) - \frac{(J^2-1/4)}{J(2J+1)} d^{J-1}_{1/2,-1/2}(\theta)\right].$$

Thus for $J+1 = 5/2$, substituting the expressions for $d^{3/2}_{1/2,\pm1/2}(\theta)$ and $d^{1/2}_{1/2,\pm1/2}(\theta)$ we obtain:

$$d^{5/2}_{1/2,1/2}(\theta) = \frac{1}{2}(5\cos^2\theta - 2\cos\theta - 1)\cos(\theta/2)$$

$$d^{5/2}_{1/2,-1/2}(\theta) = -\frac{1}{2}(5\cos^2\theta + 2\cos\theta - 1)\sin(\theta/2)$$

With $d^J_{\lambda',\lambda}(\theta) = (-1)^{\lambda-\lambda'} d^J_{\lambda,\lambda'}(\theta) = d^J_{-\lambda,-\lambda'}(\theta)$,

$$d^J_{-1/2,1/2}(\theta) = -d^J_{1/2,-1/2}(\theta)$$

$$d^J_{-1/2,-1/2}(\theta) = d^J_{1/2,1/2}(\theta)$$

We now derive the angular distribution of the decay products by substituting the d-functions for $J = 1/2, 3/2, 5/2$.

A.1.1 Helicity Angular Distribution for J=1/2

$$\begin{aligned}
\frac{dN}{d\cos\theta} &= N\left[|A_{1/2}|^2(\rho_{1/2}\cos^2(\theta/2) + \rho_{-1/2}\sin^2(\theta/2))\right. \\
&\quad \left.+|A_{-1/2}|^2(\rho_{1/2}\sin^2(\theta/2) + \rho_{-1/2}\cos^2(\theta/2))\right] \\
&= N\left[|A_{1/2}|^2\left(\rho_{1/2}\frac{1+\cos\theta}{2} + \rho_{-1/2}\frac{1-\cos\theta}{2}\right)\right. \\
&\quad \left.+|A_{-1/2}|^2\left(\rho_{1/2}\frac{1-\cos\theta}{2} + \rho_{-1/2}\frac{1+\cos\theta}{2}\right)\right] \\
&= \frac{N}{2}|A_{1/2}|^2\left[(\rho_{1/2}+\rho_{-1/2}) + (\rho_{1/2}-\rho_{-1/2})\cos\theta\right] \\
&\quad +\frac{N}{2}|A_{-1/2}|^2\left[(\rho_{1/2}+\rho_{-1/2}) - (\rho_{1/2}-\rho_{-1/2})\cos\theta\right] \\
&= \frac{N}{2}\left[\left(|A_{1/2}|^2 + |A_{-1/2}|^2\right)(\rho_{1/2}+\rho_{-1/2})\times\right. \\
&\quad \left.\left(1 + \left[\frac{\rho_{1/2}-\rho_{-1/2}}{\rho_{1/2}+\rho_{-1/2}}\right]\left[\frac{|A_{1/2}|^2 - |A_{-1/2}|^2}{|A_{1/2}|^2 + |A_{-1/2}|^2}\right]\cos\theta\right)\right].
\end{aligned}$$

The unitarity of density matrices implies:

$$\begin{aligned}
\rho_{1/2} + \rho_{-1/2} &= 1 \\
|A_{1/2}|^2 + |A_{-1/2}|^2 &= 1
\end{aligned}$$

Defining

$$\beta = \left[\frac{\rho_{1/2}-\rho_{-1/2}}{\rho_{1/2}+\rho_{-1/2}}\right]\left[\frac{|A_{1/2}|^2 - |A_{-1/2}|^2}{|A_{1/2}|^2 + |A_{-1/2}|^2}\right],$$

yields:

$$\frac{dN}{d\cos\theta} = \frac{N}{2}(1 + \beta\cos\theta).$$

A.1.2 Helicity Angular Distribution for J=3/2

$$
\begin{aligned}
\frac{dN}{d\cos\theta} &= \frac{N}{2}\left[|A_{1/2}|^2\left(\rho_{1/2}(3\cos\theta-1)^2\cos^2(\theta/2)+\rho_{-1/2}(3\cos\theta+1)^2\sin^2(\theta/2)\right)\right.\\
&\quad \left.+\,|A_{-1/2}|^2\left(\rho_{1/2}(3\cos\theta+1)^2\sin^2(\theta/2)+\rho_{-1/2}(3\cos\theta-1)^2\cos^2(\theta/2)\right)\right]\\
&= \frac{N}{2}\left[|A_{1/2}|^2\left(\rho_{1/2}(3\cos\theta-1)^2\frac{1+\cos\theta}{2}+\rho_{-1/2}(3\cos\theta+1)^2\frac{1-\cos\theta}{2}\right)\right.\\
&\quad \left.+\,|A_{-1/2}|^2\left(\rho_{1/2}(3\cos\theta+1)^2\frac{1-\cos\theta}{2}+\rho_{-1/2}(3\cos\theta-1)^2\frac{1+\cos\theta}{2}\right)\right]\\
&= \frac{N}{4}\left[|A_{1/2}|^2\left(\rho_{1/2}(9\cos^3\theta+3\cos^2\theta-5\cos\theta+1)\right.\right.\\
&\qquad \left.\left.+\rho_{-1/2}(-9\cos^3\theta+3\cos^2\theta+5\cos\theta+1)\right)\right.\\
&\quad \left.+|A_{-1/2}|^2\left(\rho_{1/2}(-9\cos^3\theta+3\cos^2\theta+5\cos\theta+1)\right.\right.\\
&\qquad \left.\left.+\rho_{-1/2}(9\cos^3\theta+3\cos^2\theta-5\cos\theta+1)\right)\right]\\
&= \frac{N}{4}(|A_{1/2}|^2+|A_{-1/2}|^2)(\rho_{1/2}+\rho_{-1/2})\left[(1+3\cos^2\theta)+\beta(9\cos^3\theta-5\cos\theta)\right]\\
&\quad \Longrightarrow \frac{dN}{d\cos\theta}=\frac{N}{4}\left((1+3\cos^2\theta)+\beta\cos\theta(9\cos^2\theta-5)\right).
\end{aligned}
$$

A.1.3 Helicity Angular Distribution for J=5/2

$$
\begin{aligned}
\frac{dN}{d\cos\theta} &= \frac{3N}{4}\Big[|A_{1/2}|^2\left(\rho_{1/2}(5\cos^2\theta-2\cos\theta-1)^2\cos^2(\theta/2)\right.\\
&\qquad\left.+\rho_{-1/2}(5\cos^2\theta+2\cos\theta-1)^2\sin^2(\theta/2)\right)\\
&\quad+|A_{-1/2}|^2\left(\rho_{1/2}(5\cos^2\theta+2\cos\theta-1)^2\sin^2(\theta/2)\right.\\
&\qquad\left.+\rho_{-1/2}(5\cos^2\theta-2\cos\theta-1)^2\cos^2(\theta/2)\right)\Big]\\
&= \frac{3N}{4}\left[|A_{1/2}|^2\left(\rho_{1/2}(5\cos^2\theta-2\cos\theta-1)^2\frac{\cos\theta+1}{2}\right.\right.\\
&\qquad\left.+\rho_{-1/2}(5\cos^2\theta+2\cos\theta-1)^2\frac{\cos\theta}{2}\right)\\
&\quad+|A_{-1/2}|^2\left(\rho_{1/2}(5\cos^2\theta+2\cos\theta-1)^2\frac{1-\cos\theta}{2}\right.\\
&\qquad\left.\left.+\rho_{-1/2}(5\cos^2\theta-2\cos\theta-1)^2\frac{\cos\theta+1}{2}\right)\right]\\
&= \frac{3N}{8}\left[|A_{1/2}|^2\rho_{1/2}(25\cos^5\theta+5\cos^4\theta-26\cos^3\theta-2\cos^2\theta+5\cos\theta+1)\right.\\
&\quad+|A_{1/2}|^2\rho_{-1/2}(-25\cos^5\theta+5\cos^4\theta+26\cos^3\theta-2\cos^2\theta-5\cos\theta+1)\\
&\quad+|A_{-1/2}|^2\rho_{1/2}(-25\cos^5\theta+5\cos^4\theta+26\cos^3\theta-2\cos^2\theta-5\cos\theta+1)\\
&\quad\left.+|A_{-1/2}|^2\rho_{-1/2}(25\cos^5\theta+5\cos^4\theta-26\cos^3\theta-2\cos^2\theta+5\cos\theta+1)\right]\\
&= \frac{3N}{8}\left[|A_{1/2}|^2(\rho_{1/2}+\rho_{-1/2})(5\cos^4\theta-2\cos^2\theta+1)\right.\\
&\quad+|A_{1/2}|^2(\rho_{1/2}-\rho_{-1/2})(25\cos^5\theta-26\cos^3\theta+5\cos\theta)\\
&\quad+|A_{-1/2}|^2(\rho_{1/2}+\rho_{-1/2})(5\cos^4\theta-2\cos^2\theta+1)\\
&\quad\left.-|A_{-1/2}|^2(\rho_{1/2}-\rho_{-1/2})(25\cos^5\theta-26\cos^3\theta+5\cos\theta)\right]\\
&= \frac{3N}{8}(|A_{1/2}|^2+|A_{-1/2}|^2)(\rho_{1/2}+\rho_{-1/2})\times\\
&\quad\left[(5\cos^4\theta-2\cos^2\theta+1)+\beta(25\cos^5\theta-26\cos^3\theta+5\cos\theta)\right].
\end{aligned}
$$

$$\Longrightarrow \frac{dN}{d\cos\theta} = \frac{3N}{8}\left[(5\cos^4\theta - 2\cos^2\theta + 1) + \beta(25\cos^5\theta - 26\cos^3\theta + 5\cos\theta)\right].$$

A.2 Helicity Angular Distributions For $J_{\Xi_c} = 3/2$

If the primary hyperon spin is equal to or less than the spin of its charm baryon parent, and if the parent helicity states are equally populated, then the decay angular distribution of the primary hyperon is flat.

In this section, the helicity formalism is used to study the implications of the hypothesis $J_{\Xi_c} = 3/2$, on the decay angular distribution of the Ω^- taking into account that the spin states of the parent charm baryon may not be equally populated.

A.2.1 Helicity Angular Distribution For $J_\Omega = 1/2$

If $J_\Omega = 1/2$, the distribution is the same as for the spin 1/2 to 1/2 transition:

$$I \propto 1 + \beta\cos\theta_{\rm h}.$$

Assuming $\beta \sim 0$, the distribution is flat.

A.2.2 Helicity Angular Distribution For $J_\Omega = 3/2$

For $J_\Omega = 3/2$, we obtain:

$$\begin{aligned}\frac{dN}{d\cos\theta} &= \frac{N}{2}\Big[|A^{3/2}_{1/2}|^2(\rho_{3/2}|d^{3/2}_{3/2,1/2}(\theta)|^2 + \rho_{1/2}|d^{3/2}_{1/2,1/2}(\theta)|^2 \\ &\quad +\rho_{-3/2}|d^{3/2}_{-3/2,1/2}(\theta)|^2 + \rho_{-1/2}|d^{3/2}_{-1/2,1/2}(\theta)|^2) \\ &\quad +|A^{3/2}_{-1/2}|^2(\rho_{3/2}|d^{3/2}_{3/2,-1/2}(\theta)|^2 + \rho_{1/2}|d^{3/2}_{1/2,-1/2}(\theta)|^2 \\ &\quad + \rho_{-3/2}|d^{3/2}_{-3/2,-1/2}(\theta)|^2 + \rho_{-1/2}|d^{3/2}_{-1/2,-1/2}(\theta)|^2)\Big],\end{aligned}$$

where $\rho_{\pm 3/2}$, $\rho_{\pm 1/2}$ are the diagonal density matrix elements of the charm baryon and $\rho_{3/2} + \rho_{1/2} + \rho_{-1/2} + \rho_{-3/2} = 1$. This yields:

$$\begin{aligned}
\frac{dN}{d\cos\theta} &= \frac{N}{2}\Bigg[|A_{1/2}^{3/2}|^2\left(\rho_{3/2}\frac{3}{4}(1+\cos\theta)^2\sin^2(\theta/2) + \rho_{1/2}\frac{1}{4}(3\cos\theta-1)^2\cos^2(\theta/2)\right.\\
&\quad \left.+\rho_{-3/2}\frac{3}{4}(1-\cos\theta)^2\cos^2(\theta/2) + \rho_{-1/2}\frac{1}{4}(3\cos\theta+1)^2\sin^2(\theta/2)\right)\\
&\quad +|A_{-1/2}^{3/2}|^2\left(\rho_{3/2}\frac{3}{4}(1-\cos\theta)^2\cos^2(\theta/2) + \rho_{1/2}\frac{1}{4}(3\cos\theta+1)^2\sin^2(\theta/2)\right.\\
&\quad \left.+\rho_{-3/2}\frac{3}{4}(1+\cos\theta)^2\sin^2(\theta/2) + \rho_{-1/2}\frac{1}{4}(3\cos\theta+1)^2\cos^2(\theta/2)\right)\Bigg]\\
&= \frac{N}{2}\Bigg[|A_{1/2}^{3/2}|^2\left(\rho_{3/2}\frac{3}{8}(1+\cos\theta)^2(1-\cos\theta) + \rho_{1/2}\frac{1}{8}(3\cos\theta-1)^2(1+\cos\theta)\right.\\
&\quad \left.+\rho_{-3/2}\frac{3}{8}(1-\cos\theta)^2(1+\cos\theta) + \rho_{-1/2}\frac{1}{8}(3\cos\theta+1)^2(1-\cos\theta)\right)\\
&\quad +|A_{-1/2}^{3/2}|^2\left(\rho_{3/2}\frac{3}{8}(1-\cos\theta)^2(1+\cos\theta) + \rho_{1/2}\frac{1}{8}(3\cos\theta+1)^2(1-\cos\theta)\right.\\
&\quad \left.+\rho_{-3/2}\frac{3}{8}(1+\cos\theta)^2(1-\cos\theta) + \rho_{-1/2}\frac{1}{8}(3\cos\theta+1)^2(1+\cos\theta\right)\Bigg]\\
&= \frac{N}{2}\Bigg[|A_{1/2}^{3/2}|^2\left((\rho_{3/2}+\rho_{-3/2})\frac{3}{8}(1-\cos^2\theta) + (\rho_{3/2}-\rho_{-3/2})\frac{3}{8}(1-\cos^2\theta)\cos\theta\right.\\
&\quad \left.+ (\rho_{1/2}+\rho_{-1/2})\frac{1}{8}(1+3\cos^2\theta) + (\rho_{1/2}-\rho_{-1/2})\frac{1}{8}(9\cos^2\theta-5)\cos\theta\right)\\
&\quad +|A_{-1/2}^{3/2}|^2\left((\rho_{3/2}+\rho_{-3/2})\frac{3}{8}(1-\cos^2\theta) - (\rho_{3/2}-\rho_{-3/2})\frac{3}{8}(1-\cos^2\theta)\cos\theta\right.\\
&\quad \left.+ (\rho_{1/2}+\rho_{-1/2})\frac{1}{8}(1+3\cos^2\theta) - (\rho_{1/2}-\rho_{-1/2})\frac{1}{8}(9\cos^2\theta-5)\cos\theta\right)\Bigg]\\
&= \frac{N}{2}\left(|A_{1/2}^{3/2}|^2 + |A_{-1/2}^{3/2}|^2\right)(\rho_{1/2}+\rho_{-1/2})\times\\
&\quad \Big[3(\rho_{3/2}+\rho_{-3/2})(1-\cos^2\theta) + (\rho_{1/2}+\rho_{-1/2})(1+3\cos^2\theta)\\
&\quad +\tilde{\beta}\left(3(\rho_{3/2}-\rho_{-3/2})(1-\cos^2\theta) + (\rho_{1/2}-\rho_{-1/2})(9\cos^2\theta-5)\right)\cos\theta\Big];
\end{aligned}$$

where,

$$\tilde{\beta} = \frac{|A_{1/2}^{3/2}|^2 - |A_{-1/2}^{3/2}|^2}{|A_{1/2}^{3/2}|^2 + |A_{-1/2}^{3/2}|^2}.$$

Let $\rho_{3/2} + \rho_{-3/2} = x$, so that $\rho_{1/2} + \rho_{-1/2} = 1 - x$; then,

$$\begin{aligned}\frac{dN}{d\cos\theta} &= \frac{N}{2}\left(|A^{3/2}_{1/2}|^2 + |A^{3/2}_{-1/2}|^2\right)\left[(1+3\cos^2\theta) + 2x(1-3\cos^2\theta)\right. \\ &\left. +\tilde{\beta}\left(3(\rho_{3/2}-\rho_{-3/2})(1-\cos^2\theta) + (\rho_{1/2}-\rho_{-1/2})(9\cos^2\theta - 5)\right)\cos\theta\right]\end{aligned}$$

$$\Longrightarrow \frac{dN}{d\cos\theta} = \frac{N}{2}\left(|A^{3/2}_{1/2}|^2 + |A^{3/2}_{-1/2}|^2\right)\left[(1+3\cos^2\theta) + 2x(1-3\cos^2\theta)\right],$$

for $\tilde{\beta} = 0$

Obviously, the distribution is flat only if $x = 0.5$. For $x = 0$, the helicity states $\pm 3/2$ are not populated at all, and the distribution is $I \propto 1 + 3\cos^2\theta$; i.e. identical to $J_{\Xi_c} = 1/2$, $J_\Omega = 3/2$.

A.2.3 Helicity Angular Distribution For $J_\Omega = 5/2$

Using,

$$\begin{aligned} d^{3/2}_{3/2,1/2}(\theta) &= -\sqrt{3}\frac{1+\cos\theta}{2}\sin(\theta/2) \\ d^{3/2}_{3/2,-1/2}(\theta) &= \sqrt{3}\frac{1-\cos\theta}{2}\cos(\theta/2)\end{aligned}$$

and the d-functions recurrence relations, we derive:

$$\begin{aligned} d^{5/2}_{3/2,1/2}(\theta) &= -\frac{1}{2\sqrt{2}}(5\cos^2\theta + 4\cos\theta - 1)\sin(\theta/2) \\ d^{5/2}_{3/2,-1/2}(\theta) &= -\frac{1}{2\sqrt{2}}(5\cos^2\theta - 4\cos\theta - 1)\cos(\theta/2)\end{aligned}$$

$$
\begin{aligned}
\frac{dN}{d\cos\theta} &= frac3N8|A^{3/2}_{1/2}|^2 \times \\
&\Big[\frac{\rho_{3/2}}{2}(5\cos^2\theta+4\cos\theta-1)^2\sin^2(\theta/2)+\frac{\rho_{-3/2}}{2}(5\cos^2\theta-4\cos\theta-1)^2\cos^2(\theta/2) \\
&+\rho_{1/2}(5\cos^2\theta-2\cos\theta-1)^2\cos^2(\theta/2)+\rho_{-1/2}(5\cos^2\theta+2\cos\theta-1)^2\sin^2(\theta/2)\Big] \\
&+\frac{3N}{8}|A^{3/2}_{-1/2}|^2 \times \\
&\Big[\frac{\rho_{3/2}}{2}(5\cos^2\theta-4\cos\theta-1)^2\cos^2(\theta/2)+\frac{\rho_{-3/2}}{2}(5\cos^2\theta+4\cos\theta-1)^2\sin^2(\theta/2) \\
&+\rho_{1/2}(5\cos^2\theta+2\cos\theta-1)^2\sin^2(\theta/2)+\rho_{-1/2}(5\cos^2\theta-2\cos\theta-1)^2\cos^2(\theta/2)\Big] \\
&= \frac{3N}{8}|A^{3/2}_{1/2}|^2 \times \\
&\Big[\frac{(\rho_{3/2}}{2}(5\cos^2\theta+4\cos\theta-1)^2\frac{1-\cos\theta}{2}+\frac{\rho_{-3/2}}{2}(5\cos^2\theta-4\cos\theta-1)^2\frac{1+\cos\theta}{2} \\
&+\rho_{1/2}(5\cos^2\theta-2\cos\theta-1)^2\frac{1+\cos\theta}{2}+\rho_{-1/2}(5\cos^2\theta+2\cos\theta-1)^2\frac{1-\cos\theta}{2}\Big] \\
&+\frac{3N}{8}|A^{3/2}_{-1/2}|^2 \times \\
&\Big[\frac{\rho_{3/2}}{2}(5\cos^2\theta-4\cos\theta-1)^2\frac{1+\cos\theta}{2}+\frac{\rho_{-3/2}}{2}(5\cos^2\theta+4\cos\theta-1)^2\frac{1-\cos\theta}{2} \\
&+\rho_{1/2}(5\cos^2\theta+2\cos\theta-1)^2\frac{1-\cos\theta}{2}+\rho_{-1/2}(5\cos^2\theta-2\cos\theta-1)^2\frac{1+\cos\theta}{2}\Big]
\end{aligned}
$$

$$
\begin{aligned}
\frac{dN}{d\cos\theta} &= \frac{3N}{16}|A^{3/2}_{1/2}|^2 \times \\
&\quad \Big[\frac{1}{2}\left(\rho_{3/2}(-25\cos^5\theta - 15\cos^4\theta + 34\cos^3\theta + 14\cos^2\theta - 9\cos\theta + 1)\right. \\
&\quad \left. + \rho_{-3/2}(25\cos^5\theta - 15\cos^4\theta - 34\cos^3\theta + 14\cos^2\theta + 9\cos\theta + 1)\right) \\
&\quad + \left(\rho_{1/2}(25\cos^5\theta + 5\cos^4\theta - 26\cos^3\theta - 2\cos^2\theta + 5\cos\theta + 1)\right. \\
&\quad \left. + \ \rho_{-1/2}(-25\cos^5\theta + 5\cos^4\theta + 26\cos^3\theta - 2\cos^2\theta - 5\cos\theta + 1)\right)\Big] \\
&\quad + \frac{3N}{16}|A^{3/2}_{-1/2}|^2 \times \\
&\quad \Big[\frac{1}{2}\left(\rho_{3/2}(25\cos^5\theta - 15\cos^4\theta - 34\cos^3\theta + 14\cos^2\theta + 9\cos\theta + 1)\right. \\
&\quad \left. + \rho_{-3/2}(-25\cos^5\theta - 15\cos^4\theta + 34\cos^3\theta + 14\cos^2\theta - 9\cos\theta + 1)\right) \\
&\quad + \left(\rho_{1/2}(-25\cos^5\theta + 5\cos^4\theta + 26\cos^3\theta - 2\cos^2\theta - 5\cos\theta + 1)\right. \\
&\quad \left. + \ \rho_{-1/2}(25\cos^5\theta + 5\cos^4\theta - 26\cos^3\theta - 2\cos^2\theta + 5\cos\theta + 1)\right)\Big] \\
&= \frac{3N}{32}\left[|A^{3/2}_{1/2}|^2 + |A^{3/2}_{-1/2}|^2\right] \times \\
&\quad \Big\{\big[(\rho_{3/2} + \rho_{-3/2})(-15\cos^4\theta + 14\cos^2\theta + 1) \\
&\quad + (\rho_{1/2} + \rho_{-1/2})(10\cos^4\theta - 4\cos^2\theta + 2)\big] \\
&\quad + \left[\frac{|A^{3/2}_{1/2}|^2 - |A^{3/2}_{-1/2}|^2}{|A^{3/2}_{1/2}|^2 + |A^{3/2}_{-1/2}|^2}\right] \times \\
&\quad \big[(\rho_{3/2} - \rho_{-3/2})(-25\cos^5\theta + 34\cos^3\theta - 9\cos\theta) \\
&\quad + 2(\rho_{1/2} - \rho_{-1/2})(25\cos^5\theta - 26\cos^3\theta + 5\cos\theta)\big]\Big\}
\end{aligned}
$$

$$\begin{aligned}
\frac{dN}{d\cos\theta} &= \frac{3N}{32}\left[|A^{3/2}_{1/2}|^2 + |A^{3/2}_{-1/2}|^2\right] \times \\
&\quad \Big\{\left[x(-15\cos^4\theta + 14\cos^2\theta + 1) + (1-x)(10\cos^4\theta - 4\cos^2\theta + 2)\right] \\
&\quad +\tilde{\beta}\left[(\rho_{3/2} - \rho_{-3/2})(-25\cos^5\theta + 34\cos^3\theta - 9\cos\theta)\right. \\
&\quad \left.+2(\rho_{1/2} - \rho_{-1/2})(25\cos^5\theta - 26\cos^3\theta + 5\cos\theta)\right]\Big) \\
&= \frac{3N}{32}\left[|A^{3/2}_{1/2}|^2 + |A^{3/2}_{-1/2}|^2\right] \times \\
&\quad \Big\{\left[(10\cos^4\theta - 4\cos^2\theta + 2) - x(25\cos^4\theta - 18\cos^2\theta + 1)\right] \\
&\quad +\tilde{\beta}\left[(\rho_{3/2} - \rho_{-3/2})(-25\cos^5\theta + 34\cos^3\theta - 9\cos\theta)\right. \\
&\quad \left.+2(\rho_{1/2} - \rho_{-1/2})(25\cos^5\theta - 26\cos^3\theta + 5\cos\theta)\right]\Big\}.
\end{aligned}$$

Thus, with $\tilde{\beta} = 0$, the resulting distribution is,

$$\frac{dN}{d\cos\theta} = \frac{3N}{32}\left[|A^{3/2}_{1/2}|^2 + |A^{3/2}_{-1/2}|^2\right]\left[(10\cos^4\theta - 4\cos^2\theta + 2) - x(25\cos^4\theta - 18\cos^2\theta + 1)\right]$$

$$\Longrightarrow \frac{dN}{d\cos\theta} = \frac{3N}{32}\left(-5\cos^4\theta + 10\cos^2\theta + 3\right),$$

if the density matrix elements of the charm baryon are equally populated ($x = 0.5$). In addition, if $x = 0.4$,

$$\frac{dN}{d\cos\theta} = \frac{N}{4}\left(2\cos^2\theta + 1\right),$$

so that the leading term of the polynomial is only of second order.

APPENDIX B
POLARIZATION STUDY

If the Ξ_c^0 spin is 3/2, the decay angular distribution of the Ω^- depends on the Ξ_c^0 diagonal density matrix elements, as shown in section A.2. An unequal population should lead to a preferred decay direction for the Ξ_c^0. In this section, polarization effects in Ξ_c^0 decay are investigated in order to determine whether there is evidence of such a preferrence.

The polarization vector is defined with respect to the normal, $\hat{n}$, to the production plane of the Ξ_c^0 illustrated in Fig. B.1. If the Ξ_c^0 is produced polarized, the cosine of the angle between the Ω^-, boosted into the Ξ_c^0 rest-frame (Ω^{-*}), and the production plane normal ($\hat{n}$), $\cos\theta_{\rm n}(\Omega) = \hat{\rm n} \cdot \frac{\tilde{\Omega}^{-*}}{|\tilde{\Omega}^{-*}|}$, should show a linear dependence with a slope proportional to the polarization. The uncorrected $\cos\theta_n(\Omega)$ distribution is obtained using the mass side-band subtraction method previously described, and is shown in Fig. B.2. Figure B.3 shows the efficiency as a function of $\cos\theta_n$ computed from signal MC. The uncorrected distribution shown of Fig. B.2 suffers event losses in the $\cos\theta_{\rm n}(\Omega) = 0$ region, which corresponds to events for which the boosted Ω^- is perpendicular to the normal to the production plane, corresponding to small angle decays. This reconstruction feature is apparent in the behavior of the efficiency calculated from signal MC as a function of $\cos\theta_{\rm n}(\Omega)$ shown in Fig. B.3. The efficiency distribution is fitted with a fourth order polynomial. This efficiency parametrization is then used to calculate the efficiency correction for each interval of $\cos\theta_{\rm n}(\Omega)$ in data.

The efficiency-corrected distribution for data is shown in Fig. B.4, together

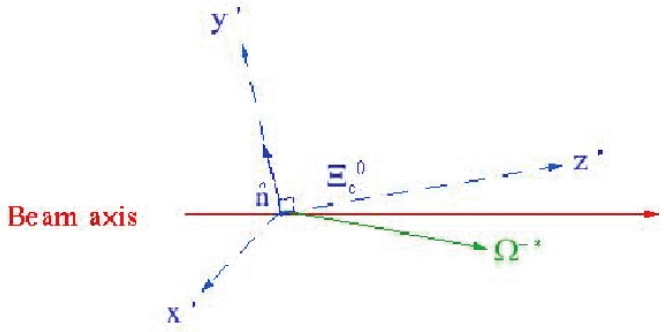

Figure B.1: The coordinate system used for the Ξ_c^0 polarization study.

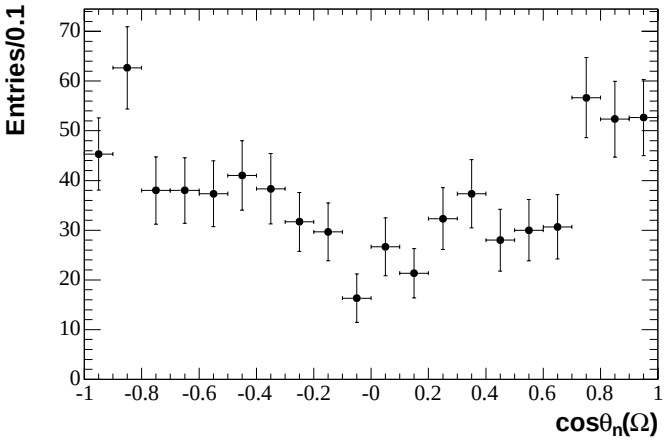

Figure B.2: The uncorrected $\cos\theta_{\rm n}(\Omega)$ distribution in data.

with the result of a straight line fit. This fit has a χ^2 probability of 14% with $\chi^2/NDF = 25/19$, and the slope is consistent with zero, so that the Ξ_c^0 sample shows no overall polarization w.r.t. the production plane normal.

As previously explained, the angular distribution of the Ω in the Ξ_c^0 rest-frame is expected to be flat. Therefore, $\frac{dN}{d\phi d\cos\theta}(\Omega) = \frac{N}{\sqrt{4\pi}}Y_0^0$. Where the polar and azimuthal angles correspond the the longitudinal and transverse direction with respect to the

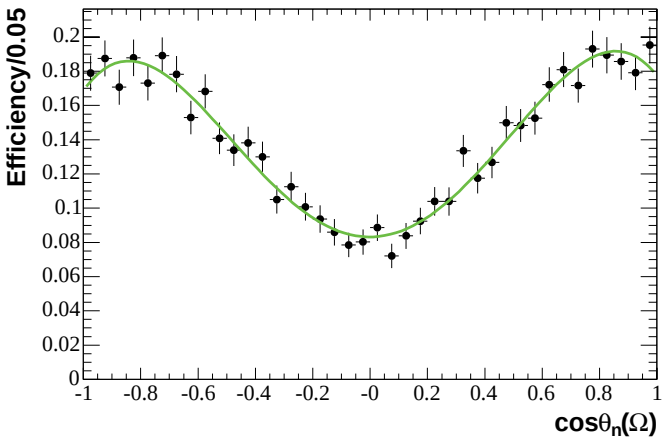

Figure B.3: The Signal MC efficiency as a function of $\cos\theta_{\rm n}(\Omega)$.

Ξ_c^0 production plane. The constant N is a normalization factor.

If the decay is isotropic, all unnormalized Y_L^M moments satisfy:

$$\left\langle Y_L^M \right\rangle = \int \left(\frac{dN}{d\phi d\cos\theta} \right) Y_L^M(\theta,\phi) d\phi d\cos\theta \approx \sum \left(\frac{\mathrm{dN}}{\mathrm{d}\phi\mathrm{d}\cos\theta} \right) \mathrm{Y_L^M}(\theta,\phi)\mathrm{d}\phi\mathrm{d}\cos\theta = 0.$$

Therefore, in order to establish that all the parent baryon helicity states are equally

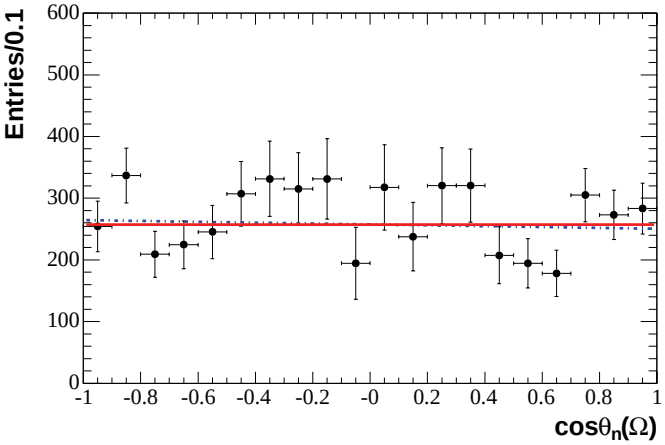

Figure B.4: The efficiency corrected $\cos\theta_{\rm n}(\Omega)$ distribution in data; the dashed line corresponds to a slope parameter of -6.9 ± 16, while the solid line corresponds to the slope of zero.

populated, the sum of the weights of the real and imaginary parts of spherical harmonics with L=0,..6 is computed; this tests parent baryon spin hypotheses ranging from 1/2 to 7/2 in the sense that it involves up to 3 units of orbital angular momentum in the $\Omega^- K^+$ system. If any of the moments deviates significantly from zero, this indicates that the parent helicity states are not equally populated, and hence that there may exist a preferred direction in the Ξ_c^0 decay space.

The distributions corresponding to the Ξ_c^0 signal and mass sideband regions are shown in Figs. B.5 and B.6, respectively. The negative peaks in the Y_1^1 bins are consistent with the loss in efficiency observed in the $\cos\theta_n(\Omega)$ spectra seen in both data and reconstructed MC events.

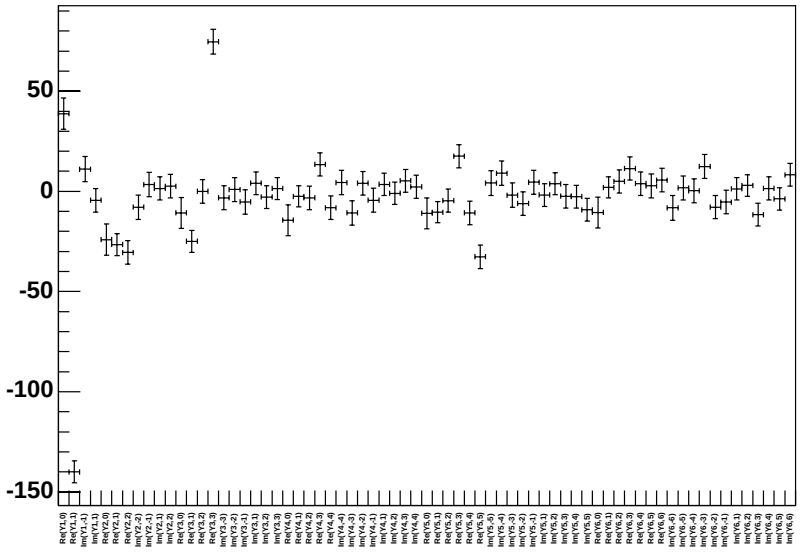

Figure B.5: The unnormalized YLM moments for the Ξ_c^0 signal region.

The mass-sideband subtracted sum of weights distribution in data is shown in Fig. B.7. A similar plot is obtained for truth-matched signal MC events, as shown in Fig. B.8 for the signal MC and the data, where the signal MC sample has been normalized to the data. The open blue dots represent the distribution for MC events and the red crosses the data, since the MC events were generated with isotropic Ξ_c^0 decay; the excellent agreement indicates that the non-zero moments are the results of acceptance effects and that it is reasonable to conclude that there is no preferred direction in the Ξ_c^0 decay space for data.

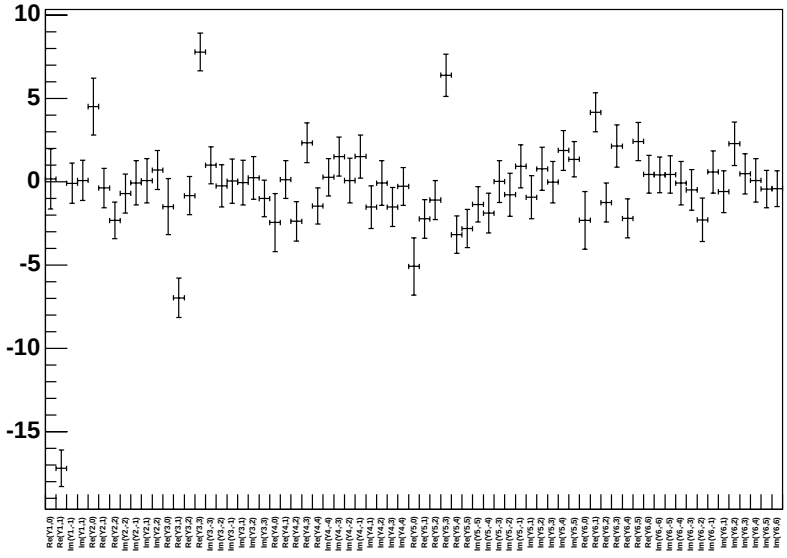

Figure B.6: The unnormalized YLM moments for the Ξ_c^0 mass sideband regions.

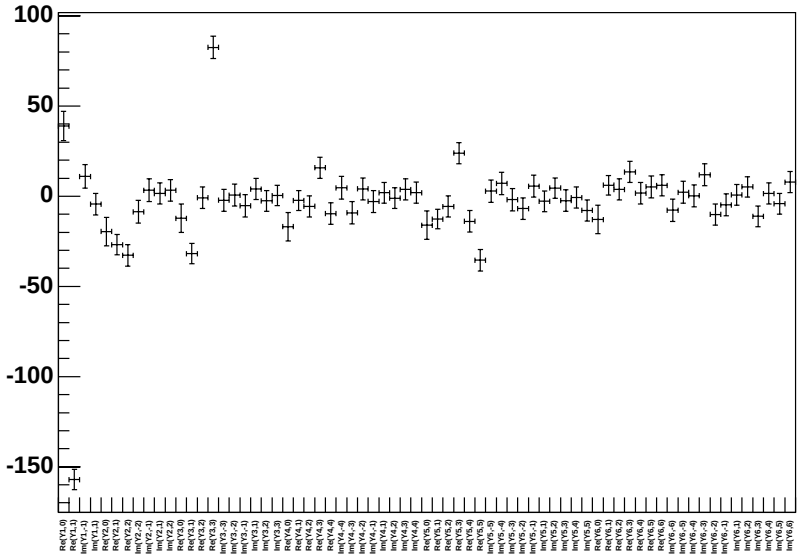

Figure B.7: The mass-sideband-subtracted unnormalized YLM moments of the Ξ_c^0 signal.

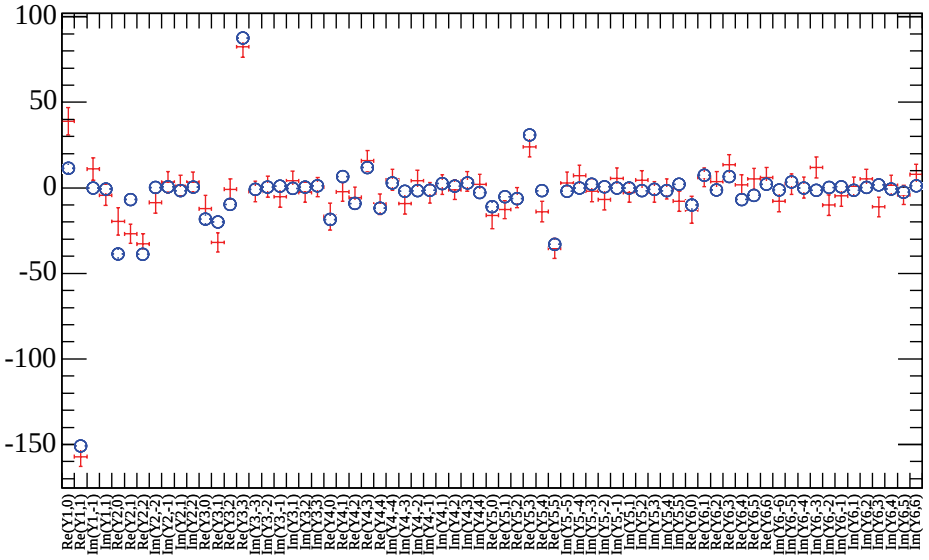

Figure B.8: The mass-sideband-subtracted unnormalized YLM moments of the Ξ_c^0 signal in data (red); superimposed are the corresponding moments for truth-matched Signal MC (blue circles).

APPENDIX C
EFFICIENCY CORRECTION FOR $\Lambda_c^+ \to \Lambda \bar{K}^0 K^+$ EVENTS

The efficiency is calculated from a sample of 230817 $\Lambda_c^+ \to \Lambda \bar{K}^0 K^+$ and $\bar{\Lambda}_c{}^- \to \bar{\Lambda} K^0 K^-$ Signal Monte Carlo events, generated uniformly over the final state phase space.

In general, the phase space volume element in the Dalitz plot corresponding to the decay $\Lambda_c^+ \to \Lambda \bar{K}^0 K^+$ is given by:

$$d\rho \sim d(m^2(\Lambda \bar{K}^0)) \cdot d(m^2(\Lambda K^+)). \tag{C.1}$$

However, when the efficiency is studied in such rectilinear area elements over the Dalitz plot, the elements at the plot boundary are partially outside the plot, and this leads to a rather cumbersome efficiency treatment. The phase space volume element of Eq. B.1 may be transformed to

$$d\rho' \sim p \cdot \frac{q}{m(\Lambda \bar{K}^0))} \cdot m(\Lambda \bar{K}^0)) d(m(\Lambda \bar{K}^0)) d(\cos\theta_\Lambda), \tag{C.2}$$

i.e.

$$d\rho' \sim p \cdot q d(m(\Lambda \bar{K}^0)) d(\cos\theta_\Lambda), \tag{C.3}$$

where

$$p = \frac{\sqrt{[m^2(\Lambda_c^+) - (m(K^+) + m(\Lambda \bar{K}^0))^2] \cdot [m^2(\Lambda_c^+) - (m(K^+) - m(\Lambda \bar{K}^0))^2]}}{2m(\Lambda_c^+)}$$

is the momentum of the K^+ daughter of the Λ_c^+ in the Λ_c^+ rest-frame, and

$$q = \frac{\sqrt{[m^2(\Lambda \bar{K}^0) - (m(\Lambda) + m(\bar{K}^0))^2] \cdot [m^2(\Lambda \bar{K}^0) - (m(\Lambda) - m(\bar{K}^0))^2]}}{2m(\Lambda \bar{K}^0)}$$

is the momentum of the Λ in the $(\Lambda\bar{K}^0)$ system rest-frame. This expression is such that the phase space density is uniform in $\cos\theta_\Lambda$ given a particular value of $m(\Lambda\bar{K}^0)$.

The range of $\cos\theta_\Lambda$ is [- 1, 1], and that of $m(\Lambda\bar{K}^0)$ is from threshold to $(m(\Lambda_c^+) - m(K^+))$, so that the resultant "Dalitz Plot" is rectangular in shape, with the factor $p \cdot q$ representing the Jacobian of the variable transformation. A plot of this kind can then be used readily to study efficiency behavior over the entire phase space region without the problems incurred at the boundary of a conventional Dalitz plot.

With this in mind, the reconstruction efficiency calculated from Signal Monte Carlo events is parametrized as a function of $m(\Lambda\bar{K}^0)$ and $\cos\theta_\Lambda$ in order to correct the distribution in data by weighting each event by the inverse of its parametrized efficiency value. For a given mass interval

$$I = [m(\Lambda\bar{K}^0), m(\Lambda\bar{K}^0) + dm(\Lambda\bar{K}^0)],$$

let N be the number of generated events with $m(\Lambda\bar{K}^0) \subseteq I$, and let n_{reco}, represent the number of such reconstructed truth-associated (i.e. correctly reconstructed) events. The generated $\cos\theta_\Lambda$ distribution is flat, but in general acceptance effects will cause the reconstructed $\cos\theta_\Lambda$ distribution to have some structure. Writing these angular distributions in terms of appropriately normalized Legendre Polynomials,

$$\frac{dN}{d\cos\theta_\Lambda} = N < P_0 > P_0(\cos\theta_\Lambda) \tag{C.4}$$

and,

$$\frac{dn_{reco}}{d\cos\theta_\Lambda} = n_{reco}\,(< P_0 > P_0(\cos\theta_\Lambda) + < \mathrm{P}_1 > \mathrm{P}_1(\cos\theta_\Lambda) + ... + < \mathrm{P}_\mathrm{L} > \mathrm{P}_\mathrm{L}(\cos\theta_\Lambda)) \tag{C.5}$$

where the normalizations are such that, $\int_{-1}^{1} P_i(\cos\theta_\Lambda)\mathrm{P}_j(\cos\theta_\Lambda)\mathrm{dcos}\theta_\Lambda = \delta_{\mathrm{ij}}$. Using this orthogonality condition, the coefficients in the expansion are obtained from

$$< P_j >= \frac{1}{n_{reco}} \int_{-1}^{1} P_j(\cos\theta_\Lambda) \frac{\mathrm{dn_{reco}}}{\mathrm{dcos}\theta_\Lambda} \mathrm{dcos}\theta_\Lambda, \tag{C.6}$$

where the integral is given, to a good approximation for a large enough MC sample, by

$$\sum_{i=1}^{n_{reco}} P_j(\cos\theta_{\Lambda_\mathrm{i}}).$$

The index i runs over the reconstructed events in mass interval I, such that

$$n_{reco} < P_j > \sim \sum_{i=1}^{n_{reco}} P_j(\cos\theta_{\Lambda_\mathrm{i}}),$$

and any effect of efficiency loss in the angular distribution is represented through these coefficients. The absolute efficiency, calculated as a function of $\cos\theta_\Lambda$ and $m(\Lambda\bar{K}^0)$, in mass interval I, is then given by

$$E(\cos\theta_\Lambda, \mathrm{m}(\Lambda\bar{\mathrm{K}}^0)) = \tag{C.7}$$
$$\frac{n_{reco}\,(< P_0 > P_0(\cos\theta_\Lambda) + < \mathrm{P_1} > \mathrm{P_1}(\cos\theta_\Lambda) + ... + < \mathrm{P_L} > \mathrm{P_L}(\cos\theta_\Lambda))}{N < P_0 > P_0(\cos\theta_\Lambda)}$$

With

$$E_0 = \frac{n_{reco}}{N} \tag{C.8}$$

and

$$E_j = 2\frac{n_{reco} < P_j >}{N} = 2\frac{\sum_{i=1}^{n_{reco}} P_j(\cos\theta_{\Lambda_\mathrm{i}})}{N}, \tag{C.9}$$

for a large enough sample (note that the factor 2 enters since $< P_0 > P_0(\cos\theta_\Lambda) = 1/2$), Eq. C.8 becomes,

$$E(\cos\theta_\Lambda, \mathrm{m}(\Lambda\bar{\mathrm{K}}^0)) = \mathrm{E_0} + \mathrm{E_1P_1}(\cos\theta_\Lambda) + ... + \mathrm{E_L P_L}(\cos\theta_\Lambda). \tag{C.10}$$

The mean value of the $P_j(\cos\theta_{\Lambda_i})$, with $i = 1, ..., n_{reco}$, corresponding to mass interval I, is written as $< P_j >$. The r.m.s. deviation of the $P_j(\cos\theta_{\Lambda_i})$ w.r.t. $< P_j >$, σ, is given by

$$\sigma^2 = \sum_{i=1}^{n_{reco}} \frac{(P_j(\cos\theta_{\Lambda_i}) - < P_j >)^2}{n_{reco} - 1}. \tag{C.11}$$

The error on the mean is then

$$\delta < P_j >= \frac{\sigma}{\sqrt{n_{reco}}}$$

and from Eq. C.11,

$$\delta < P_j > = \sqrt{\frac{\sum_{i=1}^{n_{reco}} (P_j(\cos\theta_{\Lambda_i}) - < P_j >)^2}{n_{reco}(n_{reco} - 1)}} \tag{C.12}$$

$$= \sqrt{\frac{\left[\sum_{i=1}^{n_{reco}} \frac{(P_j(\cos\theta_{\Lambda_i}))^2}{n_{reco}}\right] - < P_j >^2}{n_{reco} - 1}}. \tag{C.13}$$

The uncertainty on the parameter

$$E_0 = \frac{n_{reco}}{N}$$

is given by the expression:

$$\delta(E_0) = E_0 \sqrt{\frac{1}{n_{reco}} + \frac{1}{N}}, \tag{C.14}$$

and the uncertainty on the coefficients

$$E_j = 2\frac{\sum_{i=1}^{n_{reco}} P_j(\cos\theta_{\Lambda_i})}{N} \quad (j \geq 1)$$

is given by:

$$\delta(E_j) = \frac{2}{N} \sqrt{\sum_{i=1}^{n_{reco}} (P_j(\cos\theta_{\Lambda_i}))^2 + \frac{(\sum_{i=1}^{n_{reco}} (P_j(\cos\theta_{\Lambda_i})))^2}{N}}. \tag{C.15}$$

The efficiency analysis is carried out in six mass intervals of 30 MeV/c^2 from $m(\Lambda\bar{K}^0) = 1.61$ GeV/c^2 to $m(\Lambda\bar{K}^0) = 1.79$ GeV/c^2; the distributions for Signal Monte Carlo generated events satisfy $p^*(\Lambda_c^+) \geq 1.5$ GeV/c, as for truth-associated Signal Monte Carlo reconstructed events.

Following the prescription of Eqs. C.8, C.14, C.9, and C.15 the coefficients E_i are calculated using the truth-associated reconstructed Signal Monte Carlo events in each mass interval, where N is the number of generated events in that mass interval satisfying $p^*(\Lambda_c^+) \geq 1.5$ GeV/c.

Because not all of the generated distributions are perfectly flat as a result of statistical fluctuations, the angular dependence of the efficiency for each mass interval differs slightly from the angular structure of the corresponding generated event distributions. In order to correct for this slight discrepancy, the values of the E_i coefficients for each mass interval are obtained by fitting the corresponding efficiency distribution with the parametrization of Eq. C.10, with the values of the E_i coefficients extracted from the fit. It is determined empirically that the largest order Legendre Polynomial sufficient to describe the reconstructed events has $L = 6$.

Next, the dependence of the coefficients E_i on $m(\Lambda\bar{K}^0)$, is obtained by fitting each of the distributions for E_i ($i = 0, ..., 6$), with a second order polynomial function.

The procedure described above is applied for $\Lambda_c^+ \rightarrow \Lambda\bar{K}^0K^+$ and $\bar{\Lambda}_c^- \rightarrow \bar{\Lambda}K^0K^-$ events separately, in order to take into account slight charge asymmetries in the reconstruction due the differences between the interactions of particles and anti-particles with the detector material.

C.1 Charge-dependent Efficiency Correction for $\Lambda_c^+ \to \Lambda \bar{K}^0 K^+$ and $\bar{\Lambda}_c^- \to \bar{\Lambda} K^0 K^-$ Events

Figures C.1 and C.5 show the distribution of the Signal Monte Carlo generated events corresponding to each of the mass intervals from $m(\Lambda K_S) = 1.61$ GeV/c^2 to $m(\Lambda K_S) = 1.79$ GeV/c^2 used to obtain the mass dependence of the efficiency parametrization for the mode and anti-mode, respectively, and Figs. C.2 and C.6 show the corresponding reconstructed, truth-associated distributions. As described above, the efficiency for each mass interval is computed by taking the ratio of the reconstructed to generated distribution. The resulting dependence of efficiency on $\cos\theta_\Lambda$ is shown in Figs. C.3 and C.7, together with the curves obtained from fits of expression C.10 with $L = 6$ to these data. The mass dependence of each E_i coefficient is shown in Figs. C.4 and C.8 for the mode and anti-mode, respectively. The curve on each plot represents a fit to a second order polynomial, which enables separate mass interpolation for each E_i coefficient. These interpolations used in conjunction with expression C.10, permit the reconstruction efficiency to be calculated at any point on the rectangular Dalitz plot.

Table C.1: The χ^2/NDF and fit probabilities corresponding to the distributions of Fig. C.3.

Mass interval in GeV/c^2	χ^2/NDF	Fit probability
$\lvert m(\Lambda K_S) - 1.625\rvert < 0.015$	0.63/3	0.89
$\lvert m(\Lambda K_S) - 1.655\rvert < 0.015$	3.04/3	0.39
$\lvert m(\Lambda K_S) - 1.685\rvert < 0.015$	5.39/3	0.15
$\lvert m(\Lambda K_S) - 1.715\rvert < 0.015$	2.51/3	0.47
$\lvert m(\Lambda K_S) - 1.745\rvert < 0.015$	1.36/3	0.71
$\lvert m(\Lambda K_S) - 1.775\rvert < 0.015$	2.92/3	0.40

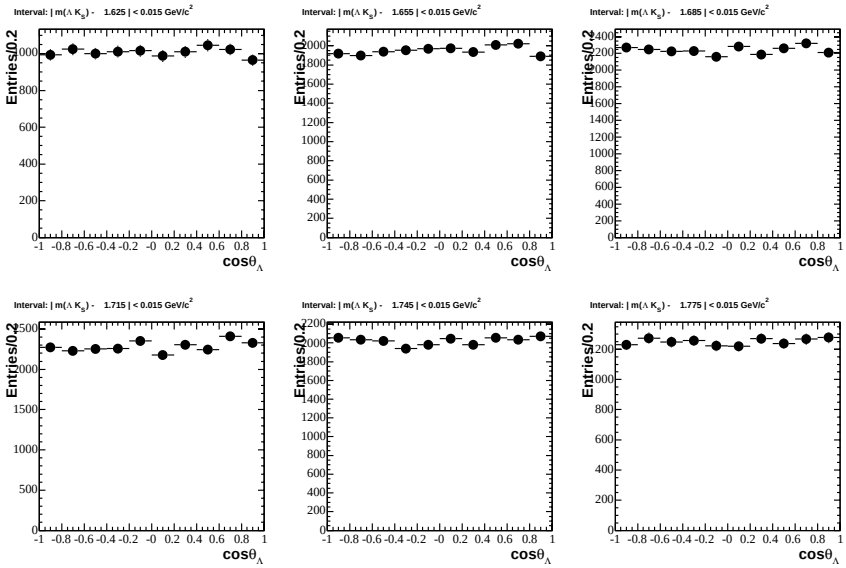

Figure C.1: The distribution of the Signal Monte Carlo generated events corresponding to each of the six 30 MeV/c^2 intervals from $m(\Lambda K_S) = 1.61$ GeV/c^2 to $m(\Lambda K_S) = 1.79$ GeV/c^2.

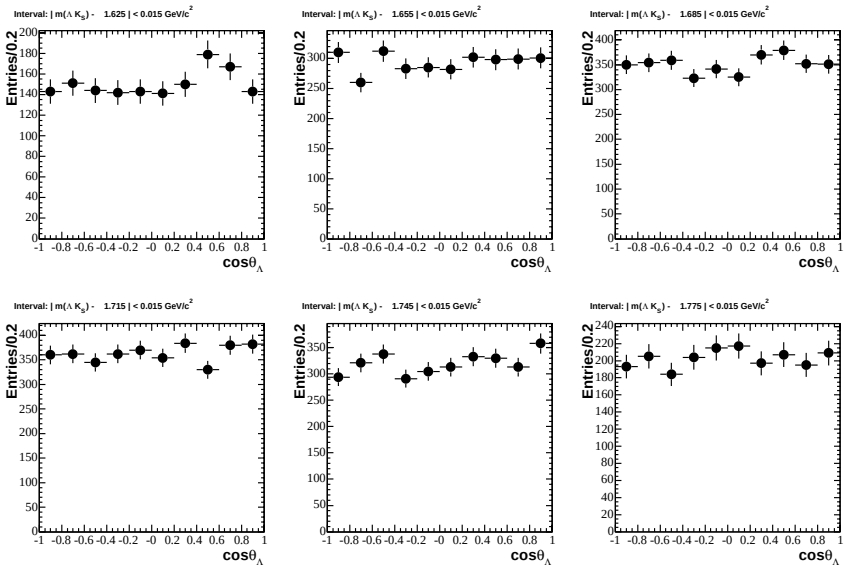

Figure C.2: The distribution of the Signal Monte Carlo truth-associated reconstructed events corresponding to each of the six 30 MeV/c^2 intervals from $m(\Lambda K_S) = 1.61$ GeV/c^2 to $m(\Lambda K_S) = 1.79$ GeV/c^2.

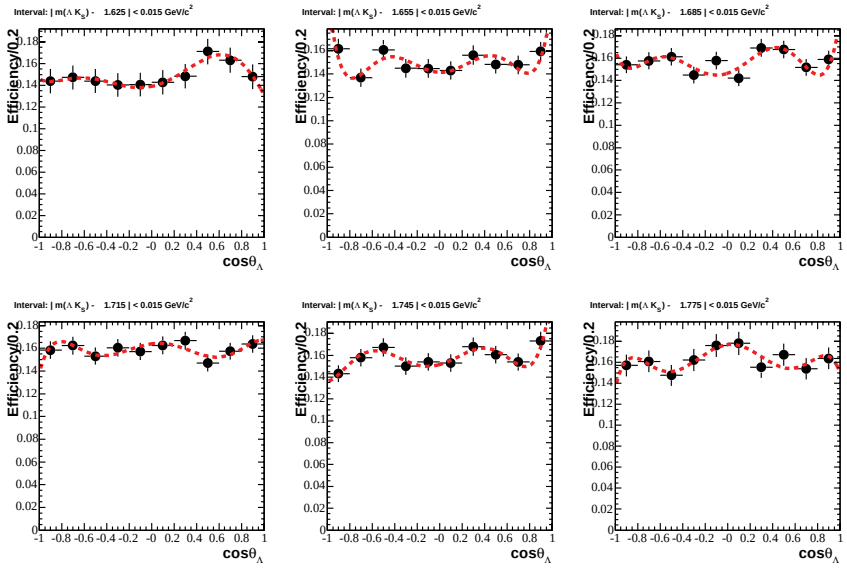

Figure C.3: The efficiency distributions corresponding to each of the six 30 MeV/c^2 intervals from $m(\Lambda K_S) = 1.61$ GeV/c^2 to $m(\Lambda K_S) = 1.79$ GeV/c^2. Superimposed are fits with the parametrization of equation C.10. The values of the parameters E_i are extracted from these fits, and the fit χ^2/NDF and probability for each mass interval are listed in Table C.1.

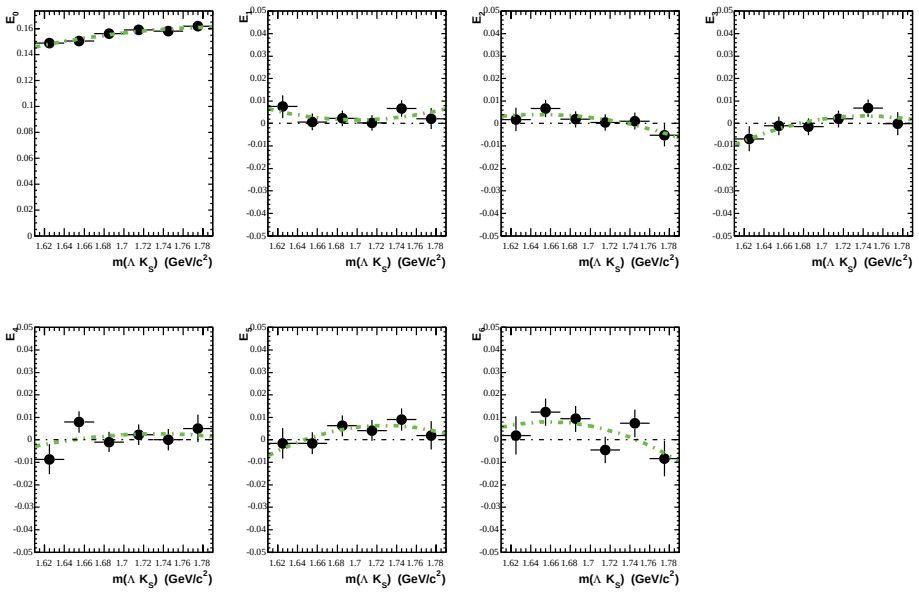

Figure C.4: The distributions of the E_i coefficients obtained from fits of expression C.10 with $L = 6$ to the efficiency calculated from Signal Monte Carlo for each mass interval. Superimposed is a fit with a second order polynomial function. The corresponding χ^2/NDF and fit probabilities are listed in Table C.2.

Table C.2: The χ^2/NDF and fit probabilities corresponding to the distributions of Fig. C.4.

E_i	χ^2/NDF	Fit probability
E_0	1.42/3	0.70
E_1	2.31/3	0.51
E_2	1.20/3	0.75
E_3	1.54/3	0.67
E_4	4.50/3	0.21
E_5	1.25/3	0.74
E_6	4.92/3	0.18

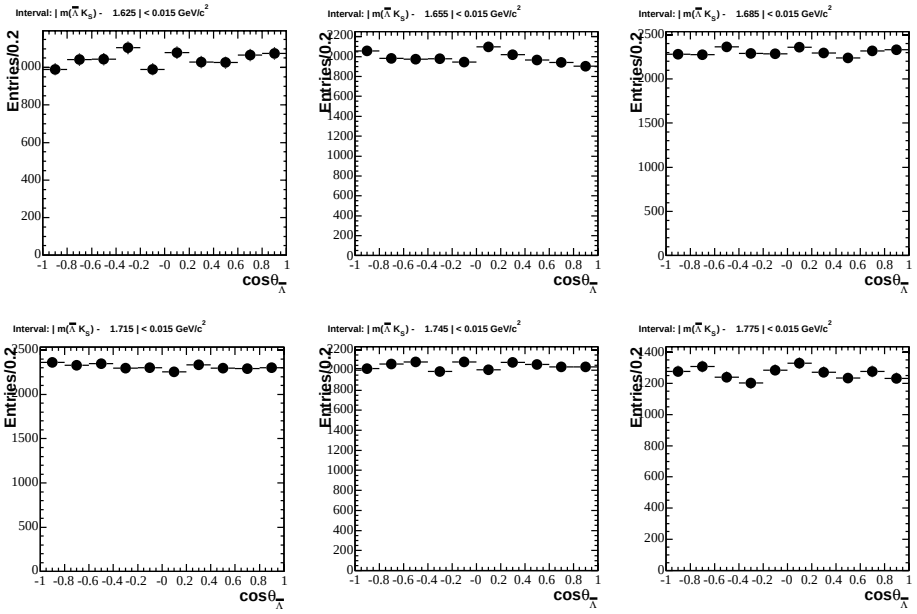

Figure C.5: The distribution of the Signal Monte Carlo generated events corresponding to each of the six 30 MeV/c^2 intervals from $m(\bar{\Lambda}K_S) = 1.61$ GeV/c^2 to $m(\bar{\Lambda}K_S) = 1.79$ GeV/c^2.

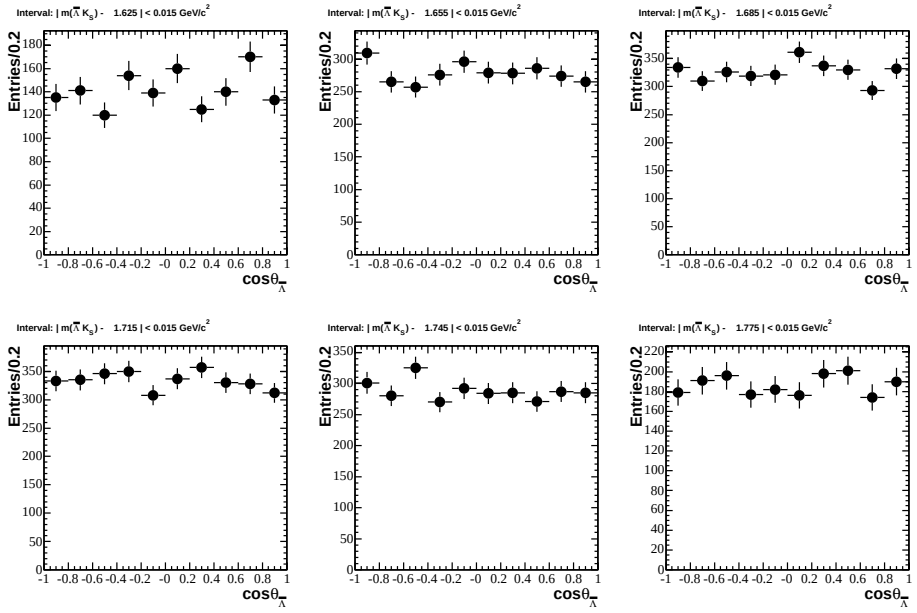

Figure C.6: The distribution of the Signal Monte Carlo truth-associated reconstructed events corresponding to each of the six 30 MeV/c^2 intervals from $m(\bar{\Lambda}K_S) = 1.61$ GeV/c^2 to $m(\bar{\Lambda}K_S) = 1.79$ GeV/c^2.

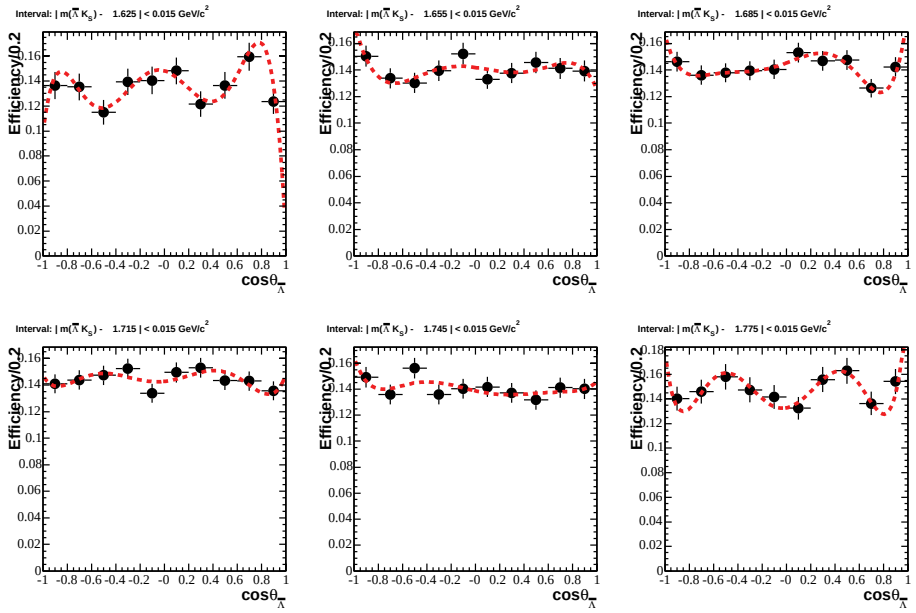

Figure C.7: The efficiency distributions corresponding to each of the six 30 MeV/c^2 intervals from $m(\bar{\Lambda}K_S) = 1.61$ GeV/c^2 to $m(\bar{\Lambda}K_S) = 1.79$ GeV/c^2. Superimposed are fits with the parametrization of equation C.10. The values of the parameters E_i are extracted from these fits, and the fit χ^2/NDF and probability for each mass interval are listed in Table C.3.

Table C.3: The χ^2/NDF and fit probabilities corresponding to the distributions of Fig. C.7.

Mass interval in GeV/c^2	χ^2/NDF	Fit probability
$\lvert m(\bar{\Lambda}K_S) - 1.625\rvert < 0.015$	1.97/3	0.58
$\lvert m(\bar{\Lambda}K_S) - 1.655\rvert < 0.015$	3.42/3	0.33
$\lvert m(\bar{\Lambda}K_S) - 1.685\rvert < 0.015$	1.13/3	0.77
$\lvert m(\bar{\Lambda}K_S) - 1.715\rvert < 0.015$	3.80/3	0.28
$\lvert m(\bar{\Lambda}K_S) - 1.745\rvert < 0.015$	4.94/3	0.18
$\lvert m(\bar{\Lambda}K_S) - 1.775\rvert < 0.015$	1.08/3	0.78

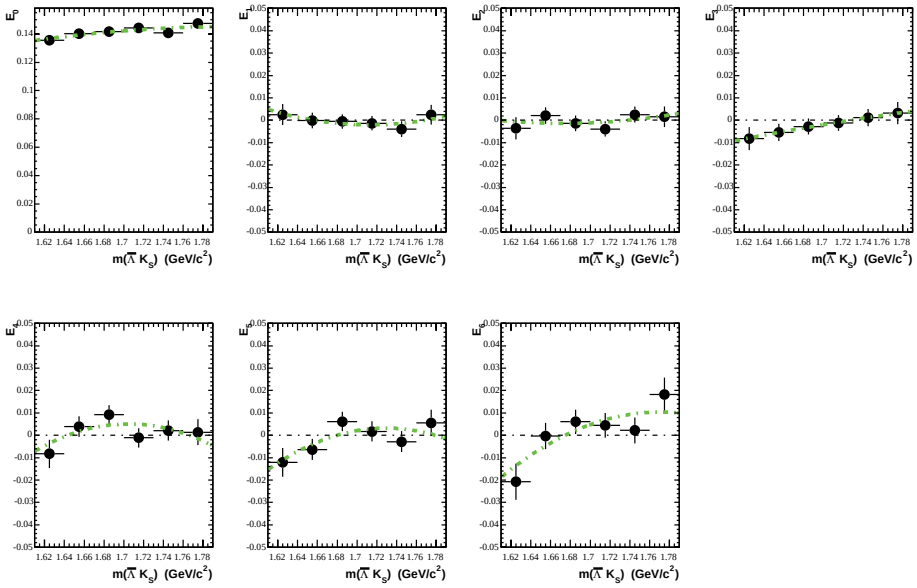

Figure C.8: The distributions of the E_i coefficients obtained from a fit with expression C.10 with $L = 6$ to the efficiency calculated from Signal Monte Carlo for each mass interval. Superimposed is a fit to a second order polynomial function. The corresponding χ^2/NDF and fit probabilities are listed in Table C.4.

Table C.4: The χ^2/NDF and fit probabilities corresponding to the distributions of Fig. C.8.

E_i	χ^2/NDF	Fit probability
E_0	3.04/3	0.38
E_1	0.89/3	0.83
E_2	2.37/3	0.50
E_3	0.03/3	0.99
E_4	4.26/3	0.23
E_5	4.19/3	0.24
E_6	4.77/3	0.19

C.2 Alternative Efficiency Correction for the Purpose of Studying Systematic Uncertainty

In order to study the systematic uncertainties in the measurement of the mass and width of the $\Xi(1690)$, a slightly different approach is adopted. The efficiency parametrization procedure is repeated in order to obtain a smooth efficiency function in 2 dimensions, by fitting the efficiency distribution obtained in each of the six $m(\Lambda K_S)$ intervals, with a fourth order polynomial function of $\cos\theta_\Lambda$ (Fig. C.9 and Table C.5). The mass dependence of the fitted values of these polynomial coefficients is shown in Fig. C.10, together with the results of third order polynomial fits which enable mass interpolation. The quality of these fits is summarized in Table C.6, and the fit results permit the calculation of efficiency at any point on the rectangular Dalitz plot, as explained previously. In this procedure, mode and anti-mode have been combined. The use of the resulting alternative weights in fits to the data provides a measure of the sensitivity of the parameter values obtained to the details of the efficiency-correction procedure used.

Table C.5: The χ^2/NDF and fit probabilities corresponding to the distributions of Fig. C.9.

Mass interval in GeV/c^2	χ^2/NDF	Fit probability
$\lvert m(\Lambda K_S) - 1.625\rvert < 0.015$	6.50/5	0.26
$\lvert m(\Lambda K_S) - 1.655\rvert < 0.015$	5.67/5	0.34
$\lvert m(\Lambda K_S) - 1.685\rvert < 0.015$	8.99/5	0.11
$\lvert m(\Lambda K_S) - 1.715\rvert < 0.015$	6.28/5	0.28
$\lvert m(\Lambda K_S) - 1.745\rvert < 0.015$	6.87/5	0.23
$\lvert m(\Lambda K_S) - 1.775\rvert < 0.015$	4.14/5	0.53

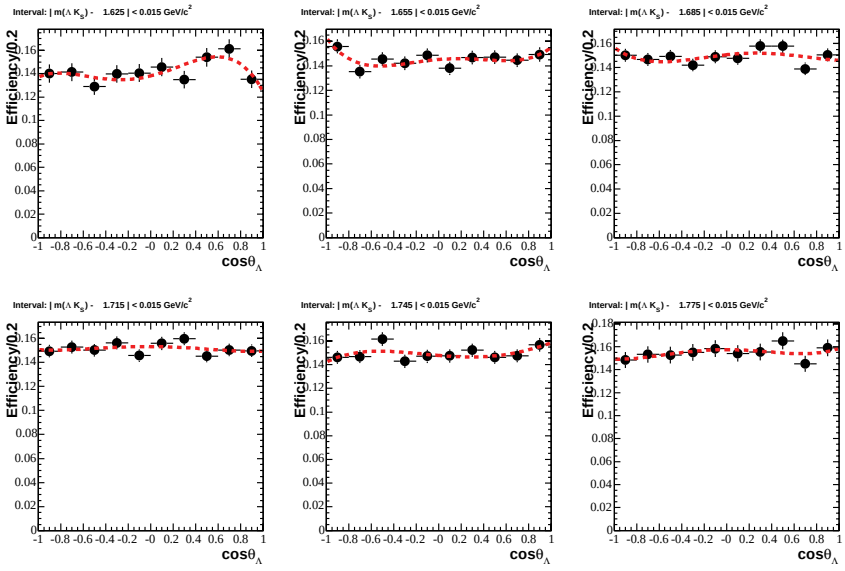

Figure C.9: The efficiency distributions corresponding to to each of the six 30 MeV/c^2 intervals from $m(\Lambda K_S) = 1.61$ GeV/c^2 to $m(\Lambda K_S) = 1.79$ GeV/c^2. Superimposed are fits with a fourth order polynomial function. The values of the coefficients of this polynomial are extracted from these fits, and the fit χ^2/NDF and probability for each mass interval are listed in Table C.5.

Table C.6: The χ^2/NDF and fit probabilities corresponding to the distributions of Fig. C.10.

E_i	χ^2/NDF	Fit probability
E_0	2.49/2	0.29
E_1	0.23/2	0.89
E_2	2.62/2	0.27
E_3	1.11/2	0.57
E_4	0.46/2	0.80

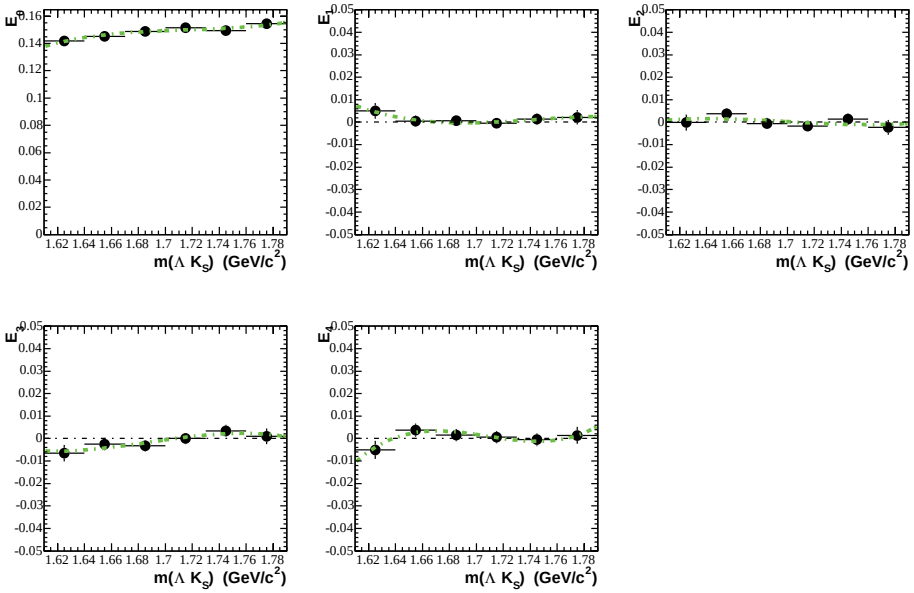

Figure C.10: The distributions of the coefficients E_i $(i = 0, ..., 4)$ obtained from fourth order polynomial fits to truth-associated reconstructed Signal Monte Carlo events for each (ΛK_S) invariant mass interval. Superimposed are the results of fits with a third order polynomial function. The corresponding χ^2/NDF and fit probabilities are listed in Table C.6.

APPENDIX D
ANALYSIS OF THE $\Lambda_c^+ \to \Lambda\bar{K}^0K^+$ DALITZ PLOT

The Dalitz plot is described using an isobar model consisting of the coherent superposition of amplitudes characterizing $\Lambda_c^+ \to \Lambda a_0(980)^+$, $a_0(980)^+ \to \bar{K}^0K^+$ and $\Lambda_c^+ \to \Xi(1690)^0K^+$, $\Xi(1690)^0 \to \Lambda\bar{K}^0$ decays. The distribution, $\frac{d^2N}{d\cos\theta_\Lambda \mathrm{dm}(\Lambda\bar{\mathrm{K}}^0)}$, of $\Lambda_c^+ \to \Lambda\bar{K}^0K^+$ signal events is described by the sum in quadrature of these two amplitudes multiplied by the phase-space density.

The amplitude for the decay $\Lambda_c^+ \to \Xi(1690)^0K^+$ is written in the helicity frame for the decay chain $\Lambda_c^+ \to \Xi(1690)^0K^+$, $\Xi(1690)^0 \to \Lambda\bar{K}^0$ (Fig. D.1), where the helicity angle is defined as the angle between the Λ in the $\Xi(1690)$ rest-frame and the direction of the $\Xi(1690)$ in the Λ_c^+ rest-frame. Similarly, the amplitude of the decay $\Lambda_c^+ \to \Lambda a_0(980)^+$ can be written in the Λ_c^+ rest-frame, but since the decay of the $a_0(980)^+$ in its rest-frame is isotropic, the Λ_c^+ amplitude depends only on the mass of the $\bar{K}^0K^+$ system.

In order to add the Λ_c^+ decay amplitudes coherently, the amplitudes describing decay to $\Lambda a_0(980)^+$ must be Lorentz-transformed to the $\Lambda\bar{K}^0$ rest-frame shown schematically in Fig. D.1. This requires a rotation in the Λ_c^+ rest-frame from the frame with spin quantization axis along the Λ direction to one with axis in the $\Lambda\bar{K}^0$ direction, and a subsequent boost to the $\Lambda\bar{K}^0$ rest-frame. The boost factor (i.e. $\beta\gamma$) values are quite small, ranging from 0 at maximum $\Lambda\bar{K}^0$ mass to ~ 0.15 at the $\Xi(1690)^0$, to 0.24 at $\Lambda\bar{K}^0$ threshold, and so initially the induced Wigner rotations are ignored for simplicity. The corresponding distributions are discussed in section C.3, and the

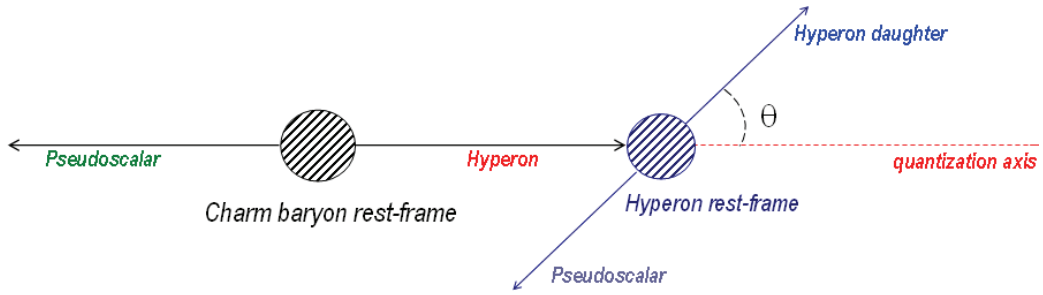

Figure D.1: Schematic definition of the helicity angle θ. Defining the primary hyperon as the hyperon produced from the charm baryon, and the secondary hyperon as the daughter of the primary hyperon, θ is the angle between the direction of the secondary hyperon in the primary hyperon rest-frame and the direction of the primary hyperon in the charm baryon rest-frame.

resulting expressions are used in the fits to the rectangular Dalitz plot described in chapter 5, sections 5.6 and 5.7. The effect of Wigner rotations is discussed briefly in section C.3, and also in chapter 5, section 5.8. It is argued that any relevant effects should be absorbed by the interference term formulated as described in section C.3.

D.1 Amplitudes for the Decay $\Lambda_c^+ \to \Xi(1690)^0 K^+$

The amplitudes for the decay chain $\Lambda_c^+ \to \Xi(1690)^0 K^+$, $\Xi(1690)^0 \to \Lambda \bar{K}^0$ where $J(\Lambda_c^+) = 1/2$, $J(\Xi(1690)) = J$, $J(\Lambda) = 1/2$, $J(\bar{K}^0) = J(K^+) = 0$, and the quantization axis is the direction of the $\Xi(1690)^0$ in the Λ_c^+ rest-frame may be written:

$$A^{\Lambda_c}_{\lambda_i \lambda_f} = H^{\Lambda_c}_{\lambda_\Xi} D^{J(\Lambda_c)*}_{\lambda_i \lambda_\Xi}(0,0,0) H^{\Xi}_{\lambda_f} D^{J\,*}_{\lambda_\Xi \lambda_f}(0,\theta_\Lambda,0),$$

where

- $\lambda_i = \pm 1/2$ is the helicity of the Λ_c^+;
- λ_Ξ is the helicity of the $\Xi(1690)^0$;

- $\lambda_f = \lambda_\Lambda - \lambda_{\bar{K}^0} = \lambda_\Lambda = \pm 1/2$ is the $(\Lambda\bar{K}^0)$ final state helicity in the $\Lambda\bar{K}^0$ rest-frame;
- the first argument of the $D^{J\,*}_{\lambda_\Xi\,\lambda_f}$, which represents the azimuthal orientation of the final state decay plane, has been chosen to be 0 for convenience.

Since

$$D^{J(\Lambda_c)\,*}_{\lambda_i\,\lambda_\Xi}(0,0,0) = D^{1/2\,*}_{\lambda_i\,\lambda_\Xi}(0,0,0) = \delta_{\lambda_i\,\lambda_\Xi}$$

this can be written

$$A^{\Lambda_c}_{\lambda_i\,\lambda_f} = H^{\Lambda_c}_{\lambda_\Xi}\, H^{\Xi}_{\lambda_f} D^{J\,*}_{\lambda_i\,\lambda_f}(0,\theta_\Lambda,0).$$

The decay $\Xi(1690)^0 \to \Lambda\bar{K}^0$ is parity conserving, hence

$$\begin{aligned} H^{\Xi}_{\lambda_f} &= H^{\Xi}_{-\lambda_f}(-1)^{J-1/2-0}\eta_\Xi\eta_\Lambda\eta_{\bar{K}^0} \\ &= H^{\Xi}_{-\lambda_f}\left(\eta_\Xi(-1)^{J+1/2}\right), \end{aligned} \tag{D.1}$$

where η denotes intrinsic parity. If the Λ_c^+ decay proceeded only through $\Xi(1690)^0K^+$ then the intensity at a point on the rectangular Dalitz plot would be

$$\begin{aligned} I &= pq\left(\rho_{1/2\,1/2}\left[\left|A^{\Lambda_c}_{1/2\,1/2}\right|^2 + \left|A^{\Lambda_c}_{1/2\,-1/2}\right|^2\right]\right. \\ &+ \left.\rho_{-1/2\,-1/2}\left[\left|A^{\Lambda_c}_{-1/2\,1/2}\right|^2 + \left|A^{\Lambda_c}_{-1/2\,-1/2}\right|^2\right]\right), \end{aligned} \tag{D.2}$$

where

$$\begin{aligned} A^{\Lambda_c}_{1/2\,1/2} &= H^{\Lambda_c}_{1/2}\, H^{\Xi}_{1/2} D^{J\,*}_{1/2\,1/2}(0,\theta_\Lambda,0), \\ A^{\Lambda_c}_{1/2\,-1/2} &= H^{\Lambda_c}_{1/2}\, H^{\Xi}_{-1/2} D^{J\,*}_{1/2\,-1/2}(0,\theta_\Lambda,0), \\ A^{\Lambda_c}_{-1/2\,1/2} &= H^{\Lambda_c}_{-1/2}\, H^{\Xi}_{1/2} D^{J\,*}_{-1/2\,1/2}(0,\theta_\Lambda,0), \\ A^{\Lambda_c}_{-1/2\,-1/2} &= H^{\Lambda_c}_{-1/2}\, H^{\Xi}_{-1/2} D^{J\,*}_{-1/2\,-1/2}(0,\theta_\Lambda,0), \end{aligned}$$

and pq is the phase-space factor.

Since from Eq. C.1, $\left|H^{\Xi}_{1/2}\right| = \left|H^{\Xi}_{-1/2}\right|$, Eq. C.2 yields

$$\begin{aligned} I &= pq\left(\rho_{1/2\,1/2}\left|H^{\Lambda_c}_{1/2}\right|^2\left|H^{\Xi}_{1/2}\right|^2\left[\left(d^J_{1/2\,1/2}(\theta_\Lambda)\right)^2+\left(d^J_{1/2\,-1/2}(\theta_\Lambda)\right)^2\right]\right. \\ &+ \left.\rho_{-1/2\,-1/2}\left|H^{\Lambda_c}_{-1/2}\right|^2\left|H^{\Xi}_{1/2}\right|^2\left[\left(d^J_{-1/2\,1/2}(\theta_\Lambda)\right)^2+\left(d^J_{-1/2\,-1/2}(\theta_\Lambda)\right)^2\right]\right). \quad \text{(D.3)} \end{aligned}$$

For $J = 1/2$, Eq. C.3 becomes

$$I = pq\left|H^{\Xi}_{1/2}\right|^2\left(\rho_{1/2\,1/2}\left|H^{\Lambda_c}_{1/2}\right|^2+\rho_{-1/2\,-1/2}\left|H^{\Lambda_c}_{-1/2}\right|^2\right); \quad \text{(D.4)}$$

so that the decay angular distribution of the $\Xi(1690)$ is flat regardless of the values of the $H^{\Lambda_c}_{\pm 1/2}$ and of the density matrix elements $\rho_{i\,i}$.

For $J = 3/2$,

$$I = pq\left|H^{\Xi}_{1/2}\right|^2\left(\rho_{1/2\,1/2}\left|H^{\Lambda_c}_{1/2}\right|^2+\rho_{-1/2\,-1/2}\left|H^{\Lambda_c}_{-1/2}\right|^2\right)\left[\frac{1+3\cos^2\theta_\Lambda}{4}\right], \quad \text{(D.5)}$$

and for $J = 5/2$,

$$I = pq\left|H^{\Xi}_{1/2}\right|^2\left(\rho_{1/2\,1/2}\left|H^{\Lambda_c}_{1/2}\right|^2+\rho_{-1/2\,-1/2}\left|H^{\Lambda_c}_{-1/2}\right|^2\right)\left[\frac{1-2\cos^2\theta_\Lambda+5\cos^4\theta_\Lambda}{4}\right], \quad \text{(D.6)}$$

in a similar way.

It follows that these angular distributions are the same as for Ω^- decay, except that there is no asymmetric term since the $\Xi(1690)$ decays strongly and hence conserves parity. Also, the angular dependence does not require the assumption $\rho_{1/2\,1/2} = \rho_{-1/2\,-1/2}$.

D.2 Amplitudes for the Decay $\Lambda_c^+ \to \Lambda a_0(980)^+$

The amplitudes for the decay chain $\Lambda_c^+ \to \Lambda a_0(980)+$, $a_0(980)^+ \to \bar{K}^0 K^+$, where $J(\Lambda_c^+) = 1/2$, $J(\Lambda) = 1/2$, $J(a_0) = 0$, $J(\bar{K}^0) = J(K^+) = 0$, and the quantiza-

tion axis is the direction of the $a_0(980)^+$ in the Λ_c^+ rest-frame may be written:

$$A^{\Lambda_c}_{\lambda_i\,\lambda_{f'}} = H^{\Lambda_c}_{\lambda_\Lambda} D^{J(\Lambda_c)\,*}_{\lambda_i\,\lambda_\Lambda}(0,0,0) H^{a0}_{\lambda_{f'}} D^{J(a_0)\,*}_{\lambda_{a0}\,\lambda_{f'}}(0,\theta_{K^+},0)$$

where

- $\lambda_i = \pm 1/2$ is the helicity of the Λ_c^+ w.r.t. the quantization axis;
- λ_Λ is the helicity of the Λ;
- $\lambda_{a_0} = 0$ is the helicity of the $a_0(980)^+$ (it is zero since $J(a_0) = 0$);
- $\lambda_\Lambda - \lambda_{a_0} = \lambda_\Lambda$ is the $(\Lambda a_0(980)^+)$ final state helicity in the Λ_c^+ rest-frame;
- $\lambda_{f'} = \lambda_{K^+} - \lambda_{\bar{K}^0} = 0$ is the $(\bar{K}^0 K^+)$ final state helicity in the $a_0(980)^+$ rest-frame.

Since

$$D^{J(a_0)\,*}_{\lambda_{a_0}\,\lambda_{f'}}(0,\theta_{K^+},0) = D^0_{0\,0}(0,\theta_{K^+},0) = 1,$$

and

$$D^{J(\Lambda_c)\,*}_{\lambda_i\,\lambda_\Lambda}(0,0,0) = 1$$

only if $\lambda_\Lambda = \lambda_i$ this can be written

$$A^{\Lambda_c}_{\lambda_i\,\lambda_{f'}} = H^{\Lambda_c}_{\lambda_\Lambda}\, H^{a0}_0 \quad (\lambda_\Lambda = \lambda_i).$$

If the Λ_c^+ decay proceeded only through $\Lambda a_0(980)^+$ then the intensity at a point on the rectangular Dalitz plot would be given by

$$I = pq\left(\rho_{1/2\,1/2}\left|A^{\Lambda_c}_{1/2,0}\right|^2 + \rho_{-1/2\,-1/2}\left|A^{\Lambda_c}_{-1/2,0}\right|^2\right),$$

where

$$\begin{aligned} A^{\Lambda_c}_{1/2,0} &= H^{\Lambda_c}_{1/2}\, H^{a_0}_0, \\ A^{\Lambda_c}_{-1/2,0} &= H^{\Lambda_c}_{-1/2}\, H^{a_0}_0, \end{aligned} \tag{D.7}$$

and pq is the corresponding phase-space factor.

This yields

$$I = pq\left[\rho_{1/2\,1/2}\left|H^{\Lambda_c}_{1/2}\right|^2 + \rho_{-1/2\,-1/2}\left|H^{\Lambda_c}_{-1/2}\right|^2\right]\left|H^{a_0}_0\right|^2,$$

where $\rho_{1/2\,1/2} + \rho_{-1/2\,-1/2} = 1$.

The dependence of the $H^{\Lambda_c}_{\pm 1/2}$ on $m_{\bar{K}K}$ is the same, and given by Eq. 5.7 of chapter 5, and $|H^{a_0}_0| = |g_{\bar{K}K}| = g_{\bar{K}K}$ in this same equation, where $g_{\bar{K}K}$ is defined to be real and positive. It follows that on the rectangular Dalitz plot, the intensity distribution due solely to Λ_c^+ decay to $\Lambda a_0(980)^+$ is proportional to the modulus squared of the right side of Eq. 5.7 multiplied by the phase space factor, pq. The dependence of $m_{\bar{K}K}$ on $\cos\theta_\Lambda$ and $m(\Lambda\bar{K}^0)$ expressed in Eq. 5.12 then yields the associated intensity variation over the rectangular plot.

D.3 Coherent Superposition of the Isobar Amplitudes for the Decay $\Lambda_c^+ \to \Lambda\bar{K}^0K^+$

The coherent superposition of the isobar amplitudes contributing to the decay $\Lambda_c^+ \to \Lambda\bar{K}^0K^+$, which have been described in sections C.1 and C.2, requires that the $\Lambda a_0(980)^+$ amplitudes of section C.2 defined in the Λ_c^+ rest-frame be transformed to the $\Lambda\bar{K}^0$ rest-frame used in the formulation developed in section C.1. This is

accomplished in two steps. The first involves a rotation in the Λ_c^+ rest-frame from the frame in which the quantization axis is along the Λ direction, to one in which the quantization axis is along the K^+ direction. In this frame the angle between the Λ and the quantization axis is denoted by θ^*_Λ.

The second step requires a Lorentz transformation along the K^+ direction, to the $\Lambda\bar{K}^0$ rest-frame. In this new frame, the Λ direction is then θ_Λ, the angle defined in Fig. D.1. As discussed in chapter 5, section 5.8, the boost parameter values involved are quite small, so that any effects due to Wigner rotation on the interference between the resulting $\Lambda a_0(980)^+$ amplitudes and the $\Xi(1690)^0 K^+$ amplitudes should not be very significant. Consequently, the discussion which follows initially ignores Wigner rotation, and considers the resulting behavior of isobar interference. There is of course no impact on the individual isobar intensity contributions described in sections C.1 and C.2.

The rotation in the Λ_c^+ rest-frame discussed above yields amplitudes as follows in the $\Lambda\bar{K}^0$ rest-frame (ignoring Wigner rotation effects):

$$\begin{aligned}
A^{\Lambda_c}_{1/2,1/2} &= H^{\Lambda_c}_{1/2}\, H^{a_0}_0\, d^{1/2}_{1/2\,1/2}(\theta_\Lambda), \\
A^{\Lambda_c}_{1/2,-1/2} &= H^{\Lambda_c}_{1/2}\, H^{a_0}_0\, d^{1/2}_{1/2\,-1/2}(\theta_\Lambda), \\
A^{\Lambda_c}_{-1/2,1/2} &= H^{\Lambda_c}_{-1/2}\, H^{a_0}_0\, d^{1/2}_{-1/2\,1/2}(\theta_\Lambda), \\
A^{\Lambda_c}_{-1/2,-1/2} &= H^{\Lambda_c}_{-1/2}\, H^{a_0}_0\, d^{1/2}_{-1/2\,-1/2}(\theta_\Lambda).
\end{aligned} \tag{D.8}$$

Before combining the isobar amplitudes, their dependence on decay angle is renormalized such as to give an intensity dependence which integrates to one. For the

amplitudes of section C.1 this requires a factor $\sqrt{2J+1}/2$, where J is the $\Xi(1690)$ spin, while for these of section C.2 it is just $1/\sqrt{2}$.

The combined amplitudes in the $\Lambda\bar{K}^0$ rest-frame then take the form

$$\begin{aligned} A^{\Lambda_c}_{\lambda_i\,\lambda_f} &= H^{\Lambda_c}_{\lambda_i} H^{\Xi}_{\lambda_f} \frac{\sqrt{2J+1}}{2} d^{J}_{\lambda_i\,\lambda_f}(\theta_\Lambda) \\ &\quad + H^{\Lambda_c}_{\lambda_i} H^{a_0}_{0} \frac{1}{\sqrt{2}} d^{J(\Lambda_c)}_{\lambda_i\,\lambda_f}(\theta_\Lambda). \end{aligned} \tag{D.9}$$

It is assumed that relative strength and phase information beyond that of the BW propagators is contained in the $\Xi(1690)^0$ and $a_0(980)^+$ products of helicity amplitudes (H).

The overall amplitude squared at a point on the Dalitz plot, $|A|^2$, is then obtained by squaring each amplitude and summing over initial and final state helicities, as in Eq. C.2. In the notation of chapter 5, Eqs. 5.5, 5.6, 5.7 and 5.10 this may be written

$$|A|^2 = C\left[p_0^2 I_1 + g^2_{K\bar{K}} I_2 + 2p_0 g_{K\bar{K}} \cdot R\right],$$

where $g_{K\bar{K}}$ is real and positive, and R represents the sum of the four interference terms which arise. Writing the RHS of Eqs. 5.5 and 5.7 as $BW(\Xi)$ and $g_{K\bar{K}}BW(a_0)$,

$$\begin{aligned} I_1 &= |BW(\Xi)|^2 \\ I_2 &= |BW(a_0)|^2, \end{aligned}$$

and for $J = 1/2$, each of the four interference terms takes the form

$$\begin{aligned} R_i &= (\rho_{1/2\,1/2} \text{ or } \rho_{-1/2\,-1/2}) \mathrm{g_i g_{K\bar{K}}} \times \\ &\quad \left(Re\left[BW(\Xi)^* BW(a_0)\right] \cos\delta_i - \mathrm{Im\left[BW(\Xi)^* BW(a_0)\right]} \sin\delta_i\right)\left(1 \pm \cos\theta_\Lambda\right), \end{aligned}$$

where the $\pm$ sign corresponds to that in $\left[d^{1/2}_{1/2\,\pm 1/2}(\theta_\Lambda)\right]$. The g_i and δ_i are different for each term in general because of the nature of the weak decay amplitudes describing $\Lambda_c^+ \to \Lambda a_0(980)^+$ and $\Lambda_c^+ \to \Xi(1690)^0 K^+$, and because the parity of the $\Xi(1690)$ is not known (see Eq. C.1).

Summing the R_i, and extracting the factor $2p_0 g_{K\bar{K}}$ for convenience, R may be written

$$\begin{aligned} R &= k_1 Re\left[BW(\Xi)^* BW(a_0)\right] - k_2 Im\left[BW(\Xi)^* BW(a_0)\right] \\ &\quad + \left(k_3 Re\left[BW(\Xi)^* BW(a_0)\right] - k_4 Im\left[BW(\Xi)^* BW(a_0)\right]\right)\cos\theta_\Lambda \end{aligned}$$

i.e.

$$\begin{aligned} R &= C_1\left(Re\left[BW(\Xi)^* BW(a_0)\right]\cos\delta_1 - \mathrm{Im}\left[\mathrm{BW}(\Xi)^*\mathrm{BW}(\mathrm{a}_0)\right]\sin\delta_1\right) \\ &\quad + C_2\left(Re\left[BW(\Xi)^* BW(a_0)\right]\cos\delta_2 - \mathrm{Im}\left[\mathrm{BW}(\Xi)^*\mathrm{BW}(\mathrm{a}_0)\right]\sin\delta_2\right)\cos\theta_\Lambda, \end{aligned} \tag{D.10}$$

where the C_i and δ_i can be considered to be effective strength and phase parameters. Similar structure results for $J = 3/2$ and $J = 5/2$ but with different $\cos\theta_\Lambda$ dependence; for $J = 3/2$ the first term is proportional to $\cos\theta_\Lambda$ and the second to $(3\cos^2\theta_\Lambda - 1)$, while for for $J = 5/2$ the first term is proportional to $(3\cos^2\theta_\Lambda - 1)$ and the second to $(5\cos^3\theta_\Lambda - 3\cos\theta_\Lambda)$.

In each case, the second term is expected to be small since it involves differences in the Λ_c^+ density matrix elements, and for inclusive production these would be expected to be approximately equal.

It is not possible to calculate the C_i and δ_i a priori, and so it was hoped that their values could be extracted from fits to the rectangular Dalitz plot. This was

tested for $J = 1/2$, but it was found that the parameter values were very highly correlated, and that the second term, which was expected to be small, was in fact of the same size as the first term. The squared $\Xi(1690)$ amplitude bacame extremely large, and hence unphysical, and was reduced to the observed scale by similarly unreasonable interference contributions from both terms in Eq. C.10. It was concluded that meaningful results could not be obtained from such an approach at the present statistical level.

Since the second term in Eq. C.10 is expected to be small, C_2 was set to zero and the net interference effect represented by

$$R = k\left(Re\left[BW(\Xi)^* BW(a_0)\right]\cos\delta - \mathrm{Im}\left[\mathrm{BW}(\Xi)^*\mathrm{BW}(\mathrm{a}_0)\right]\sin\delta\right), \qquad \text{(D.11)}$$

for $J = 1/2$, where k and δ are considered to represent effective scale and phase values, respectively.

This expression is then incorporated into Eq. 5.13, and the values of k and δ obtained from the fit to the data described in chapter 5. The corresponding expressions for $J = 3/2$ and $J = 5/2$ are shown explicitly in Eqs. 5.16 and 5.17, respectively.

The effects of Wigner rotation associated with the Lorentz transformation from the Λ_c^+ to the $\Lambda\bar{K}^0$ rest-frame, which affect only the interference term, and which are expected to be small anyway (see chapter 5, section 5.8), would modify the $\Lambda a_0(980)^+$ contributions to the amplitude superposition of Eq. C.9. However, the net effect of the summation over initial and final helicity states would be structurally the same as represented in Eq. C.10 and subsequently, Eq. C.11. In this sense, the empirical approach followed in the present analysis, which is such that effective values of the k

and δ parameters are extracted from the data, already allows for the effects of Wigner rotation, so that no benefit would result from any additional explicit attempt to take this into account. A test of the validity of this point-of-view is presented in chapter 5, section 5.8.

If the Λ_c^+ weak decay amplitudes satisfied parity conservation, or if baryon spin were ignored completely, the parameter k, which in the present fit procedure modulates the strength of the isobar interference, would take the value 1. The fits to the data indicate that this value does not yield the best representation of the observed Dalitz plot distribution.

APPENDIX E
EFFICIENCY-CORRECTION FOR $\Lambda_c^+ \rightarrow \Xi^-\pi^+K^+$ EVENTS

In this analysis, the measurement of detection efficiency is carried out in 16 mass intervals of 20 MeV/c^2 from $m(\Xi^-\pi^+) = 1.46$ GeV/c^2 to $m(\Xi^-\pi^+) = 1.78$ GeV/c^2. The criterion $p^*(\Lambda_c^+) \geq 2.0$ GeV/c is applied to $\Lambda_c^+ \rightarrow (\Xi^-\pi^+)K^+$ Signal Monte Carlo generated events. Following the prescription of equations C.8, C.14, C.9, and C.15 the coefficients E_i are calculated from the sum of the weights of the moments of truth-associated reconstructed Signal Monte Carlo events, where N is the number of generated events in a particular mass interval satisfying $p^*(\Lambda_c^+) \geq 2.0$ GeV/c. It is determined empirically that the largest order Legendre Polynomial value required to describe the reconstructed events is $L = 6$. As explained earlier, in order to incorporate the dependence of the coefficients E_i on $m(\Xi^-\pi^+)$, the variation of the E_i with $m(\Xi^-\pi^+)$ is parametrized. Figure E.1 shows the distributions for E_i ($i = 0, ..., 6$), each fitted with a third order polynomial function. Table E.1 gives the χ^2/NDF and fit probabilities corresponding to the $E_{i=0,...,6}$ distributions of Fig. E.1.

Figure E.2 shows the efficiency calculated for each mass interval from Signal Monte Carlo. The curves correspond to the efficiency parametrization described by equation C.10, where the E_i mass dependence is parametrized by the fits shown in Fig. E.1.

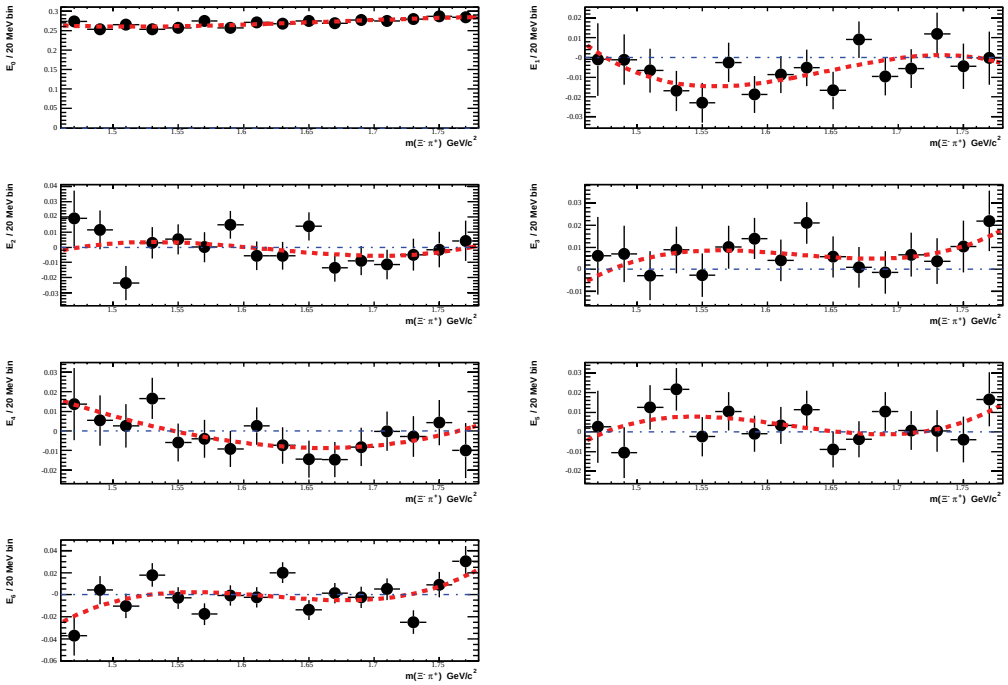

Figure E.1: The distributions of the coefficients E_i $(i = 0, ..., 6)$ calculated from the sum of the weights of the moments of truth-associated reconstructed Signal Monte Carlo events for each $(\Xi^-\pi^+)$ invariant mass interval. Superimposed on each distribution is a fit to a third order polynomial function. The corresponding χ^2/NDF and fit probabilities are listed in Table E.1.

Table E.1: The χ^2/NDF and fit probabilities corresponding to the distributions of Fig. E.1

E_i	χ^2/NDF	Fit probability
E_0	7.30 /12	0.84
E_1	8.51 /12	0.74
E_2	15.09 /12	0.24
E_3	6.20 /12	0.91
E_4	5.70 /12	0.93
E_5	9.15 /12	0.69
E_6	24.44 /12	0.02

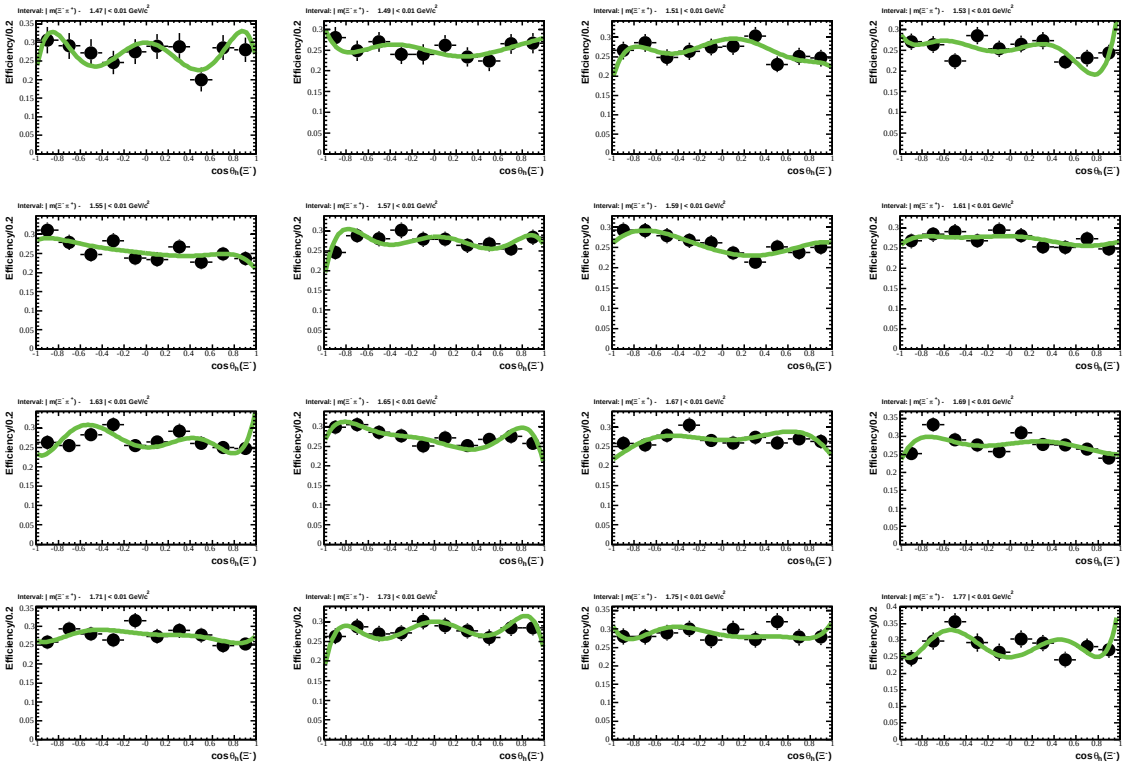

Figure E.2: The $\cos\theta_{\Xi^-}$ efficiency distributions corresponding to to each of the 16 20 MeV/c^2 intervals from $m(\Xi^-\pi^+) = 1.46$ GeV/c^2 to $m(\Xi^-\pi^+) = 1.78$ GeV/c^2. Superimposed are fits with the parametrization of equation C.10, with the values for the parameters E_i obtained from the calculated Signal Monte Carlo moments (equations C.8, C.14, C.9, C.15).

Because not all of the generated distributions are well-described by a zeroeth order polynomial function, the angular dependence of the efficiency for each mass interval differs slightly from the angular structure of the corresponding generated event distribution. Thus, in order to correct for this slight discrepancy, values of the E_i coefficients are obtained for each mass interval by fitting the corresponding efficiency distribution with the parametrization of equation C.10, where this time the values of E_i are extracted from a fit, with the input values equal to the values of E_i calculated from Signal Monte Carlo. Figure E.3 shows these fits to the $\cos\theta_{\Xi^-}$ efficiency distribution for each mass interval. The χ^2/NDF values and fit probabilities obtained from this procedure are given in Table E.2. Figure E.4 shows the simultaneous distributions of the E_i coefficients obtained by the two methods described. The open red circles correspond to the values of E_i extracted from the fit as a function of the Legendre polynomials with $L = 0, 1, ..., 6$. The black solid dots represent the values calculated from the Legendre polynomial moments. The mass dependence of the E_i coefficients extracted from the fit as a function of the Legendre polynomials, is obtained as before, from a fit with a third order polynomial function. The fitted E_i coefficients are shown in Fig. E.5 and the corresponding χ^2/NDF values and probabilities are given in Table E.3.

Figure E.6 shows the simultaneous $m(\Xi^-\pi^+)$ distributions in Signal Monte Carlo of generated events (black solid points), and of the truth-associated efficiency-corrected (with the parametrization of method 2) events (colored markers), where the pink open circles and the blue crosses correspond to the invariant mass of the $(\Xi^-\pi^+)$

Table E.2: The χ^2/NDF and fit probabilities corresponding to the distributions of Fig. E.3.

Mass interval in GeV/c^2	χ^2/NDF	Fit probability
$\lvert m(\Xi^-\pi^+) - 1.47\rvert < 0.01$	2.89 /3	0.41
$\lvert m(\Xi^-\pi^+) - 1.49\rvert < 0.01$	2.24 /3	0.52
$\lvert m(\Xi^-\pi^+) - 1.51\rvert < 0.01$	3.21 /3	0.36
$\lvert m(\Xi^-\pi^+) - 1.53\rvert < 0.01$	5.65 /3	0.13
$\lvert m(\Xi^-\pi^+) - 1.55\rvert < 0.01$	5.93 /3	0.12
$\lvert m(\Xi^-\pi^+) - 1.57\rvert < 0.01$	1.14 /3	0.77
$\lvert m(\Xi^-\pi^+) - 1.59\rvert < 0.01$	2.41 /3	0.49
$\lvert m(\Xi^-\pi^+) - 1.61\rvert < 0.01$	1.36 /3	0.72
$\lvert m(\Xi^-\pi^+) - 1.63\rvert < 0.01$	3.52 /3	0.32
$\lvert m(\Xi^-\pi^+) - 1.65\rvert < 0.01$	1.21 /3	0.75
$\lvert m(\Xi^-\pi^+) - 1.67\rvert < 0.01$	1.71 /3	0.64
$\lvert m(\Xi^-\pi^+) - 1.69\rvert < 0.01$	2.72 /3	0.44
$\lvert m(\Xi^-\pi^+) - 1.71\rvert < 0.01$	3.87 /3	0.28
$\lvert m(\Xi^-\pi^+) - 1.73\rvert < 0.01$	0.27 /3	0.97
$\lvert m(\Xi^-\pi^+) - 1.75\rvert < 0.01$	3.03 /3	0.39
$\lvert m(\Xi^-\pi^+) - 1.77\rvert < 0.01$	6.49 /3	0.09

Table E.3: The χ^2/NDF and fit probabilities corresponding to the distributions of Fig. E.5

E_i	χ^2/NDF	Fit probability
E_0	10.71 /12	0.55
E_1	10.34 /12	0.59
E_2	15.33 /12	0.22
E_3	8.67 /12	0.73
E_4	9.74 /12	0.64
E_5	9.91 /12	0.62
E_6	11.47 /12	0.49

system calculated using the true and reconstructed Monte Carlo values, respectively. No systematic deviations are observed. Figure E.7 shows the differences between the truth-associated efficiency-corrected $m(\Xi^-\pi^+)$ distributions and the generated distributions, with the invariant mass of the $(\Xi^-\pi^+)$ system calculated using the true and reconstructed Monte Carlo values, respectively.

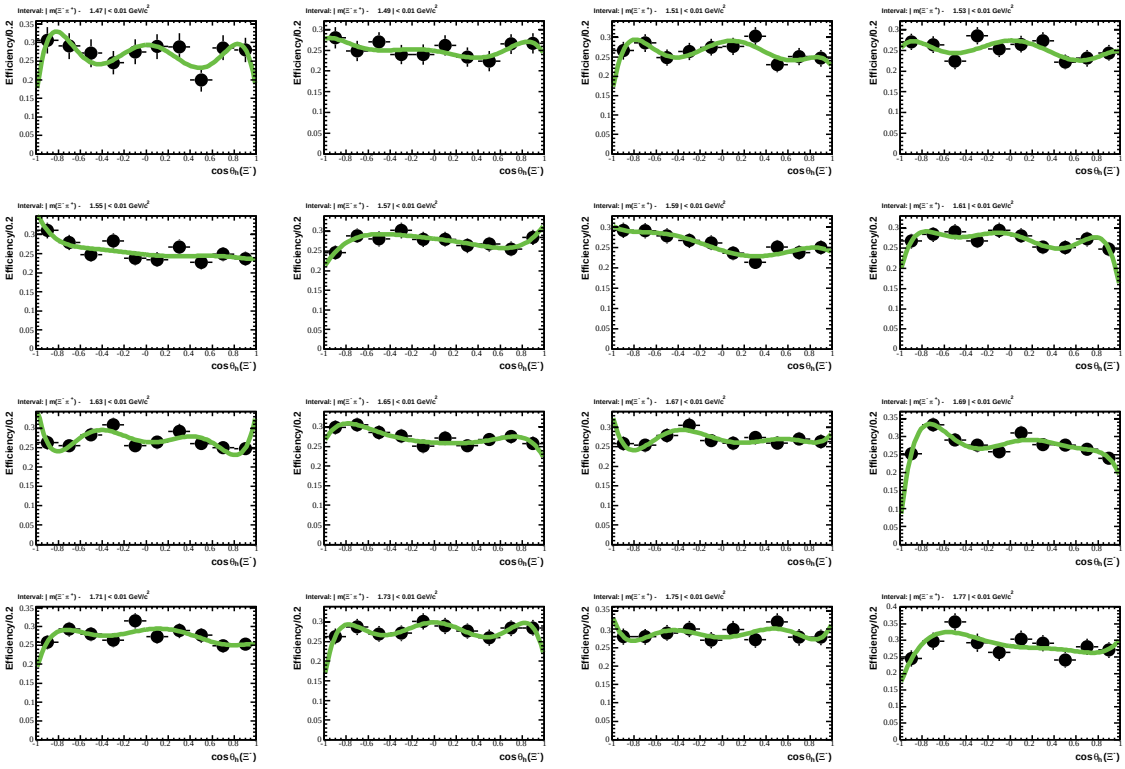

Figure E.3: The $\cos\theta_{\Xi^-}$ efficiency distributions corresponding to to each of the 16 20 MeV/c^2 intervals from $m(\Xi^-\pi^+) = 1.46$ GeV/c^2 to $m(\Xi^-\pi^+) = 1.78$ GeV/c^2. Superimposed are fits with the parametrization of equation C.10. The values of the parameters E_i are now extracted from this fit, and the fit parameter input values are the calculated E_i Signal Monte Carlo moments (equations C.8, C.14, C.9, C.15).

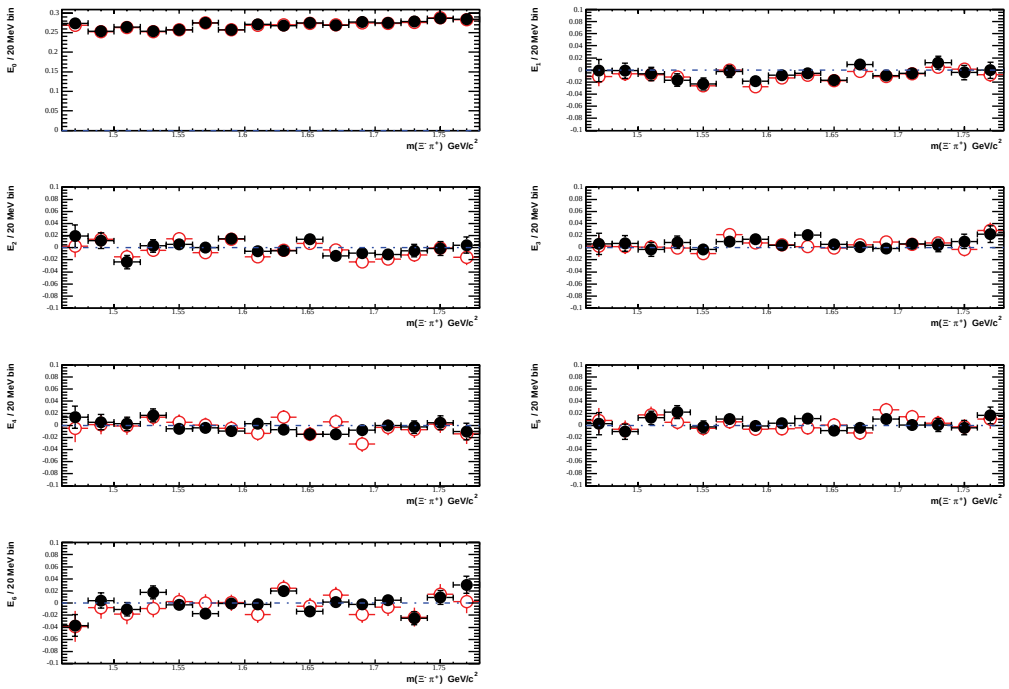

Figure E.4: The distributions of the E_i coefficients obtained from Signal Monte Carlo events. The open red circles correspond to the values of E_i extracted from a fit with a function of the Legendre polynomials with $L = 0, 1, ..., 6$. The black solid dots represent the values calculated from the Legendre polynomial moments.

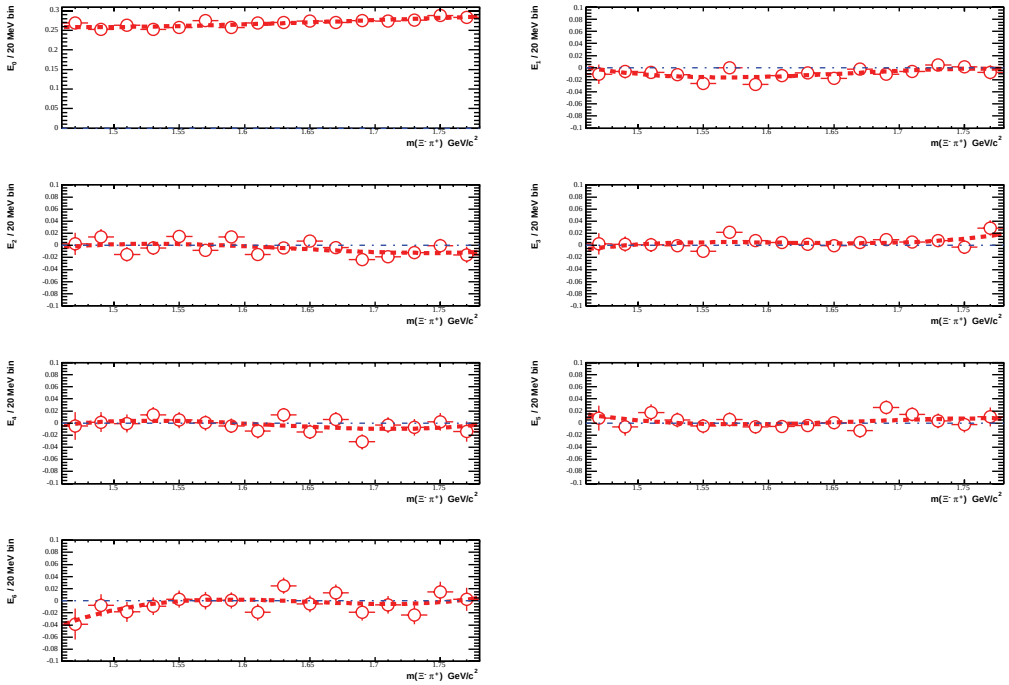

Figure E.5: The distributions of the E_i coefficients obtained from a fit with a function of the Legendre polynomials with $L = 0, 1, ..., 6$ to the efficiency calculated from Signal Monte Carlo for each mass interval. Superimposed is a fit with a third order polynomial function. The corresponding χ^2/NDF values and fit probabilities are listed in Table E.3.

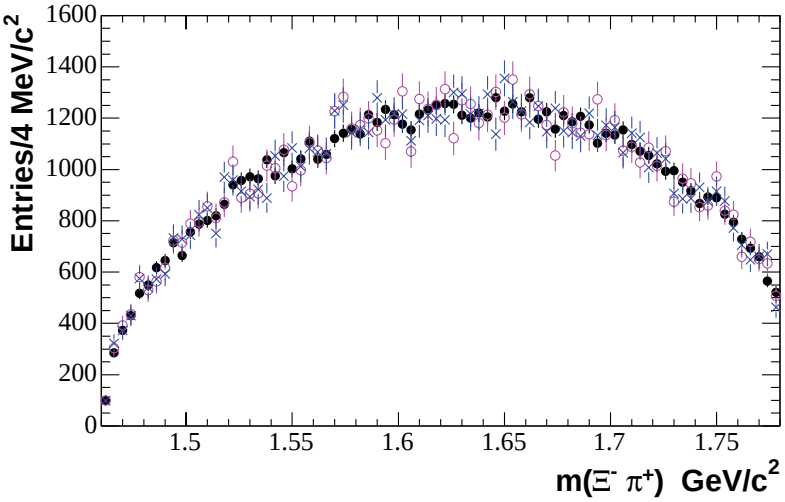

Figure E.6: The $m(\Xi^-\pi^+)$ distribution in Signal Monte Carlo. The black solid points correspond to the generated distribution. The colored data points represent the truth-associated efficiency-corrected $m(\Xi^-\pi^+)$ distributions, where the pink open circles and the blue crosses correspond to the invariant mass of the $(\Xi^-\pi^+)$ system calculated using the true and reconstructed Monte Carlo values, respectively.

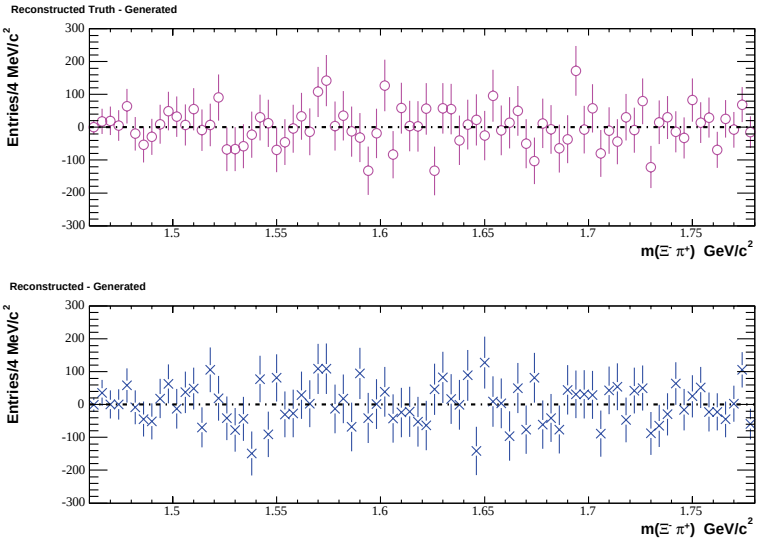

Figure E.7: The differences between the truth-associated efficiency-corrected $m(\Xi^-\pi^+)$ distributions and the generated distributions, with the invariant mass of the $(\Xi^-\pi^+)$ system calculated using the true (open pink circles) and reconstructed (blue stars) Monte Carlo values. No systematic deviations are apparent.

E.1 Efficiency-corrected Data

The uncorrected and efficiency-corrected distributions are now compared for data corresponding the Λ_c^+ mass-signal region. In Figs. E.8-E.10, the solid data points represent the uncorrected distributions, and the open circles the efficiency-corrected spectra scaled by the overall efficiency value of 26.6%. For Figs.. E.8 and E.10, the efficiency-correction procedure has little effect on the distributions, by Fig. E.9 shows that the $P_1(\cos\theta_{\Xi^-})$ moment is systematically shifted toward positive values for $\Xi^-\pi^+$ mass between $\sim$1.52 and 1.55 GeV/c^2, although the individual point uncertainties are large.

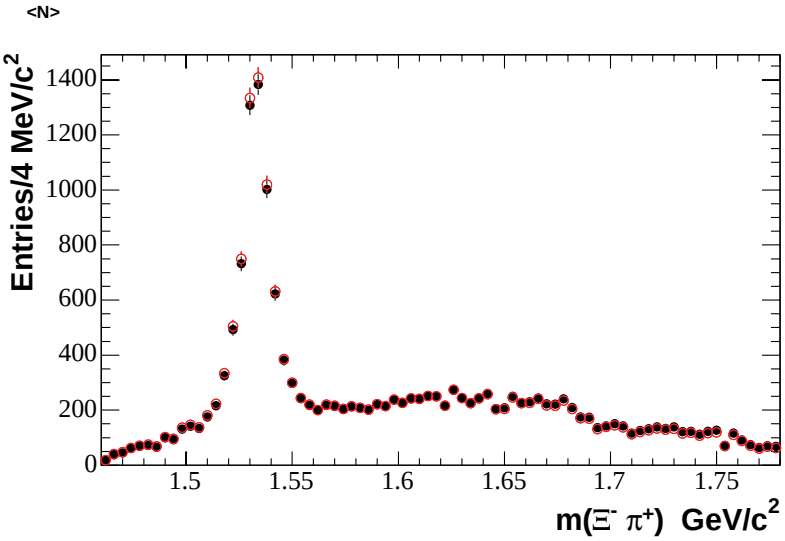

Figure E.8: The $(\Xi^-\pi^+)$ system invariant mass distribution corresponding to the Λ_c^+ mass-signal region; the solid data points represent the uncorrected distributions, and the open circles the efficiency-corrected spectrum scaled by the overall efficiency value of 26.6%.

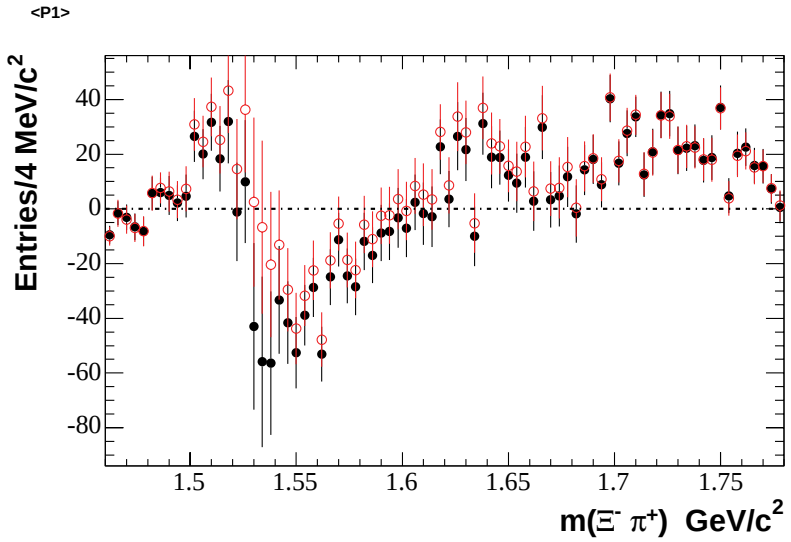

Figure E.9: The $P_1(\cos\theta_{\Xi^-})$ moment of the $(\Xi^-\pi^+)$ system invariant mass distribution corresponding to the Λ_c^+ mass-signal region; the solid data points represent the uncorrected distributions and the open circles, the efficiency-corrected spectrum scaled by the overall efficiency value of 26.6%.

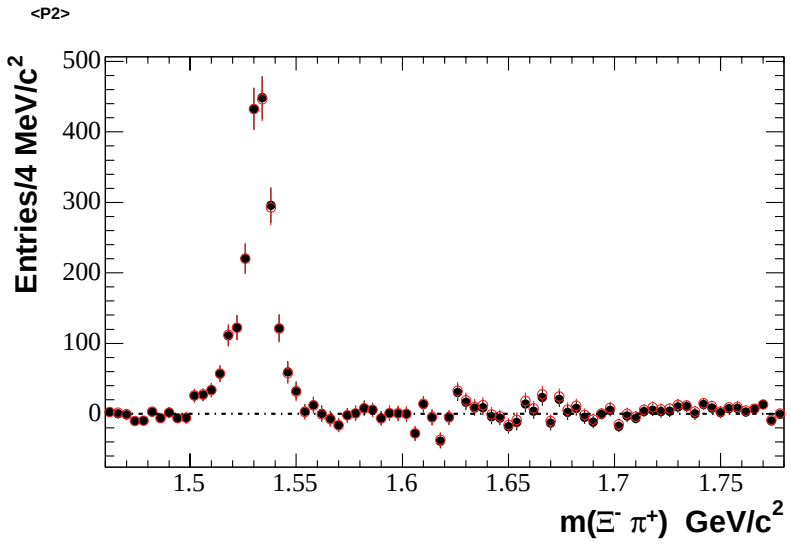

Figure E.10: The $P_2(\cos\theta_{\Xi^-})$ moment of the $(\Xi^-\pi^+)$ system invariant mass distribution corresponding to the Λ_c^+ mass-signal region; the solid data points represent the uncorrected distributions, and the open circles the efficiency-corrected spectrum scaled by the overall efficiency value of 26.6%.

APPENDIX F
THE AMPLITUDES OF THE ($\Xi^-\pi^+$) SYSTEM

As before, the following assumptions are made in order to write down the amplitudes describing the (Ξ^-, π^+) system:

- the spin of the Λ_c^+ is 1/2;
- since the Λ_c^+ are produced inclusively, it is assumed that the associated density matrix is diagonal;
- it is not assumed that the diagonal elements, denoted by $\rho_{1/2\,1/2}$ and $\rho_{-1/2\,-1/2}$ are equal.

It follows that for a choice of quantization axis along the (Ξ^-, π^+) direction in the Λ_c^+ rest-frame, the (Ξ^-, π^+) system can have helicity $\pm 1/2$, independently of its spin.

In the following derivation, we consider that at a particular $m(\Xi^-, \pi^+)$, the amplitude describing the decay to (Ξ^-, π^+) can be written as a superposition of amplitudes corresponding to total spin J values 1/2, 3/2 and 5/2. For each value of J, there can be two orbital angular momentum contributions, since $J = L \pm 1/2$; these contributions correspond to different parity values for the parent (Ξ^-, π^+) state, since parity is conserved in strong decay. The possibilities are summarized below.

Table F.1: The possible spin-parity values for the (Ξ^-, π^+) system $(P = (-1)^{L+1})$.

Spin (J)		Orbital Ang. Momt. (L)	Parity (P)	J^P
1/2	$[L + 1/2]$	0 [S-wave]	-	$1/2^-$
1/2	$[L - 1/2]$	1 [P-wave]	+	$1/2^+$
3/2	$[L + 1/2]$	1 [P-wave]	+	$3/2^+$
3/2	$[L - 1/2]$	2 [D-wave]	-	$3/2^-$
5/2	$[L + 1/2]$	2 [D-wave]	-	$5/2^-$
5/2	$[L - 1/2]$	3 [F-wave]	+	$5/2^+$

The angular distribution can then be written:

$$\begin{aligned} I &= \sum_{\lambda_i,\lambda_f} \rho_{i\,i} \left| \sum_J A^J_{\lambda_f} D^{J\,*}_{\lambda_i\,\lambda_f}(\phi,\theta,0) \right|^2 \\ &= \sum_{\lambda_i,} \rho_{i\,i} \left[\left| \sum_J A^J_{1/2} d^J_{\lambda_i\,1/2}(\theta) \right|^2 + \left| \sum_J A^J_{1/2} d^J_{\lambda_i\,-1/2}(\theta) \right|^2 \right] \end{aligned}$$

Parity conservation relates the $A^J_{\lambda_f}$ amplitudes by

$$\begin{aligned} A^J_{\lambda_f} &= A^J_{-\lambda_f} \eta_P \eta_\Xi \eta_{\pi^+} (-1)^{J - S_\Xi - S_\pi} \\ &= A^J_{-\lambda_f} \eta_P (-1)(-1)^{J-1/2} \\ &= A^J_{-\lambda_f} \eta_P (-1)^{J+1/2}. \end{aligned}$$

Here η_P is the parity of the parent state; since two orbital states can contribute to the spin J amplitude, this is not uniquely defined. It follows that the intensity needs to be expressed in terms of the orbital contributions in order to take parity conservation

into account. Writing the angular distribution explicitly:

$$\begin{aligned} I &= \rho_{1/2\,1/2}\left[\left|A^{1/2}_{1/2}d^{1/2}_{1/2,1/2}(\theta)+A^{3/2}_{1/2}d^{3/2}_{1/2,1/2}(\theta)+A^{5/2}_{1/2}d^{5/2}_{1/2,1/2}(\theta)\right|^2\right. \\ &\quad \left.+\left|A^{1/2}_{-1/2}d^{1/2}_{1/2,-1/2}(\theta)+A^{3/2}_{-1/2}d^{3/2}_{1/2,-1/2}(\theta)+A^{5/2}_{-1/2}d^{5/2}_{1/2,-1/2}(\theta)\right|^2\right] \\ &+ \rho_{-1/2\,-1/2}\left[\left|A^{1/2}_{1/2}d^{1/2}_{-1/2,1/2}(\theta)+A^{3/2}_{1/2}d^{3/2}_{-1/2,1/2}(\theta)+A^{5/2}_{1/2}d^{5/2}_{-1/2,1/2}(\theta)\right|^2\right. \\ &\quad \left.+\left|A^{1/2}_{-1/2}d^{1/2}_{-1/2,-1/2}(\theta)+A^{3/2}_{-1/2}d^{3/2}_{-1/2,-1/2}(\theta)+A^{5/2}_{-1/2}d^{5/2}_{-1/2,-1/2}(\theta)\right|^2\right] \end{aligned}$$

Substituting the appropriate d-functions into I, gives

$$\begin{aligned} I &= \rho_{1/2\,1/2}\left[\left|A^{1/2}_{1/2}+A^{3/2}_{1/2}\frac{3\cos\theta-1}{2}+A^{5/2}_{1/2}\frac{5\cos^2\theta-2\cos\theta-1}{2}\right|^2\cos^2\theta/2\right. \\ &\quad \left.+\left|A^{1/2}_{-1/2}+A^{3/2}_{-1/2}\frac{3\cos\theta+1}{2}+A^{5/2}_{-1/2}\frac{5\cos^2\theta+2\cos\theta-1}{2}\right|^2\sin^2\theta/2\right] \\ &+ \rho_{-1/2\,-1/2}\left[\left|A^{1/2}_{1/2}+A^{3/2}_{1/2}\frac{3\cos\theta+1}{2}+A^{5/2}_{1/2}\frac{5\cos^2\theta+2\cos\theta-1}{2}+A^{5/2}_{1/2}\right|^2\sin^2\theta/2\right. \\ &\quad \left.+\left|A^{1/2}_{-1/2}+A^{3/2}_{-1/2}\frac{3\cos\theta-1}{2}+A^{5/2}_{-1/2}\frac{5\cos^2\theta-2\cos\theta-1}{2}\right|^2\right] \end{aligned}$$

In order to simplify this expression taking into account parity conservation, the amplitudes $A^J_{\lambda_f}$ must be expressed in terms of the orbital angular momentum amplitudes for $L = J \pm 1/2$ which contribute.

In order to do this, use is made of the relationship between (L, S) states and helicity states. Following the prescription of Jacob and Wick [36],

$$\mid JM\,\lambda_1\lambda_2\rangle = \sum_{L,S}\beta_{LS}\mid JM\,LS\rangle,$$

where

$$\begin{aligned} \beta_{LS} &= \langle JM\,LS\mid JM\,\lambda_1\lambda_2\rangle \\ &= \frac{2L+1}{2J+1}C(LSJ;0\lambda)C(S_1S_2S;\lambda_1,-\lambda_2). \end{aligned}$$

Where $\lambda = \lambda_1 - \lambda_2$, and the C's are the Clebsch-Gordan coefficients:

$$\begin{aligned} C(LSJ;0\lambda) &= \langle L,0;S,\lambda \mid J,\lambda\rangle \\ C(S_1S_2S;\lambda_1,-\lambda_2) &= \langle S_1,\lambda_1;S_2,\lambda_2 \mid S,\lambda_1-\lambda_2\rangle \end{aligned}$$

Expressing $A^{1/2}_{1/2}$ and $A^{1/2}_{-1/2}$ in terms of S and P waves,

$$\begin{aligned} A^{1/2}_{1/2} &\equiv \mid J=1/2\, M=1/2, \lambda_1=1/2 \lambda_2=0\rangle \\ &= \beta_{L=0\,S=1/2} \mid J=1/2\, M=1/2; L=0\, S=1/2\rangle \\ &+\beta_{L=1\,S=1/2} \mid J=1/2\, M=1/2; L=1\, S=1/2\rangle, \end{aligned}$$

where

$$\beta_{L=0\,S=1/2} = \sqrt{\frac{1}{2}} C(0\,1/2\,1/2;0\,1/2) C(1/2\,0\,1/2;1/2\,0),$$

with

$$\begin{aligned} C(0\,1/2\,1/2;0\,1/2) &\equiv \langle 0,0;1/2,1/2 \mid 1/2,1/2\rangle = 1, \\ C(1/2\,0\,1/2;1/2\,0) &\equiv \langle 1/2,1/2;0,0 \mid 1/2,1/2\rangle = 1, \end{aligned}$$

$$\beta_{L=0\,S=1/2} = \sqrt{\frac{1}{2}};$$

and

$$\beta_{L=1\,S=1/2} = \sqrt{\frac{3}{2}} C(1\,1/2\,1/2;0\,1/2) C(1/2\,0\,1/2;1/2\,0)$$

with

$$C(1\,1/2\,1/2;0\,1/2) \equiv \langle 1,0;1/2,1/2 \mid 1/2,1/2\rangle = -\frac{1}{\sqrt{3}},$$

$$\beta_{L=1\,S=1/2} = -\frac{1}{\sqrt{2}};$$

so that

$$A^{1/2}_{1/2} = \frac{1}{\sqrt{2}}\left[S^{1/2} - P^{1/2}\right].$$

Similarly,

$$\begin{aligned} A^{-1/2}_{1/2} \quad &\equiv \mid J = 1/2\, M = -1/2, \lambda_1 = -1/2 \lambda_2 = 0\rangle \\ &= \beta_{L=0\,S=1/2} \mid J = 1/2\, M = -1/2; L = 0\, S = 1/2\rangle \\ &+ \beta_{L=1\,S=1/2} \mid J = 1/2\, M = -1/2; L = 1\, S = 1/2\rangle, \end{aligned}$$

where

$$\beta_{L=0\,S=1/2} = \sqrt{\frac{1}{2}} C(0\,1/2\,1/2; 0\ -1/2) C(1/2\,0\,1/2; -1/2\,0)$$

with

$$\begin{aligned} C(0\,1/2\,1/2; 0\ -1/2) &\equiv \langle 0, 0; 1/2, -1/2 \mid 1/2, -1/2\rangle = 1, \\ C(1/2\,0\,1/2; -1/2\,0) &\equiv \langle 1/2, -1/2; 0, 0 \mid 1/2, -1/2\rangle = 1, \end{aligned}$$

$$\beta_{L=0\,S=1/2} = \sqrt{\frac{1}{2}};$$

and

$$\beta_{L=1\,S=1/2} = \sqrt{\frac{3}{2}} C(1\,1/2\,1/2; 0\ -1/2) C(1/2\,0\,1/2; -1/2\,0)$$

with

$$C(1\,1/2\,1/2; 0\ -1/2) \equiv \langle 1, 0; 1/2, -1/2 \mid 1/2, -1/2\rangle = \frac{1}{\sqrt{3}},$$

$$\beta_{L=1\,S=1/2} = \frac{1}{\sqrt{2}};$$

so that

$$A^{1/2}_{-1/2} = \frac{1}{\sqrt{2}}\left[S^{1/2} + P^{1/2}\right].$$

$A^{3/2}_{1/2}$ and $A^{3/2}_{-1/2}$ are expressed in terms of P and D waves.

$$\begin{aligned} A^{3/2}_{1/2} \quad &\equiv| \; J = 3/2\, M = 1/2, \lambda_1 = 1/2 \lambda_2 = 0\rangle \\ &= \beta_{L=1\,S=1/2} \mid J = 3/2\, M = 1/2; L = 1\, S = 1/2\rangle \\ &+\beta_{L=2\,S=1/2} \mid J = 3/2\, M = 1/2; L = 2\, S = 1/2\rangle, \end{aligned}$$

with

$$\beta_{L=1\,S=1/2} = \sqrt{\frac{3}{4}} C(1\,1/2\,3/2; 0\,1/2) C(1/2\,0\,1/2; 1/2\,0),$$

with

$$C(1\,1/2\,3/2; 0\,1/2) \;\equiv\; \langle 1, 0; 1/2, 1/2 \mid 3/2, 1/2\rangle = \sqrt{\frac{2}{3}},$$

so that

$$\beta_{L=1\,S=1/2} = \sqrt{\frac{1}{2}};$$

and

$$\beta_{L=2\,S=1/2} = \sqrt{\frac{5}{4}} C(2\,1/2\,3/2; 0\,1/2) C(1/2\,0\,1/2; 1/2\,0),$$

where

$$C(2\,1/2\,3/2; 0\,1/2) \;\equiv\; \langle 2, 0; 1/2, 1/2 \mid 3/2, 1/2\rangle = -\sqrt{\frac{2}{5}},$$

$$\beta_{L=2\,S=1/2} = -\frac{1}{\sqrt{2}};$$

so that

$$A^{3/2}_{1/2} = \frac{1}{\sqrt{2}}\left[P^{3/2} - D^{3/2}\right].$$

$$\begin{aligned} A^{3/2}_{-1/2} \quad &\equiv \mid J = 3/2\, M = -1/2, \lambda_1 = -1/2 \lambda_2 = 0\rangle \\ &= \beta_{L=1\,S=1/2} \mid J = 3/2\, M = -1/2; L = 1\, S = 1/2\rangle \\ &+\beta_{L=2\,S=1/2} \mid J = 3/2\, M = -1/2; L = 2\, S = 1/2\rangle, \end{aligned}$$

with

$$\beta_{L=1\,S=1/2} = \sqrt{\frac{3}{4}} C(1\,1/2\,3/2; 0\ -1/2) C(1/2\,0\,1/2; -1/2\,0)$$

with

$$C(1\,1/2\,3/2; 0\ -1/2) \ \equiv \ \langle 1, 0; 1/2, -1/2 \mid 3/2, -1/2\rangle = \sqrt{\frac{2}{3}},$$

so that

$$\beta_{L=1\,S=1/2} = \sqrt{\frac{1}{2}};$$

and

$$\beta_{L=2\,S=1/2} = \sqrt{\frac{5}{4}} C(2\,1/2\,3/2; 0\ -1/2) C(1/2\,0\,1/2; -1/2\,0)$$

where

$$C(2\,1/2\,3/2; 0\ -1/2) \ \equiv \ \langle 2, 0; 1/2, -1/2 \mid 3/2, -1/2\rangle = \sqrt{\frac{2}{5}},$$

$$\beta_{L=2\,S=1/2} = \frac{1}{\sqrt{2}};$$

so that

$$A^{3/2}_{-1/2} = \frac{1}{\sqrt{2}}\left[P^{3/2} + D^{3/2}\right].$$

$A^{5/2}_{1/2}$ and $A^{5/2}_{-1/2}$ are expressed in terms of D and F waves.

$$\begin{aligned} A^{5/2}_{1/2} \quad &\equiv \mid J = 5/2\, M = 1/2, \lambda_1 = 1/2 \lambda_2 = 0\rangle \\ &= \beta_{L=2\,S=1/2} \mid J = 5/2\, M = 1/2; L = 2\, S = 1/2\rangle \\ &+ \beta_{L=2\,S=1/2} \mid J = 5/2\, M = 1/2; L = 3\, S = 1/2\rangle, \end{aligned}$$

with

$$\beta_{L=2\,S=1/2} = \sqrt{\frac{5}{6}} C(2\,1/2\,5/2; 0\,1/2) C(1/2\,0\,1/2; 1/2\,0)$$

with

$$C(2\,1/2\,5/2; 0\,1/2) \;\equiv\; \langle 2, 0; 1/2, 1/2 \mid 5/2, 1/2\rangle = \sqrt{\frac{3}{5}},$$

so that

$$\beta_{L=2\,S=1/2} = \sqrt{\frac{1}{2}};$$

and

$$\beta_{L=3\,S=1/2} = \sqrt{\frac{7}{6}} C(3\,1/2\,5/2; 0\,1/2) C(1/2\,0\,1/2; 1/2\,0)$$

where

$$C(3\,1/2\,5/2; 0\,1/2) \;\equiv\; \langle 3, 0; 1/2, 1/2 \mid 5/2, 1/2\rangle = -\sqrt{\frac{3}{7}},$$

$$\beta_{L=3\,S=1/2} = -\frac{1}{\sqrt{2}};$$

so that

$$A^{5/2}_{1/2} = \frac{1}{\sqrt{2}}\left[D^{5/2} - F^{5/2}\right].$$

$$\begin{aligned} A^{5/2}_{-1/2} \quad &\equiv \mid J = 5/2\, M = -1/2, \lambda_1 = -1/2 \lambda_2 = 0\rangle \\ &= \beta_{L=2\,S=1/2} \mid J = 5/2\, M = -1/2; L = 2\, S = 1/2\rangle \\ &+ \beta_{L=3\,S=1/2} \mid J = 5/2\, M = -1/2; L = 3\, S = 1/2\rangle, \end{aligned}$$

with

$$\beta_{L=2\,S=1/2} = \sqrt{\frac{5}{6}} C(2\,1/2\,5/2; 0\ -1/2) C(1/2\,0\,1/2; -1/2\,0)$$

with

$$C(2\,1/2\,5/2; 0\ -1/2) \ \equiv \ \langle 2, 0; 1/2, -1/2 \mid 5/2, -1/2\rangle = \sqrt{\frac{3}{5}},$$

so that

$$\beta_{L=2\,S=1/2} = \sqrt{\frac{1}{2}};$$

and

$$\beta_{L=3\,S=1/2} = \sqrt{\frac{7}{6}} C(3\,1/2\,5/2; 0\ -1/2) C(1/2\,0\,1/2; -1/2\,0)$$

where

$$C(3\,1/2\,5/2; 0\ -1/2) \ \equiv \ \langle 3, 0; 1/2, -1/2 \mid 5/2, -1/2\rangle = \sqrt{\frac{3}{7}},$$

$$\beta_{L=3\,S=1/2} = \frac{1}{\sqrt{2}};$$

so that

$$A^{5/2}_{-1/2} = \frac{1}{\sqrt{2}}\left[D^{5/2} + F^{5/2}\right].$$

The expressions for $A^J_{\lambda_f}$ in terms of S, P, D, and F waves are consistent with the parity conservation condition

$$A^J_{\lambda_f} = A^J_{-\lambda_f}\eta_P(-1)^{J+1/2},$$

with η_P, the intrinsic parent parity.

Substituting these amplitude expressions into I, where the $F^{5/2}$ amplitude is disregarded for simplicity,

$$\begin{aligned}
2I = {} & \rho_{1/2\,1/2} \times \\
& \left[\left|S^{1/2} - P^{1/2} + \left(P^{3/2} - D^{3/2}\right)\frac{3\cos\theta - 1}{2} + D^{5/2}\frac{5\cos^2\theta - 2\cos\theta - 1}{2}\right|^2 \cos^2\theta/2\right. \\
& \left. + \left|S^{1/2} + P^{1/2} + \left(P^{3/2} + D^{3/2}\right)\frac{3\cos\theta + 1}{2} + D^{5/2}\frac{5\cos^2\theta + 2\cos\theta - 1}{2}\right|^2 \sin^2\theta/2\right] \\
& + \rho_{-1/2\,-1/2} \times \\
& \left[\left|S^{1/2} - P^{1/2} + \left(P^{3/2} - D^{3/2}\right)\frac{3\cos\theta + 1}{2} + D^{5/2}\frac{5\cos^2\theta + 2\cos\theta - 1}{2}\right|^2 \sin^2\theta/2\right. \\
& \left. + \left|S^{1/2} + P^{1/2} + \left(P^{3/2} + D^{3/2}\right)\frac{3\cos\theta - 1}{2} + D^{5/2}\frac{5\cos^2\theta - 2\cos\theta - 1}{2}\right|^2 \cos^2\theta/2\right]
\end{aligned}$$

Using $\rho_{1/2\,1/2} + \rho_{-1/2\,-1/2} = 1$,

$$
\begin{aligned}
2I &= \left|S^{1/2}\right|^2 + \left|P^{1/2}\right|^2 + \left[\left|P^{3/2}\right|^2 + \left|D^{3/2}\right|^2\right]\left(\frac{3\cos^2\theta+1}{4}\right) \\
&\quad + \left|D^{5/2}\right|^2\left(\frac{5\cos^4\theta-2\cos^2\theta+1}{4}\right) \\
&\quad + 2\left[Re\left(S^{1/2}P^{3/2\,*}\right) + Re\left(P^{1/2}D^{3/2\,*}\right)\right]\cos\theta \\
&\quad + 2Re\left(S^{1/2}D^{5/2\,*}\right)\left(\frac{3\cos^2\theta-1}{2}\right) + 2Re\left(P^{3/2}D^{5/2\,*}\right)\cos^3\theta
\end{aligned}
$$

$$
\begin{aligned}
-2\left(\rho_{1/2\,1/2} - \rho_{-1/2\,-1/2}\right) \quad & \left[\left(Re\left(S^{1/2}P^{1/2\,*}\right) + Re\left(P^{3/2}D^{3/2\,*}\right)\left(\frac{9\cos^2\theta-5}{4}\right)\right.\right. \\
& \left.\left. + Re\left(P^{1/2}D^{5/2\,*}\right)\left(\frac{5\cos^2\theta-3}{2}\right)\right)\cos\theta\right. \\
& + \left(Re\left(S^{1/2}D^{3/2\,*}\right) + Re\left(P^{1/2}P^{3/2\,*}\right)\right)\left(\frac{3\cos^2\theta-1}{2}\right) \\
& \left. + Re\left(D^{3/2}D^{5/2\,*}\right)\left(\frac{15\cos^4\theta-12\cos^2\theta+1}{4}\right)\right]
\end{aligned}
$$

Integrating I over $\cos\theta$,

$$
N = \int_{-1}^{1} I d\cos\theta = \left|\mathrm{S}^{1/2}\right|^2 + \left|\mathrm{P}^{1/2}\right|^2 + \frac{\left|\mathrm{P}^{3/2}\right|^2 + \left|\mathrm{D}^{3/2}\right|^2}{2} + \frac{\left|\mathrm{D}^{5/2}\right|^2}{3},
$$

so that the intensity contribution for spin J has a multiplicative factor $2/(2J+1)$ before the square of the amplitudes. It follows that in order to have the integral over $\cos\theta$ to be 1 for each J value the amplitude L^J should be multiplied by the factor $\sqrt{\frac{2J+1}{2}}$.

Then,

$$
\begin{aligned}
I &= \frac{\left|S^{1/2}\right|^2+\left|P^{1/2}\right|^2}{2}+\left[\left|P^{3/2}\right|^2+\left|D^{3/2}\right|^2\right]\left(\frac{3\cos^2\theta+1}{4}\right)\\
&+\left|D^{5/2}\right|^2 3\left(\frac{5\cos^4\theta-2\cos^2\theta+1}{8}\right)\\
&+\left[Re\left(S^{1/2}P^{3/2\,*}\right)+Re\left(P^{1/2}D^{3/2\,*}\right)\right]\sqrt{2}\cos\theta\\
&+Re\left(S^{1/2}D^{5/2\,*}\right)\sqrt{3}\left(\frac{3\cos^2\theta-1}{2}\right)\\
&+Re\left(P^{3/2}D^{5/2\,*}\right)\sqrt{6}\cos^3\theta
\end{aligned}
$$

$$
\begin{aligned}
-\left(\rho_{1/2\,1/2}-\rho_{-1/2\,-1/2}\right)\quad &\left[\left(Re\left(S^{1/2}P^{1/2\,*}\right)+Re\left(P^{3/2}D^{3/2\,*}\right)\left(\frac{9\cos^2\theta-5}{2}\right)\right.\right.\\
&\left.+Re\left(P^{1/2}D^{5/2\,*}\right)\sqrt{3}\left(\frac{5\cos^2\theta-3}{2}\right)\right)\cos\theta\\
&+\left(Re\left(S^{1/2}D^{3/2\,*}\right)+Re\left(P^{1/2}P^{3/2\,*}\right)\right)\left(\frac{3\cos^2\theta-1}{\sqrt{2}}\right)\\
&\left.+Re\left(D^{3/2}D^{5/2\,*}\right)\sqrt{3}\left(\frac{15\cos^4\theta-12\cos^2\theta+1}{2\sqrt{2}}\right)\right],
\end{aligned}
$$

and,

$$
N=\int_{-1}^{1} I d\cos\theta=\left|\mathrm{S}^{1/2}\right|^2+\left|\mathrm{P}^{1/2}\right|^2+\left|\mathrm{P}^{3/2}\right|^2+\left|\mathrm{D}^{3/2}\right|^2+\left|\mathrm{D}^{5/2}\right|^2,
$$

as expected. With

$$
\begin{aligned}
P_0(\cos\theta) &= \frac{1}{\sqrt{2}}\\
P_1(\cos\theta) &= \sqrt{\frac{3}{2}}\cos\theta\\
P_2(\cos\theta) &= \sqrt{\frac{5}{2}}\left(\frac{3\cos^2\theta-1}{2}\right)\\
P_3(\cos\theta) &= \sqrt{\frac{7}{2}}\left(\frac{5\cos^3\theta-3\cos\theta}{2}\right)\\
P_4(\cos\theta) &= \frac{3}{\sqrt{2}}\left(\frac{35\cos^4\theta-30\cos^2\theta+3}{8}\right),
\end{aligned}
$$

and assuming that the density matrix elements are equal,

$$
\begin{aligned}
I &= \frac{P_0(\cos\theta)}{\sqrt{2}}\left[\left|S^{1/2}\right|^2+\left|P^{1/2}\right|^2\right] \\
&+\left(\frac{P_2(\cos\theta)}{\sqrt{10}}+\frac{P_0(\cos\theta)}{\sqrt{2}}\right)\left[\left|P^{3/2}\right|^2+\left|D^{3/2}\right|^2\right] \\
&+\left(\frac{\sqrt{7}}{4}P_4(\cos\theta)+\frac{8}{7}\frac{1}{\sqrt{10}}\mathrm{P}_2(\cos\theta)+\frac{\mathrm{P}_0(\cos\theta)}{\sqrt{2}}\right)\left|D^{5/2}\right|^2 \\
&+\frac{2}{\sqrt{3}}P_1(\cos\theta)\left[\mathrm{Re}\left(\mathrm{S}^{1/2}\mathrm{P}^{3/2\,*}\right)+\mathrm{Re}\left(\mathrm{P}^{1/2}\mathrm{D}^{3/2\,*}\right)\right] \\
&+\sqrt{2}P_2(\cos\theta)\mathrm{Re}\left(\mathrm{S}^{1/2}\mathrm{D}^{5/2\,*}\right)\sqrt{3} \\
&+\left(\frac{4}{5}\sqrt{\frac{3}{7}}P_3(\cos\theta)+\frac{6}{5}\mathrm{P}_1(\cos\theta)\right)Re\left(P^{3/2}D^{5/2\,*}\right) \\
&= \frac{P_0(\cos\theta)}{\sqrt{2}}\left(\left|S^{1/2}\right|^2+\left|P^{1/2}\right|^2+\left|P^{3/2}\right|^2+\left|D^{3/2}\right|^2+\left|D^{5/2}\right|^2\right) \\
&+P_1(\cos\theta)\left(\frac{2}{\sqrt{3}}\left[\mathrm{Re}\left(\mathrm{S}^{1/2}\mathrm{P}^{3/2\,*}\right)+\mathrm{Re}\left(\mathrm{P}^{1/2}\mathrm{D}^{3/2\,*}\right)\right]+\frac{6}{5}\mathrm{Re}\left(\mathrm{P}^{3/2}\mathrm{D}^{5/2\,*}\right)\right) \\
&+\frac{P_2(\cos\theta)}{\sqrt{10}}\left(\left|P^{3/2}\right|^2+\left|D^{3/2}\right|^2+\frac{8}{7}\left|D^{5/2}\right|^2+\sqrt{20}Re\left(S^{1/2}D^{5/2\,*}\right)\right) \\
&+\frac{4}{5}\sqrt{\frac{3}{7}}P_3(\cos\theta)\mathrm{Re}\left(\mathrm{P}^{3/2}\mathrm{D}^{5/2\,*}\right)+\frac{\sqrt{2}}{7}\mathrm{P}_4(\cos\theta)\left|\mathrm{D}^{5/2}\right|^2
\end{aligned}
$$

The orthogonality of Legendre polynomial functions implies

$$I = dN/d\cos\theta = \langle \mathrm{P}_0\rangle \mathrm{P}_0(\cos\theta) + ... + \langle \mathrm{P}_4\rangle \mathrm{P}_4(\cos\theta)$$

where,

$$\langle Pi\rangle = \int_{-1}^{1} P_i(\cos\theta)\mathrm{dN/d}\cos\theta\mathrm{d}\cos\theta \sim \sum_j P_i(\cos\theta_\mathrm{j})$$

are the background- (i.e. Λ_c^+ mass-sidebands) subtracted, efficiency-corrected Legendre polynomial averages.

Therefore the following relationship between the Legendre polynomial moments and the magnitudes of the contributing waves is given by the system of equa-

tions:

$$
\begin{aligned}
\langle P_0 \rangle &= \frac{1}{\sqrt{2}} \left(\left| S^{1/2} \right|^2 + \left| P^{1/2} \right|^2 + \left| P^{3/2} \right|^2 + \left| D^{3/2} \right|^2 + \left| D^{5/2} \right|^2 \right) \\
\langle P_1 \rangle &= \left(\frac{2}{\sqrt{3}} \left[Re \left(S^{1/2} P^{3/2\,*} \right) + Re \left(P^{1/2} D^{3/2\,*} \right) \right] + \frac{6}{5} Re \left(P^{3/2} D^{5/2\,*} \right) \right) \\
\langle P_2 \rangle &= \sqrt{10} \left(\left| P^{3/2} \right|^2 + \left| D^{3/2} \right|^2 + \frac{8}{7} \left| D^{5/2} \right|^2 + \sqrt{20} Re \left(S^{1/2} D^{5/2\,*} \right) \right) \\
\langle P_3 \rangle &= \frac{4}{5} \sqrt{\frac{3}{7}} Re \left(P^{3/2} D^{5/2\,*} \right) \\
\langle P_4 \rangle &= \frac{\sqrt{2}}{7} \left| D^{5/2} \right|^2
\end{aligned}
$$

REFERENCES

[1] M. Gell-Mann, Phys. Rev. **92**, 833 (1953).

[2] T. Nakano and K. Nishijima, Progr. of Theor. Phys. **10**, 581 (1955).

[3] M. Gell-Mann and A. Pais, Proceedings of the 1954 Glasgow Conference on Nuclear and Meson Physics (Pergammon Press, London, 1955).

[4] K. Nishijima, Progr. of Theor. Phys. **12**, 107 (1954).

[5] T. Nakano and K. Nishijima, Progr. of Theor. Phys. **13**, 285 (1955).

[6] M. Gell-Mann, Suppl. Nuovo Cimento, **848** (1956).

[7] M. Gell-Mann, Calif. Inst. of Technology Lab. Report, CTSL-20 (1961).

[8] Y. Ne'eman , Nucl. Phys. **26**, 222 (1961).

[9] M. Gell-Mann, Phys. Rev. **125**, 1067 (1962).

[10] M. Gell-Mann, p.805, Proceedings of the International Conference on High-Energy Physics, CERN (1962).

[11] Y. Eisenberg, Phys. Rev. **96**, 541 (1954).

[12] V. E. Barnes *et al.*, Phys. Rev. Lett. **12**, 204 (1964).

[13] L. W. Alvarez, Phys. Rev. **D8**, 702 (1973).

[14] M. Deutschmann *et al.*, Phys. Lett. **B73**, 96 (1978).

[15] M. Baubillier *et al.*, Phys. Lett. **B78**, 342 (1978).

[16] R. J. Hemingway *et al.*, Nucl. Phys. **B142**, 205 (1978).

[17] M. Gell-Mann, Phys. Lett. **8**, 214 (1964).

[18] G. Zweig, CERN preprints TH-401 and TH-412 (1964).

[19] J. J. Augustin *et al.*, Phys. Rev. Lett. **33**, 1406 (1974).

[20] E. G. Cazzoli *et al.*, Phys. Rev. Lett. **34**, 17 (1975).

[21] G. Goldhaber *et al.*, Phys. Rev. Lett. **37**, 255 (1976).

[22] W-M. Yao *et al.* (PDG2006), J.Phys. G:Nucl.Part.Phys. **33**, 1 (2006).

[23] The *BABAR* Collaboration, B. Aubert *et al.*, Phys. Rev. Lett. **95**, 142003 (2005).

[24] R. Armenteros *et al.*, *Phil. Mag.* **43**, 597 (1952).

[25] S. Capstick and N. Isgur, Phys. Rev. **D34**, 2809 (1986).

[26] F. Coester *et al.*, Nucl. Phys. **A634**, 335 (1998).

[27] Cascade Physics: A New Window on Baryon Spectroscopy
http://conferences.jlab.org/cascade/program.html.

[28] The *BABAR* Collaboration, B. Aubert *et al.*, Phys. Rev. Lett. **97**, 112002 (2006).

[29] V. Ziegler, Proceedings of the Meeting of the APS Topical Group on Hadronic Physics (GHP06), Journal of Physics: Conference Series.

[30] The *BABAR* Collaboration, B. Aubert *et al.*, hep-ex/0607043, Contributed Paper to ICHEP2006, Moscow, Russia.

[31] P.Oddone, in *Proceedings of the UCLA Workshop: Linear Collider $B\bar{B}$ factory conceptual Design*, edited by D.Stork, World Scientific (1987), p. 243.

[32] The *BABAR* Collaboration, B. Aubert *et al.*, Nucl. Instr. Meth. **A479**, 1 (2002).

[33] D. N. Brown, E. A. Charles, D. A. Roberts, The *BABAR* Track Fitting Algorithm, Proceedings of CHEP 2000, Padova, Italy (2000).

[34] P. F. Harrison and H. R. Quinn, The *BABAR* Physics Book, SLAC-504 (1998).

[35] *BABAR* Particle ID:
http://www.slac.stanford.edu/BFROOT/www/Physics/Tools/Pid/pid.html.

[36] M. Jacob and G. C. Wick, Ann. Phys. **7**, 404 (1959).

[37] S. U. Chung, CERN Yellow Report, CERN 71-8 (1971).

[38] E. Wigner, *Gruppentheories*, Freidrich Vieweg und Sohn, Braunschweig (1931); *Group Theory*, Academic Press, New York (1959).

[39] E. Wigner, Z. Phys. **43**, 624 (1927);
C. Eckart, Rev. Mod. Phys. **2**, 305 (1930).

[40] H. L. Anderson, E. Fermi, E. A. Land and D. E. Nagle, Phys. Rev. **85**, 936 (1952).

[41] F. James and M. Roos, "'Minuit' A System for Function Minimization and Analysis of the Parameter Errors and Correlations", Comput. Phys. Commun. **10**, 343 (1975).

[42] C. Dionisi *et al.*, Phys. Lett. **B80**, 145 (1978).

[43] S. F. Biagi *et al.*, Z. Phys. C **9**, 305 (1981).

[44] S. F. Biagi *et al.*, Z. Phys. C **34**, 15 (1987).

[45] M. I. Adamovich *et al.*, Eur. Phys. J. **C5**, 621 (1998).

[46] K. Abe *et al.*, Phys. Lett. **B524**, 33 (2002).

[47] S. M. Flatté, Phys. Lett. **B63**, 224 (1976).

[48] A. Abele *et al.*, Phys. Rev. **D57**, 3860 (1998).

[49] J. M. Blatt and V. F. Weisskopf, *Theoretical Nuclear Physics*, John Wiley and Sons (1952).

[50] B. Aubert *et al.*, Phys. Rev. **D72**, 052006 (2005).

[51] B. Aubert *et al.*, Phys. Rev. **D72**, 052008 (2005).

[52] B. Aubert *et al.*, hep-ex/0607104.

[53] P. Schlein *et al.*, Phys. Rev. Lett. **11**, 167 (1963).

[54] J. Button-Shafer *et al.*, Phys. Rev. **142**, 883 (1966).

[55] D. Aston *et al.*, Nucl. Phys. **B296**, 493 (1988).

[56] Private communication, W. M. Dunwoodie (SLAC).

[57] J. G. Korner and M. Kramer, Z. Phys. C **55**, 659 (1992).